Deformation-induced martensitic transformation under multiaxial loading

Thèse N° 7299

Wei-Neng HSU

2019

ÉCOLE POLYTECHNIQUE
FÉDÉRALE DE LAUSANNE

Acknowledgement

First and foremost, I would like to express my deep gratitude to Prof. Helena Van Swygenhoven for the opportunity to join her research group and undertake my PhD research in the ERC project MULTIAX. I sincerely thank Helena for her guidance and support as well as her passion and immense knowledge, altogether serving as the fuel for my research adventure. And I acknowledge my thesis jury members: Prof. Roland Logé, Prof. Ludovic Thilly and Dr. João Quinta da Fonseca for their dedication, time and insightful comments on this thesis.

A special thanks goes to Dr. Efthymios Polatidis, for his patience, guidance and support. Without our daily interaction and countless discussion, it would have not been possible to complete the studies presented in this thesis. My sincere gratitude extends to Dr. Miroslav Šmíd for his dedication and expertise in electron microscopy, which is indispensable for the success of the studies presented. So many good memories have been collected throughout the time that we three closely worked together. I would also like to thank Dr. Steven Van Petegem for his support and all the discussion, even at the risk that his coffee would become completely cold before I stop asking questions. I am grateful for his effort on developing the multiaxial cycling routine and the new fitting routine for the beautifully complex diffraction patterns from NiTi.

It has been a great honor for me to work in this esteemed research group. Many thanks to my colleagues in the ERC project: Dr. Ivo Kuběna, Dr. Jan Čapek, Dr. Karl Sofinowski, Dr. Manas Upadhyay, Dr. Maxime Dupraz, Dr. Monika Kubenova, and Dr. Tobias Panzner. My gratitude also goes to Dr. Malgorzata Grazyna Makowska and Dr. Sin Ting Cynthia Chang for the exchange of ideas and the share of your knowledge. I thank my PhD fellow Samy Hocine for suggesting new possibilities for sample manufacturing, and I thank Etienne Goy for the help with the French abstract of this thesis. I am grateful for all the support from PSI staff and external specialists. In particular, I thank Dr. Elisabeth Müller for her great support in preparation labs and electron microscopes, Alex Bollhalder for his expertise in the technical development, and Martina Füglister for the great assistance in all the administration works. I acknowledge Dr. Nicola Casati at MS beamline, Dr. Rolf Brönnimann at EMPA for the help in picosecond laser micromachining, and Dr. Matthieu Diserens at Micropat SA for his dedication in developing new sample preparation with me.

This journey would not have been possible without the friendships with Ainara Irastorza Landa, Esther Tsai, François Chatal, Jemila Habainy, Jui-Chia Chang, Li-Ting Tseng, Marina Garcia Gonzales, Ren Sui and Zhen Sun. Thank you all for sharing so much fun time together and your all-time strong supports in my stressful moments.

Last but not the least, I want to express my love to my family and my friends from university, for the unconditional love and support.

Abstract

The deformation-induced martensitic transformation observed in specific materials can enhance their mechanical properties or result in functional properties. For example, the transformation induced plasticity (TRIP) effect results in a good combination of ductility and strength in some stainless steels, and the superelasticity in NiTi alloys enables the materials to experience large deformation yet recover to the original shape. These unique properties have attracted significant technological interests for various structural and functional applications. Since the multiaxial deformation is expected during manufacturing and service of these components, it is crucial to understand the transformation behavior under complex loading conditions in addition to uniaxial loading. This study aims to establish the link between microstructural evolutions and the martensitic transformation induced by multiaxial deformation, by combining cruciform multiaxial mechanical tests with in situ X-ray and neutron diffraction, high-resolution digital image correlation (HRDIC) and electron microscopy characterizations. Several alloys exhibiting martensitic transformations are studied: a nanostructured superelastic NiTi alloy, a coarse-grained NiTi, and metastable austenitic stainless steels 201 and 304.

In the nanostructured superelastic NiTi, the distinctive transformation characteristics of nanoscaled subgrains under different loading directions are revealed, showing the path dependency of the martensitic variant selection. Moreover, it is found that multiaxial mechanical cycling leads to faster degradation in the superelasticity than the uniaxial cycling. The mechanisms for the material degradation, including the dislocation accumulation and the retained martensite, are discussed in terms of the crystallographic orientation and the load path.

In the coarse-grained NiTi, HRDIC captures the activation of high-Schmid-factor martensite variants and the contribution of each variant to strain accommodation under uniaxial loading. In addition to the Schmid law, it is observed that shear transmission across grain boundaries influences the martensite variant selection. A post-mortem transmission electron microscopy (TEM) investigation reveals deformation twinning occurring within the martensite as an additional strain accommodation mechanism.

In austenitic stainless steel 201, uniaxial loading is found to facilitate the martensitic transformation comparing to equibiaxial loading. However, 304 stainless steel exhibits the opposite trend: equibiaxial loading yields more martensite than uniaxial loading. The discrepancy is rationalized by the distinct deformation mechanisms depending on the evolving deformation textures under different load paths as well as the stacking fault energies of the materials. Furthermore, the HRDIC study on 304 steel shows the dependency of the slip activity on the loading direction at the grain level, supporting the nucleation mechanism of martensite proposed in literature.

Keywords

Martensitic transformation, superelastic NiTi, stainless steel, TRIP, materials degradation, multiaxial deformation, in situ mechanical testing, X-ray diffraction, neutron diffraction, high-resolution digital image correlation

Résumé

La transformation martensitique induite par déformation, pouvant-être observée dans des matériaux spécifiques, peut améliorer leurs propriétés mécaniques ou conduire à des propriétés fonctionnelles. Par exemple, l'effet de la plasticité induite par transformation (transformation induced plasticity ou TRIP) résulte en une bonne combinaison de ductilité et de résistance dans certains aciers inoxydables, ainsi qu'en la superélasticité des alliages NiTi, permettant à ces matériaux de subir une déformation importante tout en retrouvant leur forme initiale. Ces propriétés uniques ont suscité un intérêt technologique important pour diverses applications structurelles et fonctionnelles. Comme une déformation multiaxiale est attendue lors de la mise en œuvre et de l'utilisation de tels matériaux, il est crucial de comprendre le comportement de transformation dans des conditions de déformation complexes en plus d'une sollicitation uniaxiale. Cette étude vise à établir un lien entre les évolutions microstructurales et la transformation martensitique induite par une déformation multiaxiale, en combinant des essais mécaniques cruciformes multiaxiaux avec des essais in-situ de caractérisations par diffraction de rayons X et de neutrons, par de la corrélation d'images numériques de haute résolution (high-resolution digital image correlation ou HRDIC) et par microscopie électronique. Plusieurs alliages présentant des transformations martensitiques sont étudiés : un alliage NiTi superélastique nanostructuré, un alliage NiTi à grain grossier et deux aciers inoxydables austénitiques métastables 201 et 304.

Dans l'alliage NiTi superélastique nanostructuré, les caractéristiques distinctives de transformation des sous-grains nanométriques étant soumis à différentes directions de charge sont identifiées, montrant ainsi la dépendance entre la variété de martensite retenue et la séquence de déformation. De plus, on constate qu'une déformation cyclique multiaxiale entraîne une dégradation plus rapide de la superélasticité qu'une déformation cyclique uniaxiale. Les mécanismes de dégradation du matériau, y compris l'accumulation de dislocation et la martensite résiduelle, sont discutés en fonction de l'orientation cristallographique et du trajet de charge.

Dans le NiTi à grain grossier, le HRDIC saisit l'activation des variantes de martensite à facteur de Schmid élevé et la contribution de chaque variante à l'accommodation de la contrainte sous déformation uniaxiale. En plus de la loi de Schmid, il est observé que la transmission du cisaillement à travers les joints de grains à une influence sur la variante de martensite retenue. Une étude par microscopie électronique en transmission (MET) post-mortem révèle la présence de macles de déformation se produisant dans la martensite en guise de mécanisme supplémentaire d'accommodation des déformations.

Dans l'acier inoxydable austénitique 201, la déformation uniaxiale facilite la transformation martensitique par rapport à une déformation équibiaxiale. Cependant, l'acier inoxydable 304 présente la tendance inverse : la déformation équibiaxiale produit plus de martensite que la déformation

uniaxiale. La différence est expliquée par des mécanismes de déformation distincts en fonction de l'évolution des textures sous différents chemins de charge ainsi que par les énergies de défaut d'empilement des matériaux. De plus, l'étude de HRDIC sur l'acier 304 montre la relation entre le glissement et la direction de la contrainte au niveau du grain, soutenant le mécanisme de nucléation de la martensite suggéré dans la littérature.

Mots-clés

Transformation martensitique, NiTi superélastique, acier inoxydable, TRIP, dégradation des matériaux, déformation multiaxiale, essais mécaniques in-situ, diffraction de rayons X, diffraction de neutrons, corrélation d'images numériques à haute résolution

Contents

Contents

Contents

List of Figures

List of Tables

List of abbreviations

BCC	Body center cubic
BCT	Body centered tetragonal
Cf.	Confer (Latin), meaning consult or compare
CT	Computerized tomography
CVP	Correspondence-variant pair
DIC	Digital image correlation
EBSD	Electron backscatter diffraction
ECM	Electrochemical machining
ECMM	Electromechanical micromachining
EMPA	Swiss Federal Laboratories for Materials Science and Technology
EQ	Equibiaxial
Eq.	Equation
FCC	Face center cubic
FE	Finite element
FEG	Field emission gun
FIB	Focus ion beam
FOV	Field of view
FWHM	Full-width at half-maximum
HCP	Hexagonal closed packed
HPV	Habit plane variant
HRDIC	High-resolution digital image correlation
ICP-OES	Inductively Coupled Plasma-Optical Emission Spectrometry
IPF	Inverse pole figure
IQ	Image quality
LaB6	Lanthanum hexaboride
LPC	Load path change
LPD	Leading partial dislocation
Macro-DIC	Macroscopic digital image correlation
MS	Materials science

ND	Normal direction
NMP	N-Methyl-2-pyrrolidone
OPS	Oxide polishing suspensions
POLDI	Pulse overlap diffractometer
PTMC	Phenomenological crystallographic theory of martensitic transformation
RD	Rolling direction
ROI	Region of interest
RPM	Rotations per minute
SE	Superelasticity
SEM	Scanning electron microscope
SF	Schmid factor
SFE	Stacking fault energy
SINQ	Swiss Spallation Neutron Source
SLS	Swiss light source
SMA	Shape memory alloy
SPD	Shockley partial dislocation
SQ	Square
SQDP	Selected area diffraction pattern
SS	Stainless steel
STEM	Scanning Transmission Electron Microscope
TD	Transverse direction
TEM	Transmission electron microscope
TPD	Trailing partial dislocation
TR	Triangular
TRIP	Transformation induced plasticity
TWIP	Twinning induced plasticity
TX	Triaxiality
UN	Uniaxial
VSG	Virtual Strain Gauge
WD	Working distance
XRD	X-ray diffraction

Chapter 1 Introduction

1.1 Overview

Metals and alloys exhibit various deformation mechanisms in response to mechanical loading such as dislocation slip, deformation twinning and martensitic transformation. The focus of this study is the martensitic transformation induced by deformation. The martensitic transformation is a diffusionless process, during which the parent lattice, the austenite phase, transforms into the martensite phase with another crystal structure. It should be noted that the crystal structures of the austenite phase and the martensite phase depends on the alloy system, since the martensitic transformation can occur in various alloys other than steels. For example, the austenite in steels has a face-center-cubic (FCC) structure, usually denoted as γ austenite. As for NiTi alloys, the austenite phase exhibits an ordered body-center-cubic (BCC) structure, denoted as B2 austenite. The martensitic transformations improve the mechanical properties in various engineering alloys. The transformation induced plasticity (TRIP) in the steels results in a good combination of ductility and strength. The martensitic transformation in NiTi alloys gives rise to the superelasticity and a shape memory effect, enabling the material to undergo large deformation that is recoverable upon unloading or by heating. These properties have attracted significant technological interests and found applications in structural components (e.g. automotive components made of TRIP-steels [1-3]), smart structures (e.g. actuators made of NiTi [4, 5]) and medical devices (e.g. endovascular stents made of NiTi [5-8]).

Materials experience multiaxial deformation during manufacturing and their services. For example, the common sheet forming processes of steels impose complex strain paths, such as in-plane biaxial tension to the material, as well as changes in the strain path. As for an endovascular stent made of NiTi, the slender struts and bridges (Figure 1.1a) undergoes load path changes due to the systolic and diastolic blood pressures as well as the change in the artery geometry alongside body movements (Figure 1.1b).

Figure 1.1 (a) The geometry of a NiTi stent consists of struts and bridges [9]. (b) The shape change of the NiTi stent in the artery near the knee [5].

Despite undergoing multiaxial deformation during manufacturing or in operando, most important mechanical properties and transformation behaviors of materials are determined by monotonic uniaxial testing. Only few experimental works about martensitic transformations induced by multiaxial loading can be found in literature. In addition, the constitutive models based on the results of uniaxial testing may not be able to predict accurately the mechanical behavior of the material undergoing complex loading conditions in operando. In order to improve the existing models for phase transforming materials, it is crucial to understand the deformation-induced martensitic transformation under multiaxial loadings.

1.2 Deformation-induced martensitic transformation

The martensitic transformation can be induced thermally as well as by deformation. Figure 1.2a shows the chemical free energies as a function of temperature for the austenite and the martensite phases in steels [10]. The M_s shown in Figure 1.2a is the martensite start temperature. By quenching the austenite phase below M_s, martensite forms spontaneously as the thermodynamically favorable phase. The difference in the chemical free energies of austenite and martensite at M_s $\left(\Delta G_{M_s}^{\gamma \to \alpha'}\right)$ is the critical energy for martensitic transformation. The γ stands for the austenite phase in steels, and the α' denotes the BCC-martensite phase. At temperatures above M_s, the martensitic transformation can be induced by applying a mechanical load to the austenite. For example at the temperature T_1 shown in Figure 1.2a, martensite can form by providing a mechanical driving force $U' = \Delta G_{M_s}^{\gamma \to \alpha'} - \Delta G_{T_1}^{\gamma \to \alpha'}$. Patel and Cohen observed that martensite forms at temperatures higher than the M_s temperature when an external load is applied to the 0.5 wt. % C – 20 wt. % Ni steel [11], validating the concept of deformation-induced martensitic transformation. Bolling and Richmann extensively studied the deformation of Fe-Ni-C and Fe-Ni-Cr-C alloys [12-15], and they defined a temperature, M_s^{σ}, to characterize the deformation-induced martensitic transformation based on tensile tests at different temperatures. At M_s^{σ}, the critical stress to induce martensitic transformation is the same as the yield stress of the material. At temperatures below M_s^{σ} (yet above M_s), the yielding of the material was associated with the onset of the martensitic transformation, which was described as "stress-aided transformation". Similar to the concept presented in Figure 1.2a, in this "stress-aided" regime the chemical driving force (difference in free energies of austenite and martensite) increases with decreasing temperature, therefore the stress required for the transformation decreases with decreasing temperature. The regime above M_s^{σ} was defined as "transformation-aided plasticity", suggesting the formation of martensite accompanies the plastic deformation of austenite.
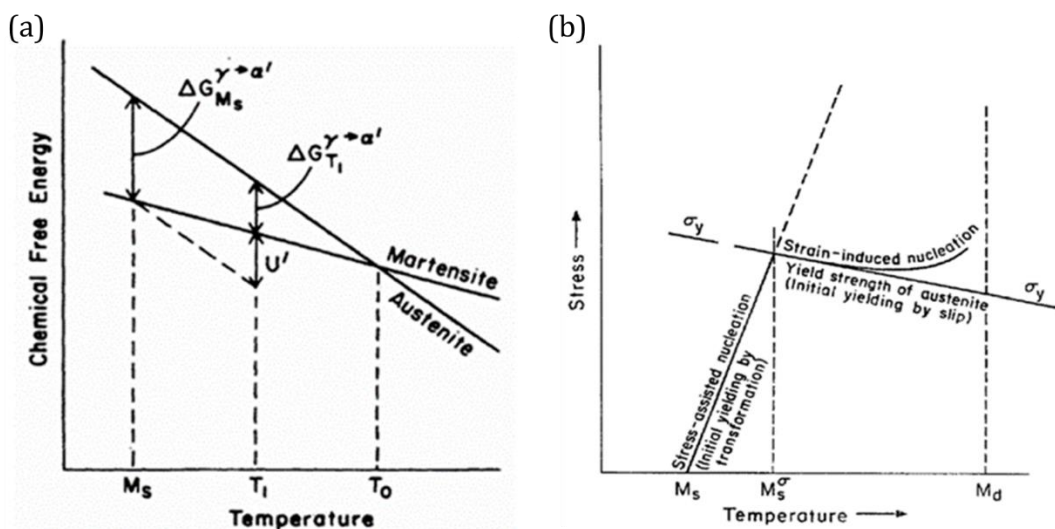
Figure 1.2 (a) The chemical free energies of austenite and martensite phases as a function of temperature [10]. (b) The plot of critical stress for the martensitic transformation in stress-assisted and strain-induced regimes [16].

3
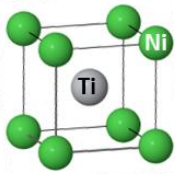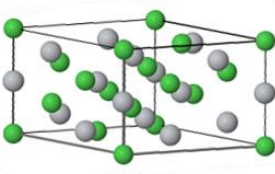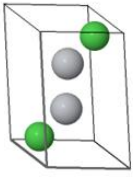
Based on the results of Bolling and Richman, Olson and Cohen further elaborated the interrelationships between the critical stress for martensite formation, the yield stress of austenite (σ_y in Figure 1.2b) and the temperature in the two regimes of transformation mechanisms with the illustration in Figure 1.2b [16]. As mentioned above, martensite forms spontaneously below M_s, while an external mechanical load can provide sufficient driving force to initiate the transformation above M_s. At temperatures between M_s and M_s^σ, the critical stress for martensite formation increases with increasing temperature, and it is within the elastic regime of austenite. This is the stress-assisted transformation regime. The critical stress reaches the yield stress of austenite at M_s^σ. The martensite formation above M_s^σ is regarded as the strain-induced transformation. In this regime, the plasticity of austenite starts to play a role in the transformation mechanism. Figure 1.2b shows that the critical stress deviates from the linear relationship extrapolated from the stress-assisted mechanism at temperatures above M_s^σ, i.e. the critical stresses are lower than the prediction based on the stress-assisted mechanism. More details about the relationships between the austenite plasticity and the strain-induced martensite are given in Section 1.4. Fahr also reported different natures of the stress-induced martensite and the strain-induced martensite in metastable austenitic steels [17]. The stress-induced martensitic transformation was reported to result in lower elongation than the strain-induced mechanism. The strain-induced martensitic transformation was able to reach an optimum combination of high ductility and high strength. Maxwell et al. reported the difference in the microstructures of stress-induced and strain-induced martensite in Fe-Ni-C alloys [18]. The stress-induced martensite exhibits the same plate morphology as thermally induced martensite. The strain-induced martensite was observed in the slip bands of the deformed austenite, suggesting the importance of austenite plasticity in the strain-induced mechanism.

Among the materials investigated in this study, the NiTi alloys exhibit stress-induced martensitic transformation, and the metastable 304 and 201 stainless steels show strain-induced martensitic transformation. The introductions to the martensitic transformations in NiTi and the stainless steels are given in more detail below.

1.3 Stress-induced martensitic transformation: NiTi alloys

The martensitic transformation in NiTi transforms the austenite phase (B2 austenite) into the B19'
martensite phase. In addition to B19' martensite, R-phase martensite has been reported as an
intermediate phase during the transformation between B2 and B19' [19]. Table 1.1 shows the crystal
structures of the B2 austenite, R martensite and B19' martensite in NiTi [20-22].

Table 1.1 The crystal structures [23] of the austenite phase [20], R-phase martensite [21] and B19' martensite [22].

Phase		B2 austenite	R martensite	B19' martensite
Unit cell c b⌐a				
Crystal system		Cubic	Trigonal	Monoclinic
Space group		P m -3 m	P -3	P 1 21/m 1
Lattice parameters	a (Å)	3.009	7.347	2.898
	b (Å)	3.009	7.347	4.108
	c (Å)	3.009	5.284	4.646
	α (°)	90	90	90
	β (°)	90	90	97.78
	γ (°)	90	120	90

Based on the "phenomenological crystallographic theory of martensitic transformation" (PTMC), the
essential parameter in martensitic transformation is that the invariant plane between austenite and
martensite should remain undistorted and un-rotated during transformation. This interface is
regarded as the habit plane of martensitic transformation. In order to maintain the habit plane, the
total shape deformation of the martensitic transformation consists of three components: (1) lattice
deformation from austenite lattice to martensite lattice, (2) lattice rotation and (3) lattice invariant
shear. The theory predicts the martensite substructure to be either slip steps or twins. Several electron
microscopy studies have reported the twinned structure of the martensite in NiTi [24-26]. Figure 1.3a
shows an example of the twinned martensite composed of wide and narrow regions (designated with
A and B, respectively, in Figure 1.3a). Knowles and Smith [25] made first calculation based on PTMC
and reported two possible twinning systems as the lattice invariant shear: {1 1 $\bar{1}$} Type I twinning and
<0 1 1> Type II twinning. Figure 1.3b illustrates the shape change from an austenite to a martensite
plate as well as the habit plane. A martensite plate composed of the martensite matrix and its twin is
called a habit plane variant (HPV). The pair of a matrix and its twin in a HPV exhibits a specific lattice
correspondence with the austenite phase [27]. Matsumoto et al. [27] studied the stress-induced
martensite in single crystal NiTi alloys and observed habit planes in a good agreement with the

theoretical predictions for both $\{1\ 1\ \bar{1}\}$ Type I twinning and $<0\ 1\ 1>$ Type II twinning. However, the Schmid factor of the HPVs for $\{1\ 1\ \bar{1}\}$ Type I twinning was too low to be considered as an active system. On the other hand, $<0\ 1\ 1>$ Type II twinning resulted in highest or second highest Schmid factor. Therefore, they concluded that the $<0\ 1\ 1>$ Type II twinning is the lattice invariant shear system for the B2 to B19' transformation in NiTi. Table 1.2 shows the good agreement between the theory and the experimental observation for $<0\ 1\ 1>$ Type II twinning. Since there are two lattice invariant shears for the Type II twinning ($[0\ 1\ 1]$ and $[0\ 1\ \bar{1}]$) and 12 lattice correspondences between the B2 and B19' lattices, there are 24 HPVs for the B2 – B19' transformation [27] .
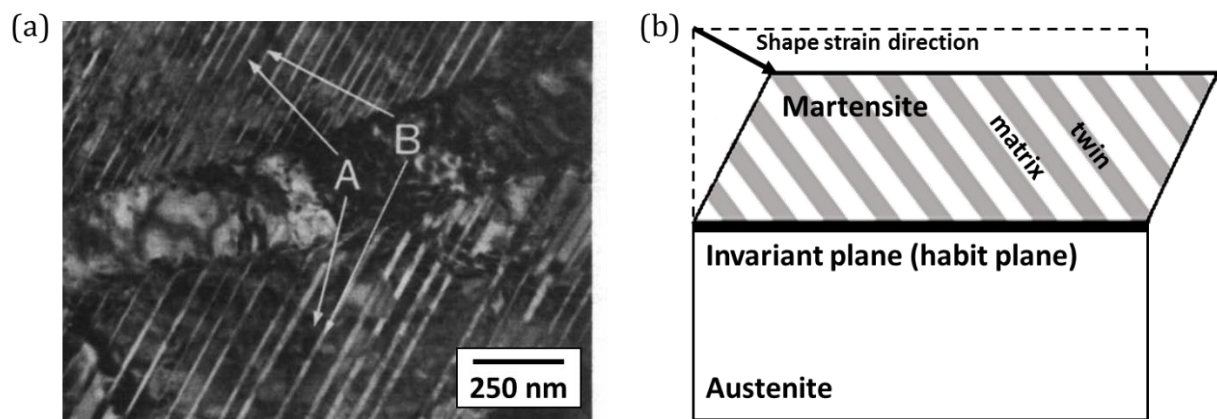
Figure 1.3 (a) The twinned structure of B19' martensite in NiTi consists of wide (A) and narrow (B) bands [25]. (b) An illustration of the martensitic transformation from austenite to twinned martensite NiTi.

Table 1.2 Comparison of the B2-B19' habit plane between theory and experiment for $<0\ 1\ 1>$ Type II twinning [27].

	Theoretical	Experimental	Deviation
Habit plane	(-0.88888 0.21523 0.40443)	(-0.8684 0.26878 0.4138)	3.3°
Direction of shape strain	[0.43448 0.75743 0.48737]	[0.4580 0.7706 0.4432]	3.0°

The reversible phase transformation between B2 austenite and B19' martensite results in two important properties of NiTi: the shape memory effect and the superelasticity (also called pseudoelasticity) [28-30]. Figure 1.4a shows the regimes of the two properties and their relations with the four characteristic temperatures for martensitic transformation: the martensite start temperature M_s, the martensite finish temperature M_f, the austenite start temperature A_s and the austenite finish temperature A_f. The shape memory effect occurs at temperatures below A_s, where the martensite phase is thermodynamically stable, and formed spontaneously upon cooling. Figure 1.4b shows an example of the stress-strain curve obtained in this regime, where the initial phase is thermally induced martensite [29]. After unloading, martensite stays deformed and results in the residual strain shown in Figure 1.4b. The residual strain can be recovered by inducing the reverse transformation by heating to a temperature above A_f. The material will then return to its original shape.

In the superelasticity regime shown in Figure 1.4a, the critical stress of the martensitic transformation is lower than the stress to introduce dislocation slip in the austenite phase. Hence, the martensitic transformation is considered stress-induced in the case of superelasticity. Superelasticity appears when deforming NiTi at temperatures above A_f, and a typical stress-strain curve is shown in Figure 1.4c [29]. Upon loading the austenite (the initial phase), stress-induced martensite forms and contributes to the large increment in strain (from 1% to 5% in Figure 1.4b), resulting in an "upper plateau" in the stress-strain curve at a nearly constant stress (~300 MPa in Figure 1.4c). Upon unloading, the reverse transformation takes place, resulting in a "lower plateau" in the curve. No residual strain is observed after fully unloading. Superelasticity enables the material to sustain large deformation without introducing residual strain after unloading.
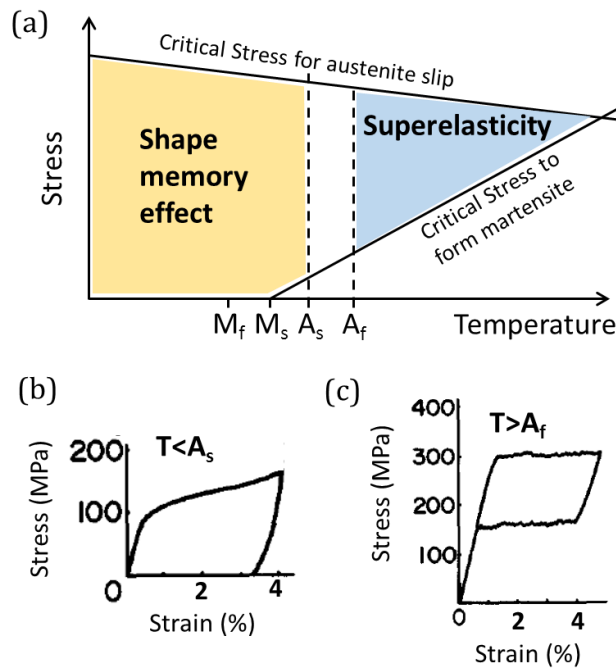
Figure 1.4 (a) The interrelations between shape memory effect, superelasticity, applied stress and temperature (adapted from [6]). (b) An example stress-strain curve measured at a temperature below A_s (the shape memory effect regime) [29]. (c) A typical stress-strain curve showing superelasticity [29].

The temperature dependency of critical stress for the stress-induced martensitic transformation can be expressed by the Clausius-Clapeyron equation [31-33]:

$$\frac{d\sigma}{dT} = \frac{\Delta S}{\varepsilon} = \frac{\rho \Delta H}{\varepsilon T_0}$$

where ΔS is the entropy of transformation, ε is the transformation strain, ρ is the density of the alloy, ΔH is the enthalpy of transformation and T_0 is the equilibrium temperature between austenite and martensite. Melton and Mercier [33] reported positive values of $\frac{d\sigma}{dT}$ for NiTi alloys, suggesting the critical stress to induce martensitic transformation increases with the increasing temperature. In [33], Melton and Mercier further pointed out that the change in the chemical composition could change the

transformation behavior of NiTi. The effect of Ni content on the transformation start temperature (M_s) has been summarized in [34]. In the range of 50 to 51.5 at. % Ni, the M_s decreases drastically with increasing Ni content. The composition dependency offers the possibility to tune the transformation behavior by changing the Ni content in NiTi. One good way to adjust the composition is aging treatment [35]. During an isothermal aging, the formation of Ni_4Ti_3 precipitates induce a decrease in Ni content of the NiTi matrix, resulting in an increase in the M_s temperature with the increasing aging time until a value corresponding to the equilibrium composition at the aging temperature. The control of Ni_4Ti_3 precipitation as well as the introduction of dislocations by cold working are common steps in the thermomechanical treatments of NiTi alloys to achieve good superelasticity and shape memory. For example, it has been reported that in a Ti-49.8Ni wire, a good superelasticity appears in a wide temperature range above A_f as a result of cold working followed by 1-hour annealing at 673K [36]. Another factor affecting superelasticity is the grain size of B2 austenite [37-40]. For example, Delville et al. [37] reported different grain sizes achieved by heat treatments from a pulsed electric current in a 50.8Ni - 49.2Ti wire. The wire with austenite grain size in the range of 25 – 50 nm showed the least degradation in superelasticity after uniaxial mechanical cycling compared to the wires with larger grain sizes. The shape of the superelastic stress-strain curve barely changed, and little residual strain was observed after mechanical cycling.

The stability of superelasticity during uniaxial mechanical cycling has been extensively studied [37, 41-55]. Degradation in superelasticity manifests itself by (1) the decrease in the critical transformation stress as the number of cycles increases, (2) the accumulation of residual strain due to dislocations and retained martensite after cycling. The repetition of the forward and reverse transformations during mechanical cycling accumulates dislocations, as evidenced by TEM studies [37, 49-52, 54, 56, 57] (see Figure 1.5). The accumulating dislocations contribute to the residual strain in B2 austenite. The stress fields around the dislocations decrease the external work required for the stress-induced martensitic transformation, thus decreasing the critical transformation stress. A locally high stress due to dislocation accumulation can also impede the reverse transformation, resulting in retained martensite after mechanical cycling [53]. In addition to the changes in the B19' martensitic transformation, dislocations introduced by cycling can promote the formation of an intermediate R-phase martensite, changing the transformation path from B2 – B19' to B2 – R – B19' [50, 55, 58-60].

Before mechanical cycling   After 10 uniaxial tension cycles
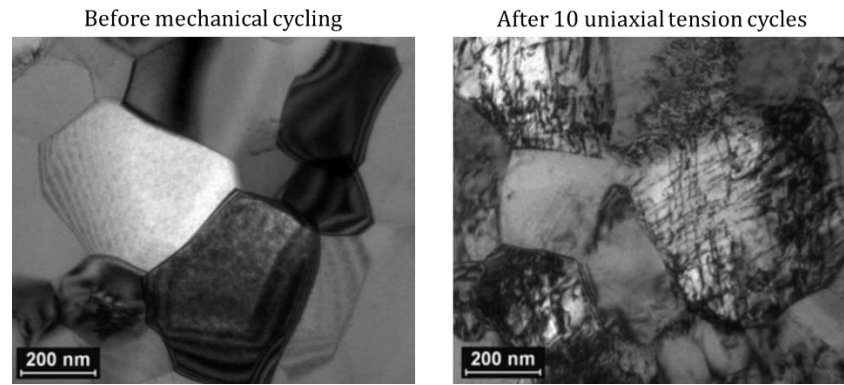
Figure 1.5 The microstructures of 50.9Ni-49.1Ti before and after 10 mechanical cycles, showing the accumulation of dislocations in austenite grains.

In literature, superelasticity in NiTi and its stability were mostly investigated with uniaxial tensile testing. Under a uniaxial tensile load, the deformation of superelastic NiTi resembles the evolution of Lüders bands in fine-grained steel strips and wires. Shaw et al. [61] observed the appearance of sharp Lüders-like bands in NiTi strips at the critical stress for martensitic transformation, suggesting the nucleation of the stress-induced martensite. Subsequent loading resulted in the propagation of the bands, in which the martensite formed continuously. The Lüders-like transformation bands in NiTi under uniaxial tension have been investigated with digital image correlation (DIC) [62-64]. The quantitative strain maps provided by DIC shows the inhomogeneous deformation of superelastic NiTi under uniaxial tension as high strains localize within the bands upon loading. The stress-induced martensitic transformation account for superelasticity depends on the loading direction and the type of loading [62, 65-70]. Daly et al. [62] performed a uniaxial tensile test on a thin strip with a hole at center, introducing multiaxial stress states around the hole. The transformation bands were found to nucleate at the edge of the hole and grow into an X shape, as shown in Figure 1.6a.

Grossmann et al. [65] studied the similar geometry using finite element simulation (only quarter of the geometry). Upon loading, the first martensite domain nucleated at the edge of the hole, as indicated by the circle in Figure 1.6b. Upon further straining, a new martensite domain appeared above the one at the edge, and it continued to propagate into a full band. The first martensite domain stopped growing as soon as the new domain formed. Wang et al. [66] employed finite element simulation to study the martensitic transformation under plane strain and plane stress conditions, and reported that the high triaxial stress under plane strain suppressed the formation of martensite. These results suggest the complex transformation events under multiaxial stress states.
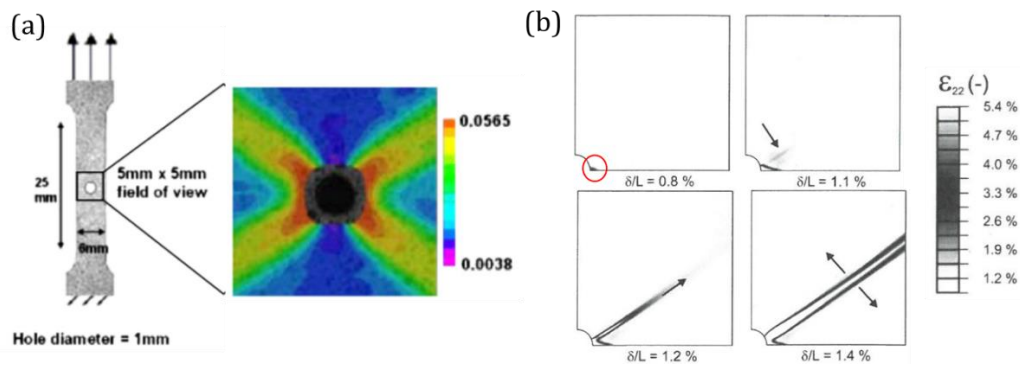
Figure 1.6 (a) An X-shape transformation band with inhomogeneous strain distribution around the central hole exhibiting multiaxial stress states [62]. (b) Finite element simulations of the formation of martensite under multiaxial stress states [65].

Elibol et al. [67] characterized the transformation behaviors of the 50.9Ni-49.1Ti under uniaxial tension, uniaxial compression and a combined compression-shear load using DIC. Transformation bands were observed under uniaxial tension and compression-shear load (Figure 1.7a), showing the inhomogeneous deformation. On the contrary, under compression martensite forms homogeneously, resulting in the uniform strain distribution shown in Figure 1.7a. McNaney et al. [68] reported lower transformation strain under a tension-torsion biaxial load than under uniaxial tension in a 50.8Ni-49.2Ti tube. In addition to proportional biaxial loading, they performed load-path-change experiments in which tension followed by torsion. A second plateau shown in Figure 1.7b appeared when changing the loading condition from tension to torsion, suggesting the formation of new martensite variants. Niendorf et al. [69] compared the formation of martensite variants under uniaxial tension and a biaxial stress state using a notched sample (Figure 1.7c). Only one variant formed in the [1 1 1]-oriented austenite grain upon uniaxial loading. In contrast, at least two martensite variants were observed under the biaxial state. Few studies have reported the effect of multiaxial mechanical cycling on the degradation in superelasticity. Song et al. [71, 72] performed uniaxial tension cycling and tension-torsion cycling with non-proportional multiaxial paths on a superelastic NiTi. The residual strain accumulation was observed to depend on the load paths. Based on the mechanical data, they concluded that multiaxial cycling introduces higher residual strains and a shorter fatigue life than uniaxial cycling.

Most multiaxial studies mentioned above investigated the degradation in superelasticity by addressing macroscopic parameters such as the decrease in the transformation stress and the development of the residual strain based on the mechanical data. However, the details on the degradation in the microstructure were not discussed. Khodaei et al. reported that constitutive modelling failed to predict the mechanical response under multiaxial loading, as the current models do not capture the dependency of the martensitic transformation on the crystallographic orientation and the loading path [73]. Detailed experimental data is required to improve the micromechanical models.

(a) Compression-shear loading

(b) Tension followed by torsion

(c) Uniaxial tension / Biaxial stress state near the notch
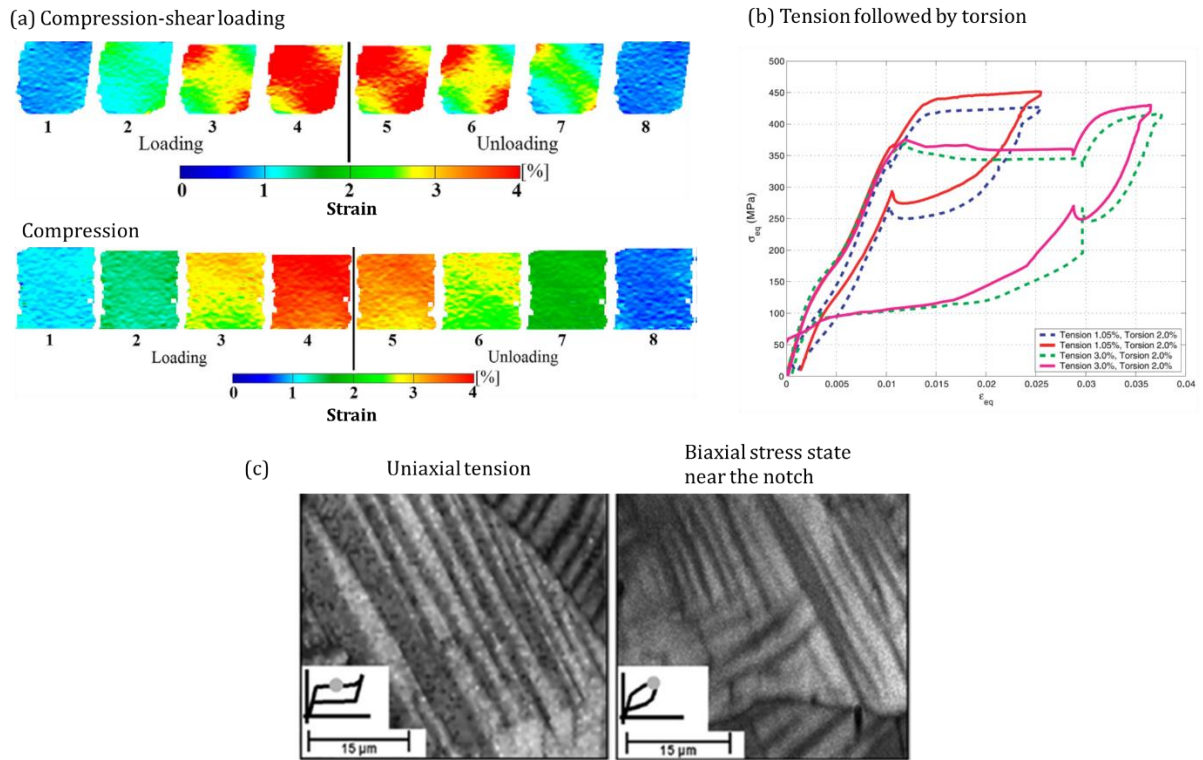
Figure 1.7 (a) The DIC strain maps for compression-shear and compression loadings [67]. (b) The equivalent stress-strain curves of tension followed by torsion tests [68]. (c) Single variant upon uniaxial loading and multiple variants under biaxial loading. The grey dots indicate the loading state where the micrographs were taken [69].

1.4 Strain-induced martensitic transformation: austenitic steels

In metastable austenitic steels (e.g. stainless steel 304), the TRIP effect enhances both the ductility and the strength of the materials [74]. The mechanism behind the TRIP effect is the strain-induced martensitic transformation occurring during the plastic deformation of the parent austenite phase. Upon mechanical loading, the γ austenite with FCC structure can transform into the ε martensite with HCP structure and/or α' martensite. The crystal structures of these phases are shown in Figure 1.8. It has been reported that α' martensite exhibits BCC or BCT structure depending on the carbon content, and the c/a ratio of α' martensite increases with increasing carbon content [75, 76]. In the stainless steels containing lower than 0.5 wt. % carbon, α' martensite is BCC. The orientation relationships between the γ austenite and ε martensite are $\{1\,1\,1\}_\gamma\,||\,\{0\,0\,0\,1\}_\varepsilon$, $<1\,1\,0>_\gamma\,||\,<1\,1\,\bar{2}\,0>_\varepsilon$. As for the α' martensite, there are two commonly reported orientation relationships, i.e. the Kurdjumov-Sachs relationship [77]: $\{1\,1\,1\}_\gamma\,||\,\{1\,1\,0\}_{\alpha'}$, $<1\,1\,0>_\gamma\,||\,<1\,1\,1>_{\alpha'}$ and the Nishiyama-Wassermann relationship [78, 79]: $\{1\,1\,1\}_\gamma\,||\,\{1\,1\,0\}_{\alpha'}$, $<2\,1\,1>_\gamma\,||\,<1\,1\,0>_{\alpha'}$.
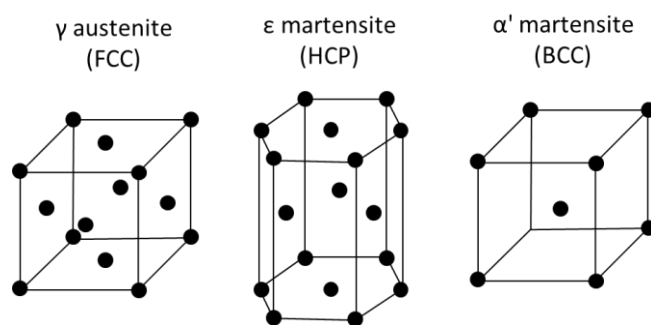
Figure 1.8 The crystal structures of the γ austenite, ε martensite and α' martensite in stainless steels.

The HCP ε martensite has been reported to be an intermediate phase between γ austenite and α' martensite [80]. From the aspect of the atomic arrangement, a stacking fault introduced by plastic deformation locally changes the stacking sequence of FCC into an HCP structure, providing a potential nucleation site for the ε martensite. Brooks et al. has observed the formation of the ε martensite in the region where multiple stacking faults overlap, as shown in Figure 1.9a [81]. Since the stacking fault is a result of a perfect dislocation dissociating into two Shockley partials on every second $\{1\,1\,1\}$ plane in FCC, the formation of ε is closely related to the movement of the partial dislocations. The dissociation has been reported to depend on the Schmid factor of each partial dislocation and the direction of the applied stress [82]. The effect of different loading directions on the partial dislocations and the formation of ε martensite is discussed in Chapter 4.

Apart from the γ – ε - α' transformation path, another commonly observed transformation path is the direct transformation from γ austenite (FCC) to α' martensite (BCC). Bogers and Burgers [83] proposed a hard-sphere model for FCC to BCC transition taken into account two shears resulted from the Shockley partials movements on $\{1\,1\,1\}$ planes in the FCC lattice. A typical shear of $\frac{a_{FCC}}{6}<1\,1\,2>$ is

regarded as the twinning shear in FCC (hereafter denoted as T shear). The two shears essential for the BCC transformation are T/3 shear and T/2 shear. According to the hard-sphere model, a T/3 shear attains a near-BCC geometry with an incorrect stacking sequence. The proper stacking is then achieved with a T/2 shear, generating a true BCC structure. Based on [83], Olson and Cohen [16] further elaborated the mechanism for the nucleation of the BCC martensite, pointing out the importance of the double shears, $\frac{a_{FCC}}{18}$ <1 1 2> (T/3) and $\frac{a_{FCC}}{12}$ <1 1 2> (T/2), in FCC. Figure 1.9b illustrates the doubly faulted area resulted from the intersection in the double shear. Note that the array of T/3 consists of partial dislocations on every third {1 1 1}$_{FCC}$ plane, and the array T/2 has partial dislocations on every second {1 1 1}$_{FCC}$. The doubly faulted area can be obtained by the intersection of two ε martensite plates. However the formation of the ε martensite is not a necessary condition for the nucleation of the α' martensite. The double shear can also be achieved by the intersections of a twin boundary with another twin boundary or a grain boundary, the intersection of twinning and slip or the intersection of two slip bands (Figure 1.9c) [16, 84, 85]. Das et al. [85] further reported that multiple transformation mechanisms such as γ → α', γ → ε and γ → ε → α' can co-exist, as shown in Figure 1.9d.
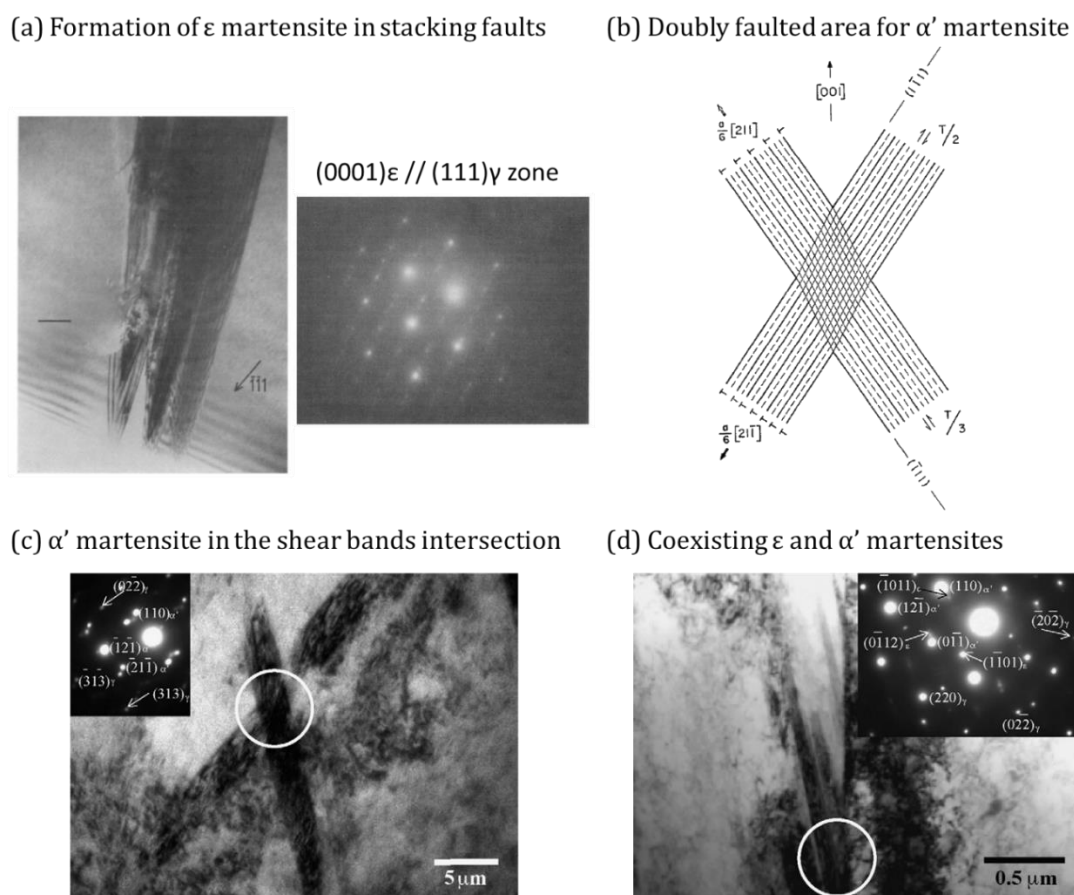
Figure 1.9 (a) ε martensite nucleated from the overlapping stacking faults [81]. (b) The intersection of a double shear creates the nucleation site for α' martensite [16]. (c) A bright field TEM micrograph showing α' martensite at the intersection of two shear bands [85]. (d) ε and α' martensite coexist at a grain boundary – shear band intersection.

Several factors affect the strain-induced α' martensitic transformation. Nohara et al. [86] proposed a formula showing the effect of the chemical composition and the grain size of the γ austenite, and reported that coarse-grained austenite are more susceptible to strain-induced transformation. The increasing deformation temperature has been shown to suppress the formation of the α' martensite [87, 88]. Increasing the strain rate of a uniaxial tensile test decreases the amount of the strain-induced α' martensite due to the adiabatic heating [88-90].

In addition to the deformation temperature and the strain rate, the loading conditions influence the formation of the α' martensite. Hecker et al. [91] reported the effect of deformation mode on the strain-induced α' martensitic transformation in stainless steel 304. The equibiaxial tension achieved by punch-stretch tests resulted in higher volume fraction of α' martensite than uniaxial tension (Figure 1.10a). Murr et al. [92] further investigated the microstructure of the deformed specimens from [91] with TEM and reported that α' embryos were always confined in micro-shear band intersections such as stacking faults and deformation twins. More shear-bands intersections serving as the nucleation sites for α' martensite were observed in the case of equibiaxial tension than uniaxial tension, as shown in Figure 1.10b.

(a) The volume fraction of α' martensite   (b) The number of shear band intersection
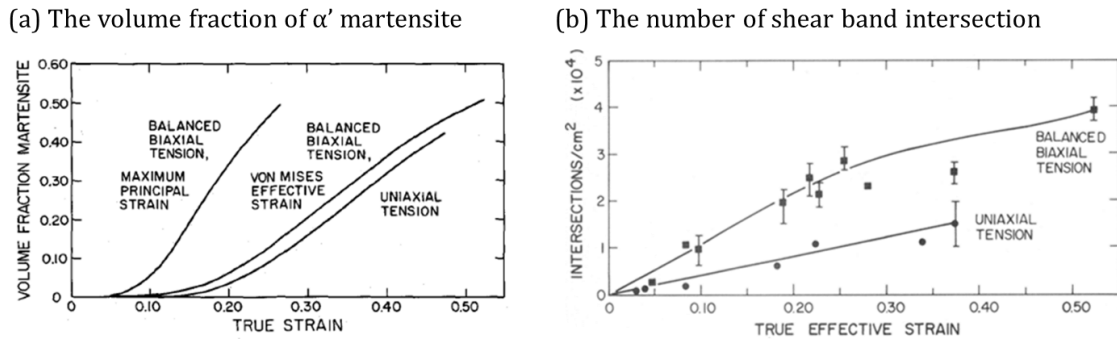
Figure 1.10 (a) The volume fraction of α' martensite [91] and (b) the number of shear bands intersections [92] as functions of true strain in stainless steel 304.

Nanga et al. [93] studied the phase transformation in metastable austenitic 301LN stainless steel and examined the effect of the stress triaxiality (TX) on the α' transformation. The stress triaxiality is defined as the ration between the hydrostatic stress (σ_h) and the Von Mises equivalent stress (σ_{VM}):

$$\frac{\sigma_h}{\sigma_{VM}} = \frac{\frac{1}{3}(\sigma_1 + \sigma_2 + \sigma_3)}{\frac{1}{\sqrt{2}}\left(\sqrt{(\sigma_1 - \sigma_2)^2 + (\sigma_2 - \sigma_3)^2 + (\sigma_3 - \sigma_1)^2}\right)}$$

where σ_1, σ_2 and σ_3 are the principal stresses. They reported comparable α' martensite volume fractions under equibiaxial tension (TX = 0.66) and uniaxial tension (TX = 0.33), higher than that under plane strain (TX = 0.57), suggesting the transformation does not follow the triaxiality solely. Beese et al. [94] studied the α' transformation in stainless steel 301LN under uniaxial tension and equibiaxial tension, yet reported contradictory results to [93]: equibiaxial tension resulted in less α' martensite

than uniaxial tension. They proposed a new model taking into account the Lode angle in addition to the stress triaxiality to explain the different transformation kinetics under different loading conditions. Chakrabarty also reported lower volume fraction of the α' martensite under biaxial tension than uniaxial tension in stainless steel 201 [95]. Yan et al. [96] studied the effect of different deformation modes on the mechanical behavior of TRIP 600 steel. By comparing the amount of retained austenite phase measured with X-ray diffraction, they reported that plane strain tension results in the highest martensitic transformation rate, followed by biaxial tension and finally uniaxial tension. Kosarchuk et al. [97] studied two grades of stainless steels and showed that the transformation under equibiaxial tension is less than under uniaxial tension. Table 1.3 summarizes the dependency of α' martensite formation on the loading conditions in metastable austenitic stainless steels, showing the discrepancy in the effect of deformation modes on the transformation behavior. It is clear that information on the microstructures is required to understand the differences.

Table 1.3 The amount of α' martensite formed under different loading conditions in austenitic stainless steels.

Material	α' martensite volume fraction	References
Stainless steel 304	Biaxial tension > uniaxial tension	[91, 92]
Stainless steel 301LN	Biaxial tension ≈ uniaxial tension > plane strain > pure shear	[93]
	Biaxial tension < uniaxial tension	[94]
Stainless steel 201	Biaxial tension < uniaxial tension	[95]

1.5 Objectives and thesis structure

The aim of this study is to gain insights into deformation-induced martensitic transformations in NiTi alloys and metastable austenitic steels under multiaxial loadings, and to link the microstructural evolution to the macroscopic mechanical responses under different load paths. For the mechanical testing, the cruciform-shaped samples are used, allowing the application of proportional and non-proportional multiaxial loadings by adjusting the loading conditions in each cruciform arm. The combination of the cruciform multiaxial mechanical test with in situ characterization techniques offers the possibility to investigate the microstructural evolution and to link this with the macroscopic mechanical response.

The structure of the thesis is as follows:

Chapter 2 focuses on the experimental aspects: the investigated materials, the tensile devices, the development of the cruciform-shaped samples and the setups for different in-situ experiments.

Chapter 3 presents the studies on superelastic NiTi alloys. Each section corresponds to a publication. Section 3.1 shows the transformation behavior of a nanostructured superelastic NiTi under the square load path change. Section 3.2 presents more details about the path dependency of the transformation and the materials degradation induced by multiaxial mechanical cycling. Section 3.3 focuses on the deformation mechanisms of the coarse-grained NiTi alloy under uniaxial loading at the grain level.

Chapter 4 presents the effects of multiaxial loading on deformation mechanisms and martensitic transformations in different metastable austenitic stainless steels. Each section corresponds to a publication. Section 4.1 shows that equibiaxial load suppresses the martensitic transformation in stainless steel (SS) 201. Section 4.2 compares the slip activities under uniaxial and equibiaxial loads in SS304. In Section 4.3, the interrelations between the martensitic transformation, deformation twinning and dislocation slip under uniaxial and equibiaxial loadings of SS304 are discussed.

Lastly, in Chapter 5, conclusions are given and future works are suggested.

Chapter 2 Experimental

2.1 Materials

The martensitic transformations in NiTi alloys and metastable austenitic 201 and 304 stainless steels have been investigated. An overview of the initial microstructure of the investigated materials is given below.

Nanostructured NiTi

The commercial superelastic NiTi in sheet form is purchased from Memry GmbH (alloy type BB/S). The austenite start temperature (A_s) and the austenite finish temperature (A_f) measured by the supplier are -10°±10°C and 8°±7°C, indicating superelasticity at room temperature. The chemical compositions determined by Inductively Coupled Plasma-Optical Emission Spectrometry (ICP-OES) are 51.5±1 at% Ni and 48.5±1 at% Ti. The initial phase of the sheet is B2 austenite, as characterized by a laboratory diffractometer (D8 ADVANCE, Brucker) using a Cu Kα source. Based on the Williamson-Hall method, the estimated crystallite size is 40 nm. Electron backscatter diffraction (EBSD) characterization shows a complex microstructure. As shown in Figure 2.1a, large austenite grains (average grain size: 27 μm) contain bands. Detailed examinations reveal that the bands consist of subgrains. Figure 2.1b displays a micrograph taken with a Scanning Transmission Electron Microscope (STEM) detector, showing the subgrained structure. More details about the initial microstructure of this alloy can be found in Section 3.1.
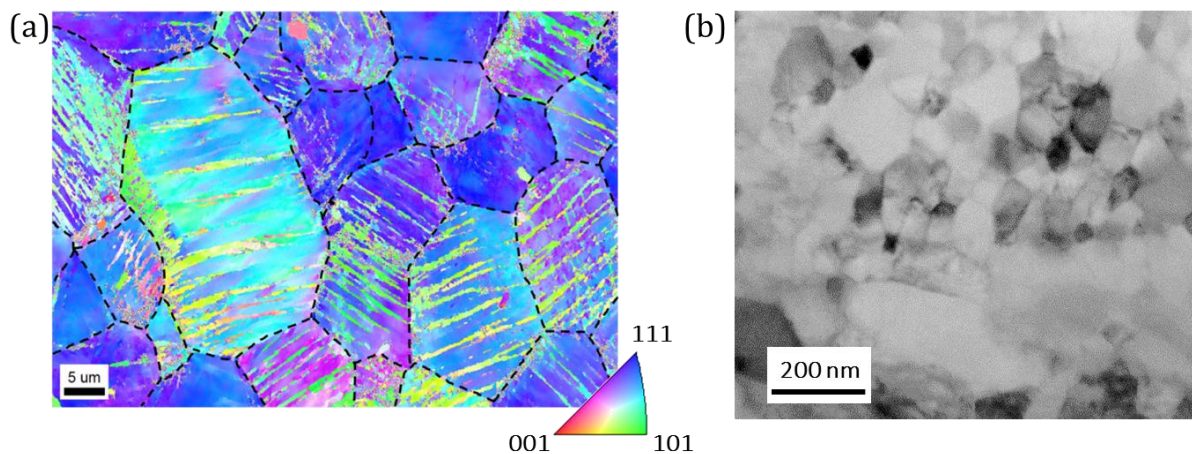
Figure 2.1 (a) Large austenite grains contain bands. The grain boundary determined by the EBSD analysis is delineated with the dashed line. (b) The STEM image of the as-received sheet shows the nanoscaled subgrains.

Coarse-grained NiTi

The polycrystalline NiTi sheet with the chemical compositions of 51 at. % Ni and 49 at. % Ti is provided by Prof. Guillaume Laplanche at the Ruhr-University Bochum. The initial microstructure consists of equiaxed austenite grains with an average grain size of 35 μm, as shown in Figure 2.2. Different from the nanostructured NiTi, this material does not contain subgrains. More details about the manufacture of this material can be found in Section 3.3.
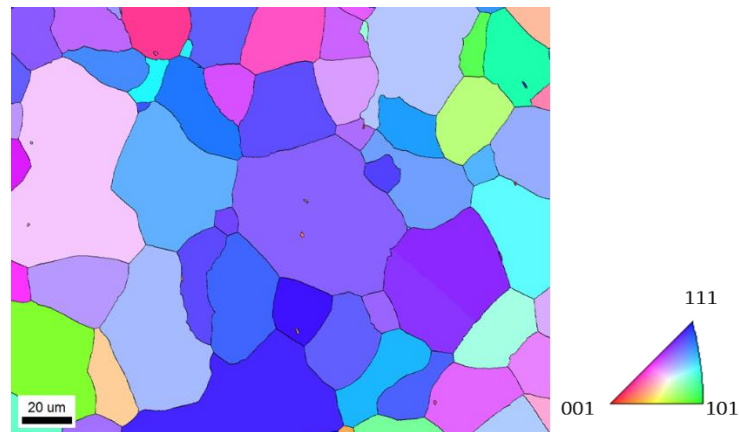
Figure 2.2 The microstructure composed of coarse austenite grains.

Austenitic stainless steels: SS201 and SS304

Two types of austenitic stainless, SS201 and SS304, are studied. The as-received SS201 sheet is 4-mm thick, and the SS304 is 8-mm thick. The initial microstructures of both steels are in the austenite phase with mild textures, as shown in the EBSD maps in Figure 2.3. The average grain sizes for SS201 and SS304 are 45 μm and 36 μm respectively. Table 2.1 lists the chemical compositions and the stacking fault energies reported in literature for both types of steels [98-102]. SS304 exhibits a higher stacking fault energy than SS201. The effect of the stacking fault energy on the deformation-induced martensitic transformation is discussed in Chapter 4.

In addition to the 8-mm sheet, SS304 is also studied in the form of a thin foil. The 150-μm foil is purchased from Goodfellow Cambridge Ltd. Figure 2.4 shows an EBSD map of the microstructure of the SS304 thin-foil. The average grain size is 19±5 μm, excluding the annealing twins.

Table 2.1 The chemical compositions and the stacking fault energies of SS201 and SS304

Type	Chemical Composition (wt. %)						Stacking fault energy (mJ/m^2)
	Cr	Mn	Ni	Si	C	N	
SS201	16-18	5.5-7.5	3.5-5.5	1	0.15	0.25	21.6[99], 20[100]
SS304	17.5-19.5	2	8-10.5	0.75	0.07	0.1	30[102] , 28-41[98], 30.4[101]
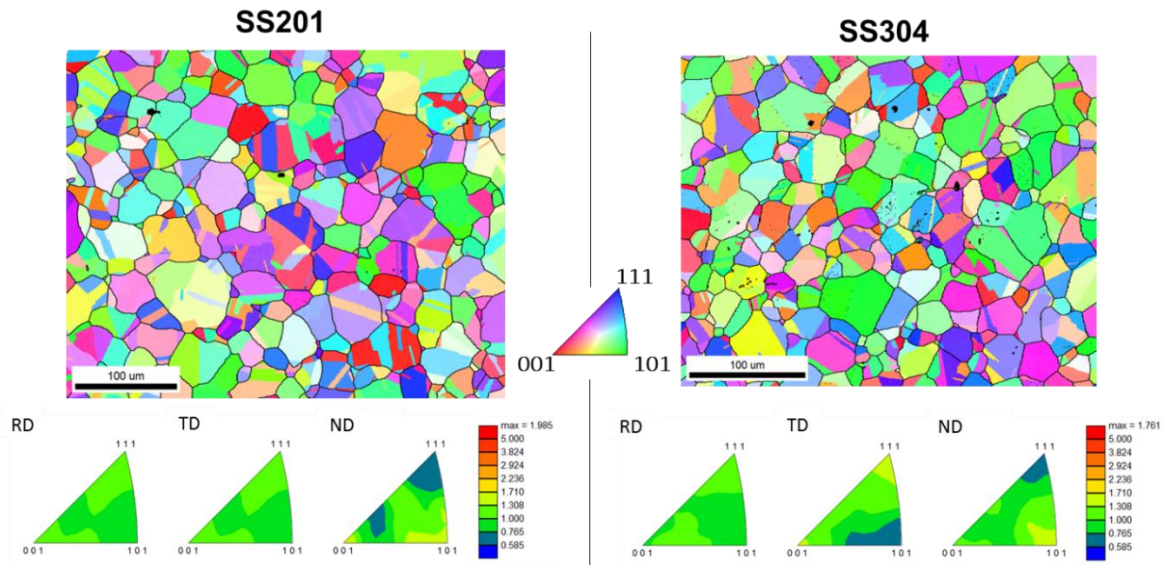
Figure 2.3 The grain orientation maps (parallel to the sample normal direction (ND)) of SS201 and SS304. The inverse pole figures demonstrate the mild textures of both materials.
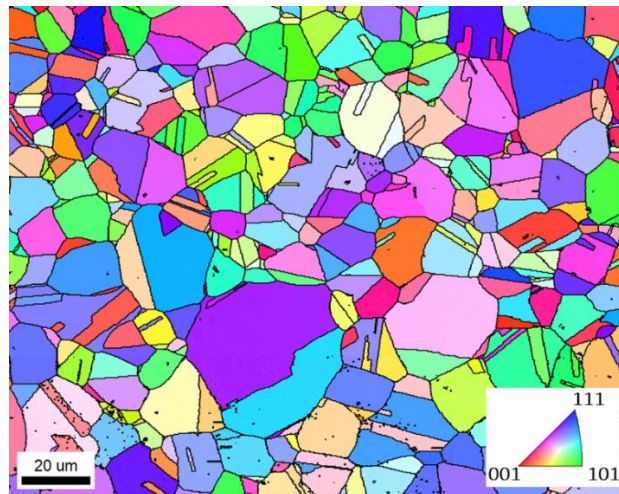
Figure 2.4 The initial microstructure of the thin-foil SS304 from Goodfellow Cambridge Ltd.

2.2 Biaxial deformation rigs

Three biaxial deformation rigs were used: the Minibiax, the Mesobiax and the Macrobiax. All rigs use cruciform shaped sample geometries. Details about these machines are given below.

Minibiax

This novel miniaturized biaxial tensile device (190 mm x 200 mm x 73.2 mm, 2.3 kg) allows uniaxial and in-plane biaxial mechanical tests on thin-sheet metals. The main components of the Minibiax are shown in Figure 2.5. The four grips connected to load cells with a load capacity of 44 N slide inside a guide system. Via the carrier plate, these components are connected to four piezo actuators with a travel range of 10 mm each. An in-house LabVIEW steering program written by Dr. Steven Van Petegem controls the device. By controlling the movement of each grip, proportional loading (e.g. in-plane equibiaxial loading) and non-proportional loading can be applied to a cruciform-shaped sample. Uniaxial tensile tests using dogbone-shaped samples can also be performed with the Minibiax. The readouts of the mechanical data include force values and piezo steps reached by each axis. An additional guide system in the form of a plate can be mounted on the grips. It allows the measurement of the grip position with nanometer resolution. More technical information can be found in [103]. The Minibiax is optimized for two types of in-situ experiments: it can be mounted inside the chamber of a scanning electron microscope (SEM) and on the sample stages of the MS beamline and the MicroXAS beamline of the Swiss Light Source for X-ray diffraction (XRD). The setup of the in-situ experiments at MS beamline will be presented in Section 2.5.1.
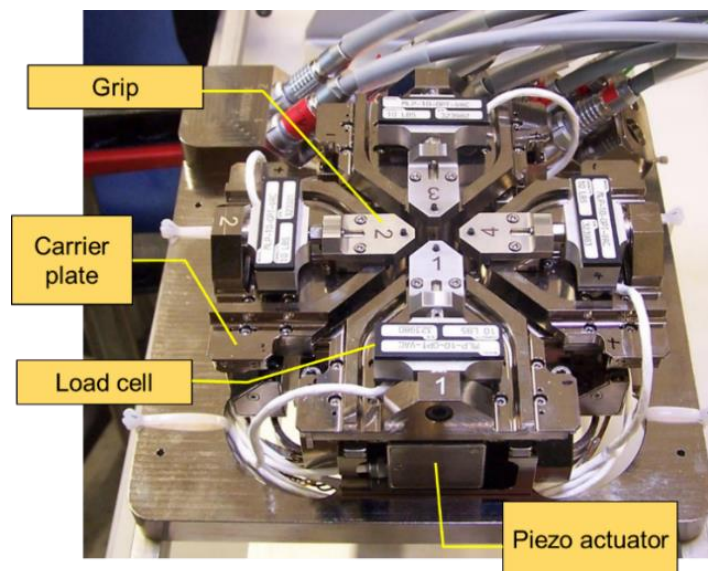
Figure 2.5 The minibiaxial biaxial tensile device.

Mesobiax

Figure 2.6 illustrates the conceptual design of the Mesobiax, which is an upgraded version of the Minibiax. The Mesobiax (426 mm x 266 mm x 459 mm, 28 kg) has a higher load capacity (1000N) than Minibiax, and therefore allows multiaxial mechanical tests on stronger materials, either in force controlled or displacement controlled mode. Uniaxial tensile tests using dogbone samples can also be performed. The maximum displacement of the arms is 8 mm, and the minimum step size is 10 nm. The Mesobiax is controlled with the same LabVIEW program as the Minibiax. By setting the target displacement or the target force for each axis in the LABVIEW program, it is possible to perform cyclic loadings. This machine is also optimized for in-situ experiments at synchrotron beamlines. The setup for the in-situ experiments at MS beamline will be presented in Section 2.5.1.
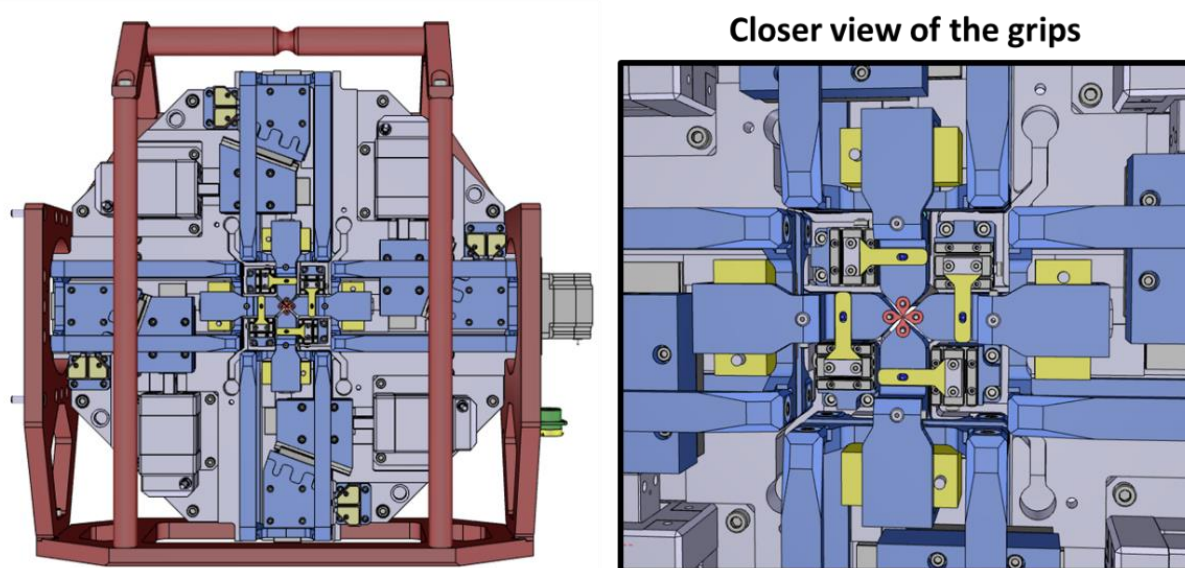
Figure 2.6 The technical drawings for the Mesobiax.

Macrobiax

The Macrobiax shown in Figure 2.7 is a large multiaxial load frame installed at the Pulse OverLap DIffractmeter (POLDI) beamline at the Swiss Spallation Neutron Source (SINQ). It is nearly 1.9 meters high and 2.7 meters wide, and it weighs 1.7 tons. The maximum tensile forces reachable along vertical and horizontal directions (labeled as Axis 1 and Axis 2 in Figure 2.7) are 100 kN and 50 kN respectively. In addition to tension, the vertical direction also allows 100-kN compression and 200-Nm torsion. The Macrobiax is used to perform in-plane proportional and non-proportional deformation tests on cruciform-shaped SS201 and SS304 samples. The TestXpert standard control software developed by Zwick/Roell, controls the machine. An interface between TestXpert and the control system of POLDI beamline has been written for in-situ neutron experiments. The setup of the Macrobiax at the POLDI beamline will be presented in Section 2.5.1.
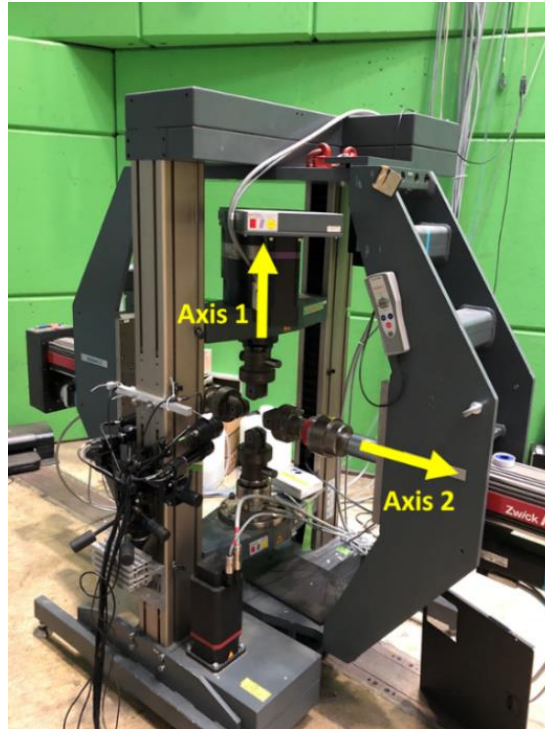
Figure 2.7 The Macrobiax at the Swiss Spallation Neutron Source.

Table 2.2 summarizes the specifications of these three mechanical testing devices and the applicable combinations with in-situ materials characterization techniques.

Table 2.2 Summary of the mechanical testing devices

	Minibiax	Mesobiax	Macrobiax
Dimensions	190 x 200 x 73.2 (mm)	426 x 266 x 459 (mm)	1.9 m in height 2.7 m in width
Weight	2.3 kg	28 kg	1.7 tons
Maximum load	44 N	1000 N	100 kN vertically 50 kN horizontally
Load path	Uniaxial tension In-plane multiaxial tension Load path change	Uniaxial tension In-plane multiaxial tension Load path change	Uniaxial tension In-plane multiaxial tension Load path change Compression (vertical) Torsion (vertical)
In-situ techniques	Macroscopic DIC SEM HRDIC Synchrotron XRD	Macroscopic DIC Synchrotron XRD	Macroscopic DIC Neutron diffraction

2.3 Optimization of cruciform geometries

The sample geometry is crucial for carrying out multiaxial deformation tests. Depending on the material tested and the machine employed, there are different requirements for an optimized cruciform geometry. In general, an ideal cruciform geometry should provide a uniform strain distribution in the gauge section (i.e. the center of the cruciform sample) and allow significant plastic strains before failure occurring in the center [104, 105]. To investigate martensitic transformations in situ in cruciform shaped samples, the SEM electron beam, the synchrotron X-ray beam or the neutron beam are positioned at the center of the cruciform and therefore the sample geometry should ensure the occurrence of the transformation in the center during multiaxial loading.

The optimization of the cruciform geometry has been done for each material, following the steps shown in Figure 2.8. The first step is to design the experiment and decide which biaxial device will be employed for the in-situ measurement, since this determines the maximum load that can be applied to induce martensitic transformation in the center of the cruciform during uniaxial and equibiaxial loading. Several factors need to be taken into account at this step. For example, the grain size of the investigated material is important for choosing the suitable powder diffraction technique as the data quality depends on sampling statistics (number of grains in the gauge volume). Another consideration is the amount of material available. The design of the cruciform geometry is carried out with finite element (FE) simulations (Abaqus 6.14 software). Finally yet importantly, it must be possible to manufacture the optimized geometry, which is a major challenge in this workflow. Once the fabrication of cruciform samples is completed, mechanical tests are combined with macroscopic digital image correlation (Macro-DIC) to verify the simulated mechanical response from the cruciform geometry. The details about the optimization for each material are discussed in the following sections.
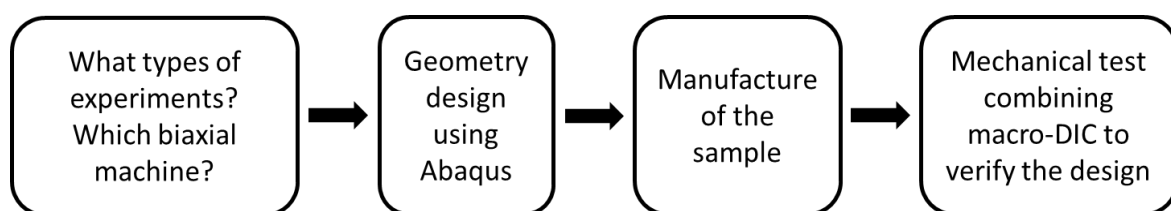
Figure 2.8 The workflow for the design of the cruciform sample geometry.

2.3.1 Flat geometry cruciform

Initially a flat geometry without reducing the thickness in the central gauge area, was designed for testing with the Minibiax and the Mesobiax device. The flat sample is shown in Figure 2.9a. The mechanical response of the flat geometry is simulated using the constitutive equations for a superelastic NiTi provided in Abaqus. Table 2.3 lists the material parameters used for the simulation. These were obtained from preliminary uniaxial tensile tests using dogbone samples. These tests revealed also the plateau in the stress-strain curve of the nanostructured NiTi, which is typically for a superelastic material. More details about the parameters required for superelasticity simulation of NiTi are given in [106].
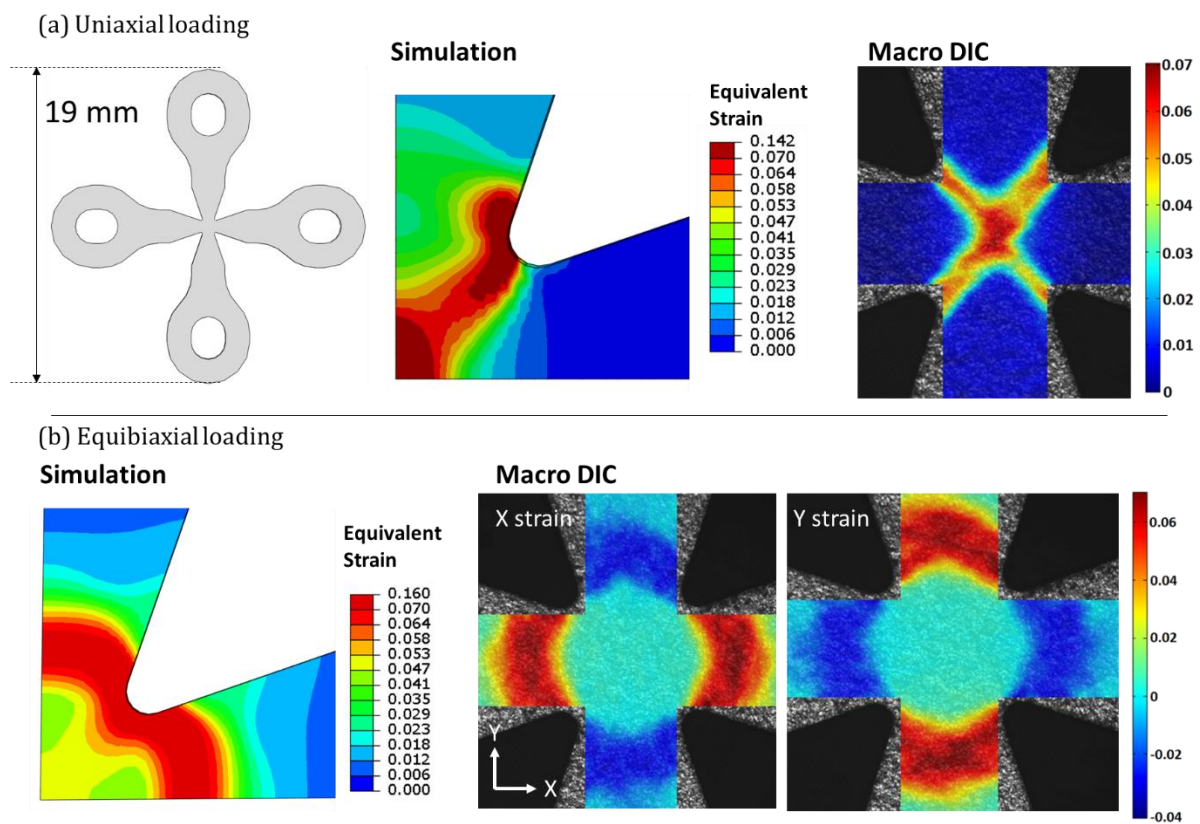
Figure 2.9 (a) The flat geometry and strain distributions in a flat cruciform obtained from Abaqus simulation and Macro-DIC analysis under a uniaxial load of 40 N in the vertical direction. (b) Simulation and the Macro-DIC strain maps under equibiaxial loading of 40 N.

Table 2.3 Parameters for the built-in superelastic model in Abaqus

Elastic modulus of austenite	31.2 GPa
Elastic modulus of martensite	20.7 GPa
Forward transformation stress	413 MPa
Reverse transformation stress	245 MPa
Transformation plateau strain	0.05

One eighth of the cruciform geometry is simulated with symmetric boundary conditions. A uniaxial load (40N) along the vertical direction is applied to the cruciform. The simulation shows that a strain > 0.07 can be reached at the center of the cruciform during uniaxial loading, as shown in Figure 2.9a, suggesting that martensitic transformation will occur. To verify the simulation, flat cruciform samples are manufactured and tested uniaxially while measuring the strain distribution with Macro-DIC. The samples are cut from a 90-µm thick sheet (Memry GmbH) using a frequency tripled Nd:YVO picosecond pulsed laser (10 picoseconds pulse width and 355 nm wavelength) at the Swiss Federal Laboratories for Materials Science and Technology (EMPA, Dübendorf). The power for laser cutting is 870 mW with 160 kHz pulse frequency. Details about the setup for Macro-DIC measurement are provided in Section 2.5.2. The DIC strain map for a uniaxial test shown in Figure 2.9a, evidences an X-shaped high strain bands in the center, which is in good agreement with the simulation result, confirming the occurrence of martensitic transformation.

On the other hand, the simulation of equibiaxial loading (40N in both vertical and horizontal directions) shows that the martensite forms in the arms of the cruciform instead of the center (see Figure 2.9b). The DIC strain maps (Figure 2.9b) confirm that high-strain bands appear at the arms. Upon loading, the bands propagate along the arms instead of toward the center. The center is hardly deformed since the strain is nearly 0, indicating that the material retains the austenite phase in the center. Figure 2.10 shows the stress distribution in the simulated sample, confirming that the transformation stress (413 MPa) is first reached in the arms in both x and y directions, hence triggering the formation of martensite in the arms, explaining the high strain observed by Macro-DIC. Based on these results, the flat geometry is not suitable for equibiaxial tests.
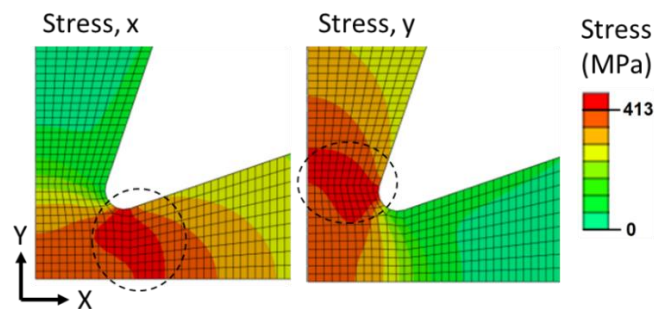
Figure 2.10 The stress distribution in a flat cruciform under an equibiaxial load of 40 N.

2.3.2 Geometry optimization using FE simulations

Thin-down geometry

The good match between the FE simulation and experiments shown in Figure 2.9 validates that Abaqus can serve as an effective tool for designing and optimizing cruciform geometries. Since the flat geometry fails to produce martensite in the center during equibiaxial loading, the geometry has to be optimized for equibiaxial loading. It has been reported that locally thinning the center of the cruciform can increase the achievable plastic strain [104, 105]. Following this idea, a geometry with a circular "pocket" (600 μm diameter) in the center, as illustrated in Figure 2.11, is investigated.
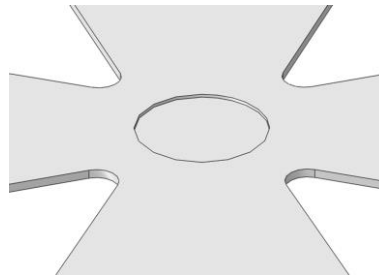
Figure 2.11 The geometry with local thinning in the center.

Figure 2.12a shows the simulated stress distributions in x and y directions under an equibiaxial load, for a sample where the center is thinned down from 80 μm to 50 μm with a sharp transition. In this geometry, the stress concentration in the arms is less pronounced than what was observed for the flat geometry. The highest stress concentrations are reached near the cross-arm area. It is also worth noting that higher stresses are obtained inside the pocket. This geometry serves as the base for further optimization. By introducing in our model a gradual thinning from the arm to the edge of the central pocket, a higher stress can be reached simultaneously at the cross-arm and inside the pocket, as shown in Figure 2.12b. It has been reported that the ratio of gauge thickness to arm thickness influences the achievable plasticity in the center [107]. Figure 2.12c shows the simulation for the geometry with 200 μm-thick arms. Compared to Figure 2.12b, the stress now mostly concentrates in the pocket rather than the cross-arm area, suggesting that the martensite can form in the pocket. Amina et al. have proposed a promising geometry with a rounded square pocket in the center [107]. Figure 2.13 shows the geometry containing a rounded square pocket together with the simulated stress distributions. It is clear that the geometry with a rounded square pocket allows reaching sufficiently high and homogeneously distributed stress inside the pocket to induce the martensitic transformation.
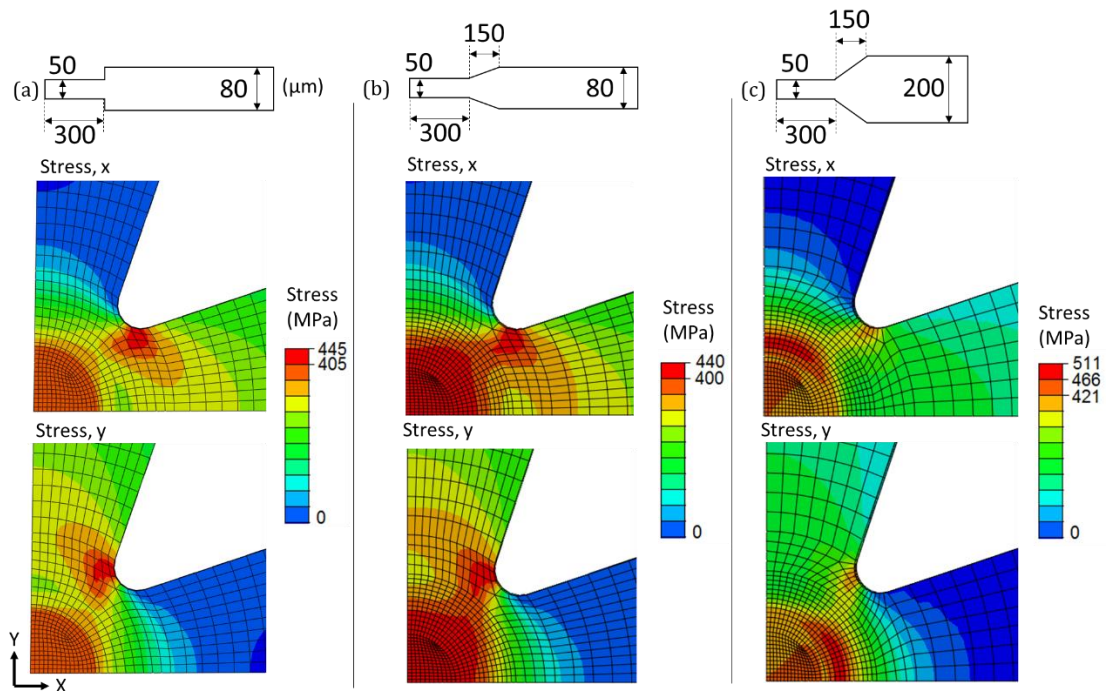
Figure 2.12 Different cross-section geometries and the corresponding stress distributions under equibiaxial loading. Note that all three designs consist of a circular pocket in the center.
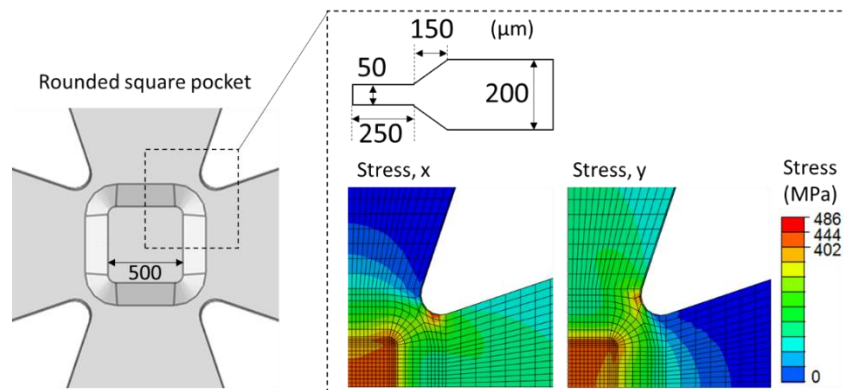
Figure 2.13 The geometry with a rounded square pocket and the stress distributions under equibiaxial loading.

Bi-material geometry

Because the nanostructured NiTi is already a very thin foil, the possibility to create cruciform geometry using a "bottom-up" strategy was considered and investigated together with the master student Amina Matt [107]. Figure 2.14 illustrates the concept. Instead of removing materials to thin down the center of the cruciform, additional layers of materials are applied onto both sides of the NiTi sheet while leaving an opening in the center. Figure 2.14 shows the FE simulation results for a bi-material geometry consisting of electroplated Ni layers on the NiTi sheet showing that a high stress can be reached in the center of the NiTi layer, suggesting the formation of martensite in the bi-material geometry under equibiaxial loading.
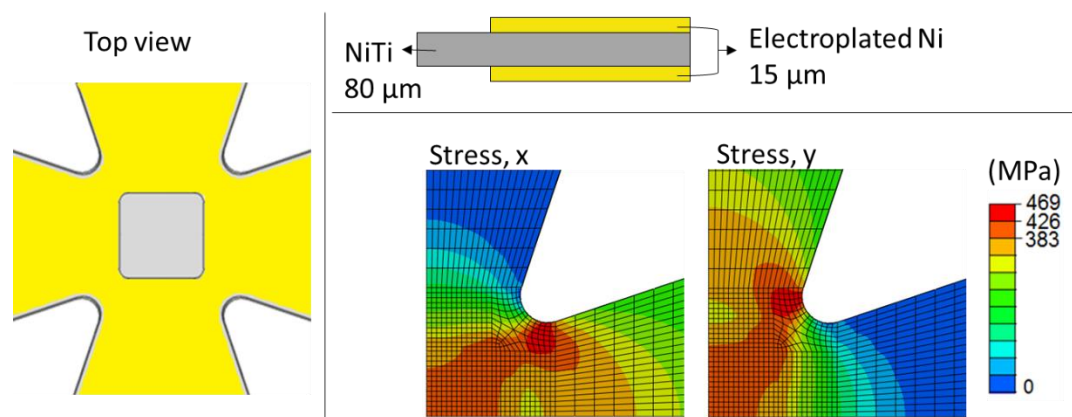
Figure 2.14 The bi-material geometry and the stress distributions in the NiTi layer under am equibiaxial load.

2.3.3 Manufacture of mini cruciform samples

One of the biggest challenge is to manufacture these two optimized cruciform geometries i.e. the thin-down geometry and the bi-material geometry. Traditional machining is not applicable for the fabrication of the thin-down geometry as the dimensions of the pocket feature is too small. The first attempt to thin down the center was done with the picosecond laser at EMPA, which has been employed to thin down polycrystalline Cu in [108] and Al cruciform samples. However, this method deteriorates drastically the surface quality of the well-polished NiTi sheet, as shown in Figure 2.15. Since the surface after laser ablation is no longer mirror-like, it is not suitable anymore for EBSD characterization or HRDIC experiments. Other concerns raised by laser ablation is the heat effect that can alter the microstructure and local chemical composition. As superelasticity in NiTi is sensitive to the chemical composition, it is risky to fabricate the pocket with laser ablation. A better candidate for fabricating the pocket feature is electrochemical machining (ECM), i.e. removing material by an electrochemical process. ECM is suitable for complex geometries, and it can result in a stress-free, smooth and bright surface [109].
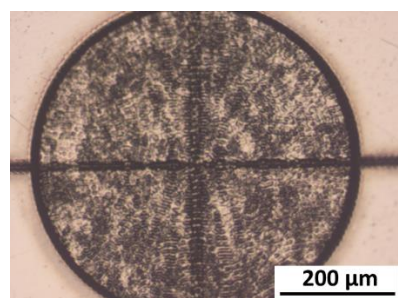
Figure 2.15 The bad surface quality of the circular area thinned down by the laser ablation.

As for the bi-material geometry with electroplated Ni, one crucial step is to develop a mask covering the center of the cruciform during the deposition of Ni layer. One difficulty lies in selecting proper mask material, which needs to be resistant to sulfuric acid during the electroplating process and removable after the deposition of Ni. Furthermore, since both sides of the sample have an opening in

the center, a precise alignment during the deposition process is required. One possible solution is to employ photolithography microfabrication. However, this requires the development of an adequate microfabrication process, which is out of the scope of the aimed research. Therefore we continued with ECM to manufacture the thin-down geometry.

Electromechanical micromachining

The fabrication of the thin-down geometry is done with an electromechanical micromachining (ECMM) process developed and carried out by Micropat SA, Switzerland. The ECMM process employs the same principle as traditional ECM to remove metal by electrochemical process, providing a well-polished surface, yet it combines a laser lithography system to increase the flexibility in designing the engrave shape. The steps in the ECMM process for thinning down the commercial NiTi sheet are:

1. The epoxy-based resist (KMPR 1010) is applied onto the sheet by spin coating at 3000 rpm.
2. Soft baking at 100 $^{\circ}$C for 20 min and hard baking at 180 $^{\circ}$C for 20 min.
3. The resist layer (~10 μm) is locally exposed to a short-pulse UV laser (Spectra Physics Explorer 355 nm) to define the rounded-square openings to the underlying metal surface. Multiple openings at different positions can be defined with the laser in this step.
4. The openings are neatly etched at the rate of 2.79 x 10^{-2} mm^3/C in the 3 M sulphuric acid-methanol solution at room temperature.
5. After completion of the electrochemical dissolution, the protective coating is stripped in N-Methyl-2-pyrrolidone (NMP) at 100 $^{\circ}$C.
6. Flip the sheet and repeat the steps (1) to (5).

For the pocket shown in Figure 2.16a, the ECMM process was applied directly to the as-received sheet without additional grinding and polishing. The ECMM process results in a mirror-like surface inside the pocket as shown in Figure Figure 2.16b. Microstructure features such as grain boundary and band structure can be observed in secondary electron SEM image shown in Figure 2.16c. The depth profile of the pocket is characterized with X-ray computerized tomography (CT) (GE nanotom-m micro-CT system) as shown in Figure 2.17. The ECMM process successfully thins down the sheet from both sides and a bathtub-like depth profile is obtained. The center of the pocket is rather flat with a thickness of 65 μm in this case. Figure 2.17 also evidences the good alignment achieved during the thinning process for both sides. Another advantage of the ECMM process is that multiple "pockets" with the bathtub-like depth profile can be fabricated all at once. For example, 32 pockets have been made in a 140 mm x 75 mm sheet all at once. More technical information regarding the ECMM can be found in [110-112].
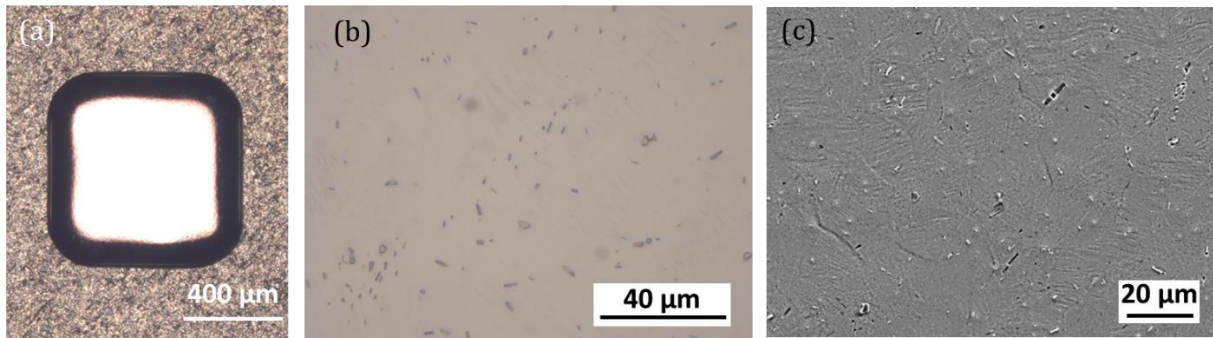
Figure 2.16 (a) A pocket in a NiTi sheet fabricated with the ECMM process. (b) A mirror-like surface inside the pocket. The bright part is the austenite phase. The NiTi2 precipitates (gray particles in the pictures) are readily observed with optical microscope. (c) Grain boundary and band structure are readily observed in a secondary electron SEM image.
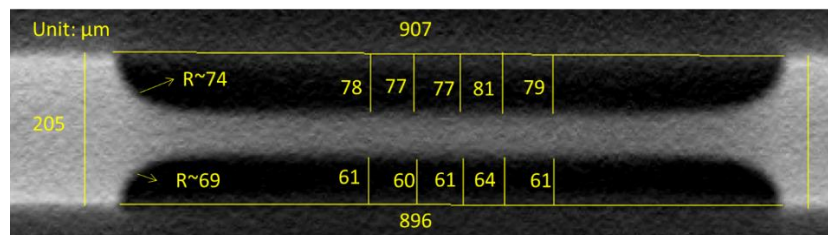
Figure 2.17 The cross section of the pocket introduced by the ECMM process to a NiTi sheet.

2.3.4 Design and manufacture of geometries for Macrobiax

The optimization of the large cruciform geometries for the in-situ neutron diffraction experiments using the Macrobiax is also done with Abaqus simulations. The cruciform geometry proposed in [113] allows more than 0.2 strain reached in the thin-down center, serving as a good design to begin with. The geometry is modified according to the thickness of the as-received sheet. The goal is to reach high enough plasticity in the center to induce martensitic transformation. The formation of α' martensite in SS304 has been reported to start from about 0.2 strain [91]. Compared to SS304, SS201 requires lower strain to induce martensitic transformations: 0.03 strain for ε martensite and 0.13 strain for α' martensite [114]. The optimized geometries are manufactured with mechanical grinding to thin down the center and waterjet cutting. More details of the optimized large cruciform geometries for SS304 and SS201 are given in Section 2.4.2.

2.4 Sample geometries for phase transforming materials

Table 2.4 lists the sample geometries employed in this study. The details of each geometry is given in the following sections.

Table 2.4 Sample geometries for different materials and different tensile devices employed in this study

Material	Tensile device	Geometry features	Sample name
Nanostructured NiTi	Minibiax/Mesobiax	Flat cruciform	ncNiTi-mini-flat
		Thin-down center, cruciform	ncNiTi-mini-TD
SS304 (150-μm foil)	Minibiax	Thin-down center, cruciform	SS304-mini-TD
SS304 (8-mm sheet)	Macrobiax	Thin-down center , cruciform	SS304-macro-TD
	Uniaxial load frame	Dogbone	SS304-largeDB
SS201	Macrobiax	Thin-down center , cruciform	SS201-macro-TD
	Uniaxial load frame	Dogbone	SS201-largeDB
Coarse-grained NiTi	Minibiax	Miniaturized dogbone	cgNiTi-miniDB

2.4.1 Cruciform geometries for Minibiax and Mesobiax

Flat geometry for nanostructured NiTi: ncNiTi-mini-flat

As discussed in Section 2.3.1, the flat geometry for the nanostructured NiTi (Figure 2.18) allows martensite to form at the center upon uniaxial loading. Therefore, the ncNiTi-mini-flat sample geometry was used to study how a change in load path affects the martensite formed during the first loading sequence (details in Section 3.1).
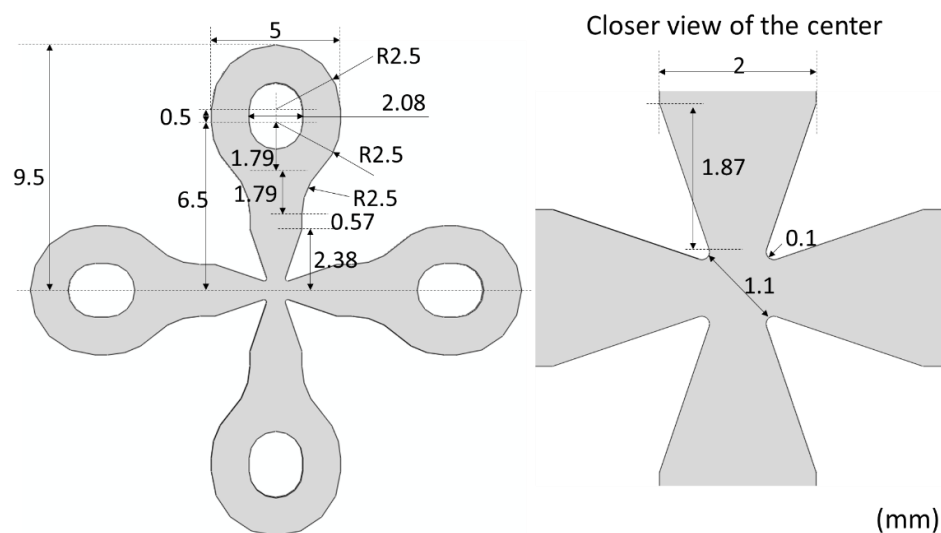
Figure 2.18 The drawings of the flat geometry

Thin-down geometry for nanostructured NiTi: ncNiTi-mini-TD

Combining the ECMM process with laser cutting, cruciform samples of nanostructured NiTi with thin-down geometry were manufactured. Figure 2.19a shows the drawing of ncNiTi-mini-TD. The outer shape of the cruciform is the same as the flat geometry shown in Figure 2.19. The central pocket has a "bathtub-like" depth profile: the thickness is reduced from 150 μm at the arm to 50 μm at the center. Based on the FE simulation shown in Figure 2.19b, the sufficiently high stress reached inside the pocket will induce the martensitic transformation. After fabricating the pockets following the ECMM process mentioned in section 2.3.3, the outer shape of the cruciform sample is cut using the picosecond laser at EMPA with a laser power of 870 mW and a pulse frequency of 160 kHz. The Macro-DIC strain map in Figure 2.19c shows that ~0.06 equivalent strain is reached at the center of the pocket during equibiaxial loading, suggesting the formation of martensite. This geometry is used for studying multiaxial deformation and the materials degradation induced by multiaxial mechanical cycles in the commercial superelastic NiTi, which is presented in Section 3.2.
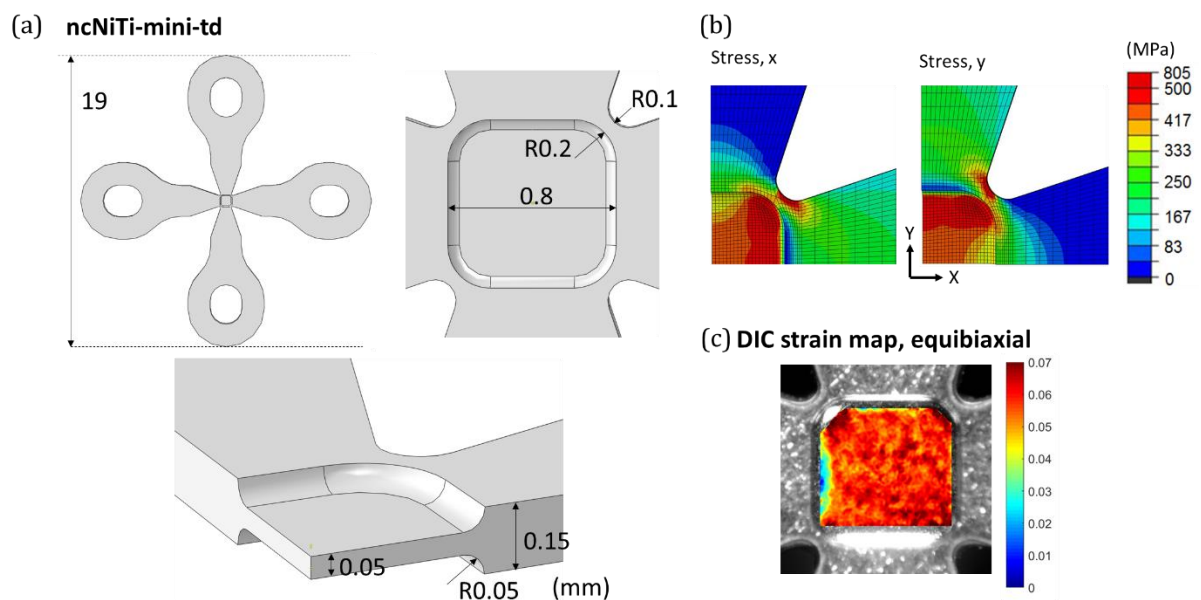
Figure 2.19 (a) The dimensions of the ncNiTi-mini-TD geometry. (b) The stress distribution under an equibiaxial load in FE simulations. (c) DIC strain map showing high strain inside the pocket under equibiaxial loading.

SS304-mini-TD

In order to study the slip activities in SS304, in-situ HRDIC measurement is combined with multiaxial deformation tests using the Minibiax device. The circular openings at the cross-arm regions (see the drawings in Figure 2.20a) effectively increase the achievable strain in the pocket. Based on the FE simulations, 0.25 strain can be achieved in the center of the pocket under equibiaxial loading, as shown in Figure 2.20b. The samples were manufactured with the combination of laser cutting and the ECMM process. The optimized dissolution rate in the ECMM process of SS304 is 2.08 x 10^{-2} mm^3/C. The ECMM process ensures that the materials inside the pocket retains the austenitic phase, i.e. avoiding the martensitic transformation induced by the deformation during mechanical surface preparation. Furthermore, no recrystallization, carbide formation or surface oxidation is to be expected at the temperatures used (i.e. maximum temperature of 180 $^{\circ}$C). Figure 2.21 shows the high surface quality in the pocket fabricated with the ECMM process. The light micrograph shows a smooth surface in the pocket. Furthermore, the polycrystalline microstructure is visible by secondary electron imaging with SEM. The HRDIC study of the multiaxial deformation of SS304 using SS304-mini-td samples is discussed in Section 4.2.
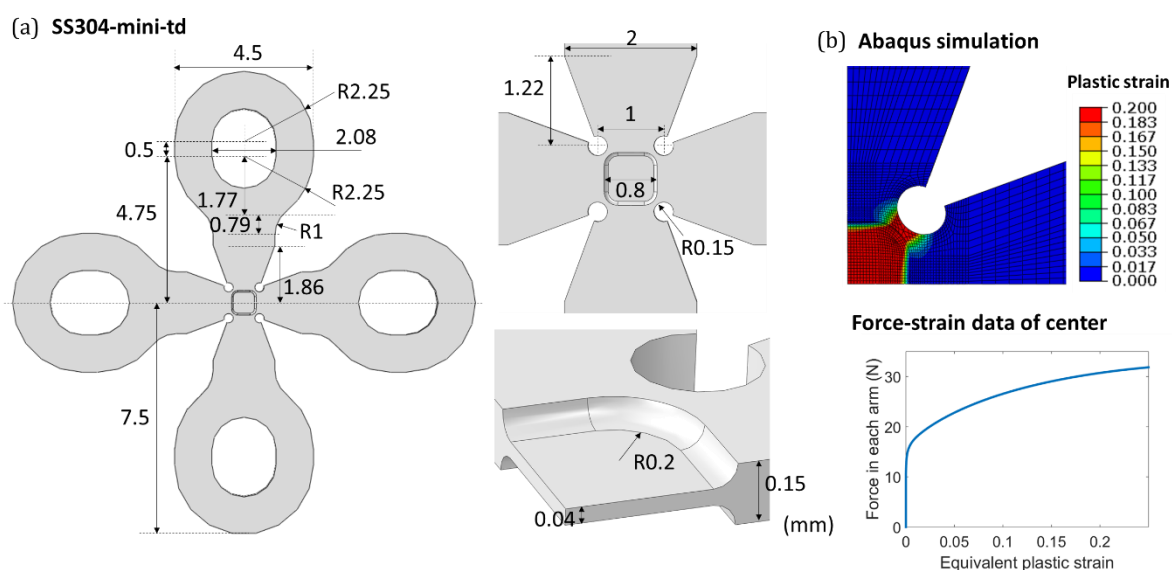
Figure 2.20 The drawing of Mini cruciform of SS304.
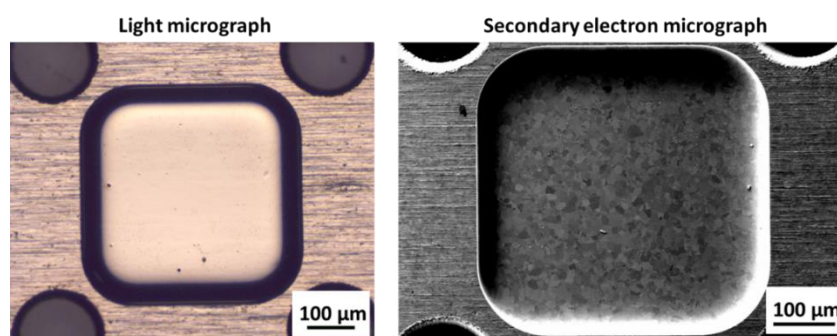
Figure 2.21 The Mini cruciform of SS304 with ECMM and laser cutting exhibits high surface quality inside the pocket.

2.4.2 Cruciform geometries for Macrobiax

SS304-macro-TD

The requirement for SS304 large cruciform geometry is that the strain reached in the center of the cruciform being high enough to induce martensitic transformation, which is around 0.2 strain. The geometry reported in [113] is adapted for SS304 by changing the arm thickness and gauge thickness to 8 mm and 2 mm, since the thickness of the purchased SS304 sheet is 8 mm. Figure 2.22 shows the drawings of SS304 large cruciform. The simulation shows that more than 0.3 strain can be reached in the center under an equibiaxial load. The resulting force shown in the plot is calculated from $\sqrt{F_{axis\,1}^2 + F_{axis\,2}^2}$ where F_{axis1} and F_{axis2} are the forces reached in the two axes of Macrobiax. AEROTECH GmbH carried out the fabrication of SS304 large cruciform. The center of the cruciform was thinned down by mechanical grinding. The outer shape of the sample was cut using waterjet cutting.
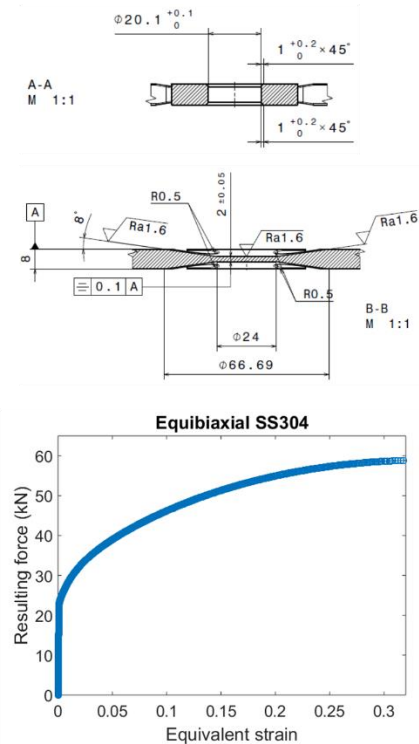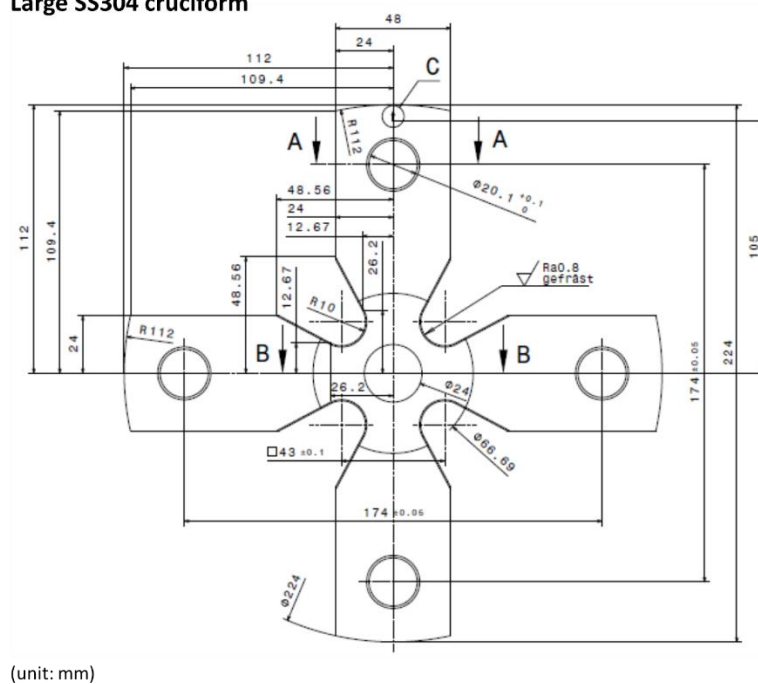
Figure 2.22 The drawing of SS304 large cruciform. The FE simulation shows more than 30% strain can be reached in the center of this geometry under equibiaxial loading (50 kN on each arm).

SS201-macro-TD

The deformation and martensitic transformation in SS201under uniaxial and equibiaxial loading are also investigated during in-situ neutron diffraction using Macrobiax. Since the thickness of the as-received SS201 sheet is 4 mm, a new geometry shown in Figure 2.23 is designed. Different from SS304, the martensitic transformation in SS201 does not require high strain. It has been observed that ε martensite forms after 0.03 strain, and α' martensite form after 0.13 strain [114]. The FE simulations show that $\sim$ 0.2 strain can be reached in the center during equibiaxial loading, suggesting the formation of martensite in this geometry. AEROTECH GmbH carried out the manufacture of SS201 large cruciform with mechanical grinding to thin down the center and water jet to cut the outer shape.
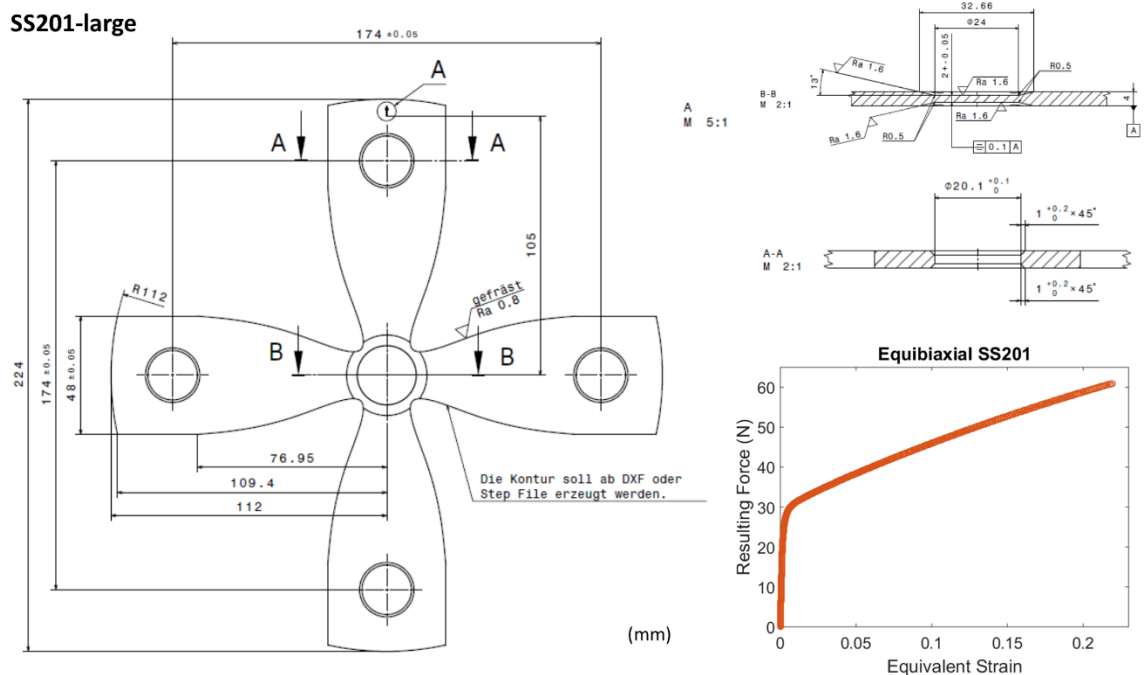
Figure 2.23 The drawing of SS201 large cruciform geometry. The FE simulation shows that 0.2 strain can be reached in the center of this geometry under equibiaxial loading (50 kN on each arm).

2.4.3 Uniaxial dogbone samples

Coarse-grained NiTi: cgNiTi-miniDB

In addition to cruciform multiaxial deformation test, uniaxial tensile tests can be performed with dogbone-shaped sample mounted on Minibiax. Figure 2.24 shows the dogbone geometry compatible with the grips system of Minibiax. In the cgNiTi-miniDB geometry (thickness around 80 μm), a maximum stress of 750 MPa can be reached in the gauge section, which is well above the transformation stress characterized in a preliminary test (450 MPa). This geometry is employed to study uniaxial deformation mechanisms of the coarse-grained NiTi with in-situ HRDIC. The dogbone samples are cut using the picosecond laser at EMPA.
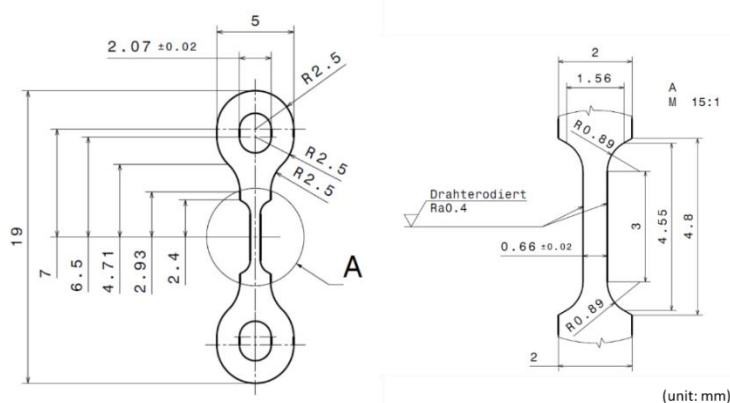
Figure 2.24 The drawing of the uniaxial dogbone sample used in the study of coarse grained NiTi.

Large dogbone samples for neutron diffraction

Uniaxial tensile tests of SS304 and SS201 combining in-situ neutron diffraction are performed with the uniaxial load frame at POLDI beamline [8]. The dogbone geometry shown in Figure 2.25 is employed. With the load capacity of 10 kN, 1000-MPa stress can be reached in the gauge section in the flat dogbone. This geometry allows SS201 and SS304 to reach about 0.25 and 0.4 strain respectively in the gauge section, forming substantial amount of martensite in both cases.
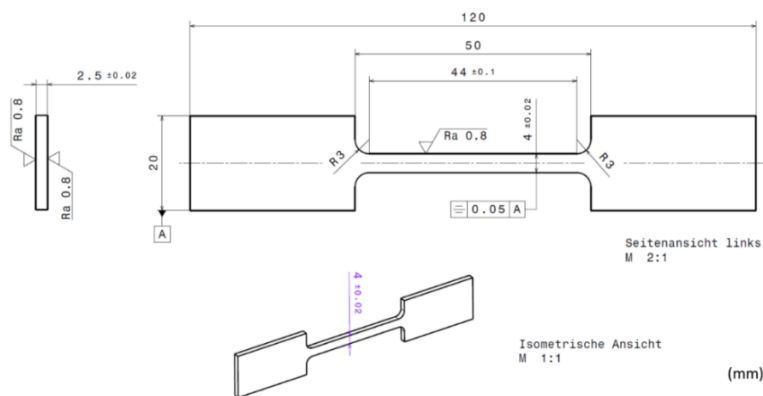
Figure 2.25 The uniaxial dogbone geometry for the uniaxial load frame.

2.5 In-situ characterization techniques

2.5.1 Powder diffraction

The microstructural evolution during uniaxial and multiaxial deformation is investigated with in-situ powder diffraction. The diffraction peak profile analysis provides information about the phase transformation, the accumulation of defects and the deformation of the different phases. Table 2.5 summarizes the diffraction experiments performed on different materials.

Table 2.5 The summary of the diffraction techniques adopted for different materials

Material	Diffraction technique	Facility
Nanostructured NiTi	Synchrotron X-ray powder diffraction	MS beamline at SLS
SS201	Neutron diffraction	POLDI beamline at SINQ
SS304		

The setups of the Minibiax and the Mesobiax at the MS beamline are shown in Figure 2.26a and Figure 2.26b respectively. For the diffraction (XRD) experiments at MS beamline, the Minibiax and the Mesobiax are mounted on the goniometer of the powder diffraction station. A translational stage with three degrees of freedom allows us to move the machine and place the center of the sample at the position of the synchrotron X-ray beam. All the in-situ XRD measurements are performed in transmission mode, using two detectors (Mythen II microstrip detector and Pilatus 6M detector) simultaneously. The maximum frame rates of the Mythen II and Pilatus are 20 Hz and 25 Hz respectively. For the in-situ measurements done in this study, the counting time is 20s. The setup of the two detectors is illustrated by Figure 2.26c. The Mythen detector records diffraction data along the scattering vector parallel to the F1 direction. The Pilatus detector captures 2D images, showing part of the Debye-Scherrer rings. The diffraction data along the F2 direction is obtained by caking and integrating a 2D image along an azimuthal range of 175° - 185° using the software FIT2D.
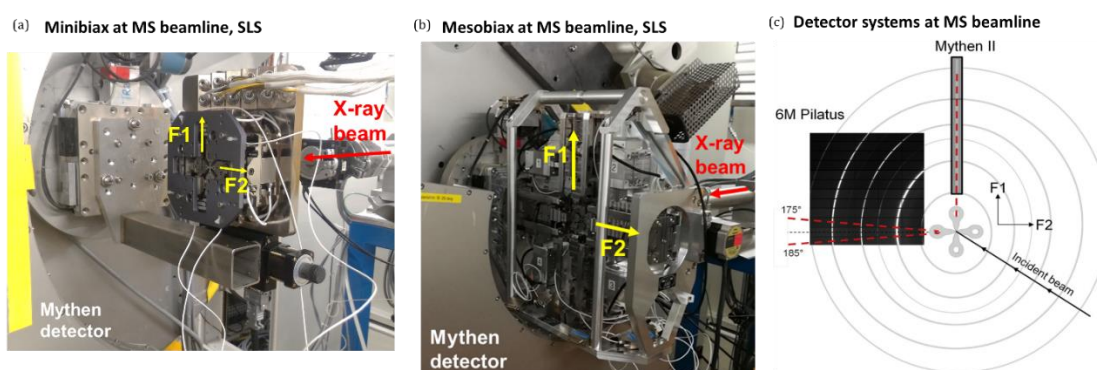
Figure 2.26 The setup at the MS beamline at SLS for (a) Minibiax and (b) Mesobiax. (c) The setup for two detectors at MS beamline.

The martensitic transformation induced by multiaxial deformation in SS201 and SS304 are investigated with neutron powder diffraction at the POLDI beamline at SINQ. Figure 2.27a shows the experimental setup with the Macrobiax. A DIC system by GOM Aramis is implemented in the experimental setup in order to measure the macroscopic strain at the center of the cruciform sample. The incoming neutron beam probes the center of the cruciform. The neutron diffraction data with a scattering vector Q parallel to the F2 direction is collected with the detector, as shown in Figure 2.27b. In the elastic regime during loading, the neutron spectra are accumulated for 30 min. As for the plastic regime, the neutron spectra are accumulated for 60 min.

(a) Setup for in-situ neutron diffraction at POLDI, SINQ
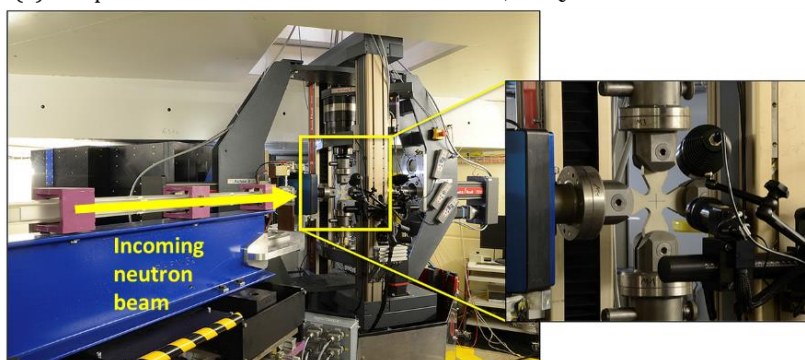
(b) Diffraction geometry
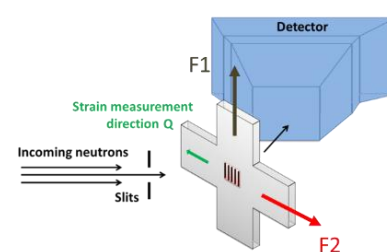
Figure 2.27 The large multiaxial load frame installed inside the bunker of POLDI. A cruciform shaped specimen is mounted on the machine. (This figure is adapted from [113].)

XRD data analysis of nanostructured NiTi

The X-ray powder diffraction spectra are analyzed with single-peak fitting routines. Diffraction patterns of the NiTi are analyzed with the software WinPLOTR using Pseudo-Voigt functions. More details about the fitting procedure and the algorithms in WinPLTOR can be found in [115]. The quantitative results obtained from WinPLTOR are peak position, full-width at half-maximum (FWHM), integrated intensity and maximum intensity. The peak positions allow the calculation of lattice spacing of (h k l) planes, i.e. d_{hkl}. The indexing of diffraction pattern is done by comparing the d_{hkl} obtained from experiments with the theoretical lattice spacing calculated from the crystal structure reported in literature. The references used for the B2 austenite phase, the R-phase martensite and the B19' martensite in NiTi are respectively [21, 22, 116]. The integrated intensity is utilized to calculate the martensite volume fraction (f_M):

$$f_M = \frac{\sum I_{(hkl)M}}{\sum I_{(hkl)M} + \sum I_{(hkl)A}}$$

Where $\sum I_{(hkl)M}$ is the sum of the integrated intensities of the B19' martensite reflections and $\sum I_{(hkl)A}$ is the sum of the integrated intensities of the austenite reflections. Note that in the volume fraction analysis, only B2 austenite and B19' martensite are taken into account. As the intensity of the observed

R-phase martensite peak is significantly lower than B2 and B19' peaks, the low contribution of R-phase is thus neglected in the phase fraction analysis.

The diffraction spectra recorded during the multiaxial mechanical tests for the commercial NiTi are analyzed with an in-house fitting procedure written by Dr. Steven Van Petegem using MATLAB. This fitting routine includes Pseudo-Voigt functions, allowing the fitting of asymmetric peak shapes as observed in diffraction spectra after several mechanical cycles. An example of such an asymmetric peak shape is shown in Figure 2.28.
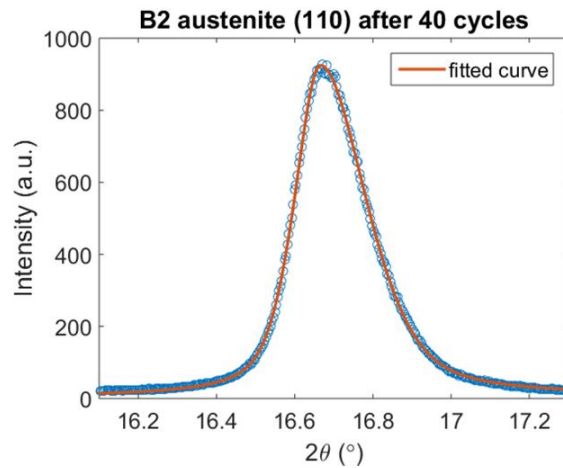
Figure 2.28 An asymmetric B2 austenite (110) peak fitted with the MATLAB fitting routine using an asymmetric Pseudo-Voigt function and a linear background.

Neutron diffraction data of austenitic stainless steels

The neutron diffraction data are analyzed with the POLDI standard fitting routine implemented in the software Mantid [117]. For the indexation of diffraction spectra of austenitic stainless steels, three phases are considered: FCC γ austenite, HCP ε martensite and BCC α' martensite. Note that when the carbon content is lower than 0.6 wt. %, the α' martensite exhibits a BCC structure rather than a body-centered-tetragonal structure [76]. The in-situ data captures the appearance of different phases and allows us to characterize the transformation sequences in SS201 and SS304.

2.5.2 Macroscopic digital image correlation (Macro-DIC)

In order to study the macroscopic force-strain response of cruciform samples under multiaxial deformation and load path changes, mechanical tests employing the Minibiax/Mesobiax are combined with Macro-DIC analysis. By comparing images of the test pieces at different deformation stages and tracking subsets of pixels, the DIC algorithm measures the displacement and calculates the strain. The Macro-DIC measurement is performed by placing a PixeLINK camera in front of the center of a cruciform sample mounted on Minibiax/Mesobiax. Digital images with a resolution of 2484 x 3840 pixels are taken during the mechanical test. The data analysis is undertaken with the open-source 2D-DIC software Ncorr implemented in MATLAB [118]. Different surface patterns prepared for Macro-DIC analysis are presented in the following section.

Macro-DIC of NiTi flat cruciform

The surface roughness of the as-received commercial superelastic NiTi sheet serves as the pattern for the Macro-DIC, as shown in the Figure 2.29a. The center of the cruciform highlighted by red lines is the region of interest (ROI) for the strain calculation. Figure 2.29b demonstrates a strain map obtained upon uniaxial loading along the y direction. The magnitude of strain is presented in terms of colors. The mechanical responses of NiTi flat cruciform to a uniaxial load followed by a load path change are discussed in Chapter 3.
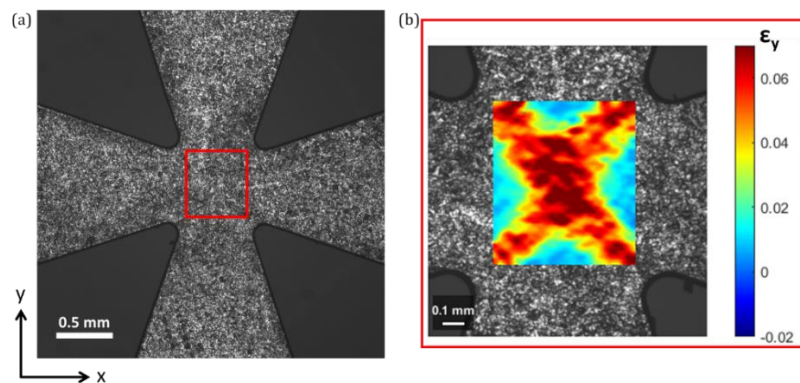
Figure 2.29 (a) The surface roughness of the as-received commercial sheet serves as the pattern for Macro-DIC analysis. (b) A strain map obtained from the DIC analysis shows the deformation at the center of the cruciform.

Macro-DIC of SS304 mini cruciform

The ECMM thinning process produces a mirror-like surface. The low surface roughness cannot serve as DIC pattern. Therefore, the surface obtained from ECMM is slightly etched with a solution of 170 ml H_2O, 230 ml HCl and 20 ml HNO_3 for 5 minutes in order to introduce surface roughness, which serves as the surface features to be tracked for the Macro-DIC analysis. Figure 2.30 shows an example of the DIC-strain map obtained from equibiaxial loading. The average equivalent strain is calculated from an area of 150 µm x 150 µm at the center of the pocket using the relationship:

$$\varepsilon_{eq} = \frac{2}{3} \times \frac{1}{\sqrt{2}} \sqrt{\left(\varepsilon_x - \varepsilon_y\right)^2 + \left(\varepsilon_y - \varepsilon_z\right)^2 + \left(\varepsilon_z - \varepsilon_x\right)^2 + 6\varepsilon_{yz}^2 + 6\varepsilon_{zx}^2 + 6\varepsilon_{xy}^2}$$

where ε_x, ε_y are the two in-plane strain components and ε_{xy} is the shear strain obtained by DIC analysis. ε_{yz} and ε_{zx} are taken as zero and ε_z is taken as $\varepsilon_z = -(\varepsilon_x + \varepsilon_y)$.
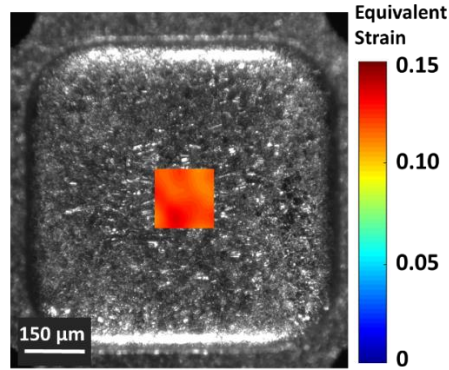
Figure 2.30 The equivalent strain calculated with Eq. 1 from the strain components obtained from Macro-DIC at the center of the cruciform, a global strain is averaged over an area of 150 μm x 150 μm (global strain ~14%).

The Macro-DIC analysis reveals the force-strain response from the center of the cruciform sample, thus it serves a tool to verify the geometry of cruciform sample designed with FE simulations. Figure 2.31 compares the force-strain curves obtained from simulations (dashed lines) and from Macro-DIC analysis (solid lines) for both load paths confirming the capability of reaching high strain levels. The resulting force in the case of equibiaxial load is taken as $\sqrt{F_{axis\,1}^2 + F_{axis\,2}^2}$ from the corresponding force readings on the two axes. The FE simulation is able to capture the experimental data relatively well. Small deviations may occur due to: (1) the development of texture during plastic deformation, whereas the simulation considers isotropic mechanical properties, (2) small differences in sample geometry between the model and the experiment due to tolerances in ECCM and laser-cutting and (3) the DIC providing only strain components ε_{xx}, ε_{yy} and ε_{xy} to calculate the equivalent strain. It is worth noting that a force-strain curve instead of a stress-strain curve is plotted for the mechanical response from a cruciform-shaped sample. Calculation of stresses requires FE simulations that takes the anisotropy of the material into account and a very accurate definition of the gauge cross-section area. It is reported that the effective cross-section changes during the cruciform deformation test. An in-depth study on converting the applied forces to the local stress state in a cruciform shape is however beyond the scope of this thesis.
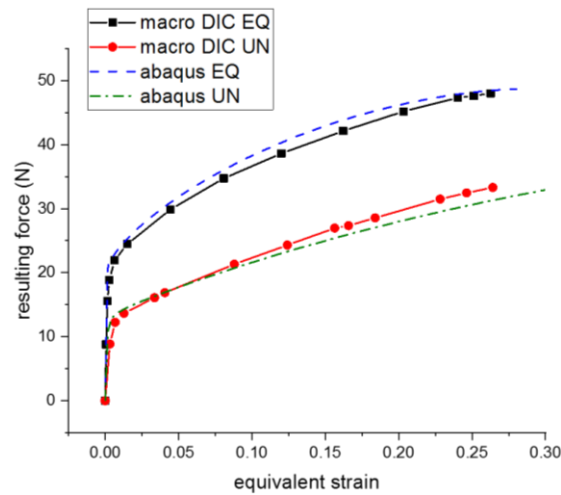
Figure 2.31 Comparison between experimental results from Macro-DIC and FE analysis for uniaxial (UN) and equibiaxial (EQ) loading.

Macro-DIC combined with in-situ neutron diffraction

As mentioned above, a DIC system (GOM Aramis) is implemented to the setup of the in-situ neutron diffraction experiment to measure the strain at the center of the cruciform sample. The details about the optical system can be found in [113]. Following the setup proposed in [113], the sprayed speckle pattern is applied to SS201 and SS304 large cruciform samples for DIC analysis. Figure 2.32 demonstrates the sprayed speckle pattern and a strain map with a field of view of 20 x 20 mm².
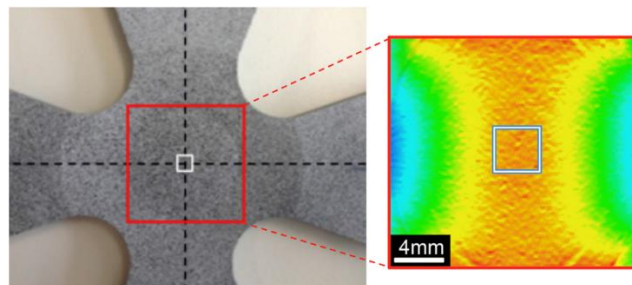
Figure 2.32 An example of the DIC strain map during uniaxial loading. The field of view for the DIC strain map is 20 x 20 mm² (red square). The size of the neutron beam is around 4 x 4 mm² (white square) [113].

2.5.3 High resolution digital image correlation (HRDIC)

The Minibiax can be mounted inside a Zeiss Ultra 55 SEM to perform in-situ HRDIC measurements. Figure 2.33 shows the illustration of the HRDIC experimental setup and a picture of the Minibiax mounted on the stage inside the SEM chamber. In order to study the deformation at a microscopic scale, a suitable pattern for HRDIC analysis should consist of fine and dense features. Various methods for achieving a sufficiently high-quality pattern for HRDIC analysis have been proposed in literature [119-121]. Two types of patterns have been adopted: colloidal silica oxide polishing suspensions (OPS) pattern and gold remodeling pattern. For the SEM image acquisition, an in-lens detector was utilized as it minimizes the topographic contrast by gathering low energy electrons, and it provides sufficiently good signal/noise for the working distance (WD) of 7.5 mm with the combination of an acceleration voltage of 3 kV and an aperture size of 20 μm.
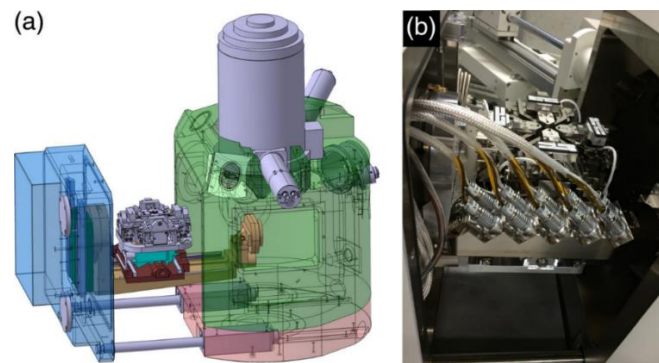
Figure 2.33 (a) The setup for in-situ HRDIC experiment. (b) Minibiax mounted inside the SEM chamber [103].

HRDIC: Colloidal silica OPS pattern

Spreading the silica particles onto the sample surface by polishing the surface with OPS can achieve a dense speckle pattern for HRDIC measurement [120]. In this study, the OPS from Microdiamant GmbH with particle size of 50 nm is used. Simply following the procedures proposed for dual phase steels in [120] does not yield a suitable pattern on the surface of NiTi. As Figure 2.34a shows, silica particles are not well spread on the surface, agglomerations of silica is observed. It is clear that the procedures need to be adapted for each material.
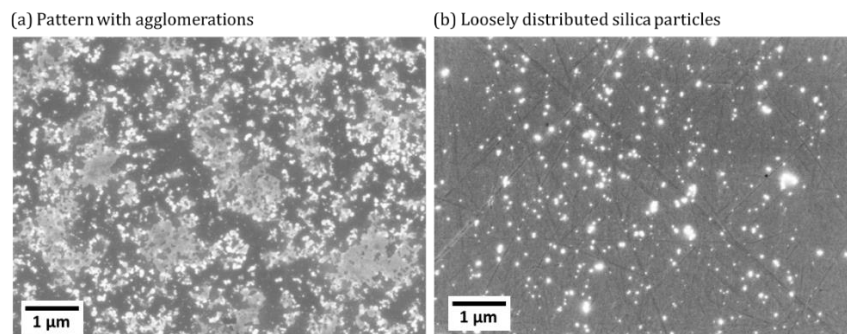
Figure 2.34 Examples of undesired OPS patterns with (a) agglomerations and (b) low density of silica particles.

By optimizing the polishing time, agglomerations can be minimized and particles can be more evenly distributed. The usage of deionized water instead of tap water effectively improves the quality of the pattern. The way to dry the sample is also found to be crucial. By blowing the surface with an air fan, there is a risk that some droplets blow across the region of interest. The passage of a droplet can remove the silica particles and results in a pattern with loosely distributed particles, as demonstrated in Figure 2.34b.

The optimized procedure for applying the speckle pattern on the surface of coarse-grained NiTi is described as follows:

1. Grind and polish the sample surface until it is mirror-like
2. Place OPS drops on a clean polishing cloth. The ChemoMet polishing cloth from Buehler is used in this study.
3. Polish the sample with a plate speed of 50 rotations per minute (RPM) for 30 seconds.
4. Flush the cloth with deionized water using a wash bottle meanwhile continue polishing for 5 seconds with 50 RPM plate speed.
5. Rinse the sample in ethanol for 1 second.
6. Rinse the sample in deionized water for 1 second.
7. Leave the sample to dry in air at room temperature.

With the OPS speckle pattern shown in Figure 2.35, the uniaxial deformation of the coarse-grained NiTi is studied with HRDIC, which is presented in Chapter 3.
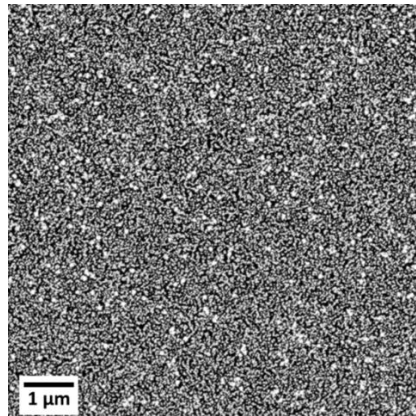
Figure 2.35 The OPS pattern used in the HRDIC study on the deformation of coarse-grained NiTi.

HRDIC: Gold remodeling pattern

The remodeling of a gold film can produce nanoscale aggregates of gold particles, which can serve as the speckle pattern for HRDIC analysis, resulting in strain mapping with sub-micron resolution. By adapting the method proposed in [119], sufficiently good speckle patterns have been obtained for the nanostructured NiTi and for SS304, as shown in Figure 2.36a and Figure 2.36b. With the gold speckle

patterns, the load path change on commercial NiTi and the slip activity in SS304 under multiaxial deformation have been studied, and the results are presented in Chapter 3 and Chapter 4 respectively.
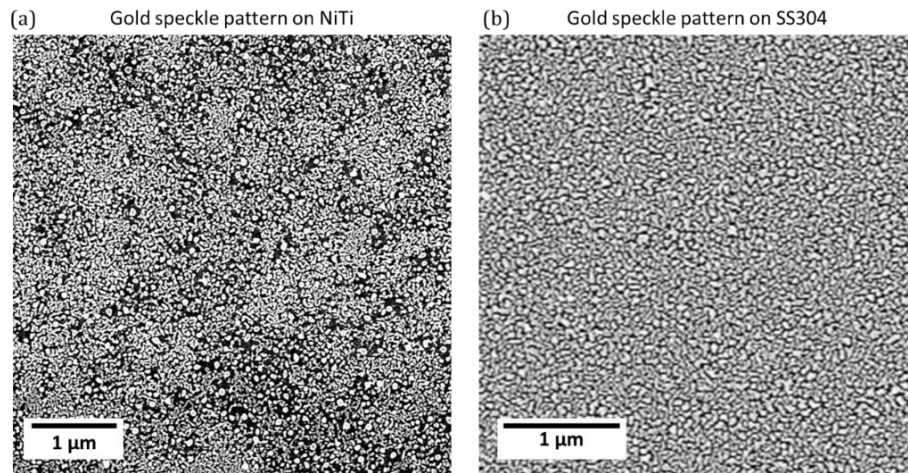
Figure 2.36 The gold speckle patterns (a) on the surface of a flat-geometry NiTi cruciform and (b) in the pocket of a small SS304 cruciform fabricated from ECMM.

The optimized procedures for gold patterns are listed below.

1. Prepare the sample surface as mirror-like. For NiTi flat cruciform, grinding and mechanical polishing was employed. For SS304 mini cruciform, the high quality surface was achieved with the ECMM process.

2. Deposit a thin layer of gold using the SPI-Module sputter coater, with the plasma current of 20 mA. The thickness of the gold layer (d) is calculated based on the empirical equation d=0.07IVt provided by SPI Supplies. In the equation, I is the plasma current, V is the voltage applied in kilovolts and t is the sputtering time in seconds. The deposition time of 90 seconds for NiTi results in a gold film of 13 nm thick. As for SS304, the thickness of the gold film after 120-seconds deposition is ~17 nm.

3. The setup of gold remodeling is shown in Figure 2.37. The temperature of the hot plate is kept at around 230°C.

4. Gold remodeling time for commercial NiTi: 30 minutes; for SS304: 60 minutes.
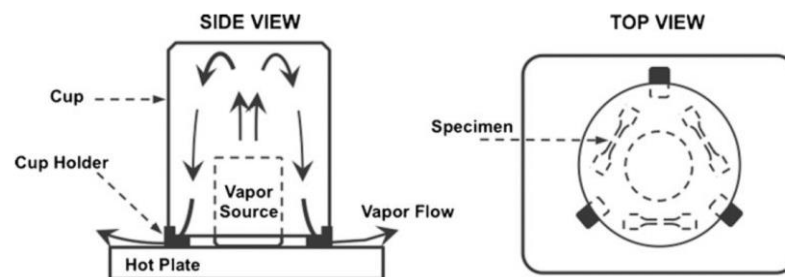
Figure 2.37 The experimental setup for gold remodeling process [119].

Throughout our trails of gold remodeling, we have found that pre-oxidation of the sample at 200 °C before depositing gold film can improve the gold remodeling pattern. As demonstrated by Figure 2.38, the remodeling process with the pre-oxidation step results in well-separated gold particles.
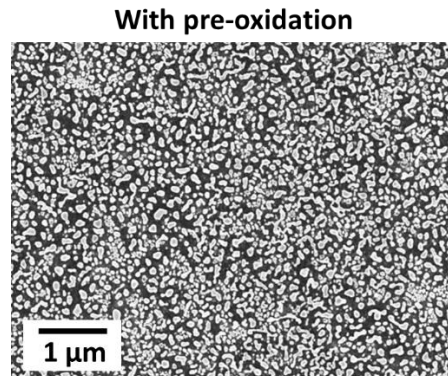
With pre-oxidation

Figure 2.38 Well separated gold particles on the surface of NiTi. The gold remodeling procedures contain a pre-oxidation step.

The remodeling procedures with the pre-oxidation step were applied to some NiTi cruciform samples. However, cracks were observed in the SEM images taken during in-situ HRDIC experiments. This was not the case for samples without pre-oxidation treatment. The appearance of cracks is rationalized as follows: the additional pre-oxidation step applied before depositing the gold layer results in the growth of an oxide layer between the material surface and the gold layer. The oxide layer is prone to crack upon loading. These cracks result in local high strains and severely disturb the DIC analysis, as Figure 2.39 shows.
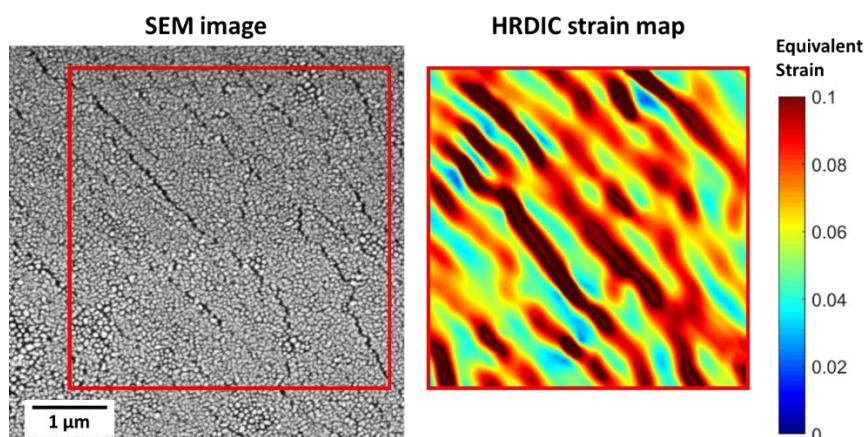
Figure 2.39 The cracks of the oxide layer formed on the surface of NiTi are visible in the SEM image. The HRDIC strain map shows only the cracking instead of the deformation of the underlying NiTi.

Orozco-Caballero et al. have proposed a setup with a controlled argon flow containing styrene vapor for gold remodeling at 150°C on materials susceptible to oxidation such as magnesium alloy AZ31 [122], resulting in finer speckles than patterns obtained using water vapor remodeling. This system could serve as an alternative to generate suitable speckle pattern on NiTi for HRDIC experiments.

2.6 Summary

The deformation-induced martensitic transformation in various engineering alloys have been studied by combining different in-situ characterization methods with multiaxial deformation tests. Table 2.6 lists all the studies including the type of characterization applied, the sample geometries used, and the corresponding chapters where results are presented.

Table 2.6 The summary of the characterizations and experiments performed on different materials

Material	Sample geometry	Tensile machine	In-situ characterization	Load path	Section
Nanostructured NiTi	ncNiTi-mini-flat	Minibiax	HRDIC Synchrotron XRD	Uniaxial Load path change	3.1
	ncNiTi-mini-TD	Mesobiax	Synchrotron XRD	Uniaxial Equibiaxial Load path change Multiaxial mechanical cycle	3.2
Coarse-grained NiTi	cgNiTi-miniDB	Minibiax	HRDIC	Uniaxial load	3.3
SS201	SS201-macro-TD	Macrobiax	Neutron diffraction	Uniaxial load Equibiaxial load	4.1
	SS201-largeDB	Uniaxial load frame at POLDI	Neutron diffraction	Uniaxial load	
SS304	SS304-mini-TD	Minibiax	HRDIC	Uniaxial load Equibiaxial load	4.2
	SS304-macro-TD	Macrobiax	Neutron diffraction	Uniaxial load Equibiaxial load	4.3
	SS304-lareDB	Uniaxial load frame at POLDI	Neutron diffraction	Uniaxial load	

Chapter 3 Deformation and degradation of superelastic NiTi

3.1 Load path change on nanostructured superelastic NiTi

This section is adapted from the published paper:

"Load path change on superelastic NiTi alloys: in situ synchrotron XRD and SEM DIC"

<u>Wei-Neng Hsu</u>, Efthymios Polatidis, Miroslav Šmíd, Nicola Casati, Steven Van Petegem and Helena Van Swygenhoven

Abstract

The transformation behavior of commercial superelastic NiTi material was studied during uniaxial tension and load path changes, by employing a novel miniaturized biaxial stage and cruciform shaped specimens. EBSD and X-rays are used to characterize the initial and final microstructure, in situ digital image correlation at the macro and micro length-scales and in situ X-ray diffraction are used to follow the transformation characteristics. The results reveal an initial microstructure where large austenitic grains are subdivided in bands containing nanoscaled subgrains. The link between the microstructure and strain accommodation during transformation is detailed and discussed in terms of Schmid behavior and strain path.

In this work, the contributions from the doctoral candidate are:

- Designed and fabricated the cruciform samples
- Optimized the procedure for applying OPS particles as speckle pattern for HRDIC
- Performed the Macro-DIC, in-situ HRDIC and in-situ XRD measurements
- Analyzed the data and summarized the results
- Wrote the first draft together with Dr. Polatidis and finalized the manuscript for submission

3.1.1 Introduction

Superelastic NiTi alloys have attracted significant attention for biomedical applications due to their property of absorbing large amounts of (deformation) energy and sustaining large strains [123, 124]. These materials have successfully been implemented, amongst others, as structural material in orthodontic arc wires, vascular stents and orthopedic devices [8, 123]. During operational conditions superelastic NiTi alloys can undergo sharp load path changes [113], which can lead to faster degradation of the superelastic properties upon repeated deformation cycles, as shown for simple uniaxial fatigue [44, 45, 48, 125].

Being able to model the superelastic behavior of components subjected to complex stress-states and load paths is particularly important, however the experimental data which are used to fit the models should not be solely obtained from simple uniaxial tension or compression tests [126, 127]. It has been shown for polycrystalline NiTi sheets that the shape of the superelastic stress–strain curve strongly depends on the orientation of the loading direction relative to the rolling direction [128]. This study showed that the magnitude of the plateau-strain is determined by the most favorably oriented martensite variants, whereas the magnitude of shape recovery strain is independent of the plateau-strain but depends on the reverse transformation of both favorably and less-favorably oriented martensite variants. Therefore, in order to allow for the development of reliable models, which can be used for complex structures and load path changes, it is important to have experimental data from complex loading experiments in order to justify the material models.

Different transformation behaviors with respect to different loading states have been reported [62, 65, 67-70, 129-132]. Unlike uniaxial tension, where the localization of the transformation has been observed optically [62, 133, 134], the application of shear loading or compression lead to a nearly uniform transformation [67, 68]. A uniform transformation accompanied with strain-hardening has been observed under equibiaxial tension in NiTi tubes [129]. Multiaxial stress states have also been applied by performing uniaxial tension on dogbone specimens with geometric defects (holes or notches) at the gauge area [62, 65, 69]. These studies revealed a dependence on martensite variant selection: at least two variants have been observed in one austenite grain in the biaxial loading, whereas only one variant appeared under uniaxial loading [69].

Despite the efforts to experimentally study NiTi under multiaxial loadings, there are only few experimental studies on the transformation behavior under load path changes [68, 70], and they are limited to the case of combining tension and torsion. Upon changing the load path on superelastic NiTi tubes, the stress-strain curve exhibited two distinct plateau regions, which was attributed to different martensite variants associated with tension and torsion loading [68]. The combined tension-torsion experiments also suggested the importance of the pre-loading [70], e.g. the amount of rotation induced by uniaxial displacement and the generation of martensitic variants were strongly affected by the

amount of pre-torsion. Among most studies mentioned above, the martensitic transformation has been examined only at the macroscopic length scale. The association between the transformation behavior under different loading conditions and the microstructure is still lacking.

The aim of the present work is to fully characterize the microstructure of a commercial superelastic NiTi alloy and to investigate its role in accommodating the strain during uniaxial loading and load path change. For this purposes a novel miniaturized biaxial device [103] is used to perform in situ experiments on cruciform-shaped samples during synchrotron X-ray diffraction and to perform digital image correlation (DIC) inside a scanning electron microscope.

3.1.2 Experimental

Materials

A superelastic NiTi sheet (50.8 at. % Ni and 49.2 at. % Ti) with a thickness of 90 μm was purchased from Memry GmbH. This material has been cold rolled and annealed in the temperature range of 400-600 °C by Memry GmbH [5, 6]. Figure 3.1a shows the "flat geometry" of the cruciform-shape specimen. Examined by Finite element simulations (FE) with the built-in model for superelasticity of shape memory alloys in ABAQUS software, the martensitic transformation is shown to occur at the center (see Figure 3.1b) when subjecting to the Load Path Change (LPC) experiment. The experimental samples were cut using a picosecond laser at the Swiss Federal Laboratories for Materials Science and Technology (EMPA).
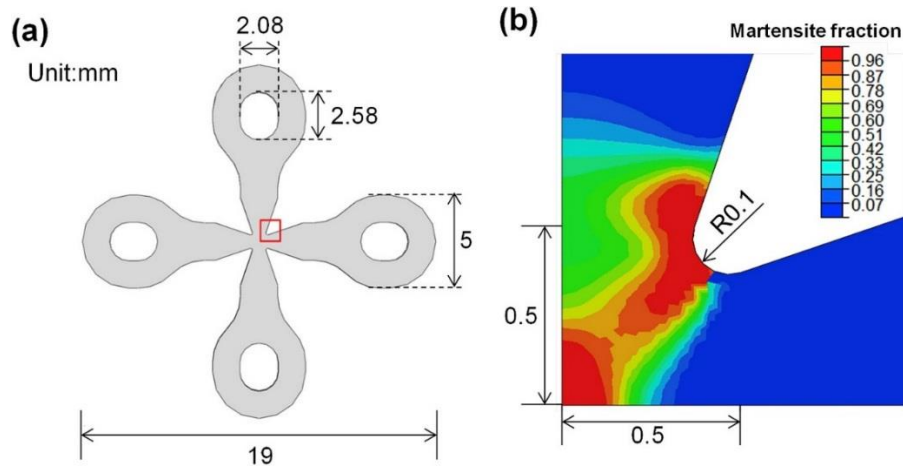
Figure 3.1 (a) The geometry of the flat cruciform-shape specimen. (b) FE result showing the distribution of martensite upon uniaxial loading vertically.

Load path change experiment

The LPC experiment was performed with the cruciform-shape specimen mounted on the mini-biaxial machine with a displacement rate of 200 nm/s for both loading/unloading [103]. Figure 3.2a shows

the loading sequence and the resulting force-displacement curves (for F1 and F2) in Figure 3.2b. The specimen was first subjected to a tensile loading along axis 1 until F1 = 24 N, this loading state is denoted as F1max. During the second loading along axis 2, the two arms along axis 1 were held at the same positions while F1 only decreased 1% in magnitude. After reaching F2 = 27 N (denoted as F1F2 in Figure 3.2a), the force applied to axis 1 was released and the loading state F2max was reached. Finally, the force applied along axis 2 was released, i.e. the specimen was fully unloaded and a full cycle of LPC was completed.
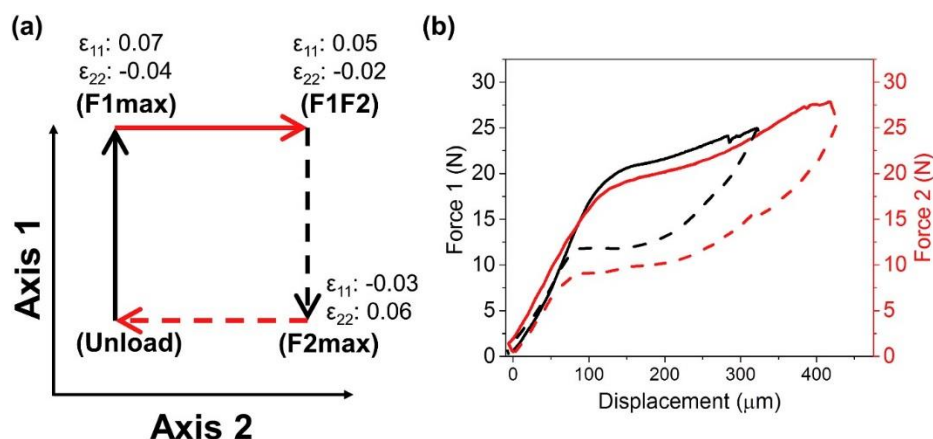
Figure 3.2 (a) The loading sequence of the load path change experiment. The forces (F1, F2) at points F1max, F1F2, F2max and Unload are (24, 0) N, (24, 27) N, (0, 27) N and (0, 0) N respectively. The strains along axes 1 and 2 (averaged over a 100×100 μm2 area at the center of the cruciform) are given for all loading states. (b) The force-displacement curves for the LPC, the colors and type of the lines correspond to the loading sections in (a).

EBSD characterization

In order to obtain a well-polished surface, suitable for electron backscatter diffraction (EBSD), microstructural characterization and high-resolution DIC (HRDIC), the cruciform-shaped samples were glued onto a Struers AccuStop holder, carefully ground from both sides with SiC sandpapers with descending roughness (600, 800, 1200, 2400, 4000 grit) and then polished with 3 μm and 1 μm diamond suspension. Finally, vibration polishing was performed for 24 hours using a Buehler Mastermet2 suspension on a Buehler VibroMet2 instrument. The entire polishing procedure reduced the sample thickness to approximately 80 μm.

EBSD investigation was undertaken using a field emission gun scanning electron microscope (FEG SEM) Zeiss ULTRA 55 equipped with EDAX Hikari Camera operated at 20kV in high current mode with 120 μm aperture. The patterns were acquired by TEAM software with 4x4 pixels binning and a condition of 8 bands for pattern recognition. The step size of the mapping varied according to the size of the region of interest from 150 to 60 nm. The EBSD raw data were post-processed using the EDAX OIM Analysis 7.3 software. For high resolution EBSD a FEG SEM FEI Helios G3 equipped with an EDAX EBSD system was used at the University of Poitiers. This instrument enables to perform mapping with a step size of 30 nm.

Digital image correlation

Digital Image Correlation (DIC) analysis was undertaken in order to study the deformation and the distribution of the transformation strain during the LPC. A PixeLINK camera with in-line 2× telecentric lens from Edmund Optics was used to perform the macroscopic DIC (Macro-DIC) investigation at the center of the cruciform. The surface roughness of the as-received material exhibited features that were tracked for performing Macro-DIC. The DIC analysis was undertaken using the Ncorr open source 2D-DIC software, implemented in MATLAB [118], using subset radius of 20 pixels, subset spacing of 2 pixels and 5-pixels strain radius. This combination of parameters was found to give a good compromise between resolution and noise.

For the in situ HRDIC measurements, the mini-biaxial machine was installed inside the chamber of FEG SEM Zeiss ULTRA 55 to study the microstructural evolution and deformation at a smaller length scale [103]. The speckles for HRDIC were prepared by the remodeling of a thin gold film deposited on the polished surface of the cruciform [119]. To obtain high contrast images for HRDIC analysis, the method proposed by Yan et al. [120] was adopted. An in-lens detector was utilized as it minimizes the topographic contrast by gathering low energy electrons, and it provides sufficiently good signal/noise for the working distance (WD) of 7.5 mm with the combination of an acceleration voltage of 3kV and an aperture size of 20 μm. A series of SEM images with a resolution of 3072×2304 were taken slightly offset the center (∼40 μm, see Figure 3.5) of the cruciform because of an optimal speckle pattern at this location. Slightly overlapping images at ×4000 magnification with dwell time of 25 μsec. (∼5 μm overlap) were taken after reaching each loading state (Figure 3.2a) in order to create strain maps of 65 μm x 43 μm. The HRDIC analysis was undertaken using the Ncorr MATLAB code [118], using a subset radius of 30 pixels, a subset spacing of 4 pixels and a strain radius of 5 pixels. This combination of parameters was found to give a good compromise between resolution and noise due to drift and lens distortions [119].

In situ synchrotron XRD

The mini-biaxial machine was mounted on the goniometer of the powder diffraction station at the Materials Science (MS) beam line at the Swiss Light Source (SLS) [135]. The XRD measurements were performed during loading/unloading and while keeping the displacement at different loading state: F1max, F1F2, F2max and after full cycle of the LPC (see Figure 3.2a).

The experiment was carried out in transmission with a 20 keV beam with $100×100$ μm^2 spot size at the center of the cruciform (see Figure 3.5 for the position). Two-detectors, a Mythen II microstrip detector and a Pilatus M6 2D detector, were employed to simultaneously record diffraction data along the scattering vectors parallel to the two in-plane directions of the cruciform specimen (see Figure 3.3). The Mythen II microstrip detector was positioned such to record data in a range of 2θ of ∼ -55° to + 55° parallel to the loading direction F1 with 30 s counting time (see Figure 3.3). The 2D diffraction

images were recorded with the Pilatus 6M 2D detector with counting time of 30 s. The 2D images were then caked and integrated using FIT2D [136] along an azimuthal range of 175°-185° that corresponds to the direction parallel to F2 (see Figure 3.3). The detector position, the tilt and rotation angles and the beam center were calibrated using a LaB6 reference powder material.

The diffraction-line profiles were fitted with a pseudo-Voight profile-shape function using the software WinPLOTR [137]. The martensite volume fraction was calculated from the integrated intensities of the austenite and martensite reflections [138]:

$$f_M = \frac{\sum I_{(hkl),M}}{\sum I_{(hkl),M} + \sum I_{(hkl),A}} \qquad \text{(Eq. 3-1)}$$

Where $\sum I_{(hkl),M}$ is the sum of the integrated intensities of the martensite reflections and $\sum I_{(hkl),A}$ is the sum of the integrated intensities of the austenite reflections.

Figure 3.3 Schematic of the experimental setup at the MS beamline showing the two-detector system.

3.1.3 Nanostructured microstructure

EBSD and XRD measurements were performed on the as-received material in order to characterize the initial microstructure and to determine the area for the HRDIC measurements. The average B2 austenite grain size was determined by EBSD to be 27±12 μm and the austenite phase exhibits strong out-of-plane texture, i.e. the majority of the austenite grains are <1 1 1> -oriented (see Figure 3.4a). The initial microstructure is complex as shown by the inverse pole figure (IPF) and the image quality (IQ) maps obtained from the EBSD analysis (see Figure 3.4a and Figure 3.4b). In Figure 3.4a, bands with crystallographic orientations different from the <1 1 1> -orientation are found within the

majority of the large austenite grains. The contrast in the IQ map in Figure 3.4b originates from the variations in the quality of the electron backscattered patterns and enables to reveal additional microstructural details when compared to the IPF maps. The darker bands correspond to regions where the multiple boundaries of the subgrains interact with the electron beam [139]. Comparing Figure 3.4a and Figure 3.4b, it is clear that each large grain contains several bands. These bands vary in width, direction and crystallographic orientation and agree with the {1 1 2} and {1 1 4} twinning systems of the austenite phase [140, 141]. The particular grain in Figure 3.4c shows two types of bands with high misorientation relative to each other (crystallographic orientations corresponding to green and blue colors of the IPF); the grain boundary is given with a dashed line. Figure 3.4d shows that a band is usually composed of agglomerations of subgrains having lower crystallographic misorientation relative to the each other; e.g., the band with crystallographic orientation close to <1 0 1> in Figure 3.4d consists of numerous subgrains (variation of green color of the IPF).

The XRD pattern of the as-received material exhibits only B2 austenite reflections. Williamson-Hall analysis [142] revealed that the crystallite size is 40 nm, which corresponds to approximately the size of the subgrains in a band, as observed by EBSD. The initial microstructure is hence characterized as a B2 austenite phase with large grains containing bands with different orientation (corresponding to {1 1 2} and {1 1 4} twinning systems) and populated by nanoscaled subgrains.
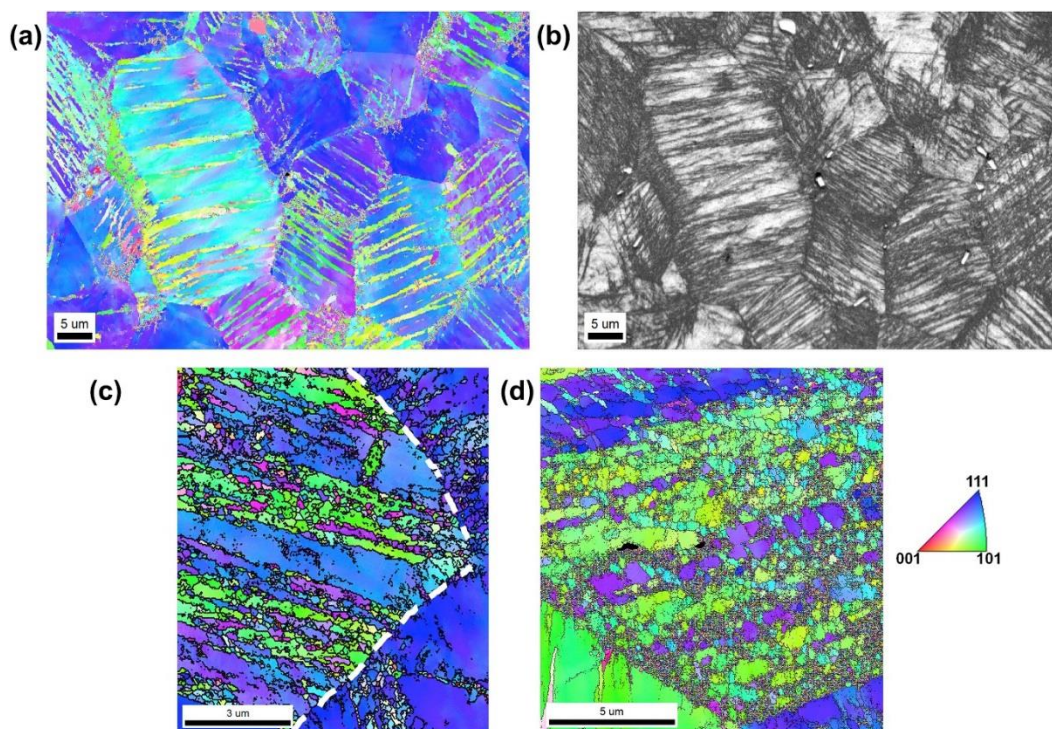
Figure 3.4 (a) EBSD out-of-plane IPF map of the as-received material. (b) The IQ map shows complex and fine microstructure of the as-received material. (c) One large austenite grain is composed of differently oriented bands. The grain boundaries are indicated with dashed lines. (d) At high magnification, it can be seen that the bands, within the large austenite grains, consist of substructures with similar crystallographic orientations.

3.1.4 Localization of martensitic transformation

Figure 3.5 shows the strain maps from the Macro-DIC analysis at the four loading states (specified in Figure 3.2). The strain magnitudes along axis 1 and axis 2 are denoted as ε_{11} and ε_{22} respectively. Macro-DIC revealed the localization of the strain, which is associated with the martensitic transformation. Upon loading axis 1 up to F1max, an X-shape band with high ε_{11} strain forms at the center of the cruciform. After loading axis 2 until F1F2 (cf. Figure 3.2), the width of the transformation band in Figure 3.5b decreases as well as the strain ε_{11} magnitude inside the band. A further strain reduction of ε_{11} is observed during unloading axis 1, from F1F2 to F2max (cf. Figure 3.2). The strain map at F2max reveals the formation of a new X-shape band at the center of the cruciform. This band appears as strain concentration of ε_{22}, and has a different inclination from the one formed under F1max (cf. Figure 3.5). The strain magnitude at both loading states F1max and F2max is equal to 7%. After a full cycle of the LPC, the strains ε_{11} and ε_{22} are within the uncertainty of the measurement fully recovered.

In summary, Macro-DIC reveals forward and reverse martensitic transformations during one LPC cycle. The formation of different X-shape bands (strain localization along either ε_{11} or ε_{22}) reflects the way the martensitic transformation accommodates the applied strain along either axis 1 or axis 2 (i.e. at either loading state F1max or F2max in Figure 3.2).
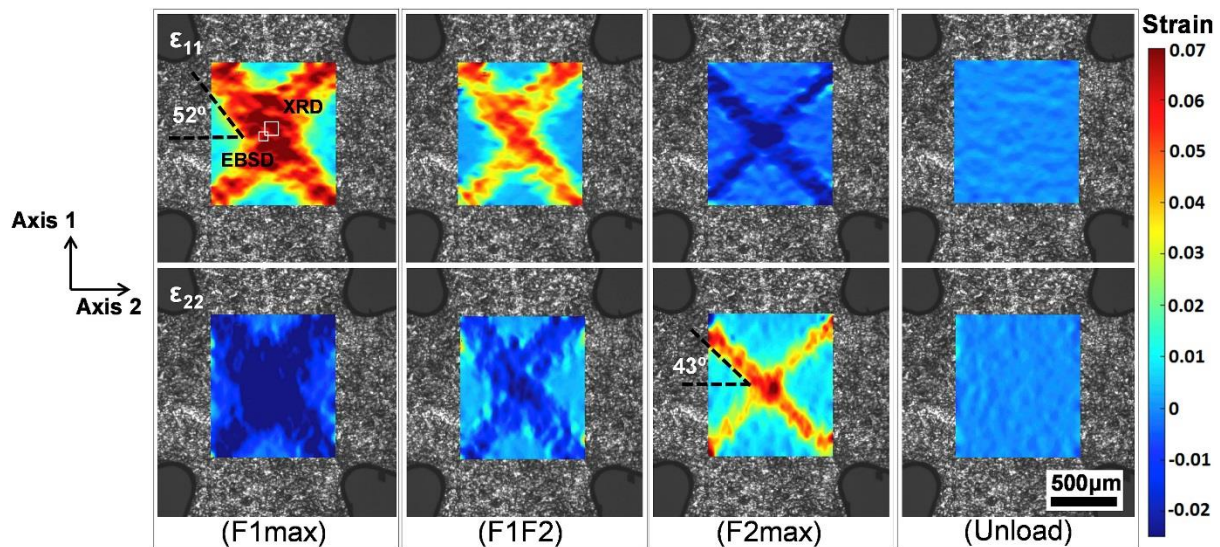
Figure 3.5 Macro-DIC results showing the evolution of the X-shaped transformation bands along the load path change shown in Figure 3.2. The white squares in the first DIC image indicate the position that the XRD and EBSD measurements were undertaken on the cruciform.

To investigate the transformation bands microscopically, HRDIC was performed close to the center of the cruciform. Figure 3.6a and Figure 3.6b show the in-plane strain maps at F1max and F2max respectively: the strain ε_{11} at F1max and the strain ε_{22} at F2max. The grain boundaries are designated with dashed lines based on the EBSD IPF map of the same area (see Figure 3.4a). The grains A – E in Figure 3.6 are discussed in more details in Section 3.1.6. Note that the left bottom part of Figure 3.6b

exhibits almost no transformation strain, which has to be ascribed to the change in shape of the X-shape transformation band: i.e. this part of the field of view is probably outside of the X-shaped band observed at F2max. This is confirmed by the average strain calculated from HRDIC under F2max which results in $\sim$ 3% instead of the expected $\sim$ 7% calculated from Macro-DIC close to the center of the cruciform. Locally it was however observed that on the right hand side of Figure 3.6b some grains generate higher transformation strains at F2max than at F1max (see e.g. grains B and E). The vertical lines appearing periodically throughout the whole map are artifacts originating from the drift distortions relating to the scanning motion of the electron beam in SEM [143].

Figure 3.6a and Figure 3.6b show that the strain accommodated by the phase transformation is microscopically heterogeneous. Under both loading states (F1max and F2max), high strains develop locally and form bands inside the large grains. Localized high-strain bands are oriented similarly to the microstructural bands observed in the IPF map (cf. Figure 3.4a), underlining the important role of the microstructural features of the as-received material in the transformation behavior. Furthermore, the localization of these high strain bands differs under different loading states as will be discussed in more details in Section 3.1.6.
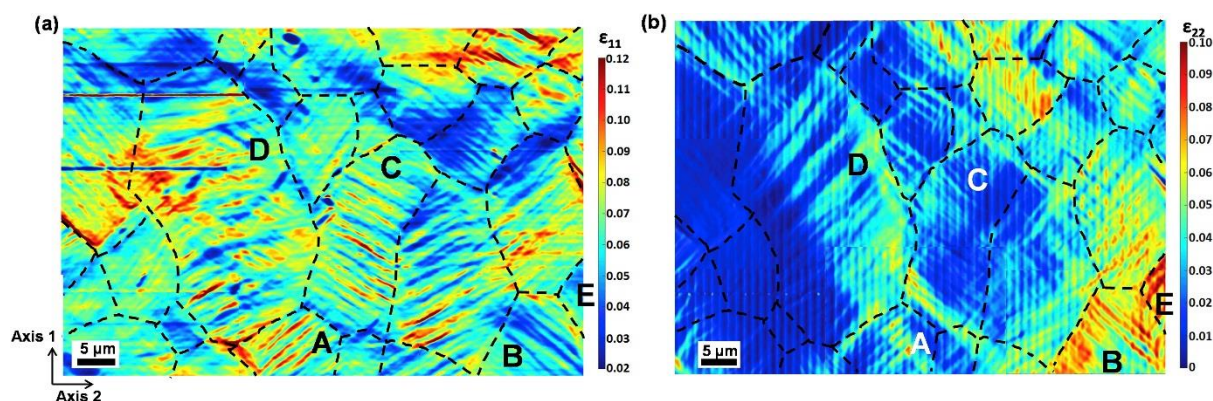
Figure 3.6 HRDIC strain maps taken under different loading conditions: (a) F1max and (b) F2max. Grains A-E are discussed in Section 3.1.6.

3.1.5 In situ synchrotron-XRD study of the LPC

Figure 3.7a shows the evolutions of the diffraction reflections in a selected 2θ range from both Mythen II and 6M Pilatus detectors during the LPC. At the beginning of the first loading, the strong reflection corresponds to the $(1\ 1\ 0)_{B2}$ reflection. During loading along axis 1, the position of the $(1\ 1\ 0)_{B2}$ reflection shifts towards a lower 2θ angle for the Mythen II detector and towards higher 2θ angle for the 6M Pilatus detector. When F1 reaches $\sim$ 24N, the intensity of the $(1\ 1\ 0)_{B2}$ reflection drops suddenly, meanwhile reflections of B19' martensite appear. Two strong martensite reflections are observed at F1max: the $(0\ 0\ 2)_{B19'}$ and the $(0\ 1\ 2)_{B19'}$ reflections. Upon loading axis 2, no new martensite reflection emerges. The position of the $(0\ 0\ 2)_{B19'}$ and the $(0\ 1\ 2)_{B19'}$ reflections move slightly to higher 2θ values (see Figure 3.7a), reflecting the action of F2 on the existing martensite.
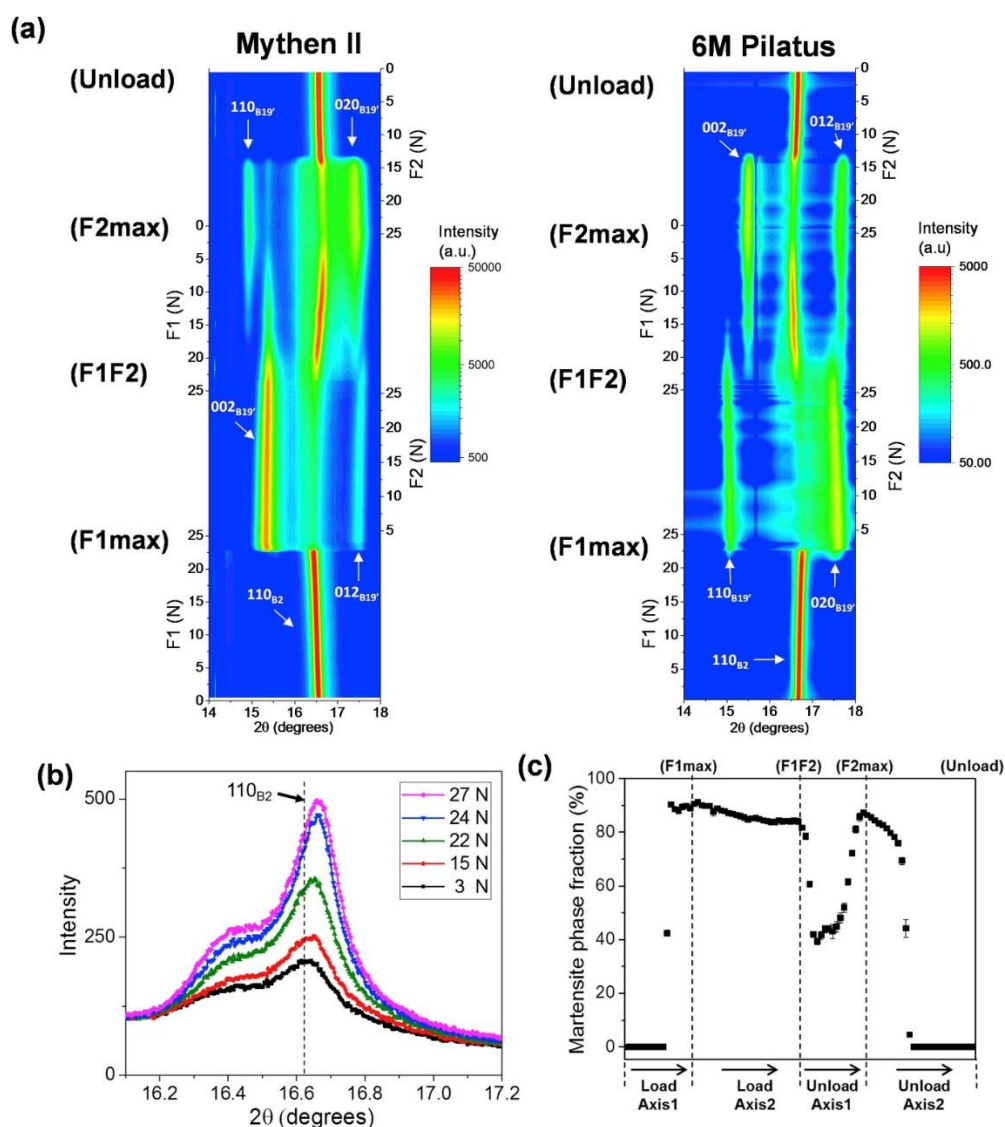
Figure 3.7 (a) Evolution of the X-ray diffraction reflections along the LPC cycle shown in Figure 3.2. (b) Evolution of the $(110)_{B2}$ reflection between loading state F1max and F1F2 (loading axis 2), data from Mythen II detector; the legend shows the values of F2. (c) Evolution of the martensite phase fraction along the LPC shown in Figure 3.2, data from the MYTHEN II detector parallel to axis 1.

This effect can be also observed in the $(1\,1\,0)_{B2}$ reflection, suggesting stress relaxation in the austenite (Figure 3.7b). This plot also shows that the intensity of the $(1\,1\,0)_{B2}$ reflection slightly increases during this loading path. Figure 3.7c shows the evolution of the martensite phase fraction obtained from Mythen II during the full LPC. Between F1max and F1F2 a slight decrease in the martensite phase fraction is observed. The reverse transformation from martensite back to austenite phase has been proposed as a possible deformation process under multiaxial loading as suggested in the micromechanical modeling of superelastic NiTi during the biaxial loading of tension and shear [144]. The present XRD results seem to confirm that upon changing loading path from uniaxial to biaxial, reverse transformation can occur. This is also evidenced by the decrease in the strain magnitude within the transformation band in Macro-DIC. At the microscopic level, a reduction in the intensity of some high-strained bands is observed. A preliminary HRDIC test, performed on another cruciform

with the same geometry shown in Figure 3.1, captured the decreasing strain upon this load path change at a microscopic level. Figure 3.8 clearly shows that the decrease in the strain magnitude and the number of the high-strain bands formed at F1max after reaching F1F2, which agrees with the observations from Macro-DIC (cf. Figure 3.5).
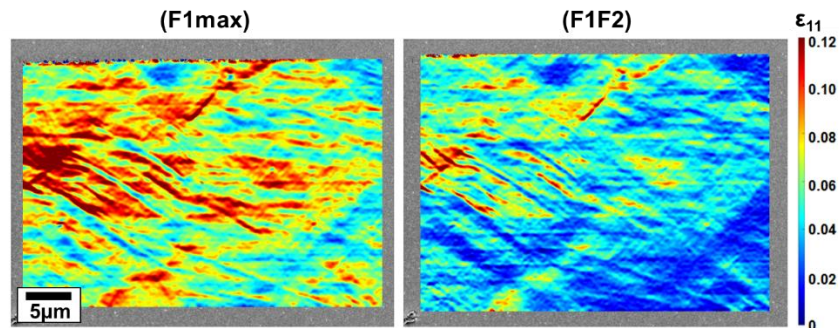
Figure 3.8 The HRDIC strain maps at F1max and F1F2 states.

If this reduction in strain magnitude can be related to local reverse transformation of some nanoscaled subgrains is a matter of further research. The above results furthermore show that the martensite variants in the F1F2 loading state are the same as in the loading state F1max, which is not necessary in agreement with the Schmid law. This observation suggests that the variants at F1F2 depend on the path followed to reach this stress state.

Between F1F2 and F2max, first the intensity of the austenite reflections continues to increase but is then followed by an abrupt decrease. During this loading path, the intensity of the $(1\ 1\ 0)_{B2}$ reflection increases (Figure 3.7a), while the intensities of the martensite reflections decrease. The position of the $(1\ 1\ 0)_{B2}$ reflection shifts back to the initial position (unloaded state), moving further towards higher 2θ angle for the Mythen II detector and towards lower 2θ angle for the 6M Pilatus detector (as expected for this loading path). When axis 1 is nearly completely unloaded (5N), a new set of martensite reflections appear together with the abrupt loss in intensity of the austenite reflections. Figure 3.7c shows that the martensite phase fraction decreases drastically and then increases again during loading between F1F2 and F2max. The set of martensite reflections formed under F1 disappear and a new set forms corresponding to the applied load F2, suggesting that different martensite variants appear upon the load path change. During the final unloading of axis 2, the martensite reflections disappear and the initial intense austenite reflections appear again. The $(1\ 1\ 0)_{B2}$ reflection in Figure 3.7a shifts back to the initial position after one full LPC cycle, suggesting full recovery of the deformation and therefore good superelasticity within one LPC cycle.

The full-width-half-maximum (FWHM) of the $(1\ 1\ 0)_{B2}$ reflection increases from 0.072^0 to 0.076^0 for the diffraction pattern obtained from Mythen II and from 0.115^0 to 0.122^0 from Pilatus 6M after a full LPC cycle. The two FWHM in the perpendicular directions are different, even before the loading, due to the different instrument resolution function in the two directions and in the two detectors. The

broadening of the peak profile indicates the accumulation of dislocations after a full LPC cycle and the accumulation of residual strain as previously observed for this material in simple tension [6]. This is confirmed in Figure 3.9, where (a) shows residual strain traces after full unloading and (b) the corresponding Electron Channeling Contrast Image (ECCI) of the same area. The narrow strain traces can be correlated to the sharp contrast features from retained dislocation bundles in the transformed areas.
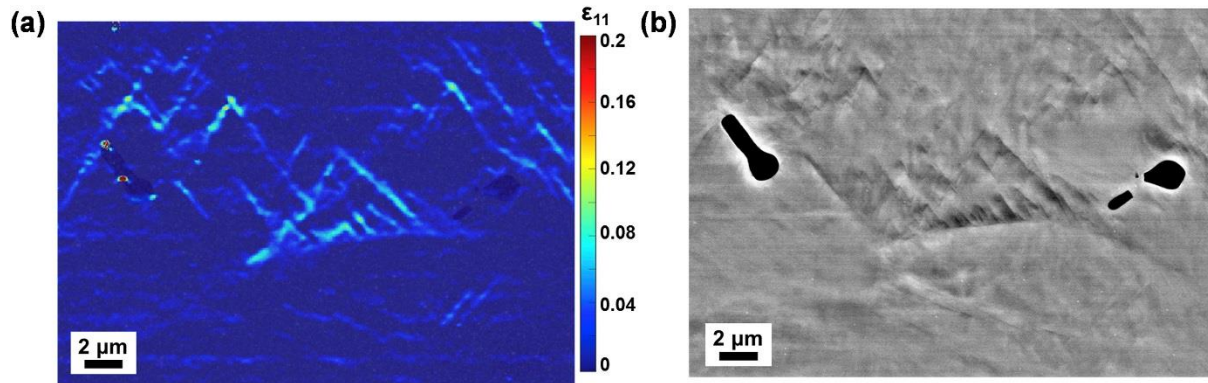
Figure 3.9 (a) HRDIC strain map after one full LPC showing residual strain traces. (b) ECCI of the same region as (a) revealed traces corresponding to dense dislocation activity. The dark features correspond to brittle $NiTi_2$ precipitates, see the localization of very high strain on the top left of the HRDIC maps which corresponds to cracking of the precipitate.

3.1.6 The role of the subgrains in the transformation behavior

Combining the results from synchrotron XRD, HRDIC and EBSD, the role of the microstructure of a commercial superelastic NiTi alloy in accommodating strain during uniaxial tension and LPC is revealed. The initial microstructure is composed of large austenite grains with an out-of-plane <1 1 1> texture. The grains contain narrow bands which can have a relative high misorientation with respect to the hosting austenitic grain. Each band is composed of numerous nanoscaled subgrains having small crystallographic misorientations with respect to each other, as previously observed by TEM [45]. The 2D diffraction images evidence continuous parts of the Debye-Scherrer rings rather than discontinuous diffracted spots, confirming that the diffraction data are issuing from the subgrains. Note that the microstructure has no in-plane texture, as shown in Figure 3.10, Figure 3.11 and Figure 3.12.

To verify the role of the bands and subgrains in the transformation behavior, details of EBSD and HRDIC results are presented for a few grains. Since the martensitic transformation in NiTi has been reported to follow the Schmid law [128, 145], (Schmid factor) SF maps were additionally calculated. These maps show the maximum values of the SF among the 24 possible variants for a given crystallographic orientation by considering different macroscopic tensor matrices under F1max and F2max respectively. For this purpose, the shear system {$\overline{0.8684}$ 0.2688 0.4138} ⟨0.4580 0.7706 0.4432⟩ for <0 1 1> Type II twinning observed by Matsumoto et al. [27] was considered. It was adapted

to rational indexes $\{\overline{4}\ 1\ 2\}\langle 1\ 2\ 1\rangle$ for the SF analysis with OIM software. The misorientation between the rational indexes and the exact shear system is within 5°. Figure 3.10, Figure 3.11 and Figure 3.12 show for a few grains (contained in Figure 3.6) the EBSD IPF maps for out-of-plane and in-plane orientations, the HRDIC strain maps and SF maps for F1max and F2max. In general, the SF of the most favorable variant is relatively high for all grains in both loading states (F1max or F2max) which explain the 90% volume fraction of martensite observed by XRD. The different maps shown in Figure 3.10, Figure 3.11 and Figure 3.12 indicate that the transformation is strongly correlated to the complex austenite microstructure. The high-strain bands observed by HRDIC correspond to microstructural bands observed in IPFs. Which microstructural band will create a high strain bands depends on the loading state as will be discussed below.

Figure 3.10 shows the details for grain A. The IPF shows narrow bands alternated with broader bands distinguished by out-of-plane and in-plane misorientations. Under F1max the narrow bands have high SF values and correspond with high-strain bands in the HRDIC map. Under F2max, the correspondence is not so clear, although the highly strained locations in the HRDIC seem to coincide with an area where the SF is higher than its surrounding. Similar observations can be made for grain B and grain E. In grain B the strain bands are a bit less pronounced, they can however also be correlated to microstructural bands observed in the IPF maps. In the SF maps there are no bands recognizable and high SF variants are available under F1 and F2 for the entire grain. This is not the case for grain E. There, the microstructural bands are also recognizable in the SF maps and the strain bands are very pronounced under F2max.
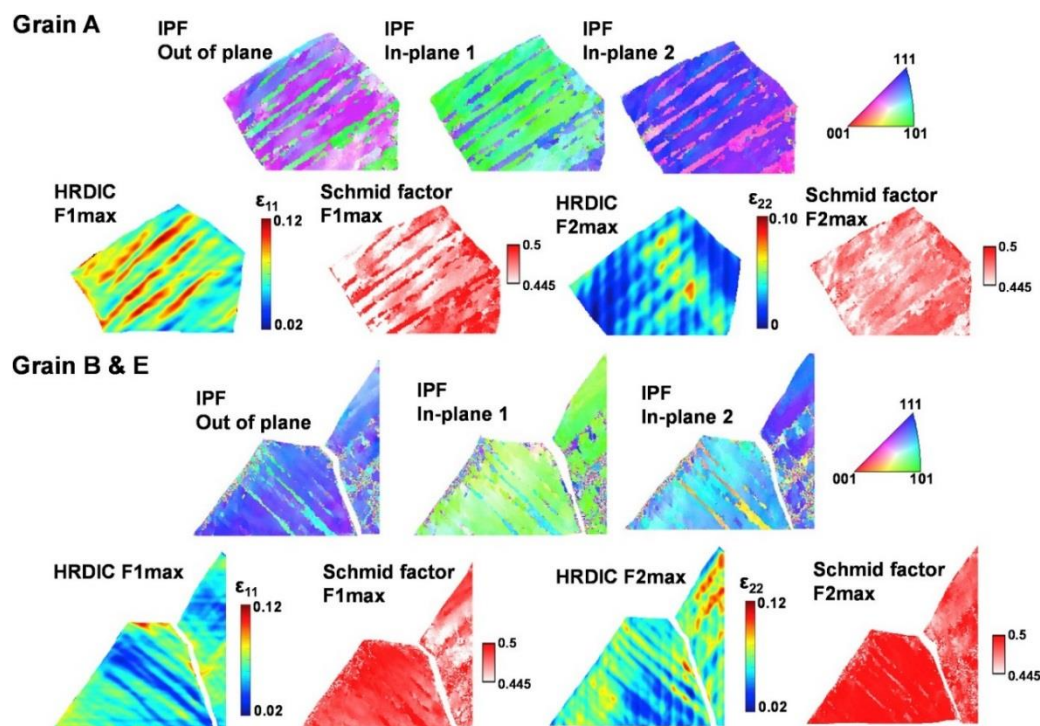
Figure 3.10 Initial austenite microstructures, HRDIC strain maps and Schmid factor maps for grains A, B and E in Figure 3.6.

Figure 3.11 shows the details for grain C. Besides the narrow bands as discussed above, this grain has a central area (dashed circle) where "clouds" of clustered subgrains are recognizable in the IPF maps. The in-plane and out-of-plane IPFs show that the clusters are misoriented relative to each other. Each cluster seems to contain nanograins with similar crystallographic orientations, as was also observed in the high magnification EBSD maps in Figure 3.4. The central area exhibits considerable scatter of the SF values under F1max. Nevertheless, high strain bands are observed in HRDIC under F1max suggesting that clusters of differently oriented subgrains transform collectively choosing a single martensite variant and thus resulting in similar (high) values of transformation strain. The latter implies that the transformation is affected by the intergranular interaction between the subgrains, which obstructs the absolute obedience to the Schmid law. Non-Schmid behavior as a result of intergranular strains was also observed in equiaxed polycrystalline NiTi with either relatively small [146] or relatively large grain size [147]. At the loading state F2max, the transformation strain in grain C is relatively low and concentrates at different locations. As discussed previously, grain C is probably situated out of the center of the transformation band which moved when changing load path from F1 to F2.
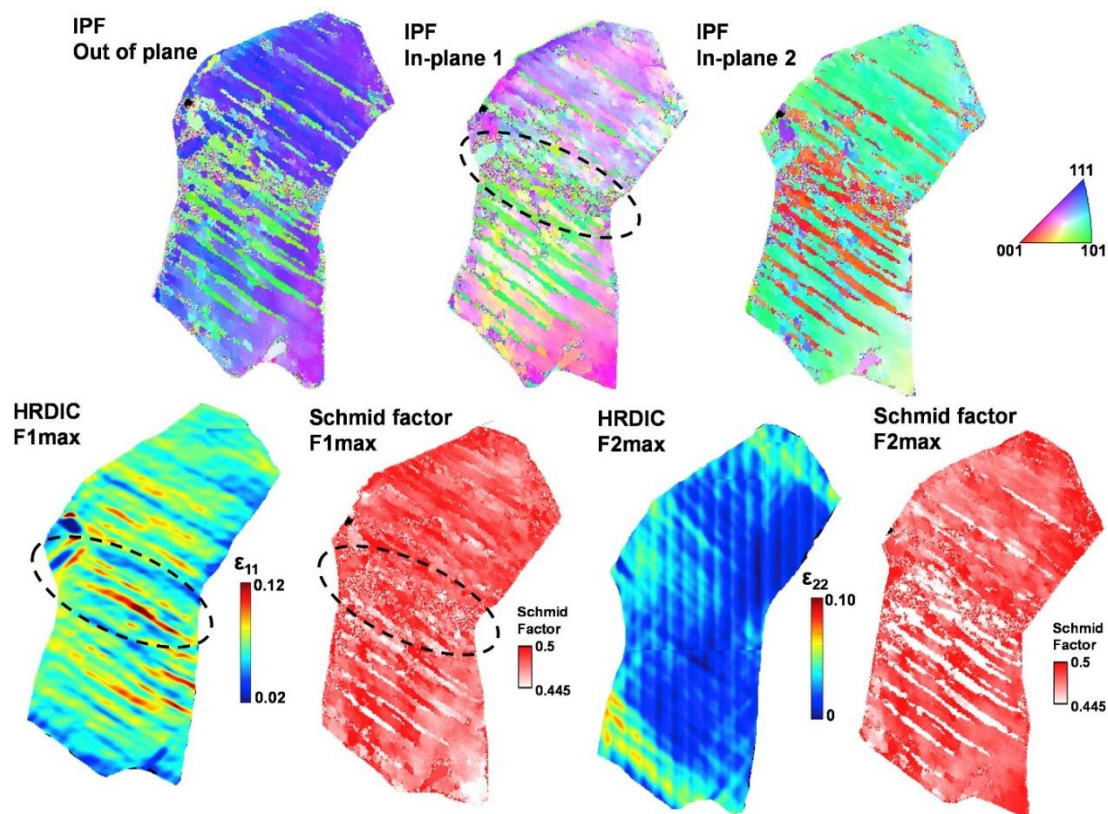
Figure 3.11 Initial austenite microstructures, HRDIC strain maps and Schmid factor maps for grain C in Figure 3.6.

Grain D in Figure 3.12 is another interesting example underlining the role of subgrained bands within an austenitic grain. According to the IPF maps, three types of bands a-c with different orientations are observed, marked with dashed lines. Type-b bands have well-defined interfaces, and they consist of subgrains having all a distinct crystallographic misorientation relative to the subgrains outside the

band. On the other hand, the crystallographic orientations of type-a and type-c are more similar to each other, and the boundaries between these two types of bands are more diffuse. Interestingly, under F1max, the locations of high strain in the HRDIC map correspond to the orientation of type-a and -b bands, whereas, under F2max, the transformation bands correspond to the type-c bands. Careful inspection reveals that the SF maps reflect the three types of bands in both loading states.

In summary, the results show the strong correlation of the transformation with the Schmid law at the loading states F1max and F2max. However, evidence of non Schmid behavior is obtained by the appearance of the same variants at F1max and F1F2 and the collective transformation of differently orientated subgrains.
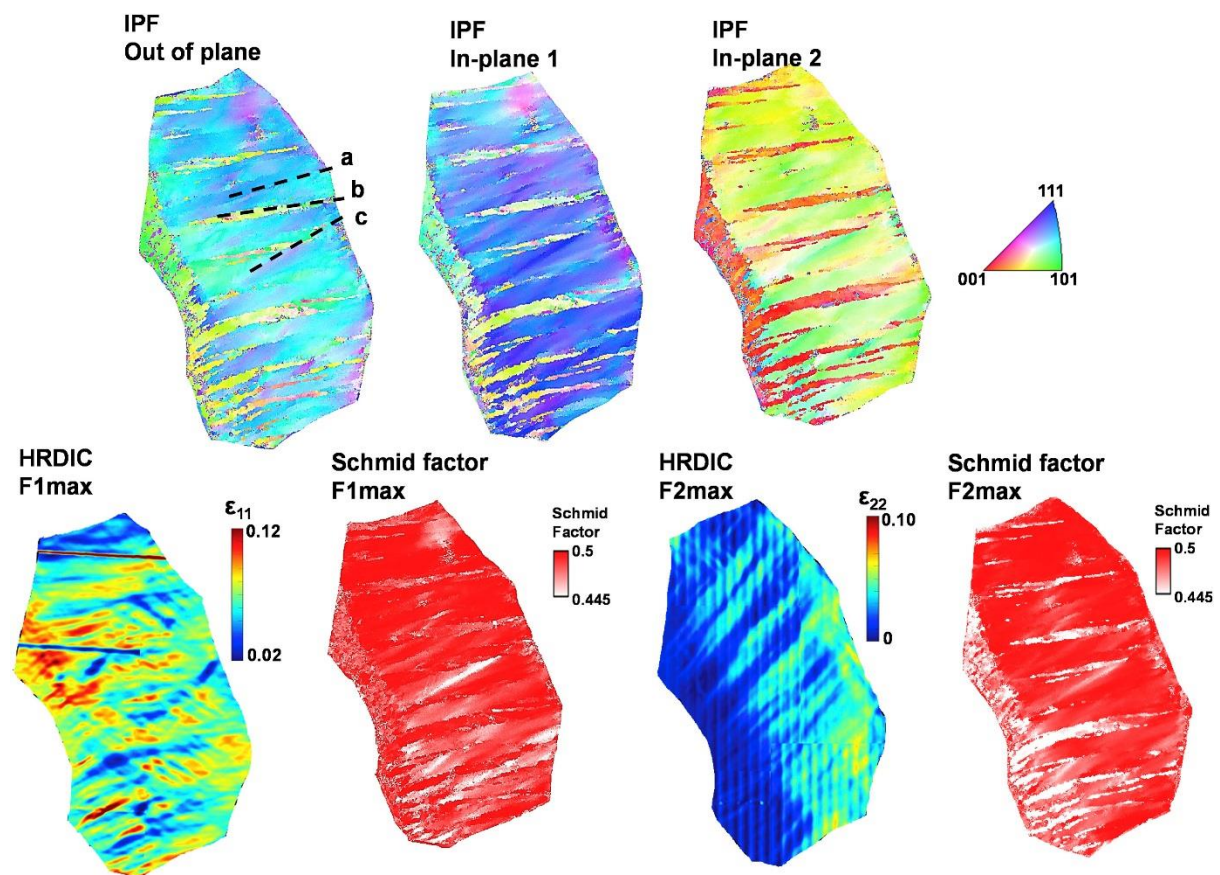
Figure 3.12 Initial austenite microstructures, HRDIC strain maps and Schmid factor maps for grain D in Figure 3.6.

3.1.7 Summary

Combining EBSD, Macro-DIC, in situ HRDIC and in situ synchrotron XRD, the localization of the stress induced martensitic transformation during uniaxial tension and load path changes was studied at the macroscopic and microscopic level for a commercial superelastic NiTi alloy (Memry GmbH). The relationship between the austenitic multi-length scale microstructure and the transformation is revealed.

The following conclusions have been reached:

- The microstructure of the superelastic NiTi alloy has a strong out-of-plane texture at the macroscale with austenite grains of several tens of microns. At the nanoscale, the material contains bands with subgrains. The misorientation among these bands is mostly higher than the misorientation among the nanograins within a band. This complex microstructure makes the material capable to sustain large strains and exhibit good superelasticity during one LPC cycle.

- Bands of nanograins transform collectively and produce high-strain bands suggesting the importance of grain interactions at the nano-length scale.

- The localization of the strain bands is different under F1max and F2max, in situ XRD confirms that martensite variants change upon changing the load path between them. However, at the loading state F1F2 no significant change of the martensite variants is observed. Instead, the variants already formed at the loading state F1max are preserved, suggesting a non Schmid behavior.

3.2 Degradation of the superelastic NiTi under multiaxial mechanical cycling

The section is adapted from the published paper:

<u>Wei-Neng Hsu</u>, Efthymios Polatidis, Miroslav Šmíd, Steven Van Petegem, Nicola Casati and Helena Van Swygenhoven

Abstract

The degradation of the superelastic properties of a commercial NiTi alloy are studied during uniaxial, biaxial and load-path-change cycling performed in-situ with synchrotron X-ray diffraction. Careful examination of the diffraction pattern during uniaxial loading shows the R-phase as a transition between the austenite and the B19' martensite. Degradation of the superelasticity is found to depend strongly on the loading and unloading path followed, and it is discussed in terms the B19' martensitic variant selection, the accumulation of dislocations, and the residual R-Phase and B19' martensite. Cycling biaxially leads to faster degradation than uniaxially due to a larger accumulation of dislocations. If the deformation cycle contains a load path change, dislocation accumulation increases further and more martensite is retained.

In this work, the contributions from the doctoral candidate are:

- Designed and fabricated the cruciform samples
- Developed the thin-down geometry cruciform in collaboration with Micropat SA
- Performed the in-situ XRD measurements
- Analyzed the data and summarized the results
- Wrote the entire draft and finalized the manuscript for submission

3.2.1 Introduction

The superelasticity (SE) of NiTi alloys enables the material to sustain large strains thanks to the reversible deformation-induced martensitic transformation. Under an external load, the material transforms from the austenite B2 crystal structure to the B19' martensite phase [22, 28]. Once the load is removed, the material returns to its original shape as martensite fully transforms back to austenite. This unique property has found applications in biomedical engineering such as in endovascular stents, cardiovascular stents and orthopedic devices [8]. These components made of SE NiTi experience multiaxial deformation in vivo [148, 149]. Hence, it is important to study the martensitic transformation under multiaxial deformation or load path changes. It has been shown that uniaxial compression exhibits a smaller recoverable strain than uniaxial tension, a steeper transformation stress-strain slope and a higher critical stress for martensitic transformation [150-152]. A limited number of studies on the effect of load path changes can be found. Upon changing the loading path from tension to torsion, McNaney et al. reported two distinct plateau regions in the stress-strain curve, which was attributed to different martensite variants associated with different load paths [68]. Combining high-resolution digital image correlation (HRDIC) and in-situ X-ray diffraction (XRD) during one loading cycle, it was shown how strain was accommodated by selecting different martensitic variants [153].

Structural and functional stability upon cyclic deformation are required for biomedical applications, i.e. structural fatigue leads to mechanical failure, and functional fatigue results in the degradation of the SE properties [154, 155]. Fatigue has been shown to lead to a reduction of the critical stress required for the transformation from austenite to martensite, accumulation of permanent deformation [41-45], appearance of the intermediate rhombohedral R-phase martensite [50, 59] and decrease in the dissipated energy of the transformation cycle [42, 45, 156-161]. The resistance of the SE NiTi to functional fatigue depends on the crystallographic texture and the presence of precipitates [49], the austenite grain size [48, 125, 162], the loading rate [163, 164] and the testing temperature [161]. To date, there are only few studies addressing the effect of multiaxial or load-path-change cycling on the degradation of SE NiTi. Song et al. performed non-proportional tension-torsion cyclic tests on SE NiTi tubes and reported that multiaxial stress states lead to faster accumulation of residual strain, compared to uniaxial loading [71]. Among most multiaxial studies mentioned above, the transformation behavior and the material degradation were examined only at the macroscopic length scale. Khodaei et al showed that constitutive modelling failed to predict the mechanical response under multiaxial loads, because the model does not capture the anisotropic transformation behavior related to the crystallographic orientation and the loading path [73]. Detailed experimental data is required to improve the micromechanical models.

Combining cruciform multiaxial mechanical tests with in-situ synchrotron XRD, employing a miniaturized biaxial device for application of in-plane biaxial loads and load path changes, the

microstructural evolution of a commercial SE NiTi during multiple cycling is studied. Microstructural degradation induced by multiaxial and load-path-change cycling are reported.

3.2.2 Experimental

A superelastic NiTi sheet with a thickness of 150 μm was purchased from Memry GmbH. The optimized cruciform geometry with a central pocket is shown in Figure 3.13. The gradual thinning from 150 μm (arm) down to 50 μm (central pocket) allows the martensitic transformation to occur at the center of the cruciform where the synchrotron X-ray investigation is positioned. The rounded-square pockets were fabricated by electrochemical micromachining (ECMM), carried out at micropat SA, Switzerland. After introducing the pockets to both sides of the sheet by ECMM, the outline of the cruciform was cut with an Nd:YVO picosecond pulsed laser at the Swiss Federal Laboratories for Materials Science and Technology (EMPA). A detailed description regarding the cruciform sample preparation can be found in [165]. The microstructure at the center of the cruciform was investigated with Electron Backscatter Diffraction (EBSD) using a field emission gun scanning electron microscope (FEG SEM) Zeiss ULTRA 55 equipped with EDAX Hikari Camera operated at 20 kV in high current mode with the 120-μm aperture and a step size of 90 nm. The post processing of the EBSD data was done with the EDAX OIM Analysis 7.3 software.
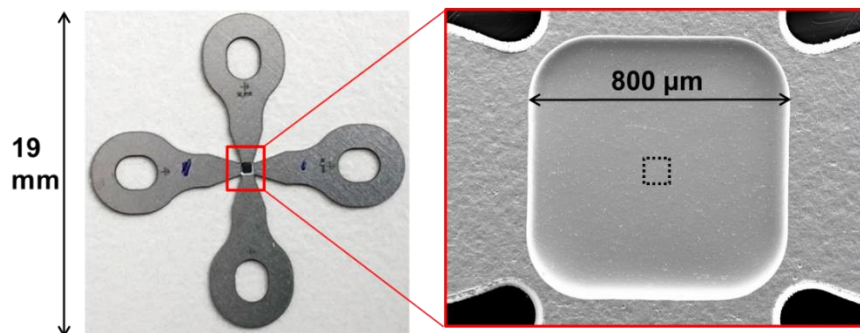
Figure 3.13 The thin-down cruciform geometry. The enlarged SEM picture shows the central pocket fabricated with ECMM. The synchrotron X-ray beam probed the center (~70x70 μm^2) of the pocket indicated by the dashed line.

The four load paths studied in this work are illustrated in Figure 3.14: uniaxial (UN), equibiaxial (EQ), triangular (TR) and square (SQ). The deformation tests were performed on the cruciform samples employing an upscale version of the minibiax tensile machine [103], hereafter called the meso biaxial tensile machine. The device has a very similar setup as the minibiax but a higher load capacity up to 1000 N. For each load path, 100 displacement-controlled mechanical cycles were performed, 9 cycles (1st, 5th, 10th, 15th, 20th, 30th, 40th, 60th and 100th) were followed with in-situ XRD measurements. The in-situ cycles were performed with a displacement rate of 0.2 μm/s; the cycles in between (non-in-situ cycles) were done with a displacement rate of 2 μm/s. Preliminary tests showed that the transformation occurs at different displacements upon loading along the two in-plane directions of

the cruciform i.e. the F1 and F2 direction. For all the load paths shown in Figure 3.14, the displacements reached along the F1 and F2 direction were 131 μm and 150 μm, ensuring the occurrence of martensitic transformation.
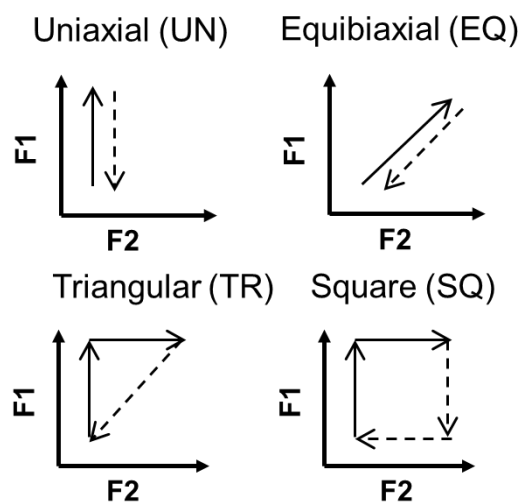
Figure 3.14 The four load paths applied to the cruciform samples. The solid lines represent the loading steps; the dashed-lines represent the unloading paths.

The meso biaxial tensile machine was mounted on the goniometer at the Materials Science (MS) X04SA beam line at the Swiss Light Source (SLS) [135]. Similar to the experimental setup in [153], the experiments were carried out in transmission with a 20 keV beam and a 70 x 70 μm^2 spot size probing the center of the cruciform. The diffraction data along the scattering vectors parallel to the two in-plane F1 and F2 directions of the cruciform were recorded by two detectors with 30 s counting time. The Mythen II microstrip detector recorded the diffraction data parallel to F1 in a range of 2θ of ∼ -55° to +55°. The 2D data from Pilatus was caked and integrated using FIT2D [136] along an azimuthal range of 175°-185°, corresponding to the direction parallel to F2. LaB$_6$ was used as the reference material for the calibration of the detector position, the tilt and rotation angles and the beam center. The single peak fitting of the diffraction data was done with pseudo-Voigt functions using an in-house code in MATLAB.

3.2.3 R-phase martensitic transformation

Figure 3.15 shows EBSD orientation maps of the center of the cruciform (field of view of 72 μm x 57 μm) taken parallel to the sample normal (ND), F1 and F2 respectively. The majority of the grain orientations in the field of view shows a strong <1 1 1> texture parallel to ND and <1 0 1> parallel to F1. Section 3.1 has shown that the grains consist of fine austenite subgrains (∼40 nm) which transform collectively into the B19' martensite phase upon mechanical loading. Figure 3.16 presents the in-situ XRD spectra for different 2θ ranges and the force-displacement curve upon loading (Figure 3.16d). As shown in Figure 3.16b and Figure 3.16c, (2 -2 2)$_R$ and (0 1 -2)$_R$ peaks appear when the sample is loaded up to 9.4 N. These peaks continue to grow as the loading proceeds. The R-phase peaks reach maximum

intensities at 15.3 N after which they start to decrease in intensity upon further loading. Meanwhile, a drastic intensity drop of the $(1\ 1\ 0)_{B2}$ peak accompanied with the growth of the $(0\ 0\ 2)_{B19'}$ peak can be seen in Figure 3.16a. Figure 3.16b shows the decreasing intensity of the $(2\ \text{-}2\ 2)_R$ peak and the growth of the $(0\ 1\ 2)_{B19'}/(1\ 1\ 1)_{B19'}$ peaks (two nearly overlapping B19' peaks) at forces larger than 15.3 N. The decrease in the slope of the force-displacement curve, as shown in Figure 3.16d, is due to the formation of the B19' martensite. The material predominantly transforms into the B19' martensite when the force reaches 20.9 N, at which the $(1\ 1\ 0)_{B2}$ peak becomes weak and the R-phase peaks nearly disappear. In other words the material transforms from B2 to B19' via an intermediate R-phase. The transformation via R-phase was not reported in [153]; however, careful examination made us realizing that we overlooked the presence, probably because no remaining R-phase is observed after unloading of one cycle.
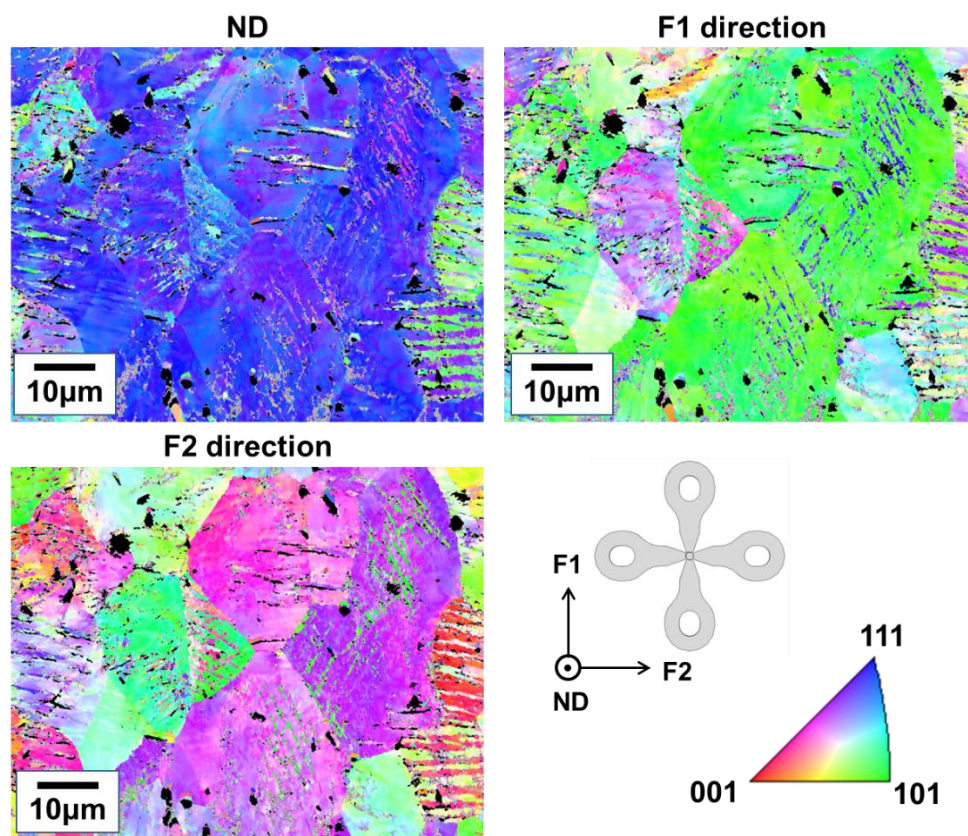
Figure 3.15 EBSD grain orientation maps of the initial microstructure in parallel to ND, F1 direction and F2 direction. The black features in the maps are NiTi$_2$ precipitates.
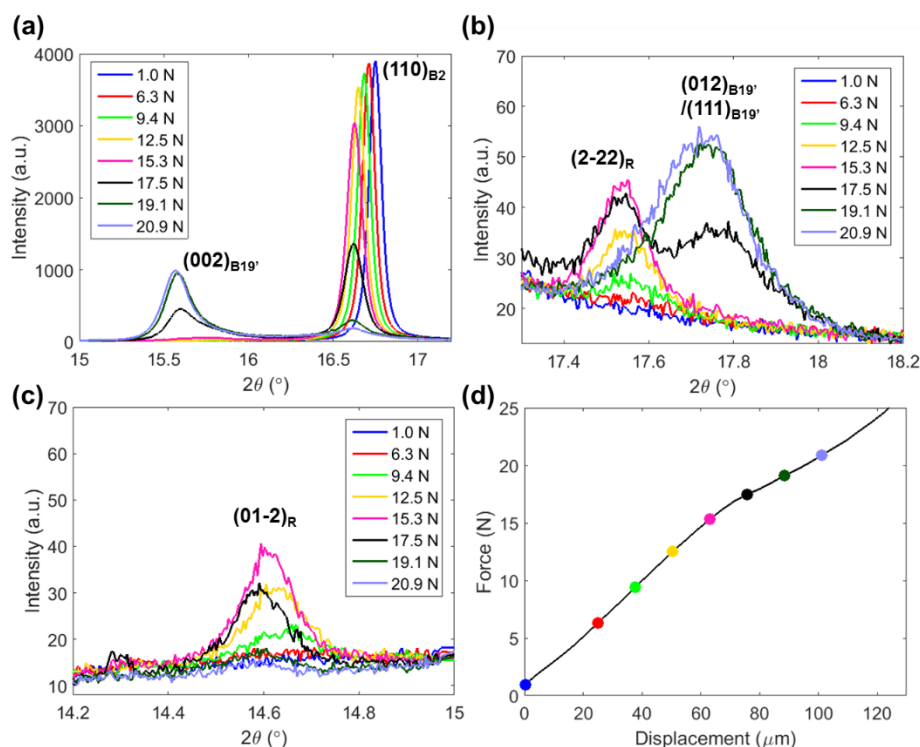
Figure 3.16 (a) - (c) In-situ XRD spectra upon loading F1 direction showing the evolution of different phases. The colors correspond to different measurement points labelled in (d) the force-displacement curve.

3.2.4 Martensitic footprints at different loading directions

The formation and selection of the B19' martensite variants depend strongly on the loading direction. Figure 3.17 shows the diffraction spectra captured at the maximum load of three different monotonic loadings: uniaxial along F1 (UN F1), uniaxial along F2 (UN F2) and equibiaxial (EQ F1F2). The highest intensities are observed for $(0\ 0\ 2)_{B19'}$ during UN F1, for $(0\ 1\ 2)_{B19'}/(1\ 1\ 1)_{B19'}$ during UN F2 and for $(1\ 1\ -1)_{B19'}$ during EQ F1F2. Additionally, the $(1\ 1\ 0)_{B19'}$ peak is observed in UN F2 whereas not in UN F1. These results demonstrate that different sets of martensite variants form when the cruciform is loaded along different directions. The different sets of martensite variants are hereafter denoted as VF1, VF1F2 and VF2.

We now look at the effect of a load path change. Figure 3.18a compares the diffraction spectra captured at two loading conditions during the first TR cycle: at F1max (F1: 27N) and after the load path change to F1F2 (F1: 33N, F2: 42N). When the loading condition is changed from F1max to F1F2, the intensity of the $(0\ 0\ 2)_{B19'}$ peak decreases meanwhile the $(1\ 1\ -1)_{B19'}$ and $(0\ 1\ 2)_{B19'}/(1\ 1\ 1)_{B19'}$ peaks grow. Figure 3.18b focuses on the formation of the $(1\ 1\ -1)_{B19'}$ when going from F1max to F1F2 and demonstrates the growth of $(1\ 1\ 0)_{B2}$ peak during the load path change. In other words, changing the load path from uniaxial to biaxial induces changes in martensite variants as well as the reverse transformation from martensite back to austenite, as already suggested in [153].
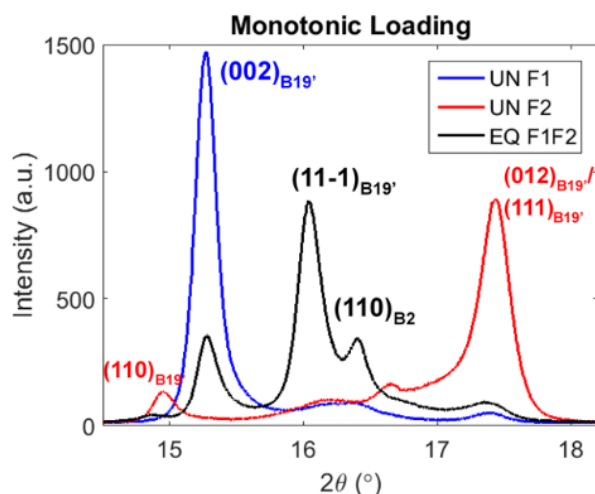
Figure 3.17 Different martensite peaks (corresponding to different variants) seen under monotonic loadings: uniaxial along F1 direction (UN F1), uniaxial along F2 direction (UN F2) and equibiaxial load (EQ F1F2).
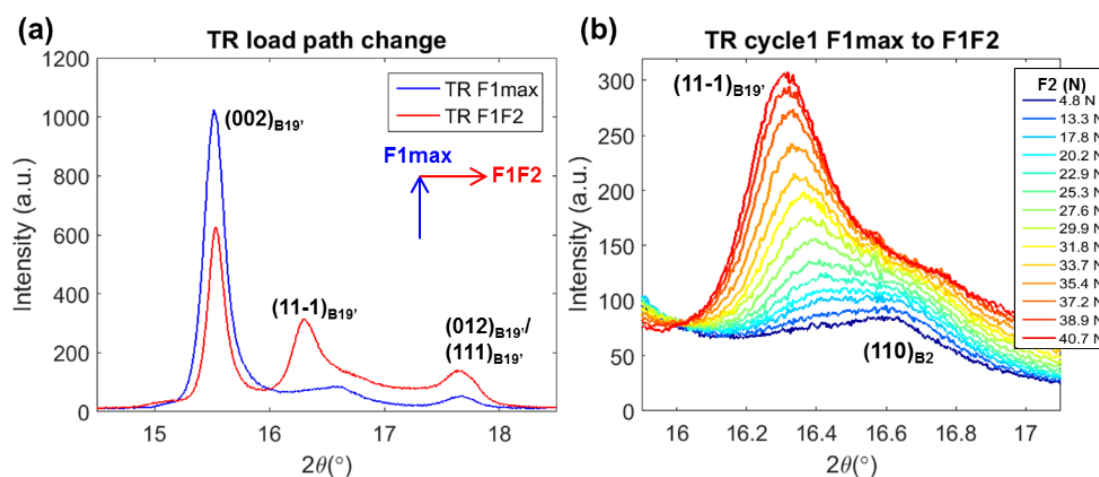
Figure 3.18 (a) Comparison of XRD spectra captured at two loading conditions during one TR cycle. (b) The evolution of XRD spectra during the load path change from F1max (blue) to F1F2 (red).

3.2.5 Degradation in superelasticity after multiaxial mechanical cycles

Figure 3.19 plots the force-displacement curves for the uniaxial cycles and particularly those that were performed in-situ (i.e. cycle 1, 5, 10 …100). The critical force for transformation decreases with the increasing number of cycles, as apparent from the change of the slope of the force-displacement curve and the force drop. Figure 3.19 also shows the development of residual displacement and the decrease in the dissipated energy (area enclosed by the superelastic loop in Figure 3.19) after uniaxial cycling. It has to be noted that the interpretation of the mechanical data from the cruciform tests are not as straightforward as from the uniaxial dogbone tests since stress concentration and martensitic transformation occur also outside the thinned cruciform area. Therefore, the macroscopic mechanical data represents a convolution of deformation inside and outside the thinned area probed by X-rays.
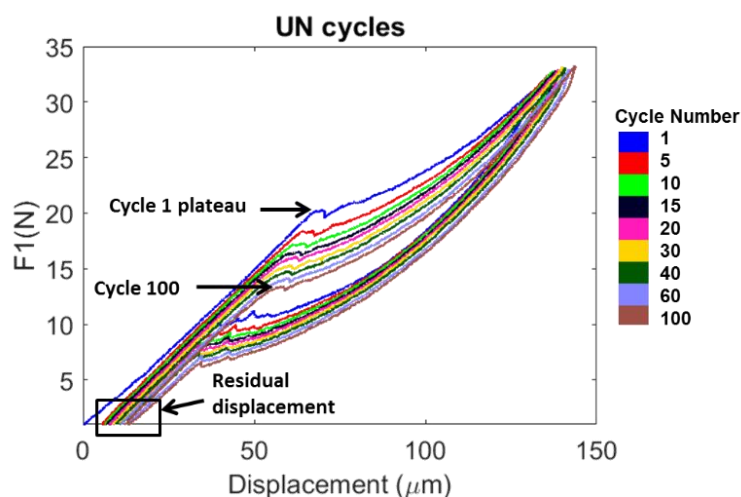
Figure 3.19 The force-displacement curves of the in-situ uniaxial cycles show typical behavior of superelastic NiTi under cycling.

We define a critical transformation force as the force corresponding to a reduction of 80% of the maximum intensity of the $(1\ 1\ 0)_{B2}$ peak, and for which meanwhile, the martensite peaks start to become apparent in the diffraction patterns. Figure 3.20 shows that multiaxial cycling (SQ, TR and EQ) decreases the critical transformation force faster than UN cycling. SQ and TR result in larger reduction in the critical transformation force compared to the monotonic EQ cycling.
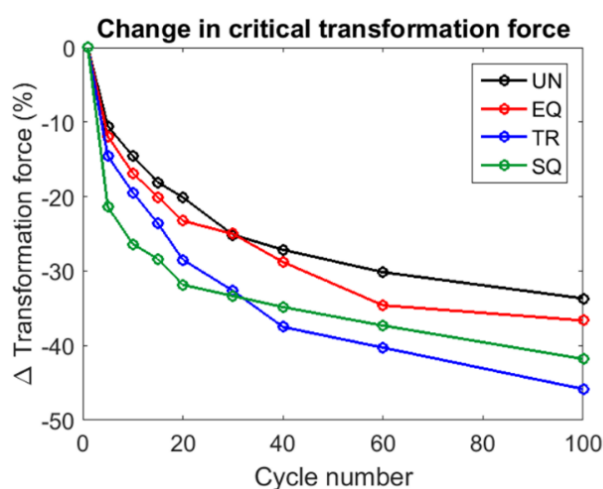
Figure 3.20 Evolution of the critical transformation force as a function of the number of cycles.

Figure 3.21 compares the in-situ XRD spectra of loading in the F1 direction during the TR cycle 1 and 10. It clearly shows that the B19' martensitic transformation occurs at lower force as the cycling advances. Furthermore, the $(0\ 0\ 2)_{B19'}$ peak appears after 16.2 N during cycle 1 (see Figure 3.21a), whereas during cycle 10, the $(0\ 0\ 2)_{B19'}$ peak can be observed already at 12.5 N (see Figure 3.21c). Apart from the B19' martensitic transformation, the mechanical cycles also facilitate the formation of R-phase martensite. During the first cycle, the $(1\ \text{-}2\ 4)_R$ peak does not appear. However at cycle 10 shown in Figure 3.21d, the $(1\ \text{-}2\ 4)_R$ peak becomes apparent next to the $(2\ 1\ 1)_{B2}$ after reaching 8.5 N.

71

As the loading continues, both $(1\,\text{-}2\,4)_R$ and $(2\,1\,1)_{B2}$ peaks decrease in intensity, meanwhile the $(0\,0\,2)_{B19'}$ peak grows significantly.
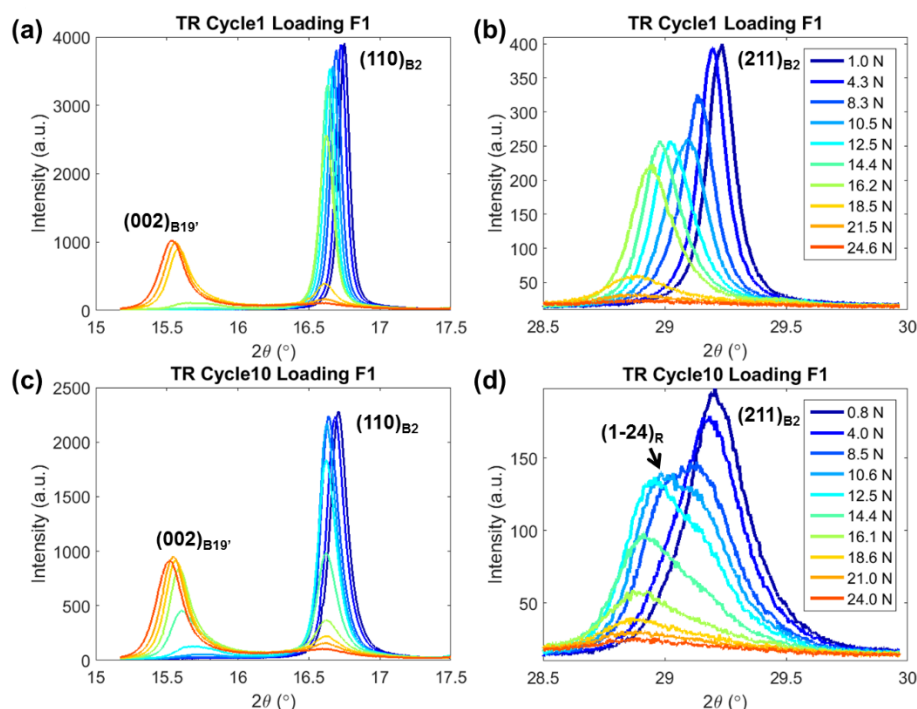
Figure 3.21 The evolution of the XRD spectra during loading F1 in the (a) - (b) 1st TR cycle, and (c) - (d) 10th TR cycles.

The degradation induced by mechanical cycles is also manifested by the broadening of the XRD peaks due to accumulation of dislocations. Figure 3.22 compares the broadening of the $(1\,1\,0)_{B2}$ peak during different types of cycles. The full-width-at-half-maximum (FWHM) of $(1\,1\,0)_{B2}$ increases significantly more under multiaxial cycling than uniaxial cycling. The strongest austenite peak, $(1\,1\,0)_{B2}$, broadens the most after the SQ cycles, followed by the TR cycles and the EQ cycles. Although the data from the Pilatus detector is available only until the 40th SQ cycle, it is evident that SQ produces the most pronounced broadening. The broadening of the second strongest austenite peak, $(2\,1\,1)_{B2}$, follows the same trend albeit not shown here. These findings imply that multiaxial cycling accumulates more dislocations than uniaxial cycling.
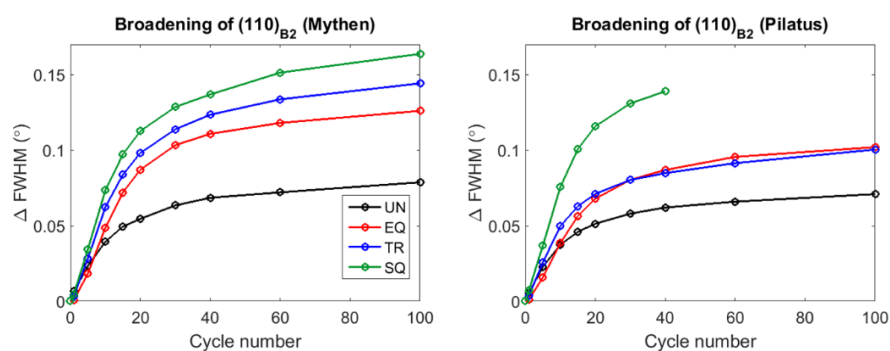
Figure 3.22 The evolution of FWHM of the $(1\,1\,0)_{B2}$ with increasing the number of cycles, along two diffraction vectors, parallel to F1 (Mythen detector) and parallel to F2 (Pilatus detector) for different loading paths.

Another characteristic of SE degradation induced by mechanical cycling is the accumulation of retained martensite since the material is no longer able to transform fully back to austenite when removing the external load. The retained martensite found after mechanical cycling also contributes to the accumulation of residual strain. Figure 3.23 presents the evolutions of the retained martensite after different types of cycling. The retained $(2\ -2\ 2)_R$ peak can be observed in all loadings after 100 cycles, but is less pronounced in the monotonic loadings UN and EQ. TR results in the growth of retained $(0\ 0\ 2)_{B19'}$ peak. As for SQ, the $(0\ 0\ 2)_{B19'}$ and $(1\ 1\ -1)_{B19'}$ peak present in the diffraction patterns after cycling and unloading. Figure 3.23 highlights the importance of both loading and unloading paths in the development of retained martensite. Reaching F1F2 via a load path change (TR cycles) results in more retained martensite than monotonic equibiaxial loading (EQ cycles). Despite the same loading sequence for TR and SQ, the different unloading sequences develop different retained martensite peaks.
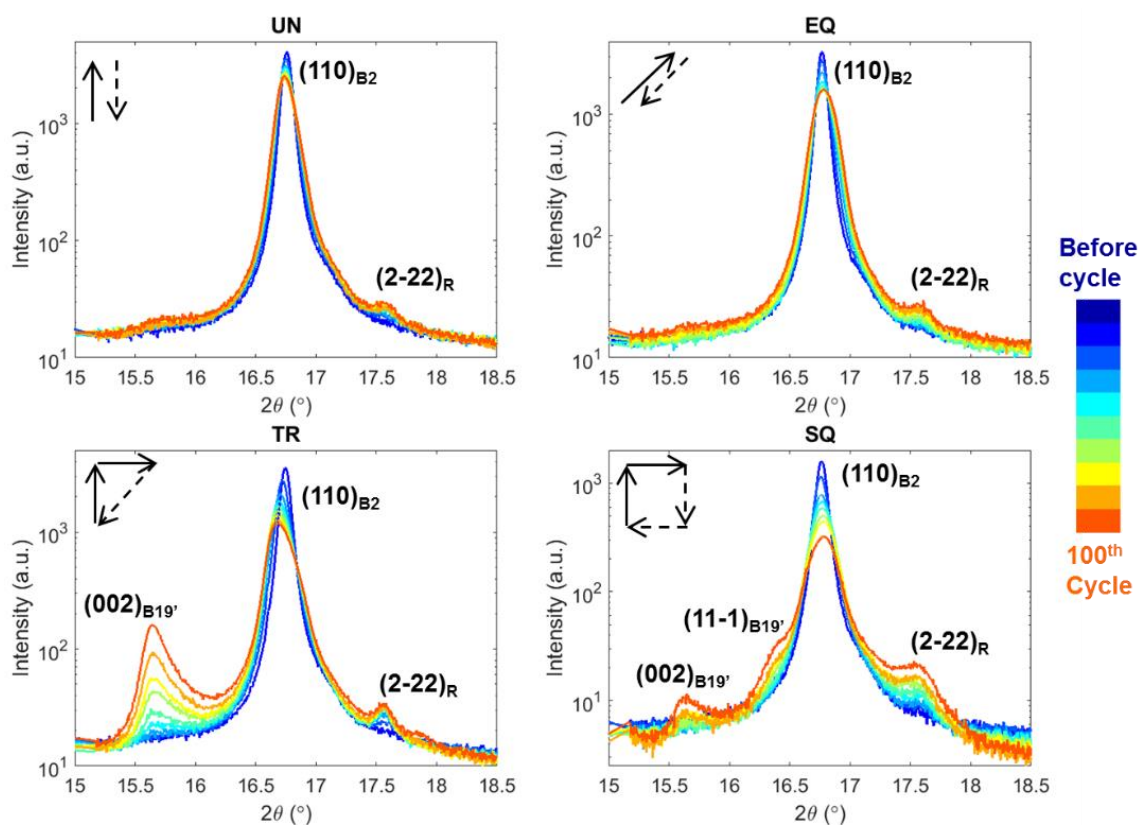
Figure 3.23 Diffraction patterns (Mythen detector) showing the evolution of retained martenste and R-phase under different loading paths.

The degradation in the superelasticity i.e. the decrease in the critical transformation force can be attributed to the increasing dislocation density as cycling proceeds, as witnessed by the broadening of the B2 austenite peaks. Transmission electron microscope (TEM) studies have reported that the forward martensitic transformation accompanies the creation of the dislocations, which retain in the austenite phase after reverse transformation [54, 56, 57]. The accumulation of dislocations induced by mechanical cycling, as evidenced by TEM in [49-52, 125], contribute to the residual strain in the

austenite phase. In addition, the dislocations retained in the austenite phase facilitate the nucleation of B19′ martensite: the stress fields around dislocations decrease the external work required for the stress-induced martensitic transformation [45], i.e. decreasing the required transformation force as observed in Figure 3.20. The dislocations introduced by cycling are also essential for promoting the R-phase transformation [55, 58, 60]. Consequently, the mechanical cycling lowers the transformation force for R-phase martensite, as exemplified by Figure 3.21b and Figure 3.21d.

It is worth noting that both the decrease in the transformation force and the peak broadening slow down after 20 cycles, i.e. the degradation in SE properties tends to reach a saturation with increasing number of cycles. Such saturation has also been reported in the literature, and it is due to the steady-state dislocation structure which is difficult to change with further cycling [45, 53, 166].

3.2.6 Monotonic load-unload cycles: EQ and UN cycles

The present study shows the dependency of SE degradation on the loading path. Multiaxial mechanical cycling (SQ, TR and EQ) is found to degrade the SE NiTi faster than uniaxial cycling. One question that comes up from these results is: why does EQ cycling degrade the material more than UN cycling? The UN cycles were conducted by loading the cruciform along the F1 direction. As for the EQ cycles, two in-plane loads along the directions F1 and F2 were simultaneously applied to the cruciform. Since in-plane equibiaxial loading has the same normalized strain tensor as uniaxial compression along the direction perpendicular to the sample surface, i.e. ND [113], the comparison is now between uniaxial compression along ND and uniaxial tension along the F1 direction. The martensitic transformation in NiTi depends on both the loading state (tension or compression) and the austenite crystallographic orientation, showing large anisotropy in the transformation strain. Lattice deformation calculations for single crystals have shown that uniaxial compression along [1 1 1]-oriented austenite generates the lowest transformation strain [167, 168], implying that this crystallographic orientation exhibits poor SE properties and the imposed strain is accommodated by transformation but also by dislocations multiplication and slip. Poor SE with large irreversible strain and the high cyclic instability due to a significant increase in dislocation density have been observed in [1 1 1]-oriented austenite grains under uniaxial compression [169]. The same calculations showed that uniaxial tension along [1 0 1] can result in more than 8% transformation strain [168], suggesting that solely the martensitic transformation is able to accommodate high strains induced by the applied load. Assuming that the crystallographic responses of a single crystal and a highly textured polycrystalline NiTi are comparable [170], the difference in EQ and UN can be explained by the texture shown in Figure 3.15. Owing to the strong <1 0 1> // F1 direction texture, UN exhibits better superelasticity as large strain could be accommodated solely by the formation of martensite. On the other hand, EQ (uniaxial compression along the <1 1 1> texture) would exhibit more dislocation slip activity in addition to the martensitic transformation. This explains also the difference in residual peak broadening in the austenite: more dislocations accumulate during the EQ cycling compared to the UN

cycling. These results demonstrate that the initial austenite texture and the load path influence SE degradation. Avoiding <1 1 1> out-of-plane texture would reduce microstructural degradation during in-plane-equibiaxial cycling.

3.2.7 Load-path-change cycles: SQ and TR cycles

The load-path-change cycles SQ and TR degrade the material faster than the monotonic load-unload cycling EQ and UN. Both loading and unloading paths affect the degradation. Figure 3.24 summarizes the possible deformation mechanisms during each load path for both TR and SQ cycles.
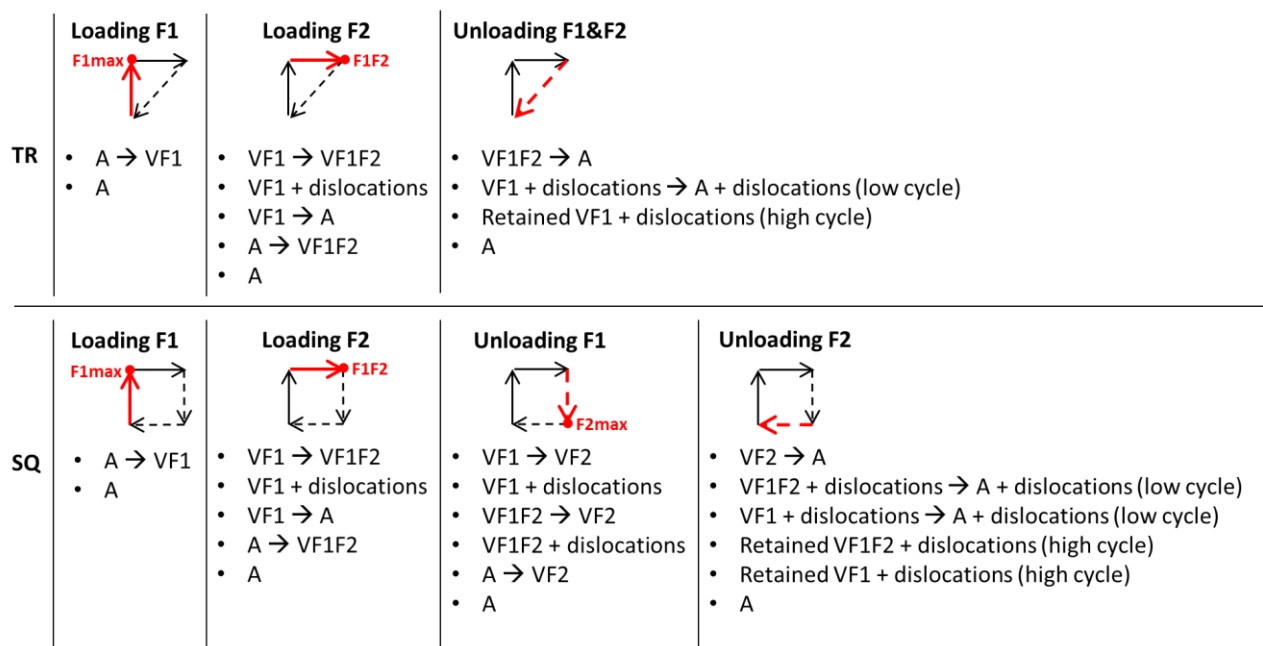
Figure 3.24 The microstructure and mechanisms during each loading and unloading step in TR and SQ cycles. "A" stands for the austenite phase. "VF1, VF1F2 and VF2" stand for the certain martensite variants favored in different deformation states. The red arrows indicate the loading/unloading direction during each load path (full line for loading, dashed line for unloading).

For the TR load path, the majority of the austenite grains (denoted as A in Figure 3.24) transform into a set of martensite variants (VF1) upon loading F1. There are still untransformed austenite grains after reaching F1max, as reported in [153]. Additionally, the change in loading condition from F1max to F1F2 can induce the reverse transformation as evidenced by the growth of the $(1\ 1\ 0)_{B2}$ peak in Figure 3.18b. Since the material is mostly in the martensite phase (VF1) at F1max, the subsequent loading along the F2 direction deforms the pre-existing VF1 martensite. In [171, 172], it is seen that martensite can exhibit reorientation/detwinning and formation of dislocations depending on the loading direction. Taking these mechanisms into account, the VF1 martensite undergoing loading along F2 (towards F1F2) can exhibit simultaneously: (1) reorientation/detwinning into VF1F2 variants (denoted as VF1 -> VF1F2 in Figure 3.24), (2) plastic deformation generating dislocations (denoted as VF1+dislocations in Figure 3.24), and (3) reverse transformation (denoted as VF1 -> A in Figure 3.24). Note that VF1 likely contains more dislocations than VF1F2 since it undergoes plastic

deformation. Moreover, some of the untransformed austenite at F1max can transform into VF1F2 upon loading F2 (denoted as A -> VF1F2 in Figure 3.24), contributing to the VF1F2 footprint. It is possible that some austenite grains still stay untransformed. The last step in one TR cycle is unloading the material along F1 and F2 directions simultaneously. For a low number of cycles, the full reverse transformation is observed. The dislocations created upon the load path change remain in the material and result in the broadening of the austenite peaks. For a high number of cycles, the accumulation of dislocations creates local stress fields that stabilize the martensite, seen as the retained martensite in Figure 3.23. Based on the deformation mechanisms proposed above, VF1 accumulates more dislocations than VF1F2 after cycling, resulting in more retained VF1 martensite. As shown in Figure 3.23, the TR cycles result in a strong retained $(0\ 0\ 2)_{B19'}$ peak, which agrees with the martensite footprint VF1 shown in Figure 3.17.

In contrast to TR, SQ contains two unloading paths: F1 is unloaded before unloading F2. The first unloading along the F1 direction changes the deformation from the F1F2 state to the F2max state. As the cruciform is still loaded in the F2 direction, the center of the cruciform that contains both VF1 and VF1F2 continues to experience additional deformation as witnessed by the shift in the peak position. Similar to the above discussion, VF1 may reorient into the VF2 martensite favored by the F2max state or accommodate the deformation by creating dislocations. In order to investigate the effect of unloading along the F1 direction on the VF1F2 martensite, an additional load-path-change experiment has been done: a cruciform was directly loaded to F1F2 condition, followed by unloading along the F1 direction. Figure 3.25 shows the evolution of the diffraction peaks during unloading F1. The intensities of the martensitic peaks $(0\ 0\ 2)_{B19'}$ and $(1\ 1\ \text{-}1)_{B19'}$ reduce and the peak positions change to higher 2θ values, demonstrating that the unloading changes VF1F2 variants to VF2 and put the remaining VF1F2 under strain. Based on [171, 172], one can assume that during this process: (1) VF1F2 reorients/detwins into VF2 (denoted as VF1F2 -> VF2 in Figure 3.24) and (2) the remaining VF1F2 deformed by dislocations (denoted as VF1F2 + dislocations in Figure 3.24). Furthermore, during this unloading, it is also observed that the $(1\ 1\ 0)_{B2}$ peak reduces its intensity, implying that VF2 variants are formed from the austenite retained at F1F2. The cruciform is fully unloaded after unloading F2. As Figure 3.23 shows, the material transforms fully back into the austenite phase after a low number of cycles. Based on Figure 3.24, SQ cycling involves more steps where dislocations can accumulate, therefore the chance of retaining VF1 and VF1F2 variants increases. After higher number of cycles, the retained martensite peaks, $(0\ 0\ 2)_{B19'}$ and $(1\ 1\ \text{-}1)_{B19'}$, are a combination of VF1 and VF1F2 footprints (see Figure 3.23).
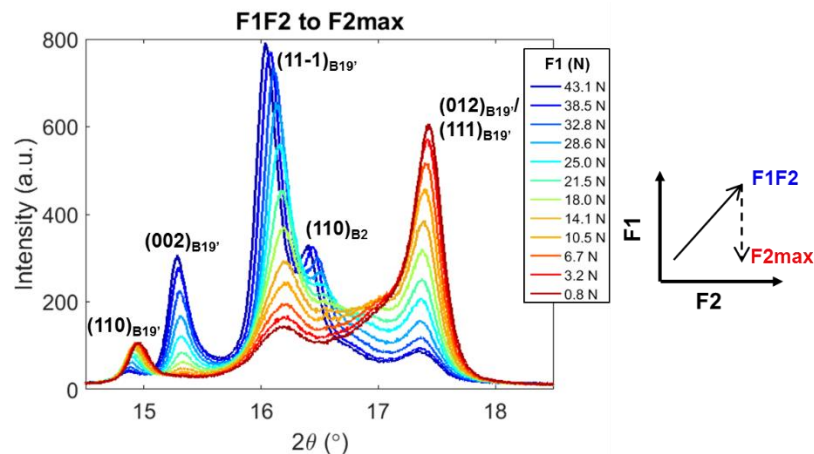
Figure 3.25 The change in the martensite footprint induced by the load path change from F1F2 (blue) to F2max (red).

Compared to the load-path-change cycling (TR and SQ), the monotonic UN cycling proceeds mainly with the forward and backward transformation of the favorable variants (VF1) and results in significantly lower broadening as shown in Figure 3.22. This result suggests that the accumulation of dislocations solely from the forward and backward martensitic transformation is much less than the deformation of the martensite during load path changes.

3.2.8 Summary

Combining the cruciform multiaxial mechanical tests and in-situ synchrotron X-ray diffraction, the deformation and degradation of a commercial superelastic NiTi alloy (Memry GmbH) under multiaxial mechanical cycling are studied. The decrease in the critical force for both R-phase and B19' martensitic transformation, the austenite peak broadening and the retained martensite are discussed in terms of the accumulation of dislocations induced by mechanical cycling. Multiaxial cycling (SQ, TR and EQ) leads to significantly more accumulation of dislocations and faster degradation than uniaxial cycling (UN). Degradation of the material properties shows a strong dependency on the load path. Due to the strong crystallographic texture (<1 1 1> // ND) of the austenite phase, EQ cycling accumulates more dislocations than UN cycling. Comparing to monotonic loading, SQ and TR create more dislocations due to the deformation of the martensitic variants upon changing the load path. In summary, texture, loading and unloading path play important roles in the degradation of the microstructure. Since medical devices are made of wires and tubes, tuning microstructural texture to the design of the device could offer a path for optimization.

3.3 Strain accommodation in the coarse-grained superelastic NiTi

This section is adapted from the paper currently under review in Acta Materialia:

"Strain accommodation in a superelastic NiTi alloy: a high resolution digital image correlation and transmission electron microscopy study"

Efthymios Polatidis, Miroslav Šmíd, Ivo Kubena, <u>Wei-Neng Hsu</u>, Guillaume Laplanche and Helena Van Swygenhoven

under review in Acta Materialia

Abstract

An in-situ high resolution digital image correlation (HRDIC) investigation during uniaxial tensile deformation reveals the activated martensite variants and the contribution of each variant to strain accommodation in a coarse-grained NiTi alloy with a mean grain size of ∼35 µm. The results show that more than one variant can be activated per grain and the majority of the activated variants exhibit a high Schmid factor (SF). The variant selection can be influenced by shear transmission across grain boundaries, when the geometrical compatibility between the neighboring habit plane variants is favorable; in these cases variants that do not have the highest SF, with respect to the macroscopically applied load, may be activated. The experimentally determined transformation strains agree relatively well with theoretical calculations for single crystals. A post-mortem transmission electron microscopy (TEM) investigation reveals deformation twinning occurring within the stress-induced martensite as an additional strain accommodation mechanism. In addition to phase transformation and twinning in martensite, slip in austenite is observed.

In this work, the contributions from the doctoral candidate are:

- Designed and fabricated the dogbone and cruciform-shape samples
- Prepared the OPS speckle pattern for HRDIC
- Performed the in-situ HRDIC experiment and analyzed the HRDIC data
- Participated in the FIB sessions (FIB operated by Dr. Kubena) to select the positions to extract TEM lamellae
- Summarized the results together with Dr. Polatidis, Dr. Šmíd and Dr. Kubena
- Revised and edited the draft of the paper (first draft written by Dr. Polatidis)

3.3.1 Introduction

NiTi alloys in near-equiatomic compositions are well known for their superelasticity which derives from the reversible austenite-martensite transformation. These alloys can be found amongst various applications for the biomedical industry [8] and in actuators and robotics [4]. The anisotropic behavior of NiTi has been correlated with the crystallographic orientation-dependence of the martensitic transformation in NiTi single crystals [167, 173], and to the texture in polycrystalline NiTi alloys [128, 173]. The martensitic transformation has been studied by EBSD in austenitic superelastic NiTi and martensitic shape memory alloys (SMAs) [174]. The characterization of the activated variants has been successfully conducted with EBSD under tension, compression [145, 175] and nanoindentation [176]. While several self-accommodation twinning modes are predicted by the phenomenological theory of martensitic transformation [177], type II twinning has been found experimentally to be the main twinning mode in SE NiTi alloys [25, 27, 54, 145, 175-180] and have been extensively used in simulations. Liu in [128] has described the orientation-dependent mechanical properties in strongly textured NiTi alloys assuming the activation of a single variant with the highest Schmid factor (SF) in each austenite grain and by considering the theoretical transformation strain that each variant can accommodate. However, such an approach neglects the material behaviors at the microscopic level:

1. The activated variants may not strictly obey the Schmid law.
2. More than one martensite variants may form in each austenite grain.
3. There are additional strain accommodation mechanisms other than martensitic transformation e.g. slip and/or twinning.
4. The theoretical transformation strain has not been experimentally verified at the microscopic level.

A unique method that can reveal all this information is high-resolution digital image correlation (HRDIC) performed in a scanning electron microscopes (SEM), in combination with EBSD. DIC is a non-destructive, non-contact technique used to observe full-field displacements on the surface of a test sample during mechanical testing. By employing high magnifications, achieved by SEM, HRDIC has recently become a powerful tool to study the deformation behavior with a sub-micron resolution in various steels [119, 128, 181-184], Ti-alloy [185], Mg alloys [122], and oxide layers [186]. In most of the studies mentioned above, HRDIC in combination with EBSD is used to study the activation of slip systems and to correlate these with the corresponding SF. The determination of the active slip systems by combining trace analysis and SF analysis can however also lead to misinterpretations, especially when multiple slip systems are operational and more than one can result in similar slip traces or when the material exhibits non-Schmid behavior [187]. In addition, when grain-grain interactions and/or precipitates alter the stress state locally, this may result in the activation of slip systems not expected from the SF analysis based on the macroscopic stress state. Recently, new

approaches have been proposed to increase the confidence of identification of the active slip trace analysis based on the geometric compatibility of neighboring grains, as applied to Ti-7Al alloy [187].

Similar to the study of slip trace analysis, HRDIC can be applied to investigate the transformation mechanisms via variant selection analysis in phase-transforming materials [188]. Recently HRDIC and EBSD have been combined to study the martensitic transformation during multiaxial loading and strain path changes in a superelastic nanostructured NiTi alloy [153]. In this latter study, it was found that the strain path change induces the martensitic transformation in different families of sub-grains. However, due to the nanometer-sized grain structure of this particular material, HRDIC was not able to resolve the activated martensite variants within each nanometer-sized grain. Therefore, to overcome this issue, a SE NiTi with a mean grain size in the micrometer range was used in the present study.

An additional asset of HRDIC is that it shows the location where martensitic transformation occurs, and it provides the transformation strain magnitude. The recoverable strain upon unloading in superelastic NiTi alloys can be determined from HRDIC strain maps. Therefore, HRDIC enables the use of the recoverable strain criterion to identify phase transformations from other possible deformation mechanisms that do not recover strain, such as slip or deformation twinning which can co-exist [125]. Additionally, the obtained strain magnitude is essential for understanding the strain accommodation mechanisms and the residual strain after unloading. Such information will foster improvement of the existing models used to predict the strain accommodation in single crystals [167] and polycrystalline materials [128].

The alloy chosen in the present study is a coarse-grained polycrystalline superelastic NiTi that exhibits the forward B2 to B19' phase transformation upon loading and the reverse transformation upon unloading [189]. It will be shown that the recoverable strain obtained by HRDIC facilitates the distinction between slip and phase transformation. SF analysis and the inclination of the trace on the sample surface are then performed by combining EBSD with HRDIC results that can resolve the martensite variants in each grains. The results are discussed in terms of variant activation and the appearance of additional strain accommodation mechanisms. Finally, complementary TEM investigations are carried out revealing deformation twinning in martensite as an additional strain accommodation mechanism.

3.3.2 Experimental

Experimental procedures

A rectangular ingot ($20 \times 76 \times 90$ mm³) with nominal composition $Ni_{51}Ti_{49}$ (in at. %) was produced by vacuum induction melting using nickel (Ni purity > 99.98 wt. %) and titanium (Ti purity > 99.995 wt. %) at the Ruhr-University Bochum (Germany). Melting was performed in a graphite crucible using

a VSG 010 furnace from PVA TePla AG in a high-purity Ar Atmosphere (99.998 vol.%) under a pressure of 500 mbar. The melt was then poured into a pre-heated mould (500°C) that had been coated with an yttria slurry. The ingot was solution heat treated for 5 h at 1000 °C under an argon atmosphere with a constant flow rate of 4 dm^3/min. The thickness of the cast ingot was then reduced in 22 steps from 20 mm to 1.8 mm by hot rolling at 800 °C (thickness reduction: 90 %). Prior to each step, the $Ni_{51}Ti_{49}$ sheet was annealed for 10 min at 800°C. The 1.8 mm sheet was further rolled at room temperature in three steps into a thinner sheet (thickness: 1.2 mm, thickness reduction: 30%). Between each cold rolling step, the $Ni_{51}Ti_{49}$ sheet was annealed for 10 min at 800 °C followed by water quenching. After cold rolling, the 1.2 mm $Ni_{51}Ti_{49}$ sheet was recrystallized for 10 min at 800 °C and water quenched. More details about the microstructure and texture of the recrystallized $Ni_{51}Ti_{49}$ sheet can be found in Ref. [190].

The dog-bone shaped tensile specimens were cut parallel to the rolling direction of the sheet, using a picosecond laser at the Swiss Federal Laboratories for Materials Science and Technology (EMPA). The surfaces of the tensile specimens were mechanically ground (with 600, 1200, 2500, 4000 grid SiC papers) and one of the surface was further polished with diamond-suspension (3 μm and 1 μm) followed by final polishing using a vibratory polisher (Buehler Vibro-Met2 using a suspension Buehler Mastermet2 with a particle size of 0.02 μm for 24 h). The final thickness of the tensile specimen is ~80 μm. Based on the average grain size and the sheet thickness, two to four grains are contained within the thickness of the tensile specimen.

EBSD investigations were performed using a field emission gun scanning electron microscope (FEG SEM) Zeiss ULTRA 55 equipped with EDAX Hikari Camera. The microscope was operated at 20 kV in high current mode with 120 μm aperture. The electron backscatter patterns were acquired by the TEAM software with 4 × 4 pixels binning and the crystal orientation was determined by 8 indexed Kikuchi bands for each pattern. The step size of the mapping varied from 150 to 60 nm, according to the size of the region of interest. The EBSD raw data were post-processed using the EDAX OIM Analysis 7.3 software.

Patterns for HRDIC were applied by rotating the samples on a polishing cloth with a few droplets of an OPS suspension from Microdiamant GmbH (particle size ~0.04 μm) and subsequently cleaned with deionized water, as introduced in [120]. The tensile sample was deformed up to a maximal engineering stress of ~450 MPa using a mini-biaxial machine mounted on a SEM stage [103]. During the tensile deformation, a macroscopic Lüders band was found to propagate at a constant stress of 450 MPa in good agreement with results reported in literature for superelastic [44, 45, 191-194] and shape memory alloys [174, 195, 196].

HRDIC measurements were performed at the centre of the gauge length of the tensile specimen at two loading states. (1) When the Lüders band reached the area of interest corresponding to an average

strain in the field of view (FOV) of ~8%, and (2) when the Lüders band had passed through the area of interest corresponding to an average strain in the FOV of ~10%. The average strain of 8% is not significantly different compared to the macroscopic strain obtained by low resolution DIC within the macroscopic strain (Lüders) band, while the average strain of 10% represents a deformation beyond the transformation plateau where irreversible deformation of martensite through dislocation slip and deformation twinning may have occurred. The images for HRDIC were acquired with a Zeiss ULTRA 55 FEG-SEM using an in-lens secondary electron detector at 6.9 mm working distance with 3 kV acceleration voltage and an aperture size of 30 μm. A series of SEM images with a resolution of 3072 × 2304 pixels were taken at ×2000 magnification with 25 μsec dwell time. The Ncorr MATLAB code [118] was used for the HRDIC analysis using a subset size of 15 pixels and subset spacing of 1 pixel. Previous HRDIC measurements [165] have shown that the error due to drift and lens distortion is insignificant, compared to the magnitude of strains in slip and transformation bands and therefore no corrections have been applied.

After the in situ HRDIC measurements, the sample surface was re-polished using diamond pastes (1 μm down to 0.25 μm) followed by a final vibration polishing for 24 hours in order to smoothen the deformation-induced surface relief and to achieve better surface quality for post-mortem EBSD investigations. Even after removal of material from the surface, the same grains as investigated by HRDIC could be observed post-mortem in EBSD. Note that vibration polishing did not induced deformation and did not changed the grain morphology.

TEM was undertaken by milling a rectangular lamella in the surface plane of the sample using a focused ion beam (FIB) on a Zeiss NVision-SEM/FIB equipped by an EDS system. The FIB-milling was undertaken using a 30 kV and 3 nA FIB. After the lift-out, the lamella was thinned by FIB using 30 kV and successively 700 pA, 300pA and 80 pA current as the thickness was reducing. The final surface cleaning was done using a 5 kV and 100 pA FIB.

Habit plane traces analysis

Upon loading, the austenite (cubic B2 phase, ordered BCC) transforms into twinned martensite (monoclinic B19' phase) bands where the interface between the austenite and the twinned martensite is an invariant plane also called the habit plane. The habit-plane variants (HPV), also called correspondence-variant pair (CVP), of type II twinning {0.8684 0.2688 0.4138} <-0.4580 0.7706 0.4432> are listed in Table 3.1. Note that indices of the habit plane and those of the twinning shear direction were normalized and that they are all expressed in the coordinate system of the B2 austenite.

The inclination of the habit plane trace with respect to the loading direction can be calculated as follows [145]: The habit plane m and the transformation shear direction b of the shape strain is given in the form: $(h\ k\ l)_\alpha[u\ v\ w]_\alpha$ (where α = 0, 1, 2,…24), for the 24 possible habit plane variants. The orientation of the parent B2 phase is given in the form: $(H\ K\ L)_\beta\ [U\ V\ W]_\beta$ for the β-th grain of a

polycrystal where $(H\ K\ L)$ and $[U\ V\ W]$ are parallel to the grain surface and tensile axis, respectively. The habit plane trace direction of the α-th variant in the β-th grain is then given by the following cross product [197]:

$$\left[R_\beta^\alpha S_\beta^\alpha T_b^\alpha\right] = [hkl]_\alpha \times [HKL]_\beta \qquad \text{(Eq. 3-2)}$$

where $R,\ S,\ T$ are the indices of the habit plane trace direction. The angle φ_β^α between the habit plane trace of the α-th variant and the loading direction in the β-th grain is given by [145]:

$$\varphi_\beta^\alpha = \cos^{-1} \frac{R_\beta^\alpha U_\beta + S_\beta^\alpha V_\beta + T_\beta^a W_\beta}{\sqrt{\left(\left[R_\beta^\alpha\right]^2 + \left[S_\beta^\alpha\right]^2 + \left[T_\beta^\alpha\right]^2\right)\left(U_\beta{}^2 + V_\beta{}^2 + W_\beta{}^2\right)}} \qquad \text{(Eq. 3-3)}$$

The same approach can be used to calculate the trace inclination of a slip system where instead of the habit plane the slip plane is used in Equation (3-2).

Table 3.1 Shear systems for the 24 habit plane variants (also called correspondent variant pairs) using the notation introduced in [200] and their habit plane/invariant shear direction.

HPV	Habit plane	Invariant shear direction	HPV	Habit plane	Invariant shear direction
1(+)	(0.8684 0.2688 -0.4138)	[-0.458 0.7706 -0.4432]	4(+)	(0.4138 0.8684 0.2688)	[0.4432 -0.458 0.7706]
1(-)	(0.8684 0.4138 -0.2688)	[-0.458 0.4432 -0.7706]	4(-)	(0.2688 0.8684 0.4138)	[0.7706 -0.458 0.4432]
1'(+)	(-0.8684 0.4138 -0.2688)	[0.458 0.4432 -0.7706]	4'(+)	(0.2688 -0.8684 0.4138)	[0.7706 0.458 0.4432]
1'(-)	(-0.8684 0.2688 -0.4138)	[0.458 0.7706 -0.4432]	4'(-)	(0.4138 -0.8684 0.2688)	[0.4432 0.458 0.7706]
2(+)	(0.8684 0.2688 0.4138)	[-0.458 0.7706 0.4432]	5(+)	(0.2688 -0.4138 0.8684)	[0.7706 -0.4432 -0.458]
2(-)	(0.8684 0.4138 0.2688)	[-0.458 0.4432 0.7706]	5(-)	(0.4138 -0.2688 0.8684)	[0.4432 -0.7706 -0.458]
2'(+)	(-0.8684 0.4138 0.2688)	[0.458 0.4432 0.7706]	5'(+)	(0.4138 -0.2688 -0.8684)	[0.4432 -0.7706 0.458]
2'(-)	(-0.8684 0.2688 0.4138)	[0.458 0.776 0.4432]	5'(-)	(-0.2688 0.4138 0.8684)	[-0.7706 0.4432 -0.458]
3(+)	(-0.4138 0.8684 0.2688)	[-0.4432 -0.458 0.77706]	6(+)	(0.2688 0.4138 0.8684)	[0.7706 0.4432 -0.458]
3(-)	(0.2688 -0.8684 -0.4138)	[0.7706 0.458 -0.4432]	6(-)	(0.4138 0.2688 0.8684)	[0.4432 0.7706 -0.458]
3'(+)	(0.2688 0.8684 -0.4138)	[0.7706 -0.458 -0.4432]	6'(+)	(0.4138 0.2688 -0.8684)	[0.4432 0.7706 0.458]
3'(-)	(0.4138 0.8684 -0.2688)	[0.4432 -0.458 -0.7706]	6'(-)	(0.2688 0.4138 -0.8684)	[0.7706 0.4432 0.458]

Maximum transformation strain analysis

Transformation strains associated with Type II twinning can be calculated and have been shown to be in good agreement with experimentally observed transformation strains in single crystals [157, 167]. Knowing the habit plane normal m (with miller indices $(h\ k\ l)_\alpha$) and the transformation shear direction b (with Miller indices $[u\ v\ w]_\alpha$) of the activated α variant, it is possible to calculate the strain matrix associated to the habit plane variant as:

$$E^\alpha = \frac{1}{2}(b \otimes m + m \otimes b + (b \cdot b)m \otimes m) \qquad \text{(Eq. 3-4)}$$

where m is the normal to the habit plane with indices $(h\ k\ l)_\alpha$ and b with indices $[u\ v\ w]_\alpha$ is the transformation shear direction (including the magnitude of shear of 0.13) of the activated variant α. Under a certain uniaxial loading, the deformation along the loading direction is then given by:

$$\varepsilon_\beta^\alpha = e_\beta \cdot E^\alpha \cdot e_\beta \qquad \text{(Eq. 3-5)}$$

where e_β is the crystallographic direction of the loading axis in the β-th grain [198]. Eq. (3-5) has been applied to each grain, β, to calculate the transformations strain that can be produced for each habit plane variant α. It is also worth noting that, as a first order approximation, neglecting the volume change associated with the austenite to martensite transformation, the transformation strain is directly proportional to the SF [199], i.e., $\varepsilon = SF \cdot |b|$ where $|b|$ is the magnitude of the transformation shear which is equal to 0.13 for type II twinning.

3.3.3 High strain traces in HRDIC maps

The initial microstructure with equiaxed grains with an average grain size of ~35 μm is shown in Figure 3.26. The grain orientation maps (Figure 3.26a and Figure 3.26b) reveal a strong <1 1 1> out-of-plane texture, as also reported in [190]. Additionally there is a strong alignment of the <1 0 1> direction parallel to the loading direction, see Figure 3.26b. Figure 3.26d shows the HRDIC map of the deformed material at 10% strain averaged over the field of view (beyond the stress plateau). The grain boundaries are delineated with white lines for clarity. The observed traces in each labelled grain is illustrated in Figure 3.26c with red lines. The traces with a high local strain magnitude correspond to either traces of activated slip systems in B2 austenite or traces of habit plane variants of B19' martensite. Besides strain traces in the grains, some amount of strain is accommodated close to the grain boundaries, see e.g. the boundary between grains G4, G8, G10 and G11 (compare Figure 3.26c and Figure 3.26d).
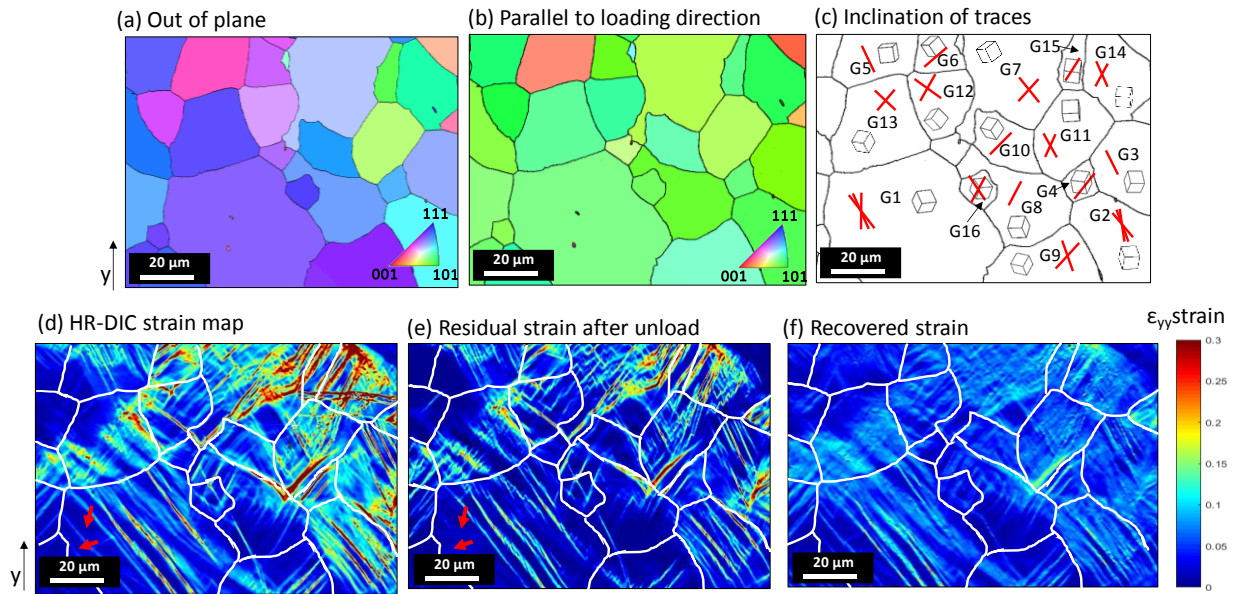
Figure 3.26 EBSD IPF maps of (a) out of plane projection and (b) loading direction projection. (c) Microstructure illustrating the unit cell orientation and the inclination of the traces shown in (d) HRDIC map at 10% global strain. (e) Map of residual strains after complete unloading. (f) Map of recovered strain.

Traces due to austenite slip

Table 3.2 lists for each austenite grain the observed trace inclinations with respect to the loading direction and the expected trace inclinations for the {1 1 0} <1 0 0> B2 slip system with the highest SF [201]. For example, grain G1 exhibits traces at 151±2° with respect to the loading direction. The slip system with the highest SF (SF≈0.40) would give a trace of 148° with respect to the loading direction. The second highest SF slip system (SF≈0.38) has a trace of 123° with respect to the loading direction. Therefore, the HRDIC traces observed in G1 with an inclination of 151±2° can correspond to dislocation slip of the system with highest SF. In grains G1, G2, G3, G4, G8 and G13 the observed trace inclinations can be correlated with those belonging to the two potential slip systems with the highest SF with a tolerance of ±5°, but no correlation can be found for the traces seen in grains G6, G7, G9, G10, G11, G12.

Table 3.2 List of the grains and the observed and expected trace inclinations for the slip system {1 1 0} <1 0 0> with the highest SF.

Grain	Angle of trace with respect to loading direction from HRDIC	Slip systems and SF values	Theoretical trace angle of highest SF	Possible activated variant rank of SF
G1	151±2	(0-11)[100], SF=0.399	148	1st
G2	143±2	(011)[-100], SF=0.377	135	2nd
		(1-10)[00-1], SF=0.374	144	
G3	153±3	(0-11)[100], SF=0.336	154	1st
G4	37±1	(0-11)[-100], SF=0.399	54	2nd
		(110)[00-1], SF=0.388	39	
G5	155±2	(1-10)[00-1], SF=0.193	164	1st
G6	50±1	(011)[-100], SF=0.348	101	No correlation
G7	141±3, 46±3	(0-11)[100], SF=0.334	156	No correlation for the 46±3 trace
		(101)[0-10], SF=0.327	98	
		(-101)[010], SF=0.298	141	3rd
G8	29±4	(0-11)[100], SF=0.354	27	1st
G9	42±1, 160±3	(011)[100], SF=0.437	36	No correlation for the 42±1 trace
		(110)[001], SF=0.416	66	
		(0-11)[100], SF=0.248	156	3rd
G10	45±2	(011)[100], SF=0.439	34	No correlation
G11	33±4, 150±2	(0-11)[100], SF=0.345	146	1st, no correlation for the 33±4 trace
G12	127±1, 37±3	(0-11)[100], SF=0.372	23	No correlation for either
G13	34±2, 133±2	(011)[100], SF=0.417	34	1st
		(0-11)[100], SF=0.271	133	4th
G14	32±3, 147±4	(0-11)[-100], SF=0.382	137	
		(1-10)[00-1], SF=0.381	35	2nd
		(1-10)[00-1], SF=0.324	143	3rd
G15	33±1	(011)[100], SF=0.408	39	3rd
		(1-10)[001], SF=0.290	29	
G16	27±1, 148±3	(011)[-100], SF=0.376	124	
		(1-10)[00-1], SF=0.369	143	2nd
		(0-11)[-100], SF=0.307	23	4th

Traces due to martensite formation

Table 3.3 lists the observed trace inclinations and the theoretical trace inclinations for the potentially activated habit plane variants (HPVs). The theoretical transformation strains are also given in Table 3.3 and will be discussed in the following paragraphs. As an example, grain G3 exhibits traces with an inclination of 153±3° with respect to the loading direction. The HPV 4'(+) with the highest positive SF (SF≈0.41) would result in a trace with an inclination of 152° with respect to the loading direction and a theoretical transformation strain of 5.2%. The experimentally determined transformation strain is 5.6%, calculated by subtracting the strain value at maximum load (Figure 3.26d) minus the strain in the unloaded state (Figure 3.26e and discussion below). Note that the variant with the highest positive SF should form under tension, whereas the variant with the most negative SF should form during compression [202]. It can be thus concluded with confidence that even though dislocation slip may play a role to some extent, some of the traces observed in grain G3 may be attributed to the HPV 4'(+). There are two reasons for that: (1) the theoretical trace inclination of HPV 4'(+) agrees well with the observed one (by HRDIC) and more importantly (2) its theoretical transformation strain agrees very well with that determined by HRDIC, see Table 3.3. If the specific trace would be ascribed to slip only, criterion (2) would not be fulfilled. In the majority of the grains, since a strain recovery could be detected by HRDIC, some traces can be safely attributed to the stress-induced formation of martensite. Interestingly, it is seen that the traces indicated by red arrows in Figure 3.26d almost completely vanished after unloading (Figure 3.26e), indicating complete reversible transformation. As shown in Table 3.3, the locally recovered strains determined by HRDIC are in good agreement with the theoretical transformation strains calculated for the formation of habit plane variants in single crystals. It should be noted that in the present study the grain size of 35 μm is large compared to the thickness of the sample (80 μm) and therefore constraints normally occurring in a polycrystal might be relaxed to some extent [203]. In other words, it is not too surprising that the behavior of each individual grain approaches the behavior of a single crystal. However, it has to be pointed out that dislocation slip may also has played a role during deformation since some traces are still visible in G3 even after unloading (see Figure 3.26e).

In grain G5, the traces are hardly recovered (see Figure 3.26 d-f) and the trace inclination agrees relatively well with $(1\,\bar{1}\,0)\,[0\,0\,\bar{1}]$ dislocation slip. Grain G5 has a significantly different crystallographic orientation compared to the rest of the grains. Its orientation, along the loading direction is close to <001>, which is not a favourable orientation for the formation of stress induced martensite [202], thus slip seems to be a dominant mechanism in this specific grain. In grains G3, G4, G5, G10 and G15, only the variant with the highest SF is found to be activated. In contrast, other grains (G1, G2, G7, G11, G13, G14) exhibit two or more variants and always include the highest-Schmid-factor HPVs. The activation of multiple HPVs in the same grain is in contrast with previous analytical studies [128, 204] where the existence of only one martensite variant (with the highest SF) led to an

overestimation of the macroscopic transformation strain, since variants with highest SF exhibit the highest transformation strain.

Table 3.3 List of the observed trace inclinations and their correlation with the habit plane variants ranked by SF values. The list includes the theoretical transformation strain of the activated variants and the experimentally observed recovery strain. * indicates the grains exhibiting non-Schmid behavior

Grain	Angle of trace with respect to loading direction	Highest SF variants	Theoretical trace angle	Possible activated variant rank of SF	Theoretical transformation strain [variant]	Recoverable strain
G1	151±2	4'(+), SF=0.460 or	145 or	1st	6.0 % [4'(+)] or	4.6%
		4'(-), SF=0.448	141	or 2nd	5.8% [4'(-)]	
G2	143±2	3(-), SF=0.439	145	1st	5.7% [3(-)]	5.5%
		3(+), SF=0.434	147		5.7% [3(+)]	
G3	153±3	4'(+), SF=0.407	152	1st	5.2% [4'(+)]	5.6%
G4	37±1	3'(+), SF=0.463	39	1st	5.9% [3'(+)]	5.8%
G5	155±2	3(-), SF=0.355	154	1st	4.5% [3(-)]	3.7%
G6*		5(+), SF=0.412	38			5.9%
	50±1	5(-), SF=0.406	48	2nd	5.2% [5(-)]	
G7	141±3	5(+), SF=0.416	145	1st	5.3% [5(+)]	6.2%
	46±3	5(-), SF=0.400	46	2nd	5.1% [5(-)]	
G8		4'(+), SF=0.412	147		5.3% [4'(+)]	2.6%
	29±4	4(-), SF=0.412	28	1st	5.3% [4(-)]	
G9*	42±1	4(-), SF=0.486	40	1st	6.3% [4(-)]	3.4%
		4(+), SF=0.470	134			
		4'(-), SF=0.406	91			
		6(+), SF=0.323	59			
	160±3	4'(+), SF=0.279	157	5th	3.6% [4'(+)]	
G10	45±2	4(-), SF=0.468	41	1st	6.2% [4(-)]	5.3%
G11	33±4	4'(+), SF=0.424	31	1st	5.2% [4'(+)]	5.2%
	150±2	4'(-), SF=0.406	147	2nd	5.4% [4'(-)]	
G12*		6(+), SF=0.477	61			5.6%
	127±1	6(-), SF=0.476	129	2nd	6.1% [6(-)]	
	37±3	6'(+), SF=0.315	38	3rd	4.1% [6'(+)]	
G13	34±2	4(-), SF=0.472	39	1st	6.0% [4(-)]	5.2%
	133±2	4(+), SF=0.464	134	2nd	5.9% [4(+)]	
G14	32±3	3'(+), SF=0.446	33	1st	5.7% [3'(+)]	6.8%
	147±4	3'(-), SF=0.444	147	2nd	5.7% [3'(-)]	
G15	33±1	4(-), SF=0.463	34	1st	5.9% [4(-)]	6.8%
G16*		3(-), SF=0.447	38			3.8%
	148±3	3(+), SF=0.439	144	2nd	5.7% [3(+)]	
	27±1	3'(-), SF=0.369	30	3rd	4.8% [3'(-)]	

3.3.4 Deformation twinning in martensite

The HRDIC maps in Figure 3.27a and Figure 3.27b reveal the evolution of the trace morphology in G1 upon straining between 8% and 10% average strain. The initially straight habit plane variant (Figure 3.27a) splits into sub-bands which form a "zig-zag" structure (Figure 3.27b) when the strain increases from 8% (end of the stress plateau) to 10% (beyond the stress plateau). Similar "zig-zag" structures were also observed in grains G2 and G9. EBSD allows two regions within the "zig-zag" structure to be indexed as austenitic phase with high confident indexes. These regions within the "zig-zag" have crystallographic orientations which differ from that of the initial parent grain, see Figure 3.27c. A twinned B2 austenite structure can be obtained through stress-induced martensitic transformation (reversible accommodation process) followed by {1 1 3} twinning in the martensite (irreversible deformation process), which upon reverse transformation results in a microstructure of twin-related austenite bands having twin planes of {1 1 2}-type [141]. Assuming this scenario, the theoretical angle between the two planes bounding the "zig-zag", i.e. ($\overline{1}\ \overline{1}\ 2$) and ($\overline{1}\ \overline{2}\ 1$), should be ~33.6° and the projection of this angle on sample surface should be ~20°. This latter value agrees with the inclination of the traces observed on the EBSD map (see Figure 3.27c). Besides, the misorientations measured along the line drawn across the "zig-zag" bands in Figure 3.27c correspond to 35° and 15° misorientation with respect to the parent grain. This results in a misorientation of ~20° between the two regions forming the "zig-zag". As shown in the next paragraph, this misorientation agrees well with that observed by TEM (see Figure 3.28d and Figure 3.28e).
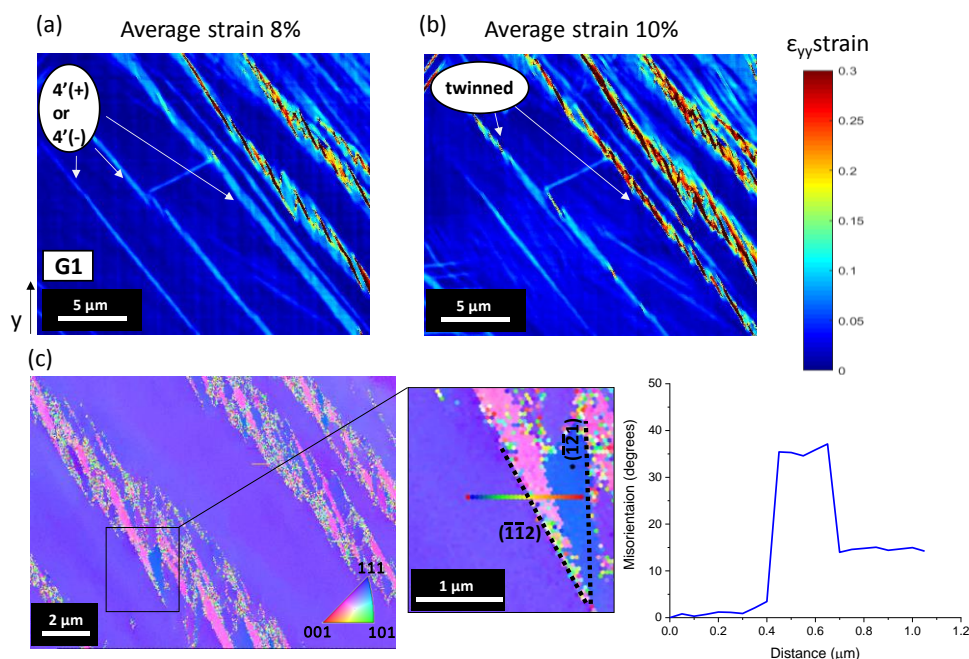
Figure 3.27 Local strain maps obtained in grain G1 at (a) 8% and (b) 10% global strains. (c) EBSD map (out of plane projection) showing that the "zig-zag" structure comprises of two austenite regions with different orientations ("pink"-<3 2 7> and "blue"-<5 4 5>) with respect to the parent grain orientation ("purple"-<6 5 8>). A line scan (rainbow line) along the "zig-zag" structure shows 35° and 15° misorientation with respect to the parent phase. The traces of the ($\overline{1}\ \overline{1}\ 2$) and ($\overline{1}\ \overline{2}\ 1$) planes are shown in (c) and align well with the "zig-zag" bands.

Figure 3.28a shows a collection of bright field TEM images of the twin-related austenite microstructure within the previously transformed zone. The red dashed lines indicate the inclination of the possible HPV traces (4'(+) or 4'(-)). Selected area diffraction patterns (SADPs) taken outside and inside the twinned area (Figure 3.28 b-e) show three different austenitic orientations. Figure 3.28b is a SADP of the parent grain in a [1 1 3]-type zone axis. While moving on the "zig-zag" bands without tilting, the SADP is no longer in a [1 1 3]-type zone axis, indicating misorientation with respect to the parent grain. Figure 3.28d-e show the SADPs of the two observed new orientations, which are ~21 degrees misorientated to each other. The misorientation is in good agreement with the misorientation obtained by EBSD (see above). Finally, TEM reveals the presence of small fractions of retained martensite. Figure 3.28 is a dark-field TEM image using the spot indexed as (0 1 1) martensite in Figure 3.28g. Martensite appears to be locked in the microstructure at the intercepts of the "zig-zag" bands, which is another mechanism for accumulating residual strain. The small fraction of residual martensite is below the EBSD detection limit and therefore the "zig-zag" bands where indexed as fully austenitic. In the diffraction pattern in Figure 3.28g, it can be seen that austenite within the selected area for diffraction (including both "zig-zag" and parent grain) has a misorientation ranging from ~20-40 degrees, this range agrees with the above mentioned misorientations that appear between the twin-related austenite bands and the parent grain. In summary, it has been shown that the applied strain is accommodated by (1) reversible martensitic transformation, (2) irreversible deformation twinning in martensite and (3) slip in austenite.
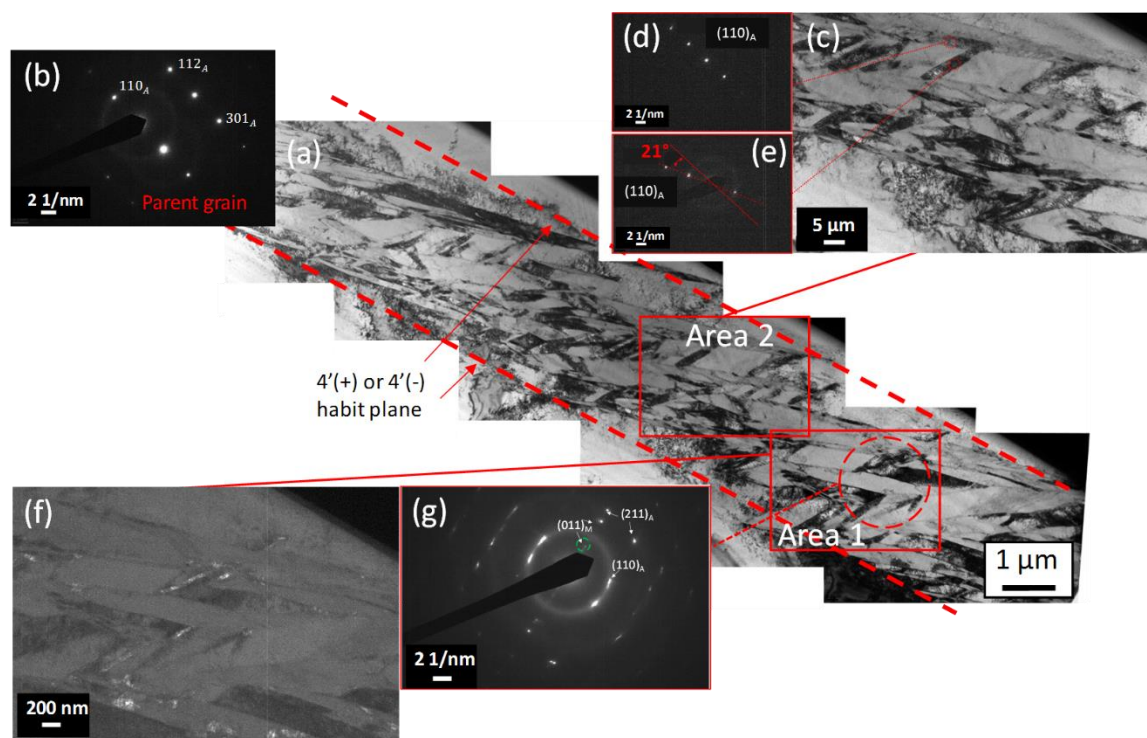
Figure 3.28 (a) Bright field TEM images of the "zig-zag" structure inside a martensite variant (either 4'(+) or 4'(-)). (b) SADP of the parent grain outside of the "zig-zag" structure. (c) Details of the Area 2 containing two austenite orientations (d) and (e). (f) Retained martensite as bright structures. The selected spot is the {0 1 1}M shown in the (g) SADP.

3.3.5 Non Schmid behavior and variant transfer across grain boundaries

Grains G6, G9, G12 and G16 exhibit a deviation from the Schmid law, as the activated variants do not have the highest Schmid factors (see Table 3.3). As illustrated in Figure 3.29, the non-Schmid variants are a result of shear transmission across the grain boundaries. For example the HPV 4'(+) in G8 is transmitted across the grain boundary to G9 where it has the 5th highest SF (deviation to the Schmid law), see Table 3.4. The formation of these variants can be rationalized with a geometrical compatibility factor, which predicts the transfer of slip between adjacent grains meanwhile maintaining coherency at grain boundaries during homogeneous deformation of polycrystalline materials [205]. This approach has been used to understand the transfer of slip systems or twin variants in Mg alloys [206, 207] across grain boundaries in Mg alloys [206, 207]. This factor, designated as m', can be calculated from the knowledge of two angles: the angle, θ, between the slip directions in grains I and II, and the angle, ψ, between the normal to the slip planes.

$$m'=cos\theta\ cos\psi \qquad \text{(Eq. 3-6)}$$

Table 3.4 lists the active variants of the neighbouring grains, and the compatibility factor between the activated habit plane variants for the grains that show variants deviating from Schmid law. For comparison, the compatibility factor between the highest SF variants and the active variants of the neighbouring grains are given. It is observed that in two cases (grains G6 and G9) the variant transmitted through the boundary from the neighbouring grain results in perfect compatibility, i.e., m' is equal to 1. The activated "non Schmid" variant and the variant of the neighbouring grain in G12 and G16 (two last lines in Table 3.4) exhibit higher compatibility than the non-activated variants with the highest SF. In all cases however the SF values of the activated variants is relatively high (3rd or 5th highest out of the 24), as the resolved shear stress on the habit plane needs to be high enough.

The transmitted variants in G8-G16 are examples of variants with relatively low geometrical compatibility. The HPV pair 4'(+) and 3(+) in grains G8-G16 exhibits lower geometrical compatibility (m'=0.16) than the HPV pair with the highest SF, i.e. 4'(+) and 3(-) (m'=0.4). It should be noted that the behavior of the grains is described in terms of the Schmid law with respect to the macroscopically applied uniaxial loading. The analysis neglects grain interactions which can locally alter the stress state so that other than the expected HPVs are activated, which can explain the discrepancy seen in G8-G16. Despite the grain interactions that locally affect the stress state, it was seen that 90-95% of the activated slip systems in TRIP steels follow the Schmid law when calculated using the macroscopic stress state [165].
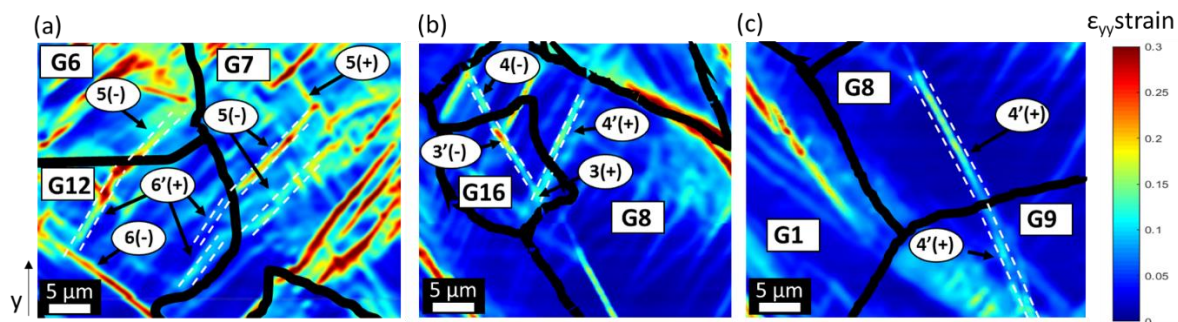
Figure 3.29 Detailed local strain maps of (a) grains G6, G12, G7, (b) G16, G8 and (c) G8, G9 which exhibit non-Schmid behavior. The transmission of traces of the habit plane variants are indicated by white dashed lines. The loading direction corresponds to the y-axis.

Table 3.4 List of grains exhibiting non-Schmid behavior and geometric compatibility factors, m', of the habit plane variants which are transmitted across grain boundaries, see Figure 3.29.

Grain	Activated variant [rank in SF value]	Transmitted variant [neighboring grain]	m' of the activated variant and the neighboring variant	m' of [highest SF variant] and the neighboring variant
G6	5(-) [2nd]	5(-) [G7]	1	[5(+)] 0.87
G9	4'(+) [5th]	4'(+) [G8]	1	[4(+)] -0.25
G12	6'(+) [3rd]	5(-) [G6 and G7]	0.4	[6(+)] 0.16
G16	3'(-) [3rd]	4(-) [G8]	0.16	[3(-)] -0.16
G16	3(+) [2nd]	4'(+) [G8]	0.16	[3(-)] 0.4

3.3.6 Summary

The uniaxial deformation behavior of a superelastic NiTi alloy with recrystallized microstructure was investigated with in-situ high-resolution DIC in combination with EBSD and TEM. Analysis based on the reversible strain (due to the reversible martensite transformation strain) and trace inclination shows that the majority of the high-strain traces correspond to the activation of habit plane variants of martensite upon loading which revert to austenite after unloading. In more than half of the grains, two habit plane variants are observed. In the majority of the observed grains, the activated habit plane variants are consistent with expectations based on the macroscopic Schmid law, i.e., the habit plane variant with the highest SF is activated. When "non-Schmid" habit plane variants are observed, their occurrence can be rationalized based on a simple transmission criterion across the grain boundary, namely, transmission occurs when the best compromise between the following two conditions is achieved:

(1) The angle between the habit planes and the shear directions of the two variants activated on each side of the grain boundary have to be small (geometrical compatibility).
(2) The SF of the activated variants has to be high.

The observed transformation strains correlate relatively well with the theoretical estimates in single crystals. Besides the martensitic transformation, significant strain is accommodated by dislocation slip in the austenite as well as deformation twinning in the stress-induced martensite, which transform back into twin-related austenite structures upon unloading as revealed by TEM investigations. Finally, small amounts of retained martensite are detected close to the twinning planes.

Chapter 4 Martensitic transformations in austenitic stainless steels

4.1 Martensitic transformation in SS201 under uniaxial and biaxial deformation

This chapter is adapted from the published paper:

Abstract

The effect of uniaxial/biaxial loading on the martensitic transformation of a low stacking fault metastable austenitic stainless steel was studied by in-situ neutron diffraction on cruciform-shaped/dogbone samples. Uniaxial loading favors the martensitic transformation following the sequence $\gamma \to \varepsilon \to \alpha'$, where at low strains ε-martensite is the precursor of α'. During equibiaxial-loading, the evolving texture suppresses the formation of ε-martensite and considerably less α'-martensite is observed at high strains. The results are discussed with respect to the deformation textures, the loading direction and the mechanism of the ε-martensite transformation.

In this work, the contributions from the doctoral candidate are:

- Participated in the cruciform sample geometry design using Abaqus together with Dr. Polatidis and Dr. Panzner
- Performed the in-situ neutron diffraction measurements with Dr. Polatidis and Dr. Panzner
- Analyzed the neutron diffraction data and summarized the results
- Revised and edited the draft of the paper (first draft written by Dr. Polatidis)

4.1.1 Introduction

In metastable austenitic stainless steels martensite forms upon deformation, the so-called transformation induced plasticity or TRIP effect, and this transformation is responsible for a good combination of strength and ductility that these materials exhibit. Two types of martensite can form during deformation: the hexagonal-closed-packed (HCP) ε-phase and the body-centered-cubic/tetragonal (BCC or BCT) α'-phase. For some steels, it has been reported that ε-martensite is a precursor of α'-martensite as it forms at early stages of plastic deformation and that α' forms at later stages of deformation in expense of ε-martensite [208-211]. For other steels the direct formation of γ (the face-centered-cubic austenite phase) $\rightarrow \alpha'$has been reported [212]. Generally, it is believed that the prevalence of $\gamma \rightarrow \varepsilon \rightarrow \alpha'$or $\gamma \rightarrow \alpha'$ depends on the stacking-fault-energy (SFE) of the austenitic phase: for low SFE steels (<20 mJ/m^2) the sequence $\gamma \rightarrow \varepsilon \rightarrow \alpha'$ is favorable whereas for high SFE steels (>20 mJ/m^2) the direct $\gamma \rightarrow \alpha'$ is often observed [210, 212]. Twinning-Induced Plasticity (TWIP) in combination with TRIP occurs in higher SFE steels [213]. The general trend is that with increasing SFE the following sequence of predominant deformation mechanism is observed: TRIP $\gamma \rightarrow \varepsilon \rightarrow \alpha'$, TRIP $\gamma \rightarrow \alpha'$, TWIP and slip [210, 212-214].

The amount of α'-martensite formed during straining has important implications on the formability during cold forming processes [215, 216]. During forming, parts of the component are subjected to uniaxial strain paths or more complex loading states. How the loading state influences the transformation characteristics has been addressed in a few studies but remains inconclusive. It has been reported for 304 steels that a biaxial tension enhances the martensitic transformation [91, 92]. However, other reports on 201, Fe18Cr10Ni (at low temperature) and 301LN steels show that uniaxial loading produces more martensite than biaxial loading [95, 217-219]. The majority of the above-mentioned studies were conducted on punched sheet samples where different locations exhibit different loading states, including uniaxial and equibiaxial tension. Microscopic observations have suggested that an increased density of dislocations under biaxial loading results in higher amount of martensite [218]. A detailed understanding of the role of the loading state is however missing.

Transformation kinetic models have helped in understanding the matter, but several points remain unclear. Some models suggest that a higher triaxiality (TX), i.e. the ratio of hydrostatic stress and the Von Mises stress, leads to a higher amount of formed martensite [220, 221]. Such models predict that when e.g. loading equibiaxialy (i.e. TX=0.67) will result in a higher amount of martensite than when loading uniaxialy (i.e. TX =0.33). On the other hand, a recent kinetic model suggests that the fraction of strain-induced martensite does not only depend on the triaxiality factor but also on the Lode angle parameter: if this is the case, uniaxial loading produces more martensite than equibiaxial, as is for example observed for 301LN steel [219]. The above-mentioned kinetic models consider solely the mechanics of plasticity and phase transformations, do not consider microstructural properties such as the evolving crystallographic texture during loading and cannot explain the dependence of the

intermediate ε-martensite on the strain path. In the present study, we address the effect of loading state on the transformation behavior of a low SFE austenitic stainless steel exhibiting the γ → ε → α′ transformation sequence.

4.1.2 Experimental

A commercial 201 stainless steel is employed having a mean grain size of 45 μm and a nominal composition of Fe-16-18Cr-5.5-7.5Mn-3.5-5.5Ni-max1Si-max0.15C (wt. %), which according to the empirical relationships of Ref. [99, 222] has a SFE ~20±3 mJ/m². Cruciform-shaped and dogbone samples where deformed (both uniaxially and cruciforms equibiaxially) during neutron diffraction allowing the observation of ε- and α′-martensite evolution. The cruciform geometry was optimized with the aid of finite-element (FE) analysis using ABAQUS, the employed geometry is shown in FFigure 2.23 in Section 2.4.2. In situ neutron diffraction tests were carried out at the POLDI beamline of the Swiss neutron spallation source SINQ which can be equipped with a biaxial machine and a tensile machine [113, 223]. A schematic of the experimental setup is shown in Figure 4.1. The in-plane strain was measured with a 2-camera digital image correlation (DIC) system (GOM, Aramis 5M). Uniaxial loading (hereafter referred as UN) and equibiaxial loading (hereafter referred as EQ) were performed with a loading rate of 80 N/s. The uniaxial loading direction F2 was parallel to the rolling direction (RD) of the sheet. The equibiaxial load was performed along RD and the transverse direction (TD). A uniaxial test was performed on a dogbone-shaped specimen (see Section 2.4.3) and the results were consistent with the cruciform sample. Neutron diffraction measurements were carried out in predefined force intervals upon interrupting the loading and holding the displacement that led to fracture of the sample. The maximum equivalent strain that could be reached during the equibiaxial test was ~16%, a limitation caused by the stress concentrations at the cross-arms of the cruciform specimen. The maximum strain reached under uniaxial tension was 29%. The neutron diffraction data were analyzed with the open source software Mantid [117].
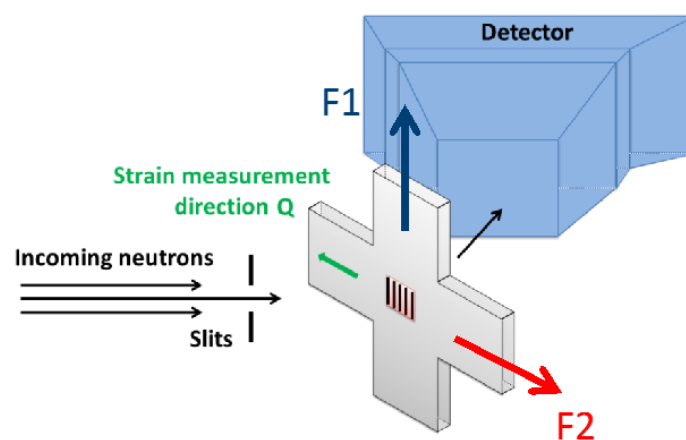
Figure 4.1 The schematic of the experimental setup on POLDI instrument, SINQ Switzerland [ref].

EBSD studies were carried out on the as-received and on the deformed material. For the latter, additional samples were deformed uniaxially (dogbone) and equibiaxially (cruciform) up to 13% equivalent strain in order to obtain samples at comparable strains. The samples were ground with 1200 grit SiC paper and then electropolished for 5s with a 16:3:1 (by volume) methanol, glycerol and perchloric acid solution. A field emission gun scanning electron microscope (FEG SEM) Zeiss ULTRA 55 equipped with EDAX Hikari Camera operated at 20kV in high current mode with 120 μm aperture was used. The EBSD raw data were post-processed using the EDAX OIM Analysis 7.3 software.

4.1.3 Equibiaxial loading suppressed the martensitic transformation

The evolution of the neutron diffraction patterns during deformation is shown in Figure 4.2a and Figure 4.2b for the UN and EQ samples respectively. Initially only austenite reflections are observed. After ~10% strain (which corresponds to a true stress value of ~645 MPa, obtained from the dogbone sample) a reflection corresponding to $(1\ 0\ \bar{1}\ 1)_\varepsilon$ from ε-martensite appears in the UN sample. The $(1\ 1\ 0)_{\alpha'}$ reflection from α′-martensite appears only after 23% strain, which corresponds to a true stress value of ~1000 MPa, obtained from the dogbone sample. The increase in the α′ peak intensity is accompanied by a decrease in the intensity of ε, as can be observed in Figure 4.2c where both reflections are compared at 20% and 29% strain.
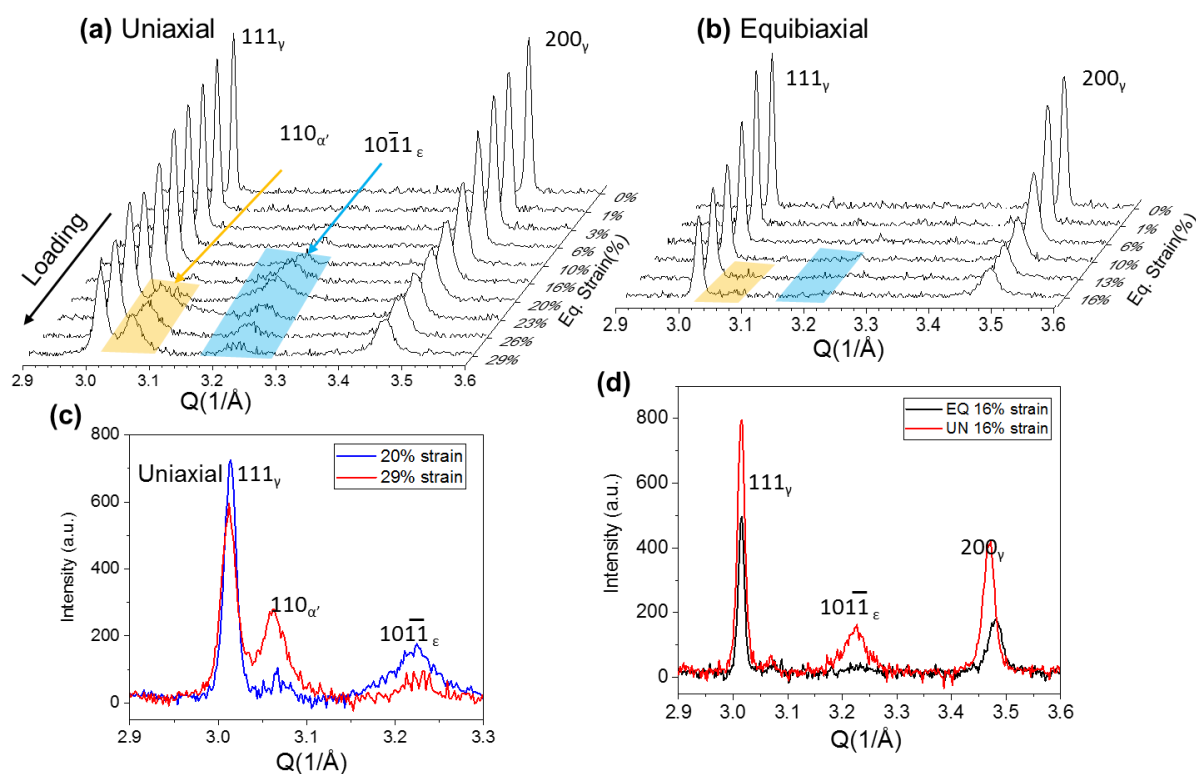
Figure 4.2 Neutron diffraction patterns with increasing the applied strain for (a) uniaxial loading and (b) equibiaxial loading. (c) Comparison of the diffraction patterns at 20% and 29% equivalent strain for the UN sample, showing the increase of α′-martensite fraction in expense of ε-martensite. (d) Comparison of the diffraction patterns from the UN and EQ samples at 16% equivalent strain.

On the other hand, no reflections corresponding to ε- or α′-martensite are observed for the EQ sample up to 16% equivalent strain. A comparison of the neutron diffraction patterns at ~16% equivalent strain is given in Figure 4.2d; showing the absence of any martensite reflection in the EQ sample, as opposed to the UN sample having a pronounced reflection. To verify whether transformation occurs under equibiaxial loading, a sample was deformed by a hemispherical punch allowing reaching much larger biaxial strains than the in-situ tests [95]. Figure 4.3 shows the phase maps from EBSD analysis taken from areas deformed up to 21% and 35% uniaxial strain (Figure 4.3a and Figure 4.3b)and from areas deformed to 22% and 34% (Figure 4.3c and Figure 4.3d) equivalent biaxial strain. These observations confirm that the formation of α′-martensite occurs also under biaxial loading state; however, the transformation is significantly less abundant than the uniaxial loading.
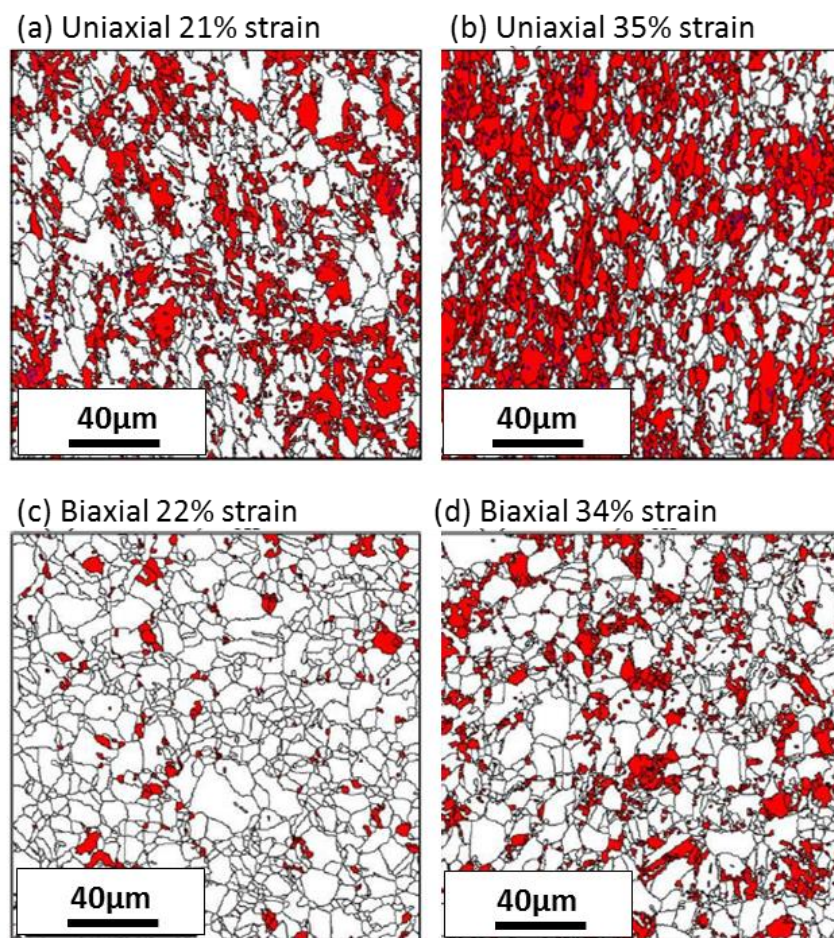
Figure 4.3 Phase maps showing γ-austenite (white) and α′-martensite (red) after: uniaxial tension at (a) 21% and (b) 35% and biaxial tension at (c) 22% and (d) 34% equivalent strain.

4.1.4 The role of the ε transformation and its dependency on the load path

The question arises why the martensitic transformation is suppressed during equibiaxial loading. To understand this, the mechanism of ε-martensite formation needs to be considered. According to the theory of Olson and Cohen [224], the deformation-induced hexagonal domains are formed by the

arrangement of stacking faults, resulting from the dissociation of perfect dislocations, into two partials on every second {1 1 1} plane. The separation between the Leading Partial Dislocations (LPDs) and the Trailing Partial Dislocations (TPDs) can be altered by local or external applied stresses: a typical equilibrium separation of ~10 nm can increase up to ~1 μm [225]. This is for instance the case when the LPD has a higher Schmid factor than the TPD: the large separation between the partials results in the local appearance of the hexagonal ε-martensite phase [225, 226]. In the opposite case, when the TPD has a higher Schmid factor, the system becomes unfavorable to the formation of ε-martensite and hence conventional dislocation slip occurs. During uniaxial and equibiaxial loadings, different deformation textures are formed which in turn would influence the Schmid factors of the partial dislocations under the different loading conditions. The Schmid factors of the partial dislocations corresponding to the slip system with the highest Schmid factor were calculated under uniaxial loading along RD and in-plane equibiaxial loading for the <1 1 1>, <0 0 1>, <1 0 1>, <1 0 2> and <1 1 3> orientations (see Table 4.1and Table 4.2). For the equibiaxial case it should be noted that for the Schmid factor calculation, the in-plane equibiaxial loading is equivalent to uniaxial compression along the normal direction (ND). Moreover, in the case of compressive loading the situation is reversed since changing the direction of the applied stress changes the sense of glide motion of the partial dislocations, such that the LPD becomes TPD and vice versa [82].

Table 4.1 List of the 12 possible slip systems for the fcc structure and their equivalent pair of partial dislocations. LP stands for lead partial and TP stands for trailing partial.

	Slip system		Partial dislocations	
	Slip plane	**Burgers vector**	**LP Burgers vector**	**TP Burgers vector**
1	$(1\ 1\ 1)$	$[1\ 0\ \bar{1}]$	$[1\ 1\ \bar{2}]$	$[2\ \bar{1}\ \bar{1}]$
2	$(1\ 1\ 1)$	$[0\ \bar{1}\ 1]$	$[1\ \bar{2}\ 1]$	$[\bar{1}\ \bar{1}\ 2]$
3	$(1\ 1\ 1)$	$[\bar{1}\ 1\ 0]$	$[\bar{2}\ 1\ 1]$	$[\bar{1}\ 2\ \bar{1}]$
4	$(\bar{1}\ 1\ 1)$	$[1\ 1\ 0]$	$[2\ 1\ 1]$	$[1\ 2\ \bar{1}]$
5	$(\bar{1}\ 1\ 1)$	$[0\ \bar{1}\ 1]$	$[\bar{1}\ \bar{2}\ 1]$	$[1\ \bar{1}\ 2]$
6	$(\bar{1}\ 1\ 1)$	$[\bar{1}\ 0\ \bar{1}]$	$[\bar{1}\ 1\ \bar{2}]$	$[\bar{2}\ \bar{1}\ \bar{1}]$
7	$(1\ \bar{1}\ 1)$	$[1\ 1\ 0]$	$[1\ 2\ 1]$	$[2\ 1\ \bar{1}]$
8	$(1\ \bar{1}\ 1)$	$[0\ \bar{1}\ \bar{1}]$	$[1\ \bar{1}\ \bar{2}]$	$[\bar{1}\ \bar{2}\ \bar{1}]$
9	$(1\ \bar{1}\ 1)$	$[\bar{1}\ 0\ 1]$	$[\bar{2}\ \bar{1}\ 1]$	$[\bar{1}\ 1\ 2]$
10	$(1\ 1\ \bar{1})$	$[1\ 0\ 1]$	$[2\ \bar{1}\ 1]$	$[1\ 1\ 2]$
11	$(1\ 1\ \bar{1})$	$[0\ \bar{1}\ \bar{1}]$	$[1\ \bar{2}\ \bar{1}]$	$[\bar{1}\ \bar{1}\ \bar{2}]$
12	$(1\ 1\ \bar{1})$	$[\bar{1}\ 1\ 0]$	$[\bar{1}\ 2\ 1]$	$[\bar{2}\ 1\ \bar{1}]$

Table 4.2 List of the slip systems with the highest Schmid factor (SF) for slip and Schmid factor of their equivalent leading partials (LP) and trailing partial (TP) dislocations for the characteristic orientation of the IPFs. The highest value of the SF between the leading and the trailing partial dislocations is underlined.

Orientation	Slip systems with highest SF	SF for perfect dislocation	Uniaxial		Equibiaxial	
			SF for LP	SF for TP	SF for LP	SF for TP
<0 0 1>	1, 2, 5, 6, 8, 9, 10,11	0.408	0.236	<u>0.471</u>	<u>0.471</u>	0.236
<1 0 1>	2, 3, 7, 8	0.408	<u>0.471</u>	0.236	0.236	<u>0.471</u>
<1 1 1>	4, 6, 7, 8, 10, 11	0.272	<u>0.314</u>	0.157	0.157	<u>0.314</u>
<1 1 3>	6, 8	0.445	<u>0.386</u>	<u>0.386</u>	<u>0.386</u>	<u>0.386</u>
<1 0 2>	3, 8	0.490	<u>0.424</u>	<u>0.424</u>	<u>0.424</u>	<u>0.424</u>

The inverse pole figures (IPFs) for RD, TD and ND of the material before deformation (Figure 4.4a) and after uniaxial (Figure 4.4b) and biaxial deformation (Figure 4.4c), both at 13% equivalent strain are shown in Figure 4.4. For uniaxial deformation along RD (Figure 4.4b for the IPF along RD) the LPDs have a higher Schmid factor on the right hand side of the boundary, as indicated by area enclosed by the dashed line. For these grains, the formation of ε-martensite is possible. For grains with orientations on the left side of the boundary, the LPDs have lower Schmid factor than the TPDs and therefore ε-martensite is not likely to form. For equibiaxial deformation the grains that will facilitate the formation of ε-martensite are contained in the dashed area on the left hand side of the <1 1 3> - <1 0 2> boundary as shown in Figure 4.4c for the IPF along ND. In both cases, the closer to the <1 1 3> - <1 0 2> boundary an orientation is, the smallest the difference of the Schmid factors between the two partial dislocations is.

The above results indicate that the deformation textures formed during uniaxial and equibiaxial loading play a significant role on the appearance/absence of ε-martensite. The as-received material exhibits only a very mild texture as shown in the IPFs of Figure 4.4a. However, as shown in the IPF maps along RD, TD and ND shown in Figure 4.4b and Figure 4.4c, the textures formed after 13% strain during uniaxial and equibiaxial deformation are already different. In the uniaxial deformed sample a bimodal texture exhibiting a strong <1 1 1> and a less pronounced <0 0 1> pole parallel to the RD direction (loading direction) is obtained. The strongest pole in the UN sample is lying in the area for which the LPDs have higher Schmid factor than the TPDs. In contrast, under equibiaxial loading, a <1 1 0> texture forms parallel to the ND direction: the strongest pole belongs to that part of the IPF where the TPDs have higher Schmid factor than the LPDs and these grain orientations are not favorable for

the formation of ε-martensite. Quantitatively, by integrating the IPFs, weighted by grain area, it is obtained that ~81% of the EBSD scanned area favors the formation of ε-martensite in the uniaxial loading case, whereas only ~49% in the equibiaxial loading case.
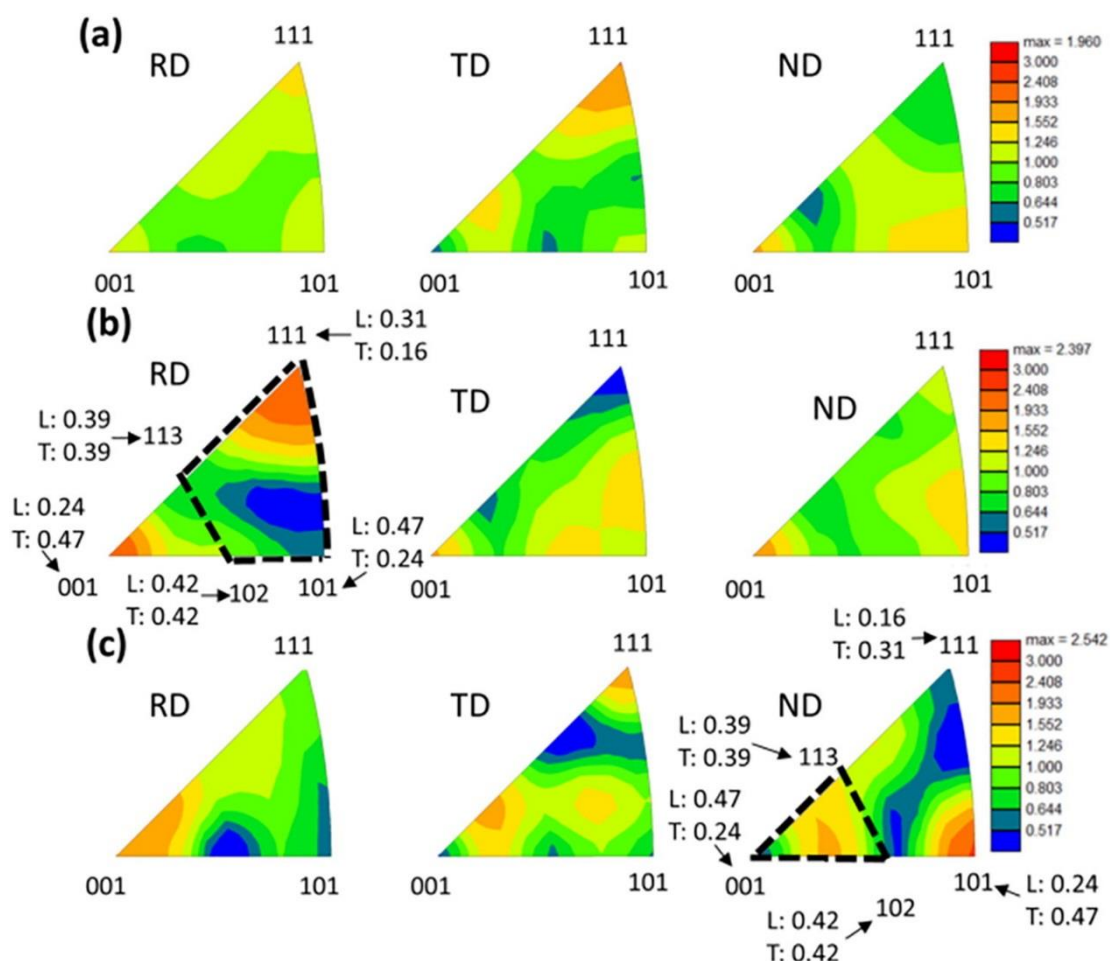
Figure 4.4 IPFs of the (a) as-received (b) uniaxialy-deformed (along RD) up to ~13% strain and (c) equibiaxially-deformed (along RD and TD) up to ~13% equivalent strain 201 SS material along the three principle sample directions. The enclosed regions, with dashed lines, indicate the orientations for which the LPDs have higher Schmid factor than the TPDs. The Schmid factor values for the leading and trailing partial dislocations (denoted with L and T respectively) are also given.

Figure 4.5 illustrates parts of these areas where these differences are shown in a more detailed microstructural view after 13% strain. In these figures, the grains that belong to the orientations for which the LPDs have a higher Schmid factor are colored blue, the grains for which the TPDs have a higher Schmid factor are red, the ε-martensite is green and the α′-martensite is yellow. After uniaxial deformation (Figure 4.5a and Figure 4.5c), the majority of the grains are blue and most of them contain significant amounts of martensite. After equibiaxial deformation (Figure 4.5b and Figure 4.5d), there are less blue grains with little martensite. Interestingly, the blue grains in the EQ sample contain very little ε-martensite compared to the blue grains in the UN sample. To understand this, the orientation of the grains containing most martensite which are the blue grains A-D in the UN sample and the blue grains H-G in the EQ sample are shown in Figure 4.5e and Figure 4.5f.
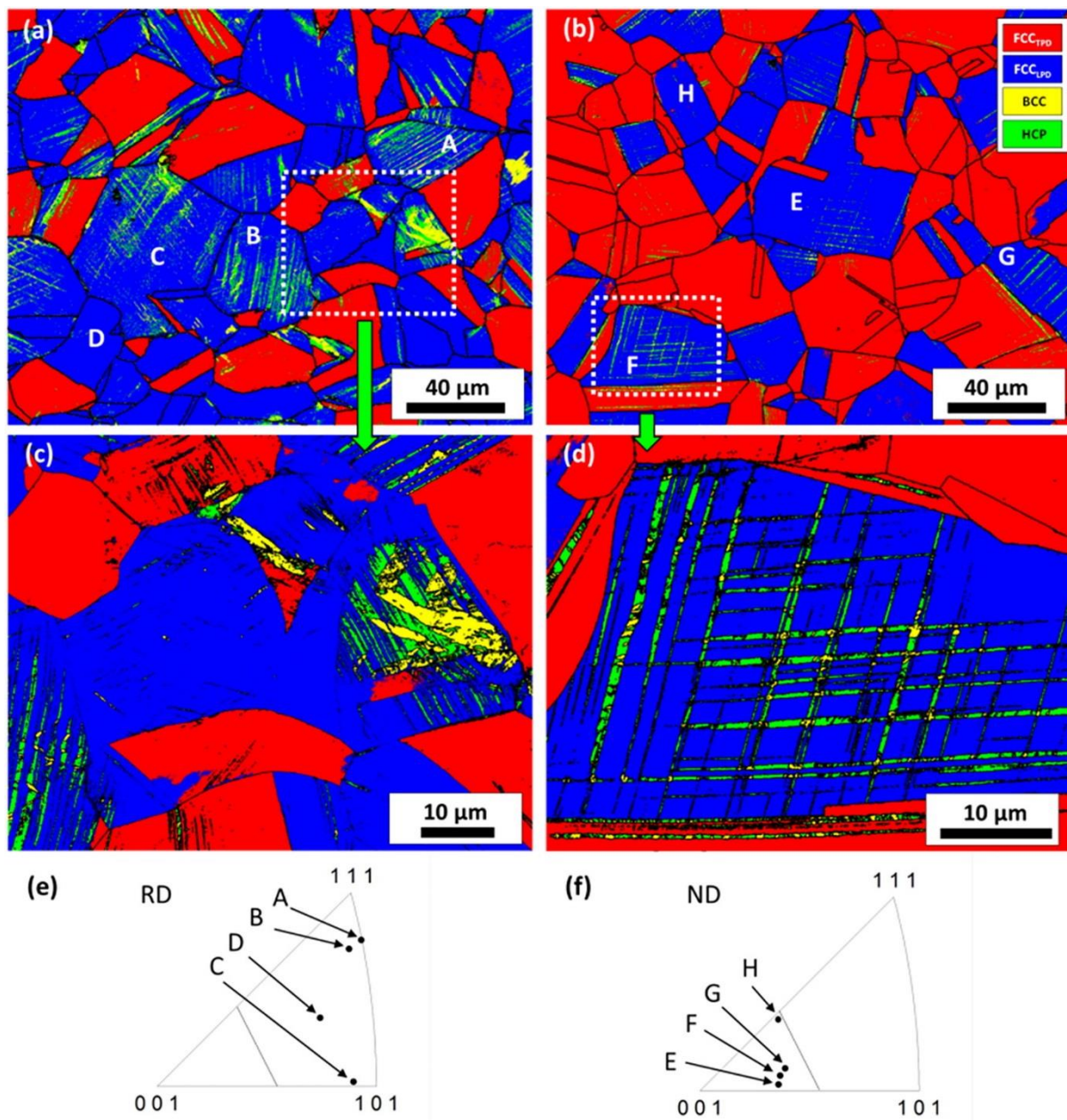
Figure 4.5 Phase maps showing the γ-austenite grains which belong to the high Schmid factor orientation regime for the LPDs (with blue) and the high Schmid factor orientation regime for the TPDs (with red), ε-martensite (with green) and α′-martensite (with yellow) for: (a) uniaxial and (b) equibiaxial both at ∼ 13% equivalent strains. (c) Magnification of the highlighted area in (a) showing significant amount of α′-martensite within the bands of ε-martensite. (d) Magnification of the highlighted area in (b) showing that α′-martensite forms at the intersection of ε-martensite. The indicated grains A-H and their corresponding position in the IPF are shown in (e) for uniaxial tension and (f) equibiaxial tension.

In the UN sample, the orientation of grains A - D lies close to the <1 1 1> orientation for which the difference between the Schmid factor of the LPDs and the TPDs is the highest (see Figure 4.5e). In contrast, the grains that exhibit transformation under equibiaxial loading have orientations close to the "neutral" <1 1 3> - <1 0 2> boundary (see grains E, F, and G in Figure 4.5f). Because the difference between the Schmid factor of LPDs and TPDs is not very high, the transformation here is limited. This is confirmed by the absence of visible martensite in grain D in the UN sample and grain H in the EQ sample, both having their orientation close to the "neutral" <1 1 3> - <1 0 2> line. Furthermore it can

be noted that, since α'-martensite appears at the intersections of the ε-martensite bands in the EQ sample, the EBSD measurements confirm that ε-martensite is a precursor for α'-martensite during uniaxial and equibiaxial deformation, as was also demonstrated in the neutron diffraction results for uniaxial deformation. The fact that ε-martensite is not observed by the neutron measurement, during equibiaxial deformation, has to be ascribed to a combination of the suppression of formation, the limited equivalent strain reached with the cruciform geometry and the detection limit of the method.

4.1.5 Summary

In summary, in-situ neutron diffraction studies performed on metastable 201 stainless steel combined with EBSD measurements confirm that ε-martensite is a precursor for α'-martensite during uniaxial and equibiaxial deformation at the same loading rate. In both loading states, the grains that contain martensite belong to orientations for which the LPDs have higher Schmid factor than the TPDs. The martensitic transformation is suppressed during equibiaxial loading as a consequence of the different textures formed during deformation.

4.2 Dislocation slips in SS304 under multiaxial deformation

This chapter is adapted from the published paper:

Efthymios Polatidis, <u>Wei-Neng Hsu</u>, Miroslav Šmíd and Helena Van Swygenhoven

Abstract

In this study, a miniaturized cruciform-shaped sample geometry which allows reaching high plastic strain under equibiaxial loading with reduced thickness at the test section is presented. The thinning method results in excellent surface quality that can be used for Electron backscatter diffraction and high-resolution digital image correlation investigations (HRDIC). The new cruciform geometry is used to study with HRDIC the slip activity in metastable austenitic stainless steel 304 during uniaxial and equibiaxial deformation. The results are discussed with respect to the Schmid law and the effect of multiple slip activity on the nucleation of martensitic transformations.

In this work, the contributions from the doctoral candidate are:

- Designed and optimized the geometry using FE simulations
- Fabricated the cruciform-shaped samples
- Performed Macro-DIC experiments and in-situ HRDIC experiments
- Analyzed the HRDIC data and summarized the results
- Wrote the first draft together with Dr. Polatidis, revised and edited the draft of the paper

4.2.1 Introduction

Metals and alloys are subjected to biaxial stresses and strain path changes during sheet forming, drawing processes and under service conditions. Under these complex loading conditions, the deformation behavior and the mechanical properties can differ from those obtained under uniaxial loading conditions [89, 227]. The origin of such strain path dependence has to be found at the inter- and intra-granular level and hence understanding the materials deformation behavior requires a thorough characterization at these length scales [228]. Dislocation slip is an inherent anisotropic mechanism and upon strain path changes anisotropic dislocation substructures develop. Moreover, other deformation mechanisms such as twinning and/or deformation-induced phase transformations occur e.g. in Transformation Induced Plasticity (TRIP) steels [100, 226, 227, 229-232]. Since these mechanisms depend not only on materials parameters but also on the resolved shear stress, their activation depends on the strain path.

To gain insight into the dependence of the mechanical behavior on the strain paths, several biaxial deformation devices, using cruciform-shaped samples, have been employed in combination with microscopy, X-ray and neutron diffraction methods [100, 103, 113, 153, 233-237]. Significant work has been done to optimize the cruciform geometries in order to reach high plasticity at the center, avoid fracture at the cruciform arms, reduce the stress heterogeneity in the center of the cruciform and prevent shear loading in the cruciform arms [105]. It is commonly accepted that in order to reach high enough plasticity (i.e. >5% equivalent von Mises strain) at the place of observation, the center of a cruciform sample has to be thinned. This can be achieved by machining or laser ablation. The surface quality which can be reached by these methods is good enough for e.g. X-ray diffraction techniques but not sufficiently good for being used in microscopy studies such as Electron Backscatter Diffraction (EBSD).

Recently a miniaturized biaxial tensile device that can be installed on synchrotron beamlines and inside scanning electron microscopes (SEMs) had been developed [103]. The implementation in an SEM allows performing in-situ deformation studies while undertaking high-resolution digital image correlation (HRDIC). The latter provides full-field displacement maps at high magnification upon deformation and has been successfully employed for studying deformation mechanisms, strain partitioning and crack propagation under uniaxial loading tests using dogbone-shaped samples [119, 122, 143, 181, 184-187, 238]. A flat cruciform geometry has been used in combination with HRDIC to investigate the martensitic transformation of superelastic NiTi in [153], where it was seen that the flat geometry can be used for performing uniaxial and strain path changes, but it does not allow reaching high plastic strains at the center of the sample under equibiaxial loading.

Here we present an optimized cruciform shape geometry which enables performing in-situ SEM biaxial tests coupled with HRDIC analysis. The sample is fabricated using electrochemical

micromachining (ECMM), a micromachining method providing high surface quality which can be readily used for metallography characterization [111], and a picosecond laser for cutting the outline of the sample. The novel sample preparation method employed on a foil of austenitic stainless steel 304 (SS304) gives the possibility to reach high plastic deformation strains under uniaxial and equibiaxial load paths. The localization of plastic strain at the microstructural scale under uniaxial and biaxial strain conditions are discussed with respect to the obedience to the Schmid law for the activation of the slip systems within individual grains.

4.2.2 Experimental

Cruciform samples

The optimization of the cruciform sample geometry is carried out with finite element simulations using the commercial ABAQUS/Standard software [239]. The stress-strain curve and isotropic elastic properties of SS304 obtained from uniaxial loading of a dogbone sample are used as materials properties input to the built-in model based on the Von Mises yield criterion and the associated flow rule [105]. Figure 4.6a shows the optimized geometry and a close view of the central pocket exhibiting a gradual thinning from 150 μm (arm) down to 40 μm (center). In order to improve the computational efficiency, only 1/8 of the entire cruciform geometry is simulated with symmetric boundary conditions being applied on the appropriate surfaces. A structured hexahedron mesh is employed with linear 8-node C3D8 elements as shown in Figure 4.6b. The simulations are done with a linear loading (surface traction mode) to a target force of 35N on each arm along 500-time steps. The forces are applied on the inside area of the holes at the arms; the arrows in Figure 4.6b indicate the loading directions.
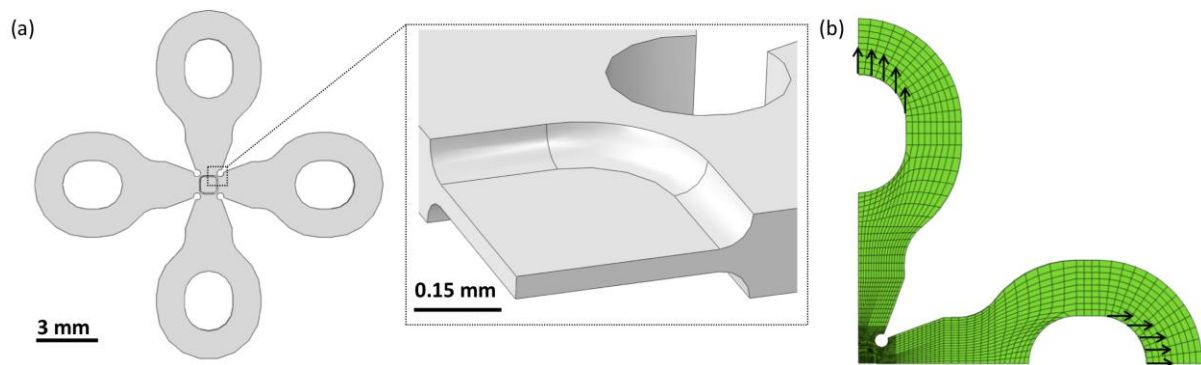
Figure 4.6 (a) Schematics of the cruciform shaped sample with a detailed view of the pocket. (b) The finite element mesh with C3D8 element used for 1/8 of the cruciform geometry. The arrows indicate the direction of the applied load.

A SS304 foil of 0.150 mm thickness in annealed state with a mean grain size of 19±5 μm, excluding the annealing twins, was purchased from Goodfellow, UK. The rounded-square pockets are fabricated with ECMM carried out at Micropat SA, Switzerland on both surfaces of the foil. First, an epoxy-based resist (KMPR 1010) is applied onto the foil by spin coating at 3000 rpm, followed by soft baking at 100

^{0}C for 20 min and hard baking at 180 ^{0}C for 20 min. After curing, this layer (~10 µm) is locally exposed to a short-pulse UV laser (Spectra Physics Explorer 355 nm) to define the rounded-square openings to the underlying metal surface. The unprotected areas are neatly etched at the rate of 2.08 x 10-2 mm³/C in the 3 M sulphuric acid-methanol solution at room temperature. A "bathtub-like" depth profile in the pocket (Figure 4.6a) and a smooth surface are obtained with high dimensional accuracy and good top-bottom pocket alignment. More details on the technique and its limitations can be found in [110, 112]. After completion of the electrochemical dissolution, the protective coating is stripped in N-Methyl-2-pyrrolidone (NMP) at 100 ^{0}C. Once the pockets are introduced to the foil, the outline of the cruciform is cut using a frequency tripled Nd:YVO picosecond pulsed laser at the Swiss Federal Laboratories for Materials Science and Technology (EMPA). The power of the laser for cutting is 870 mW with 160 kHz pulse frequency, a pulse width of 10 picoseconds and wavelength of 355 nm is used.

The above described sample preparation method ensures the material to retain the austenitic phase, i.e. avoiding the martensitic transformation induced by the deformation during mechanical surface preparation. Furthermore, no recrystallization, carbide formation or surface oxidation is to be expected at the temperatures used (i.e. maximum temperature of 180 ^{0}C). Figure 4.7 shows the high surface quality achieved by the ECMM process, the polycrystalline microstructure can be clearly revealed by secondary electron imaging with SEM.
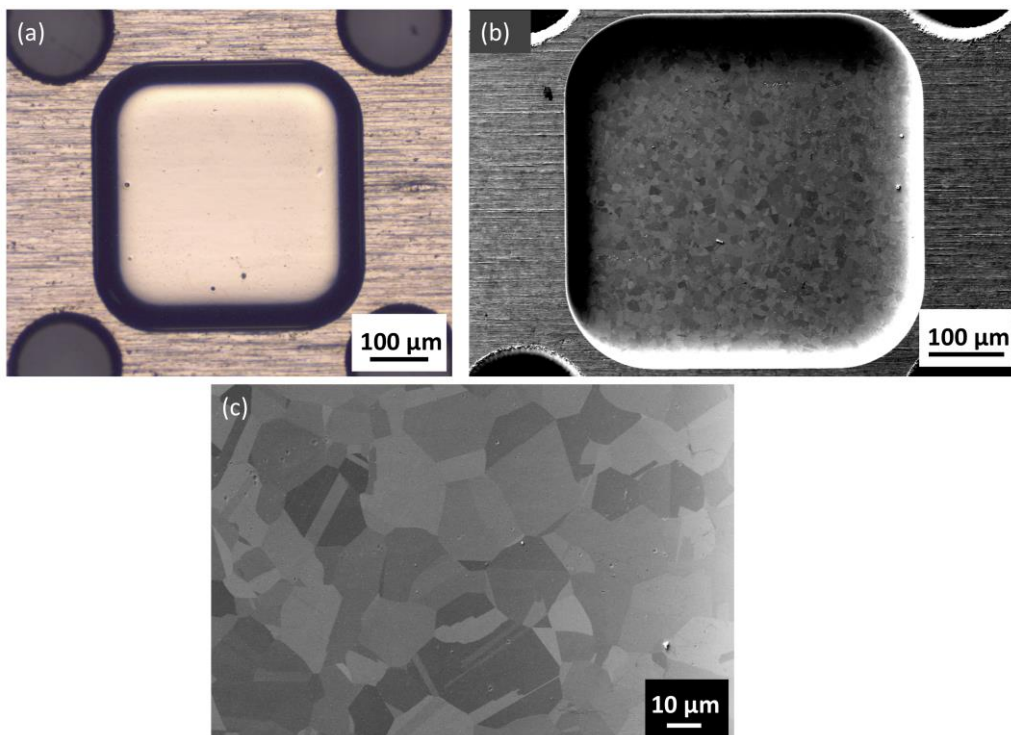
Figure 4.7 (a) Optical microscopy image and (b) secondary electron image from SEM showing the smooth and high surface quality after the sample preparation by ECMM. (c) High magnification SE imaging of the polycrystalline microstructure.

Macroscopic digital image correlation

In order to study the force-strain response of cruciform samples under uniaxial and equibiaxial load paths, deformation tests using a mini-biaxial machine developed at Paul Scherrer Institute [103] are performed in combination with macroscopic Digital Image Correlation (Macro-DIC) analysis. The ECMM thinning process produces a mirror-like surface that does not give reflections to serve as DIC pattern. Therefore, the surface obtained from ECMM is slightly etched with solution of 170 ml H_2O, 230 ml HCl and 20 ml HNO_3 for 5 minutes in order to introduce surface roughness, which serves as the surface features to be tracked for the Macro-DIC analysis. During the displacement-controlled deformation (displacement rate 0.4 μm/s), series of images (with resolution of 2484 x 3840 pixels) are taken at the center of the cruciform (field of view, FOV of 0.9×1.38 mm^2) using a PixeLINK camera. The analysis of the DIC data is undertaken using the open source 2D-DIC software Ncorr [118]. The average equivalent strain is calculated from an area of 150 μm x 150 μm at the center of the pocket using the relationship:

$$\varepsilon_{eq} = \frac{2}{3} \times \frac{1}{\sqrt{2}} \sqrt{\left(\varepsilon_x - \varepsilon_y\right)^2 + (\varepsilon_y - \varepsilon_z)^2 + (\varepsilon_z - \varepsilon_x)^2 + 6\varepsilon_{yz}^2 + 6\varepsilon_{zx}^2 + 6\varepsilon_{xy}^2}$$ (Eq. 4-1)

where ε_x, ε_y are the two in-plane strain components and ε_{xy} is the shear strain obtained by DIC analysis. ε_{yz} and ε_{zx} are taken as zero and ε_z is taken as:

$$\varepsilon_z = -(\varepsilon_x + \varepsilon_y)$$ (Eq. 4-2)

EBSD

The high surface quality of the pocket after ECMM makes it suitable for EBSD mapping without further preparation. EBSD studies of the initial microstructure (undeformed) were undertaken at the center of the cruciform pocket. The area of interest for the HRDIC study is mapped for two samples, one that will be deformed under uniaxial and the other under equibiaxial load paths. The EBSD maps are acquired with a field emission gun (FEG) SEM Zeiss ULTRA 55 equipped with an EDAX Hikari Camera, at 20 kV in high current mode with a 120 μm aperture. The EDAX OIM Analysis 7.3 software is used for post-processing the EBSD raw data and plotting the {1 1 1} traces in each grain and to reveal the average Schmid factor of all slip systems under uniaxial or equibiaxial loading.

HRDIC

The fine gold speckle pattern for HRDIC is obtained by the remodeling process of a thin gold layer [119] deposited on the mirror-like surface obtained from ECMM. For the in-situ HRDIC measurements, the mini-biaxial machine is installed inside the chamber of a FEG SEM Zeiss ULTRA 55. The deformation tests are performed in displacement control with a displacement rate of 0.4 μm/s. The electron beam with acceleration voltage of 3 kV in combination with a 20 μm aperture is used for the

image acquisition. The images are acquired with an in-lens detector at a working distance (WD) of 7.5 mm in order to minimize the topographic contrast by gathering low energy electrons, providing a good signal/noise ratio.

The force-strain response obtained from Macro-DIC is used to decide the force values at which HRDIC is performed. Hence both in-situ uniaxial and equibiaxial tests with SEM can be monitored at the same equivalent strains. SEM images are taken at 2500x magnification with a resolution of 3072×2304 pixels (the FOV is 41×30.8 μm^2) at the center of the cruciform after reaching global equivalent strains of 2%, 6%, 10% and 14%. The total FOV consists of 4, slightly overlapping, images (2 x 2 grid) that cover an area of 78x55 μm2. The HRDIC data is analyzed with Ncorr [118], using a subset radius of 15 pixels, 0 subset spacing and a strain radius of 3 pixels. These settings give a virtual strain gauge (VSG) of 1 pixel according to Ref. [240].

Thermal drifts and lens distortions in SEM imaging have been found to cause pseudo-strains in SEM DIC studies, methods for removing these artifacts and obtaining reliable strain magnitudes have been suggested [241-246]. In order to investigate the drift distortions under the conditions of the HRDIC measurements, tests using a G-1 Si calibration grid from Pelcotec™ are performed before the cruciform tests. Two SEM images with a 10 min time gap between them are captured and analyzed with Ncorr following the guide and parameters in Ref. [241]. The analysis shows an average equivalent pseudo-strain of 0.11% due to thermal drifts within a 10 min time gap. This magnitude of pseudo-strain is low compared to the strain concentrations that are observed due to slip (typically in the range of ~10-35%), and do not affect the qualitative characterization of the activated slip systems which is based on the inclination of the slip traces. Hence, correcting the strain magnitude for the present analysis is not crucial.

4.2.3 HRDIC strain maps under uniaxial and equibiaxial loading

Figure 4.8 shows the EBSD map of the initially random texture of the fully austenitic microstructure. Figure 4.8a shows the area for which HRDIC images are taken under uniaxial deformation and Figure 4.8b the area examined under biaxial deformation. The IPF maps are shown with respect to the loading direction (see the inset with the axes labels in Figure 4.8), i.e. along direction-2 under uniaxial loading and along direction-3 for equibiaxial (equibiaxial loading along directions-1 and -2 is equivalent with compression along direction-3). In both areas the grains are labeled to facilitate further discussion related to the deformation mechanism. Figure 4.9 and Figure 4.10 show the HRDIC maps obtained at 2%, 6%, 10% and 14% global strains under uniaxial and equibiaxial loads respectively. The above equivalent strain values correspond to respectively 355, 456, 543 and 624 MPa equivalent stress at the center of the cruciform, as calculated from the FE simulation of the corresponding load paths. Table 4.3 summarizes a relatively good agreement between the microscopic strain obtained from

averaging equivalent strain within the FOV of the HRDIC map and the macroscopic strain obtained from the Macro-DIC.
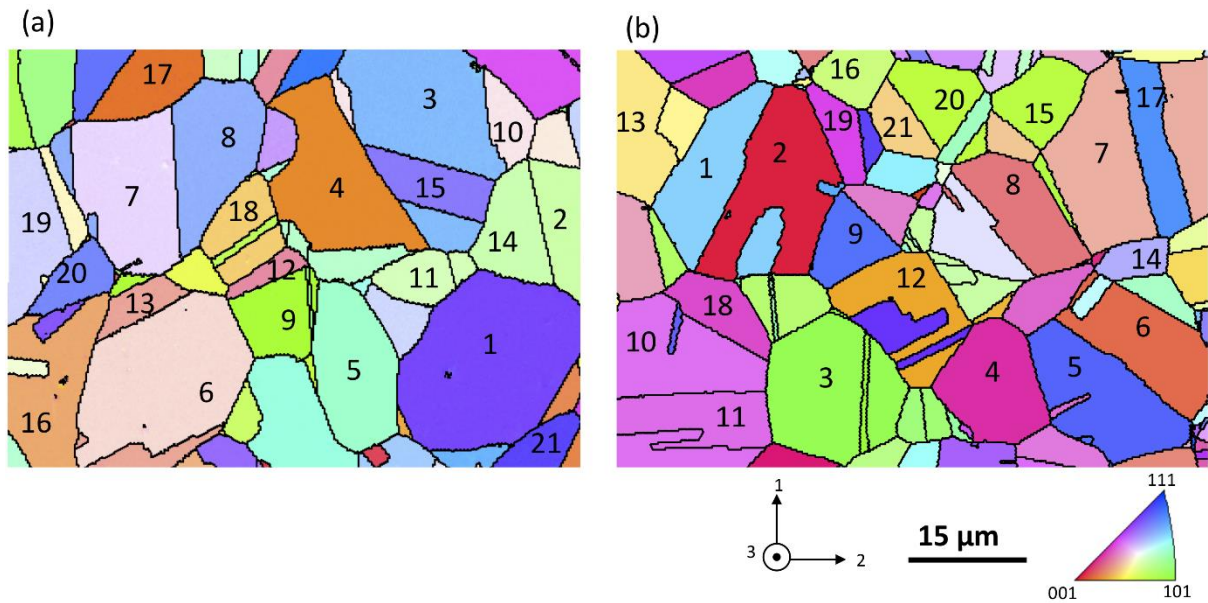
Figure 4.8 Inverse pole figure color maps parallel to the loading direction of the area of interest showing grains 1-21 for the samples under (a) uniaxial load (IPF direction-2) and (b) equibiaxial load (IPF direction-3).
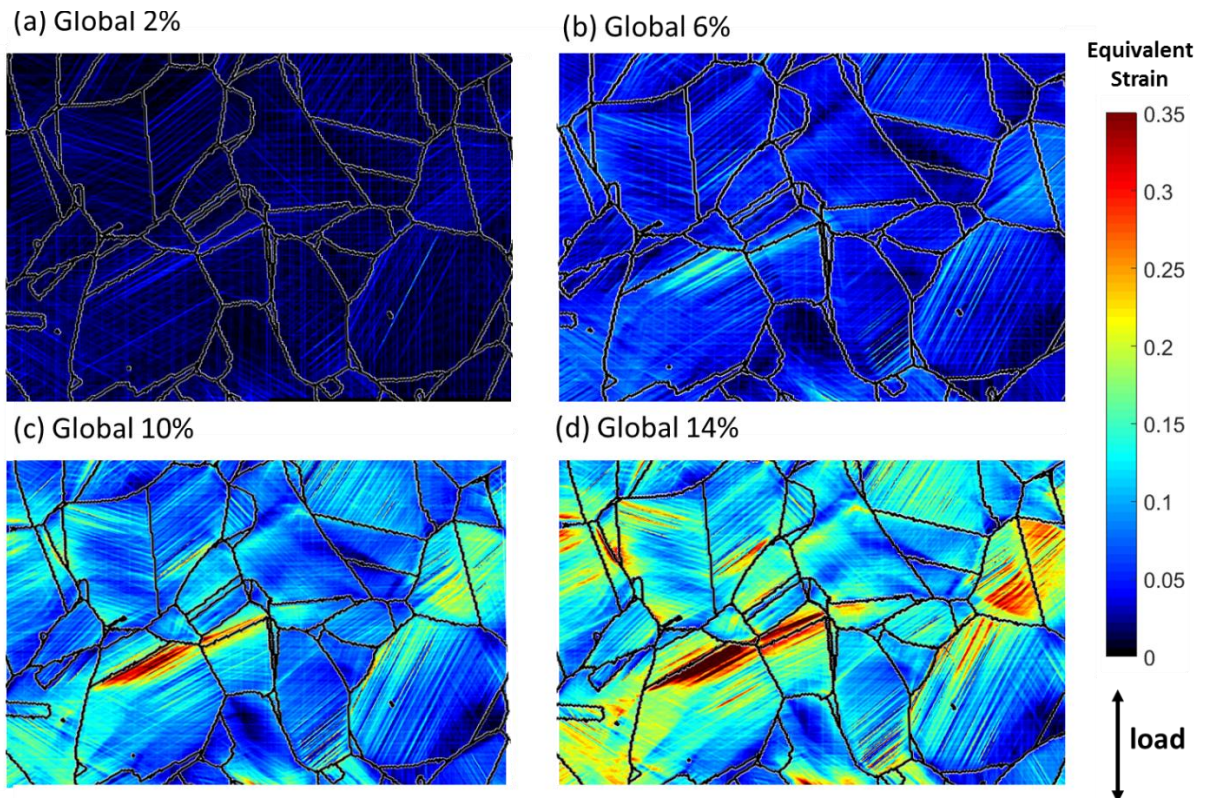
Figure 4.9 HRDIC maps showing the evolution of slip activity upon uniaxial deformation at equivalent strain (a) 2%, (b) 6%, (c) 10% and (d) 14% strain.
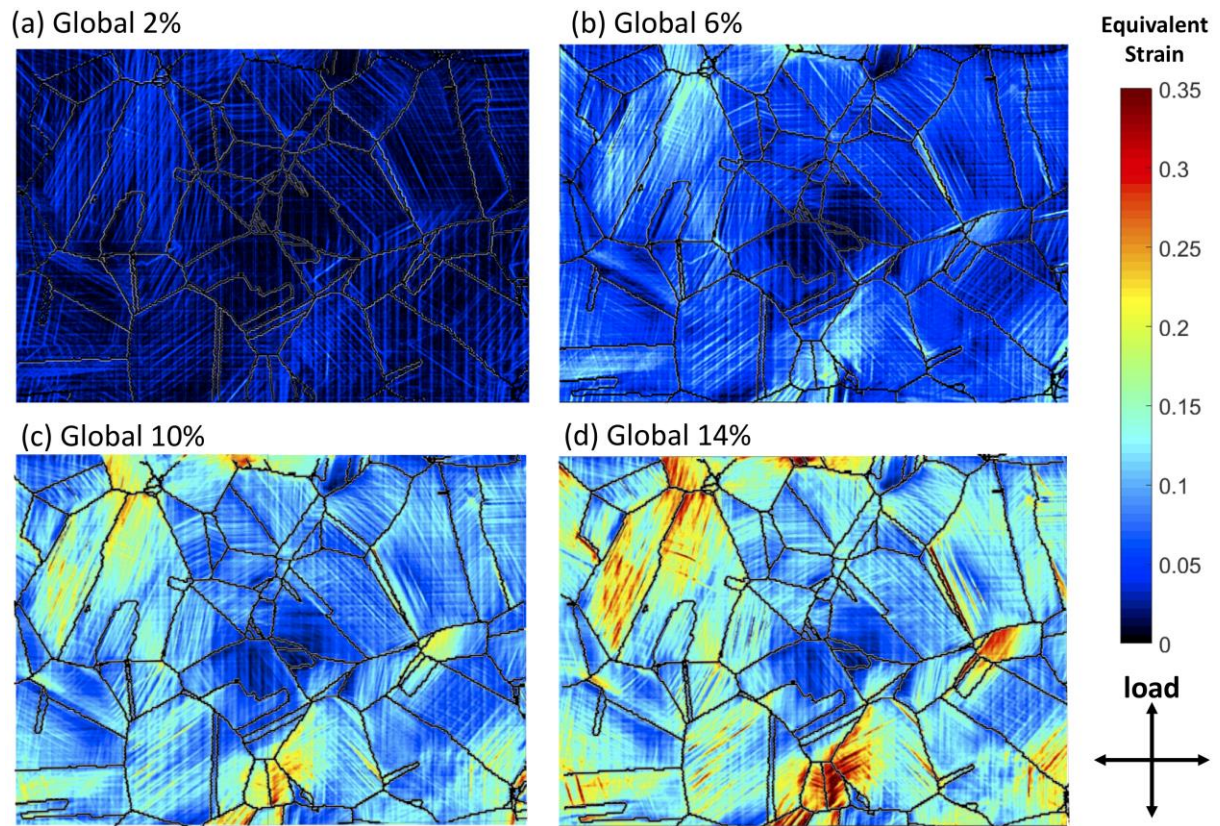
Figure 4.10 HRDIC maps showing the evolution of slip activity upon equibiaxial deformation at equivalent strain (a) 2%, (b) 6%, (c) 10% and (d) 14% equivalent strain.

Table 4.3 Comparison of the macroscopic equivalent strain (macroscopic DIC) and the equivalent strain averaged over the HRDIC field of view.

Equivalent strain (%)		
Global (Macro-DIC)	Uniaxial HRDIC	Equibiaxial HRDIC
2	1.6	2
6	4.8	5.8
10	9.5	9.8
14	13.8	13.1

4.2.4 Slip traces in HRDIC strain maps

The evolution of the plastic deformation within the FOV of HRDIC is evidenced by the increasing density and strain magnitude of the slip traces. Each grain exhibits its own slip traces with a characteristic trace inclination which corresponds to one of the possible {1 1 1} slip-plane traces. Table 4.4 and Table 4.5 list the observed slip traces, the corresponding Schmid factor and the equivalent macro strain at which each slip trace is observed for the first time for the grains marked in Figures 4.8a and 4.8b (uniaxial and equibiaxial loading respectively). Figure 4.11 shows an example of grain 1 under uniaxial loading for which the slip system (1 -1 1)[0 -1 -1] with the highest SF (0.3858)

is first observed at 2% global strain and the secondary slip system (1 1 1)[-1 1 0] becomes pronounced only after 10% global strain. In some grains slip traces of two systems are already present at 2% strain.

Table 4.4 List of activated {1 1 1} <1 1 0> systems and their Schmid Factor (SF) for each grain under uniaxial loading.

Grain	Activated	Rank of SF	Equivalent strain seen (%)
1	(1-11)[0-1-1]	1 (0.3858)	2
	(111)[-110]	2 (0.3630)	10
2	(-11 1)[01-1]	1 (0.4842)	2
3	(1-1 1)[-1-10]	1 (0.4263)	2
4	(111)[01-1]	1(0.471)	2
5	(-111)[01-1]	1(0.4472)	2
6	(1-11)[-1-10]	1(0.4942)	2
	(11-1)[1-10]	2(0.4331)	2
7	(-111)[01-1]	1(0.4821)	2
	(1-11)[0-1-1]	2(0.3934)	2
8	(111)[01-1]	1(0.4376)	2
9	(1-11)[0-1-1]	1(0.4501)	2
10	(1-11)[0-11]	1(0.4908)	2
11	(1-11)[0-1-1]	1(0.4879)	2
12	(1-11)[-1-10]	2(0.4493)	2
13	(1-11)[0-1-1]	1(0.4944)	2
	(-111)[01-1]	2(0.4597)	10
14	(-111)[01-1]	1(0.4842)	2
15	(-111)[110]	1(0.4207)	2
	(-1-11)[0-1-1]	2(0.3369)	10
16	(-1-11)[0-1-1]	1(0.4927)	2
	(111)[01-1]	2(0.4760)	2
17	(1-11)[-1-10]	1(0.4615)	2
	(111)[01-1]	2(0.3935)	6
	(-111)[01-1]	3(0.3837)	10
18	(-1-11)[1-10]	1(0.4979)	2
	(1-11)[-1-10]	2(0.4799)	2
19	(-111)[01-1]	1(0.4748)	2
20	(1-11)[10-1]	1(0.4088)	2
21	(111)[0-11]	2(0.3319)	2

Table 4.5 List of activated {111}<110> systems and their Schmid Factor (SF) for each grain under uniaxial loading.

Grain	Activated system	Rank of SF (value)	Equivalent strain seen (%)
1	(-1-11)[011]	1(0.4296)	2
	(111)[-101]	3(0.2208)	6
2	(-1-11)[101]	1(0.4300)	2
	(1-11)[-101]	2(0.4284)	2
3	(-1-11)[101]	1(0.4196)	2
4	(111)[-101]	1(0.4596)	2
	(-111)[101]	3(0.4235)	2
5	(-111)[101]	1(0.3650)	2
	(1-11)[011]	2(0.3003)	2
6	(-1-11)[101]	1(0.4653)	2
	(1-11)[-101]	2(0.4599)	2
7	(1-11)[-101]	2(0.4575)	2
8	(-111)[101]	1(0.4811)	2
	(111)[-101]	2(0.4608)	2
9	(111)[0-11]	1(0.3696)	2
10	(-111)[0-11]	1(0.4651)	2
	(-1-11)[011]	3(0.3838)	2
11	(-1-11)[011]	1(0.4659)	2
	(111)[-101]	2(0.4150)	2
12	(-111)[101]	1(0.4814)	2
13	(-111)[0-11]	2(0.4749)	2
14	(111)[-101]	1(0.4580)	2
15	(111)[-101]	1(0.4708)	2
	(-111)[101]	2(0.4649)	6
16	(-111)[101]	1(0.4873)	2
	(111)[-101]	2(0.4541)	2
17	(-1-11)[101]	1(0.3751)	2
18	(-111)[101]	1(0.4631)	2
	(111)[-101]	3(0.4039)	10
19	(111)[0-11]	1(0.4522)	2
20	(-111)[0-11]	1(0.4733)	2
	(-1-11)[011]	2(0.4695)	10
21	(111)[-101]	1(0.4991)	2
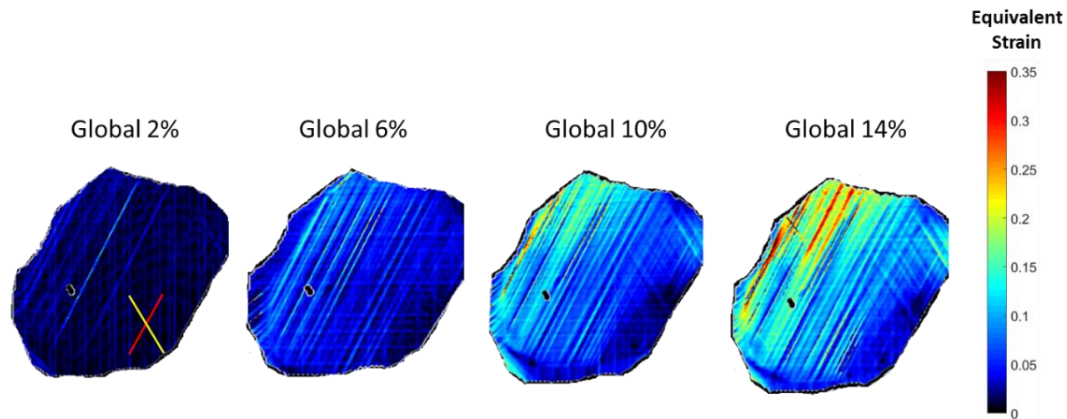
Figure 4.11 Grain 1 under uniaxial loading where the deformation changes from single slip to multiple activated slip systems with increasing strain. Superimposed are the {111} traces for the first highest (with red lines) and the second highest (with yellow lines) Schmid factor.

The Schmid law is mostly respected during uniaxial and equibiaxial loading as previously reported for uniaxial deformation on SS301 and SS304 [181, 184]. Figure 4.12 shows a statistical analysis of the obedience to the Schmid law. More than 80% of the grains in the field of view exhibit primary activated slip systems with the highest SFs for both load paths (see Figure 4.12a). Secondary or tertiary slip systems are observed in some grains; however, under equibiaxial loading multiple slip is observed in more grains than under uniaxial loading (see Figure 4.12b). Under uniaxial loading, the second and third slip system follow the Schmid ranking (see Figure 4.12c), e.g. in grain 6 under uniaxial loading, two slip systems are observed: (1 -1 1) [-1 -1 0] with the highest SF (0.4942) and (1 1 -1) [1 -1 0] with the second highest SF (0.4331). Under equibiaxial load there are however a few grains for which this ranking is not followed as for instance grains 1, 4, 10 and 18 (see Table 4.4 for details on the ranking). It should be noted that in the present analysis, grain interactions which can locally alter the stress state and activate other slip systems are neglected. Therefore, the behavior of the grains is described in terms of the Schmid law with respect to the macroscopic stress state.

Equibiaxial load is found to enhance the activation of multiple slip systems at the same equivalent strain as uniaxial load. Nearly 57% of the grains contain secondary or tertiary slip systems when subjected to equibiaxial load, whereas, under uniaxial loading, only 38% of the grains exhibit multiple slip systems (see Figure 4.12b). This result is in good agreement with a previous study of 304L austenitic stainless steel, where 10 out of 26 studied grains (38%) exhibit multiple slip system under uniaxial tension [181]. The 304 steel studied here is known to partially transform into martensite at equivalent strains larger than 20% [91]. It has been observed that the transformation occurs earlier under equibiaxial deformation than under uniaxial [91]. The activation of more slip systems suggests the existence of more shear band intercepts during equibiaxial deformation, hence providing more nucleation sites for martensite [16, 92, 209]. The present study supports well this explanation and shows that in-situ HRDIC provides statistically relevant information at the grain level for the observed difference in the martensite formation under uniaxial and equibiaxial loading at large strains. Further

quantitative investigation of the deformation-induced martensite and of the dominant deformation mechanisms under different load paths is the scope of another study.
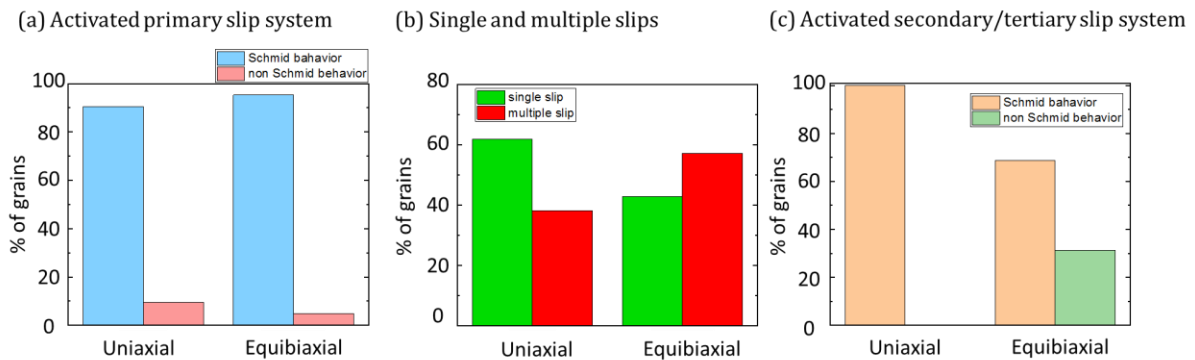
Figure 4.12 Statistical analysis showing (a) the fraction of grains obeying the Schmid law for the activation of the primary slip system, (b) the fraction of grains in which single or multiple slip system activation occurs and (c) the fraction of grains obeying the Schmid law for the activation of the secondary/tertiary slip systems, under uniaxial and equibiaxial loading.

4.2.5 Summary

A miniaturized biaxial cruciform geometry is presented that allows combining HRDIC in-situ during uniaxial and biaxial deformation. Utilizing electrochemical micromachining for preparing the sample geometry offers:

1. Thickness reduction at the center of the cruciform and concentration of uniform deformation at the center.
2. Excellent surface quality allowing EBSD characterization and HRDIC studies after deposition of gold particles.

The experimental mechanical results are in good agreement with FE simulations, allowing for estimating the stress values at the center of the cruciform sample for the strain values at which HRDIC was performed. Application of this new geometry combined with HRDIC on SS304 shows that after yielding, the activated {1 1 1} <1 1 0> slip systems are in good agreement with the Schmid law for the majority of the grains. For similar equivalent strain values, equibiaxial loading activates more slip systems compared to uniaxial loading, which according to the martensite nucleation theory would increase deformation-induced martensite nucleation sites.

4.3 The interplay between deformation mechanisms in SS304 during uniaxial and equibiaxial loading.

This chapter is adapted from the published paper:

"The interplay between deformation mechanisms in austenitic 304 steel during uniaxial and equibiaxial loading"

Efthymios Polatidis, Miroslav Šmíd, Wei-Neng Hsu, Monika Kubenova, Jan Capek, Tobias Panzner and Helena Van Swygenhoven

Abstract

The preferred deformation mechanisms with respect to the load path are studied in a medium stacking fault energy 304 austenitic stainless steel that exhibits both transformation-induced plasticity and twinning induced plasticity. In situ neutron diffraction and post-mortem EBSD show that the transformation from γ-austenite to α'-martensite is facilitated by equibiaxial loading rather than uniaxial loading. The results are discussed with respect to the evolving crystallographic texture, the presence of deformation twins and martensite under different load paths. The evolving crystallographic texture under uniaxial loading favors the deformation twinning and delays the martensitic transformation. In contrast, under equibiaxial loading the strain is accommodated by slip along multiple slip planes, which provide nucleation sites for martensitic transformation. It is found that the preferred deformation mechanism is not only an inherent property related to the stacking fault energy, but it also greatly depends on the load path and the deformation texture.

In this work, the contributions from the doctoral candidate are:

- Optimized the large cruciform geometry using FE simulations
- Wrote the proposals for the neutron diffraction beam times
- Performed the in-situ neutron diffraction measurements with Dr. Polatidis and Dr. Panzner
- Analyzed the neutron diffraction data and summarized the results
- Revised and edited the draft of the paper (first draft written by Dr. Polatidis)

4.3.1 Introduction

Contradicting reports have been published on the influence of the loading state on the martensitic transformation. Some studies reported that uniaxial loading facilitates the deformation-induced martensitic transformation [100, 219], others showed that the martensitic transformation is favored under biaxial loading [91, 96]. The loading state has been taken into account in martensite kinetic models by scalar variables [219, 221]. A more recent physically-driven model implemented in a elasto-plastic framework accounts for the effect of load path by modeling the splitting of the Shockley partial dislocations (SPDs) as a precursor for phase transformations [247]. However, the above mentioned kinetic models neglect the interaction of several co-existing deformation mechanisms, such as transformation induced plasticity (TRIP) and/or twinning induced plasticity (TWIP), and assume a single deformation mechanism regardless the load path (i.e. only martensitic transformation).

The stacking fault energy (SFE) of an austenitic stainless steel strongly influences the preferred deformation mechanisms [230]. It has been generally observed that with increasing SFE, deformation mechanisms gradually change from martensitic phase transformations (TRIP) [100, 210, 231] to mechanical twinning (TWIP) [212, 231] and plasticity by dislocation slip [231].

The effect of uniaxial/biaxial loading on the martensitic transformation of a low SFE was studied by in-situ neutron diffraction [100]. It was shown that uniaxial loading favors the martensitic transformation following the sequence $\gamma \rightarrow \varepsilon \rightarrow \alpha'$, where at low strains ε- martensite is the precursor of α'. During equibiaxial-loading however, the evolving texture suppresses the formation of ε-martensite and considerably less α'-martensite is observed at high strains. It was shown that the grains containing martensite belong to orientations for which the leading partial dislocation (LPD) has a higher Schmid factor than the trailing partial dislocation (TPD). The martensitic transformation is suppressed during equibiaxial loading as a consequence of the different textures formed during deformation.

In materials with higher SFE, for which nucleation and growth of twins is observed [224, 248], several models have been proposed for the nucleation of twins as a result of dislocation interactions [249-251]. As the growth of twins is described by the glide of Shockley partial dislocations (SPD)s, the precursor for twin growth is the separation of the SPDs under an external load [225, 252] and the difference in the stress between LPD and TPD has been also applied to explain the growth of twins [253].

Some steels with appropriate compositions/SFEs exhibit a combination of TWIP/TRIP effects [231, 253-255]. It has been observed experimentally that twins form at lower strains than α'-martensite [253, 256, 257], and the intercepts of twins with other planar defects can act as nucleation sites for α'-martensite as the imposed strain increases [256]. A study on medium-Mn maraging steels [258]

reported the competition between twinning and martensite formation: large grains exhibited only twinning whereas smaller grains only the martensitic transformation.

The aim of this study is to compare the interplay of the deformation mechanisms in a non-textured austenitic SS304 with medium SFE under monotonic uniaxial and equibiaxial loading. The deformation mechanisms (TWIP and TRIP effects) are discussed with respect to the load path and the evolving crystallographic texture.

4.3.2 Experimental

A commercial 304 stainless steel with nominal composition of Fe18Cr8Ni (wt. %) in sheet form of 8 mm thickness was used for this study. The inverse pole figure (IPF) map along the normal direction (ND) in Figure 4.13 shows the initial microstructure exhibiting a relatively random crystallographic texture. The average grain size (excluding the annealing twins) is 35 μm. In situ neutron diffraction studies were carried out at the POLDI instrument of the Swiss neutron spallation source SINQ (Paul Scherrer Institute, Switzerland) using the biaxial deformation rig [100, 113]. Cruciform-shaped samples with the geometry proposed in [113] were employed for the equibiaxial tests.
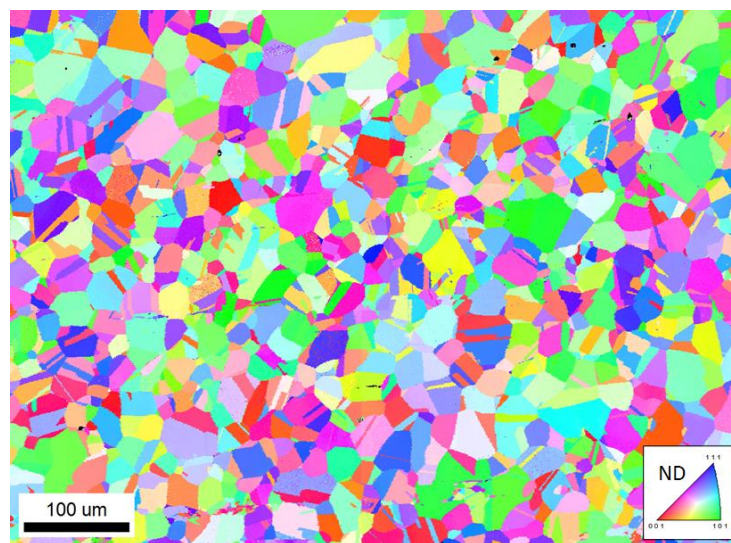
Figure 4.13 IPF map along the ND direction of the as-received 304 sheet.

For the uniaxial loading, dog-bone shaped samples with the geometry given in Ref. [105] were used. The biaxial deformation system is equipped with a 2-camera digital image correlation (DIC) system (GOM, Aramis 5M) for measuring the in-plane strain at the center of the cruciform sample. Uniaxial loading and equibiaxial loading were performed with a loading rate of 80 N/s. The uniaxial loading direction was parallel to the rolling direction of the sheet (RD), and the equibiaxial load was applied along the RD and the transverse direction (TD). The neutron diffraction measurements were carried out in predefined force intervals after interrupting the loading and holding the displacement. The maximum equivalent strain reached during the equibiaxial and uniaxial tests were ~28% and ~26%

respectively. For studying the uniaxial deformation under high strain, an additional dogbone sample was deformed up to 41.9% true strain with the uniaxial test rig of the POLDI instrument. The neutron diffraction data were reduced and fitted using the open source software Mantid [117].

EBSD studies were carried out on the as-received and on the deformed material by extracting samples from the center of the deformed cruciform and dogbone samples. The samples were ground with 1200 grit SiC paper and then electropolished for 12 s with a 16:3:1 (by volume) ethanol, glycerol and perchloric acid solution at 42 V. A field emission gun scanning electron microscope (FEG SEM) Zeiss ULTRA 55 equipped with EDAX Hikari Camera operated at 20 kV in high current mode with 120 μm aperture was used. The EBSD raw data was post-processed using the EDAX OIM Analysis 7.3 software.

High-resolution digital image correlation (HR-DIC) was performed in an SEM on miniaturized cruciform samples under uniaxial and equibiaxial load paths. A detailed description of the sample preparation, experimental and analysis of the HR-DIC data is given in ref. [165].

4.3.3 Martensitic transformation

The mechanical data from both uniaxial and equibiaxial load paths are given in Figure 4.14a and Figure 4.15a, the resulting force is calculated as $\sqrt{F_{axis\ 1}^2 + F_{axis\ 2}^2}$ from the corresponding force readings on the two axes of the Macrobiax device. The neutron data are collected while keeping the displacement fixed and letting the sample to relax, as shown by the red points on the force-strain curve. Martensite reflections do not appear in the neutron diffraction patterns during uniaxial deformation up to 25% strain, as shown in Figure 4.14b. By continuing straining the uniaxial loaded sample to 41.9% strain, α'-martensite appears at strains above approximately 25%. Figure 4.16 shows the increasing intensity of the $\{1\ 1\ 0\}_{\alpha'}$ as the strain increases. In contrast to uniaxial loading, new reflections corresponding to the α'-martensite phase, i.e. $\{1\ 1\ 0\}_{\alpha'}$ and $\{2\ 1\ 1\}_{\alpha'}$, appear already at approximately 16% of equivalent strain under equibiaxial loading, as shown in Figure 4.15b. The equibiaxial loading facilitates the formation of α'-martensite and the transformation is seen to occur from austenite directly to α'-martensite, i.e. $\gamma \to \alpha'$.
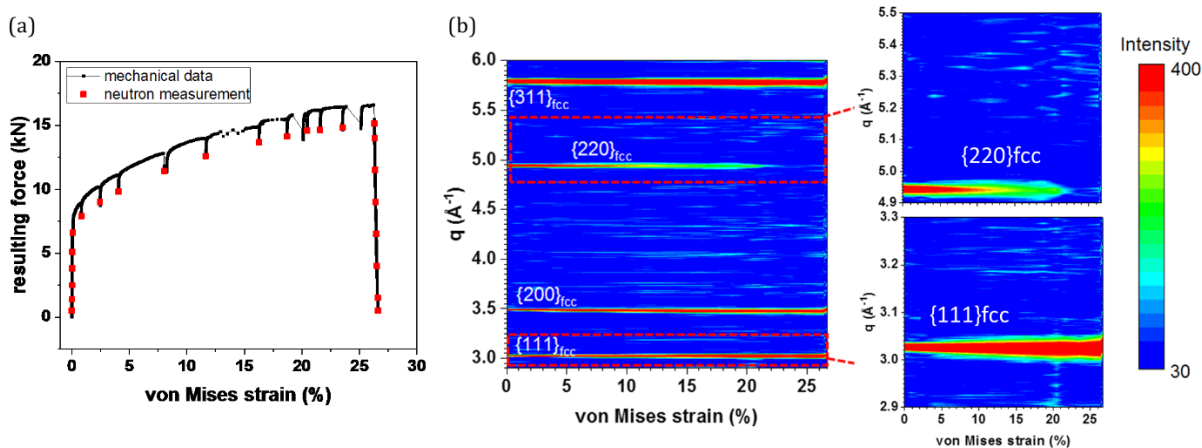
Figure 4.14 (a) Force-strain plot of uniaxial loading. The red points indicate the strain values at which neutron measurements were conducted. (b) The evolution of the neutron diffraction patterns with increasing strain. Parts of the q range are magnified showing no martensite formation under uniaxial loading up to 25% strain.
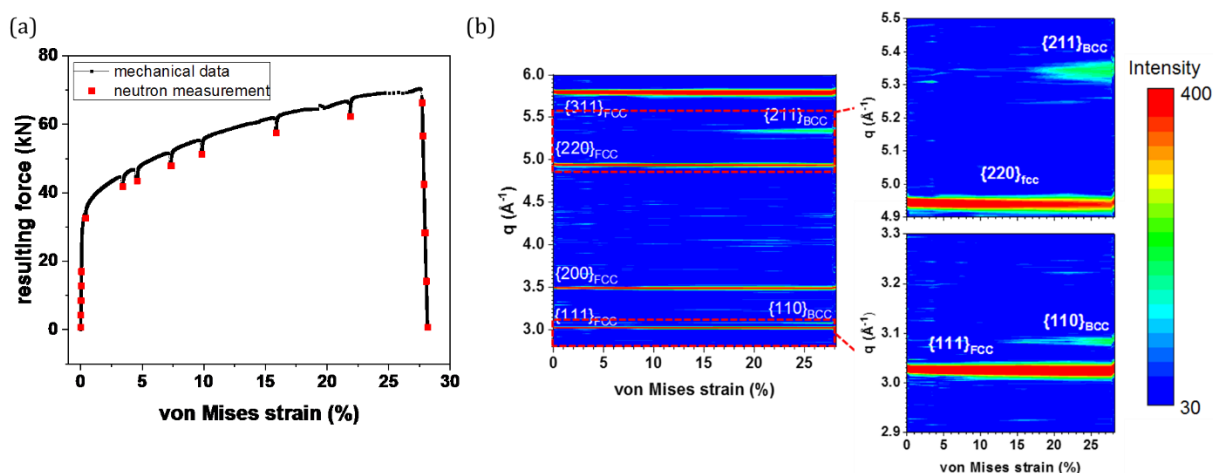
Figure 4.15 (a) Force-strain plot of equibiaxial loading. The red points indicate the strain values at which neutron measurements were conducted. (b) The evolution of the neutron diffraction patterns with increasing strain. Parts of the q range are magnified showing the appearance of martensite under equibiaxial loading at strain higher than 15%.
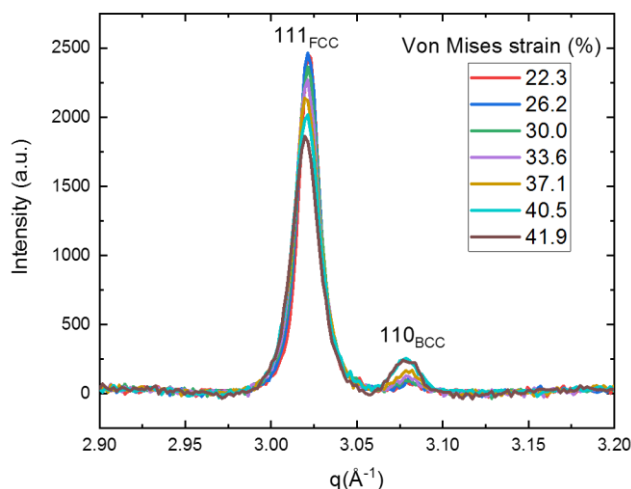
Figure 4.16 Sequence of neutron diffraction patterns under uniaxial loading (at strains from 22.3% to 41.9%) showing the increasing intensity of the {1 1 0} martensite reflection at higher strains.

120

4.3.4 Crystallographic texture

Different crystallographic textures develop during uniaxial and equibiaxial deformation [100]. The almost random crystallographic texture of the as-received material (Figure 4.17a) evolves to a strong <1 1 1>-texture along the loading direction (LD) that is parallel to RD during uniaxial loading, as shown in Figure 4.17b. The in-plane equibiaxial loading has the same normalized strain tensor as uniaxial compression along ND [113] and it results in the typical <1 1 0>-texture along the out-of-plane direction (Figure 4.17c) [100, 234, 259, 260].
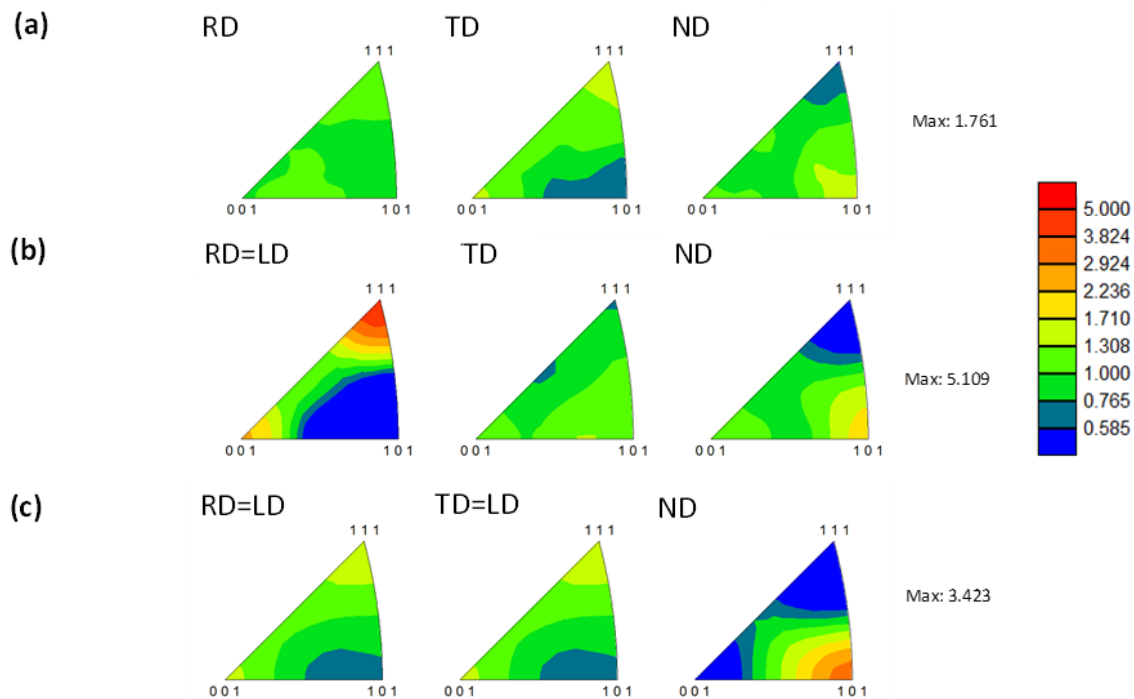
Figure 4.17 IPFs along the 3 principal sample directions showing (a) the relatively random orientation of the initial state of the material and the deformation textures after (b) uniaxial (c) equibiaxial loading.

Figure 4.18 shows the grain orientation maps after uniaxial (the IPF is given along the loading direction) and equibiaxial loading (the IPF is given along ND in compression, which is equivalent to in-plane equibiaxial tension). The austenite grains with crystallographic orientations for which the LDPs experience higher stress than the TDPs i.e. the splitting distance between the partials increases, are colored blue, while the rest of the orientations are colored red and α'-martensite is shown in yellow. It is observed that after uniaxial deformation (Figure 4.18a) most grains favor the splitting of the SPDs (most grains are blue), however a very small fraction of martensite forms and it appears in both the red and the blue grains. The low volume fraction of martensite under uniaxial loading explains why martensite is not detected by neutron diffraction before 30% strain is reached (shown in Figure 4.16). Under equibiaxial load, the majority of α'-martensite forms in the grains which do not favor the splitting of the SPDs (red grains) as shown in Figure 4.18b. The difference in martensitic transformation between uniaxial and biaxial deformation in this medium SFE material cannot be

explained by the difference in stress experienced by LPT and TPD, as was the case for the low SFE material where ε-martensite was formed upon deformation [100].
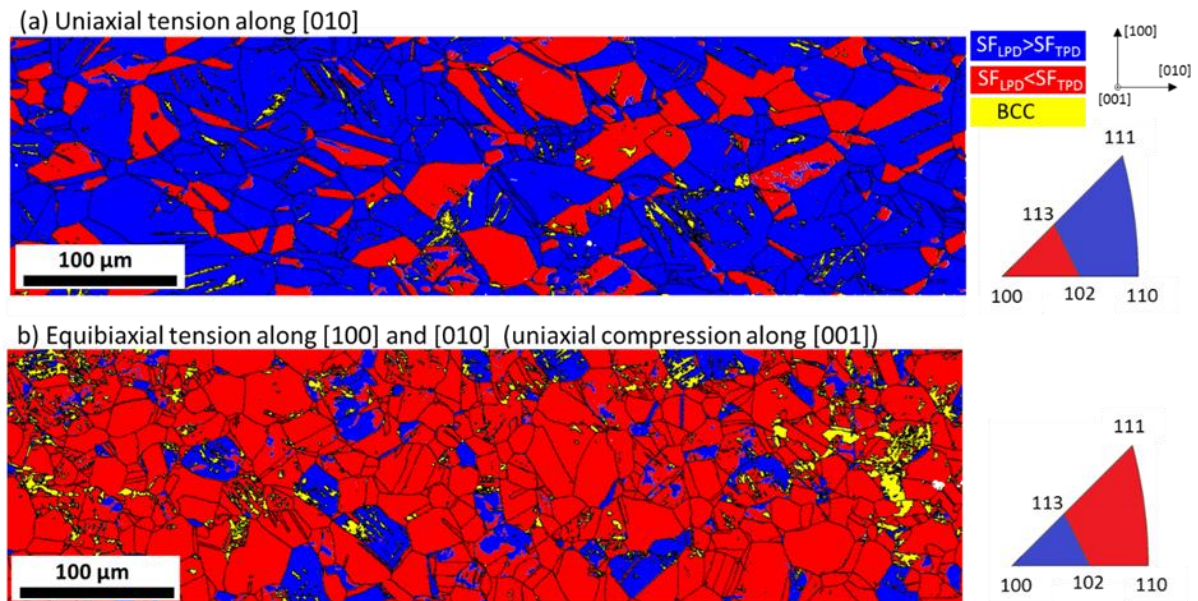
Figure 4.18 Post mortem EBSD maps, color-coded for showing austenite orientations that favor the splitting of the SPDs (blue) or not (red) and strain-induced α'-martensite (yellow) for the sample deformed a) uniaxially in the direction parallel to the rolling direction, [0 1 0], and b) equibiaxially (equivalent to compression in the ND, i.e. [0 0 1] direction). The IPF triangles show which orientation favor splitting of the SPDs under uniaxial and equibiaxial loading.

4.3.5 Deformation twinning

Twinning, as another possible deformation mechanism in medium SFE steels, is also influenced by the stresses experienced by the SPDs. In the EBSD map shown in Figure 4.19a, grains favorably oriented for splitting of the SPDs under uniaxial loading are marked as A, B, C, D. The orientation of these grains is given in Figure 4.19b. Twins are in these grains. For instance in grain D, a characteristic misorientation of 60° relative to the parent grain is measured along the dashed line shown in Figure 4.19c. Figure 4.20 shows a similar analysis for a grain favorably oriented for twinning in the sample deformed under equibiaxial loading. The EBSD map (Figure 4.20a) collected at high magnification shows several twins in grain (E); martensite is given in yellow. As these maps (Figure 4.19 and Figure 4.20) are taken after deformation, a significant gradient in orientation is seen within each grain. The orientation distribution of the chosen grains given in Figure 4.19b and Figure 4.20b, is however within the range of favorable orientation for twinning in both loading cases.
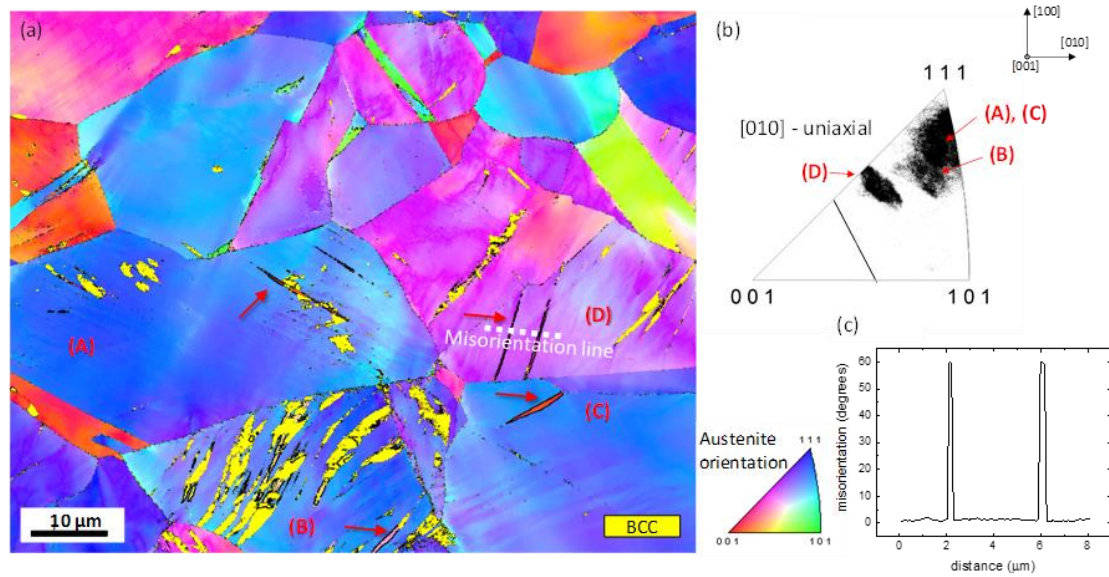
Figure 4.19 Detailed IPF map of austenite in the direction parallel to the loading direction [010], showing grains (labelled A, B, C, D) with deformation twins (shown with red arrows). The orientation distribution of these grains is shown in (b). (c) Misorientation plot along the line drawn in (a). The yellow subgrains in grains (A), (B) and (D) are martensite. The yellow color does not represent the grain orientation of BCC martensite.
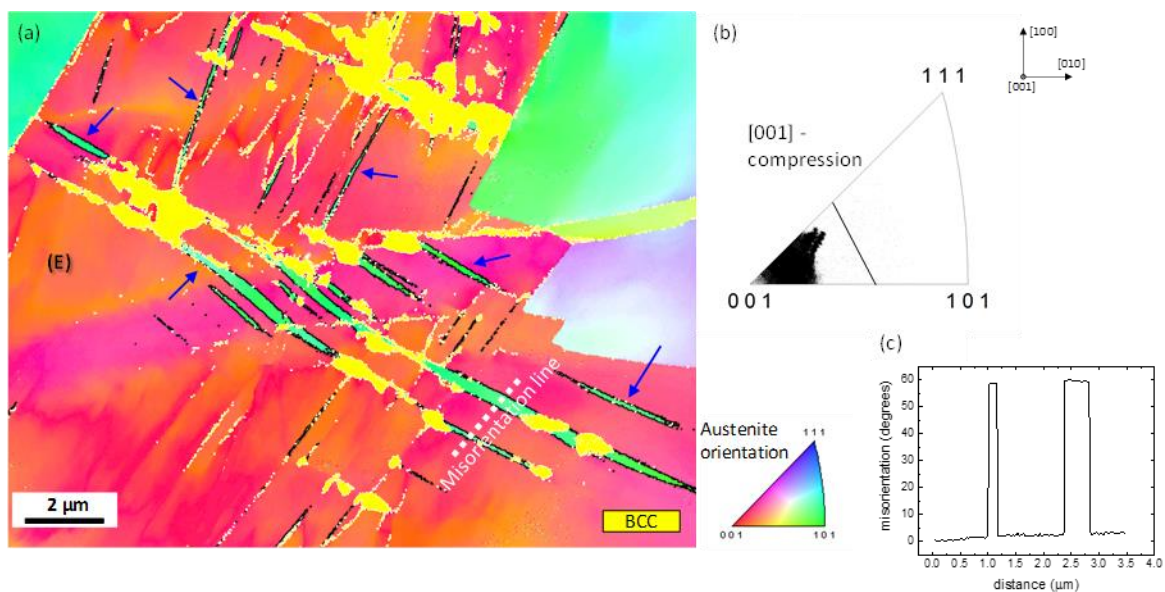
Figure 4.20 Detailed IPF map in the direction perpendicular to the sample surface [001], showing a grain with deformation twins (twins indicated with blue arrows) under equibiaxial loading. The orientation distribution of grain (E) is shown in (b). (c) Misorientation plot along the line drawn in (a). The yellow subgrains in grain (E) are martensite. The yellow color does not represent the grain orientation of BCC martensite.

The majority of the grains in the sample deformed under uniaxial loading favor the formation of deformation twins. Some grains with both favorable and non-favorable orientations for twinning contain martensite showing that the deformation twinning does not suppress the formation of martensite but rather retards it. Figure 4.19a illustrates that α'-martensite can form at twin boundaries and/or intercepts with other planar defects, such martensite is seen in grains (A) and (B).

In Section 4.2 we demonstrated that HRDIC can distinguish the slip activities under uniaxial and equibiaxial loading. A more detailed examination of the crystallographic orientations of the grains within the field of view presented Section 4.2 shows that the activation of slip in multiple slip planes is observed more frequently in the grains that do not favor twinning than those favorably oriented for twinning. In contrast, the grains with crystallographic orientations favorable for twinning, exhibit mostly slip on a single plane. Figure 4.21a shows a grain, favorably orientated for splitting of the SPDs (favorable for twinning), where only one slip system is activated under uniaxial loading; Figure 4.21b shows a grain, non-favorably orientated for splitting of the SPDs, where two slip systems are activated under uniaxial loading. The statistical analysis of the slip behavior under both uniaxial and equibiaxial loading is plotted in Figure 4.21c for grains favorably and non-favorably for twinning. This result suggests that twinning suppresses the activation of slip on secondary slip planes, thus it suppresses the formation of shear band intercepts which are potential nucleation sites for martensite. The above-explained theory is valid for approximately 60 - 65% of the grains, whereas the observed discrepancy for the rest of the grains can be explained as follows. At the strain level (14% macroscopic strain) reached in [165], grain interactions and grain rotations can cause local stress variations so that the local stress state may not coincide with the macroscopically applied load [261]. This can locally affect the activation/suppression of secondary planes for slip.
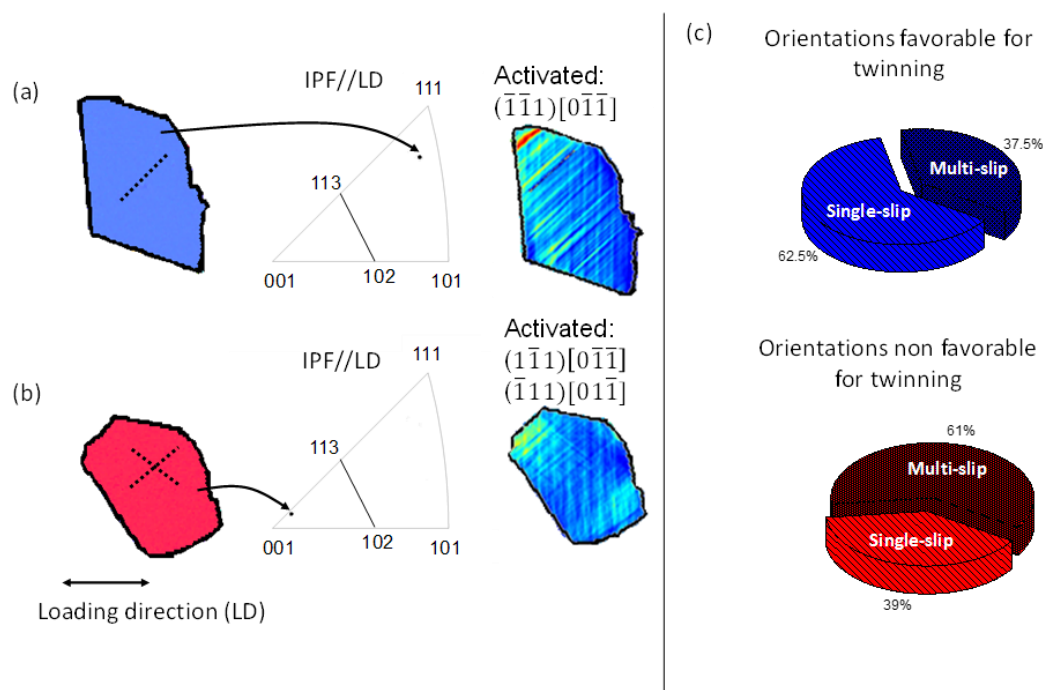
Figure 4.21 (a) Example of a grain with favorable orientation (before loading) for twinning (via splitting of the PDs) under uniaxial loading exhibiting single slip system in the HRDIC map. (b) Example of a grain with a non-favorable orientation for twinning under uniaxial loading exhibiting two slip systems in the HRDIC map. The IPFs in (a) and (b) are given along the loading direction. (c) Statistical analysis (including the grains deformed under both uniaxial and equibiaxial loading) showing that more grains non-favorably orientated for splitting of the PDs (red grains in Figure 4.18) exhibit multi-slip, whereas favorably-oriented grains exhibit predominantly slip along only one slip plane (blue grains in Figure 4.18).

124

4.3.6 Deformation mechanisms under uniaxial and equibiaxial loading

The metastable austenitic 304 stainless steel was studied under uniaxial and equibiaxial load paths in situ with neutron diffraction. Equibiaxial loading facilitates the martensitic transformation following a direct path of γ-austenite to α'-martensite, whereas under uniaxial deformation the phase transformation is delayed. The sequence of the deformation mechanism are schematically summarized in Figure 4.22. Under both strain paths, the deformation starts with single slip but after enough straining a <1 1 1> texture is formed under uniaxial deformation whereas a <1 1 0> texture under equibiaxial deformation. Under an evolving <1 1 1> texture, the majority of the grains become favorably oriented for splitting of the partial dislocations and extended stacking faults and mechanical twinning form (steps 2-3), restricting the activation of second slip systems. The lack of intersections of slip systems, which can serve as potential nucleation sites for α'-martensite form, retards the phase transformation. Under biaxial loading, the forming <1 1 0> texture does not result in grain orientations that favor twinning, therefore multiple slip starts allowing an early formation of α'-martensite at the slip intersections (steps 2-3).   These results suggest that the TRIP/TWIP effects are not only dependent on the SFE, but they can be favored/suppressed under specific combinations of load path/crystallographic texture.
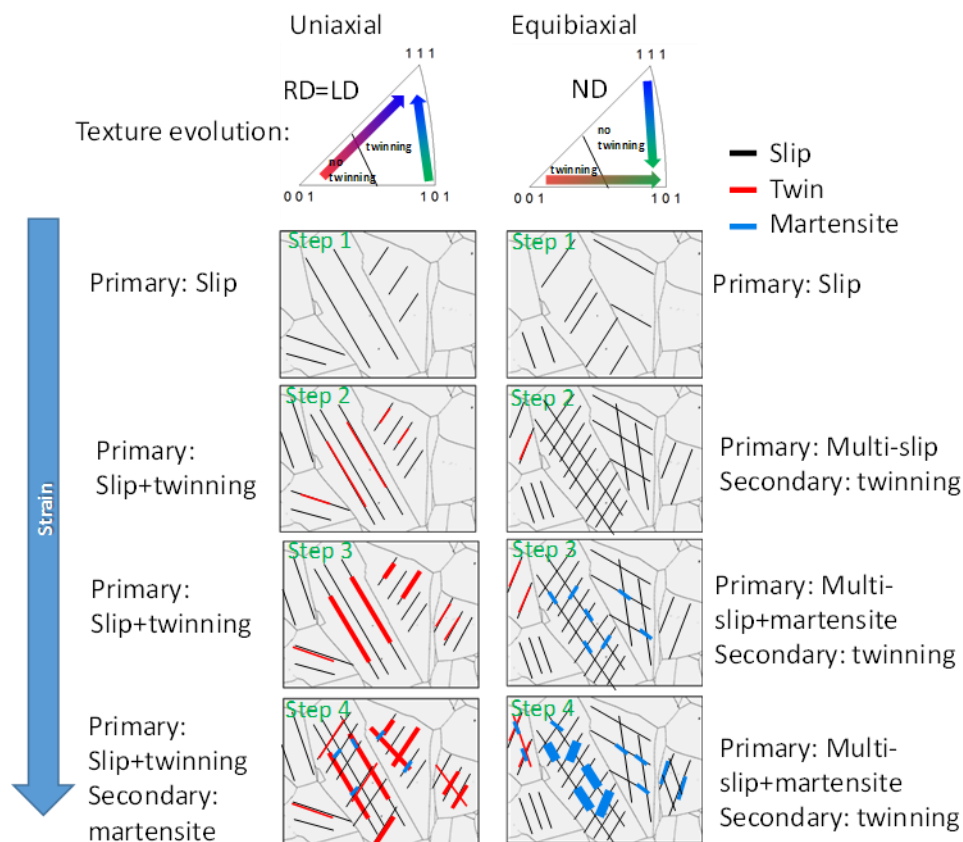
Figure 4.22 The proposed sequence of the dominant deformation mechanisms under uniaxial and equibiaxial loading with increasing the applied strain.

Chapter 5 Conclusion and outlook

5.1 Discussion and conclusion

Martensitic transformations induced by multiaxial loadings in NiTi alloys and austenitic steels have been studied by combining cruciform multiaxial mechanical testing with in-situ HRDIC in SEM, in-situ X-ray and neutron diffraction. The link between the microstructural evolution the transformation behavior under multiaxial deformation has been established. The achieved results are summarized and discussed in this section.

Optimization of cruciform sample geometry

The cruciform geometry has been optimized for each material investigated, and a novel sample manufacturing process for small-scale cruciform has been developed. In order to reach sufficiently high stress/strain to induce martensitic transformation at the center of the small-scale cruciform, the center is gradually thinned down by a novel electrochemical micromachining (ECMM) process. After thinning down the center, the outer shape of the cruciform sample is cut with picosecond laser. The optimized geometry is capable of introducing the martensitic transformation at the center of cruciform under monotonic loadings (uniaxial and equibiaxial) as well as load path changes. Moreover, the ECMM process results in a well-polished surface, and it is ready for electron microscopy inspections such as EBSD without additional metallography sample preparation. Thus the initial microstructure before deformation can be obtained, and it serves as an essential information for the trace analysis with HRDIC data.

Nanostructured superelastic NiTi under multiaxial loading

This study shows that the austenite microstructure consists of nanoscaled subgrains plays an important role in the transformation behavior and superelasticity. As revealed with HRDIC, bands of subgrains transform collectively to accommodate the strain, resulting in heterogeneous strain distribution within coarse grains. When changing the loading direction, different groups of subgrains transform into different martensite variants, as witnessed by HRDIC and XRD. The correlations between strain traces due to martensitic transformations and the bands/clusters of subgrains suggests the important role of this complex austenite microstructure for obtaining good superelasticity during one load-path-change cycle. The austenite microstructure composed of nanoscaled subgrains is able to accommodate the load path change by transforming into different martensite variants. Additionally, the nanoscaled subgrains can increase the yield strength of the austenite phase, thus ensuring the strain is accommodated by the reversible martensitic transformation instead of austenite slip.

Unfortunately, the superelasticity degrades upon mechanical cycling, which results in failure of stents in particular areas such as nodes between two struts. The degradation strongly depends on the load path. Multiaxial mechanical cycles degrade the superelasticity faster than uniaxial cycling in terms of the decrease in the critical transformation force and the accumulation of dislocations.

Equibiaxial cycling accumulates more dislocations than uniaxial cycling due to the strong crystallographic texture <1 1 1>//ND in the investigated material. In such crystallographic grain orientations, large strain under the in-plane equibiaxial load must be accommodated with both martensitic transformation and austenitic slip. On the other hand, under uniaxial cycling, the reversible martensitic transformation is able to accommodate the strain resulting in lower accumulation of dislocations than the equibiaxial cycling. This result suggests that tuning the microstructural texture to the design of the medical devices could offer a path for optimization. For a component which will experience an in-plane equibiaxial load, avoiding the <1 1 1>//ND crystallography could provide better cyclic stability in superelasticity.

The load-path-change cycles (triangular and square paths) result in more peak broadening than the monotonic cycling, suggesting higher accumulation of dislocations. In order to adapt to the load path change, the martensite formed during first loading path accommodates the strain by reorientation and/or plastic deformation, resulting in the formation of dislocations. The accumulation of the dislocations after load-path-change cycling retains both R-phase and B19' martensite. The load-path-change cycling results in a larger amount of retained martensite than the monotonic cycling. More importantly, different loading and unloading sequences result in different retained martensite variants as well as different peak broadening. These results underline the strong dependency of materials degradation on the load path.

Coarse-grained NiTi under uniaxial tension

Under uniaxial tension, the activation of different habit plane variants have been observed with HRDIC in the coarse-grained NiTi. After unloading, some of the strain-traces disappear (i.e. recoverable strain) while residual strain traces are also visible in the HRDIC map.

The recoverable strain corresponds to the reversible B19' martensitic transformation. In the majority of the investigated grains, the transformation follows the Schmid law with respect to the macroscopically applied uniaxial loading: the habit plane variant with the highest Schmid factor is activated upon loading. The appearance of non-Schmid variants is due to the high geometrical compatibility between two neighboring grains. When the angles between two habit planes and the angel between the shear directions of the two variants are small, a high geometrical compatibility is achieved, which favors the transmission of two variants across the grain boundary. Some traces are found to disagree with neither the macroscopic Schmid law nor the high geometrical compatibility,

suggesting the local stress state due to grain interactions in the polycrystalline microstructure plays a role on the martensitic variant selection.

One of the contributions to the non-recoverable strain traces is the austenite slip, as evidenced by the correlation found between trace inclinations and austenite slip systems. In addition, the uniaxial strain is also accommodated with {1 1 3} deformation twinning in the B19' martensite. The twin relationship is retained after the reverse transformation upon unloading, resulting in {1 1 2} deformation twins in the B2 austenite. Other mechanisms for the residual strain include the formation of dislocations at the interface between the austenite matrix and the martensite habit plane variant and residual martensite. The development of residual strain after only one cycle of uniaxial loading in the coarse-grained NiTi implies that the coarse-grained austenite microstructure is infeasible for good superelasticity.

Austenitic stainless steels

The results from the austenitic stainless steels show that the preferred deformation mechanism is not only determined by the stacking fault energy, but also greatly influenced by the crystallographic texture developed from the applied load path.

The observed transformation path in the SS201 with a low stacking fault energy is γ austenite – ε martensite – α' martensite, with the ε martensite being the precursor of α' martensite. Equibiaxial loading introduces a strong out-of-plane <1 0 1> deformation texture, in which the majority of the grain orientations does not favor the separation of the Shockley partial dislocations, thus suppressing the formation of ε martensite and delaying the subsequent transformation to α' martensite. On the other hand, with the deformation texture (<1 1 1> || loading direction) developed upon uniaxial loading, the separation of the Shockley partial dislocations is favored in most of the grains, thus facilitating the formation of ε martensite and eventually a large amount of α' martensite at higher strains.

With a medium stacking fault energy, the separation of Shockley partials result in deformation twinning instead of the ε martensitic transformation in SS304. The observed transformation path is from γ austenite directly to α' martensite. In SS304, uniaxial loading results in less α' martensitic than equibiaxial loading. The deformation texture introduced by uniaxial loading (<1 1 1> || loading direction) facilitates the separation of Shockley partials, formation of deformation twins in the majority of the grains. In this case, deformation twinning is the dominating deformation mechanism and delays α' martensitic transformation. The out-of-plane <1 0 1> texture developed during equibiaxial loading does not favor the deformation twinning. The majority of the grains accommodate the strain by dislocations slip. HRDIC shows that the activation of multiple slip systems is facilitated by equibiaxial loading. The interceptions of different slip systems serve as nucleation sites, allowing the formation of α' martensite.

Since the martensitic transformation can alter the mechanical behaviors of the materials, a better prediction for the mechanical response of TRIP steels could be achieved by taking into account the relationship between the stacking fault energy, the crystallographic texture and the load path.

5.2 Future developments

Our studies on NiTi alloys and austenitic stainless steels have shown the potential of combining the cruciform multiaxial mechanical testing with in-situ microstructure characterization techniques to capture the microstructural evolution of the phase transforming materials and identify the corresponded to the deformation mechanisms. The comprehensive experimental data of multiaxial deformation can serve for validating or further development of the constitutive models for phase transformation alloys. Some further works that could improve the interpretation of the results presented in this study are suggested below.

A new gold remodeling process for the HRDIC pattern on NiTi alloys

As reported in Section 2.5.3, the pre-oxidation step for improving the quality of the gold speckle pattern on NiTi surface resulted in the formation of the oxide layer that is prone to crack during mechanical testing. A new gold remodeling process proposed in [122] that minimizes the surface oxidation in the material and produces good pattern could serve as a solution to the issue of cracking observed in our experiments. With the application of such gold speckle pattern on the optimized thin-down geometry cruciform, HRDIC could be performed under load paths in addition to the uniaxial loading and the square path presented in Section 3.1. For the nanostructured NiTi, the strain maps obtained from equibiaxial loading and triangular load path change could provide more insights into the role of the austenite subgrains.

Multiaxial cycling on nanostructured NiTi combined with HRDIC

HRDIC could also be employed for studying the materials degradation introduced by mechanical cycling, by comparing the strain maps obtained during the first cycle with the maps obtained after several mechanical cycles. Correlating the HRDIC strain map with EBSD grain orientation map could reveal the interrelation between the residual strain accumulation and certain crystallographic orientation. For example, with HRDIC study, one could verify if the <1 1 1> oriented grains accumulate higher residual strains under equibiaxial loading, as proposed in Section 3.2.6. HRDIC data could also be used for verifying the mechanisms for the dislocation accumulation and retained martensite under different load-path-change cycles, as proposed in Section 3.2.7.

Equibiaxial loading and load path changes on coarse-grained NiTi

In Section 3.3, it is shown that in-situ HRDIC is able to capture the formation of martensitic variants within the grains. By performing HRDIC study on the coarse-grained NiTi under equibiaxial loading

and load path, one could investigate whether the martensitic variant selection under multiaxial deformation follows Schmid law. Besides, the effect of changing the load path on a single HPV formed during the first loading sequence could also be studied with HRDIC in the coarse-grained NiTi.

Load path changes on austenitic stainless steels

In Chapter 4, we have reported the path dependencies of the slip activity and the martensitic transformation under monotonic loading. As reported in Section 4.3, the interaction between different deformation mechanisms also shows a strong path dependency on the load path, a more complicated scenario may occur upon load path change. Since these materials often experience a sudden change in the load path during manufacturing, in-situ load-path-change experiments will provide valuable mechanical data and the corresponded microstructural evolutions for better understanding of the multiaxial deformation mechanisms. The HRDIC strain maps could show the effect of load path change on the slip systems activated during the prestrain. The in-situ diffraction techniques could provide the evolution of the martensite upon load path changes. The data could be exploited for the improvement of the existing constitutive models to include the complex interactions between different deformation mechanisms.

Physical kinetic model for martensitic transformation in SS304

In Section 4.3, we have shown the interplay between different deformation mechanisms including dislocations slip, deformation twinning and martensitic transformation. Our data would be valuable for the development of the kinetic model that takes into account other deformation mechanisms such as deformation twinning and dislocations in addition to the martensitic transformation.

Crystal plasticity study

As mentioned in Section 2.5.2, it is not possible to convert the applied forces into the local stress state in the cruciform sample directly. The crystal plasticity finite element simulation could be used to gain information about the local stresses at a grain level resulted from the complex sample geometry, anisotropy of the material and the grain-grain interaction. By implementing the microstructure of the field of view of the HRDIC map presented in Section 4.2 into crystal plasticity modeling, the simulation under different loading conditions could be helpful for interpreting the experimental data, for example the non-Schmid slip traces observed in SS304.

Bibliography

[1] B.C. De Cooman, Structure–properties relationship in TRIP steels containing carbide-free bainite, Current Opinion in Solid State and Materials Science 8(3–4) (2004) 285-303.

[2] W. Bleck, X. Guo, Y. Ma, The TRIP Effect and Its Application in Cold Formable Sheet Steels, Steel Research International 88(10) (2017) 1700218.

[3] S. Keeler, M. Kimchi, P.J. Mooney, Advanced High-Strength Steels Application Guidelines Version 6.0, 2017.

[4] Y. Furuya, H. Shimada, Shape memory actuators for robotic applications, Materials & Design 12(1) (1991) 21-28.

[5] Shape Memory Alloy Engineering: for Aerospace, Structural and Biomedical Applications, Elsevier2015.

[6] K. Otsuka, K. Shimizu, Pseudoelasticity and shape memory effects in alloys, International Metals Reviews 31(1) (1986) 93-114.

[7] S.A. Shabalovskaya, On the nature of the biocompatibility and on medical applications of NiTi shape memory and superelastic alloys, Bio-Medical Materials and Engineering 6(4) (1996) 267-289.

[8] T. Duerig, A. Pelton, D. Stöckel, An overview of nitinol medical applications, Materials Science and Engineering: A 273–275 (1999) 149-160.

[9] Cordis. https://emea.cordis.com/emea.html

[10] C.M. Wayman, H.K.D.H. Bhadeshia, CHAPTER 16 - PHASE TRANSFORMATIONS, NONDIFFUSIVE A2 - CAHN, Robert W, in: P. Haasen† (Ed.), Physical Metallurgy (Fourth, Revised and Enhanced Edition), North-Holland, Oxford, 1996, pp. 1507-1554.

[11] J.R. Patel, M. Cohen, Criterion for the action of applied stress in the martensitic transformation, Acta Metallurgica 1(5) (1953) 531-538.

[12] G.F. Bolling, R.H. Richman, The plastic deformation of ferromagnetic face-centred cubic Fe-Ni-C alloys, The Philosophical Magazine: A Journal of Theoretical Experimental and Applied Physics 19(158) (1969) 247-264.

[13] G.F. Bolling, R.H. Richman, The influence of stress on martensite-start temperatures in Fe-Ni-C alloys, Scripta Metallurgica 4(7) (1970) 539-543.

[14] G.F. Bolling, R.H. Richman, The plastic deformation-transformation of paramagnetic f.c.c. Fe–Ni–C alloys, Acta Metallurgica 18(6) (1970) 673-681.

[15] R.H. Richman, G.F. Bolling, Stress, Deformation, and Martensitic Transformation, Metallurgical Transactions 2(9) (1971) 2451-2462.

[16] G.B. Olson, M. Cohen, A mechanism for the strain-induced nucleation of martensitic transformations, Journal of the Less Common Metals 28(1) (1972) 107-118.

[17] D. Fahr, Stress-Induced and Strain-Induced Formation of Martensite and Its Effects on Strengrh and Ductility of Metastable Austenitic Stainless Steels, Metallurgical Transactions 2(7) (1971) 1883-1892.

[18] P.C. Maxwell, A. Goldberg, J.C. Shyne, Stress-Assisted and Strain-Induced Martensites in Fe-Nl-C Alloys, Metallurgical Transactions 5(6) (1974) 1305-1318.

[19] G.B. Stachowiak, P.G. Mccormick, Shape Memory Behavior Associated with the R and Martensitic Transformations in a Niti Alloy, Acta Metallurgica 36(2) (1988) 291-297.

[20] H. Sitepu, Texture and structural refinement using neutron diffraction data from molybdite (MoO3) and calcite (CaCO3) powders and a Ni-rich Ni50.7Ti49.30 alloy, Powder Diffraction 24(4) (2012) 315-326.

[21] H. Sitepu, Use of Synchrotron Diffraction Data for Describing Crystal Structure and Crystallographic Phase Analysis of R-Phase NiTi Shape Memory Alloy, Textures and Microstructures 35(3-4) (2003) 185-195.

[22] Y. Kudoh, M. Tokonami, S. Miyazaki, K. Otsuka, Crystal structure of the martensite in Ti-49.2 at. %Ni alloy analyzed by the single crystal X-ray diffraction method, Acta Metallurgica 33(11) (1985) 2049-2056.

[23] Inorganic Crystal Structure Database – ICSD. https://www.fiz-karlsruhe.de/en/produkte-und-dienstleistungen/inorganic-crystal-structure-database-icsd (accessed 03.05.2019).

[24] K. Otsuka, T. Sawamura, K. Shimizu, Crystal structure and internal defects of equiatomic TiNi martensite, physica status solidi (a) 5(2) (1971) 457-470.

[25] K.M. Knowles, D.A. Smith, The crystallography of the martensitic transformation in equiatomic nickel-titanium, Acta Metallurgica 29(1) (1981) 101-110.

[26] S.P. Gupta, A.A. Johnson, Morphology and Crystallography of β′ Martensite in TiNi Alloys, Transactions of the Japan Institute of Metals 14(4) (1973) 292-302.

[27] O. Matsumoto, S. Miyazaki, K. Otsuka, H. Tamura, Crystallography of martensitic transformation in Ti⬜Ni single crystals, Acta Metallurgica 35(8) (1987) 2137-2144.

[28] K. Otsuka, X. Ren, Physical metallurgy of Ti–Ni-based shape memory alloys, Progress in Materials Science 50(5) (2005) 511-678.

[29] S. Miyazaki, K. Otsuka, Y. Suzuki, Transformation pseudoelasticity and deformation behavior in a Ti-50.6at%Ni alloy, Scripta Metallurgica 15(3) (1981) 287-292.

[30] S. Miyazaki, Y. Ohmi, K. Otsuka, Y. Suzuki, Characteristics of Deformation and Transformation Pseudoelasticity in Ti-Ni Alloys, Journal De Physique 43(Nc-4) (1982) 255-260.

[31] H. Warlimont, L. Delaey, R.V. Krishnan, H. Tas, Thermoelasticity, pseudoelasticity and the memory effects associated with martensitic transformations, Journal of Materials Science 9(9) (1974) 1545-1555.

[32] S. Miura, T. Mori, N. Nakanashi, Y. Murakami, S. Kachi, Study of superelasticity associated with the thermoelastic martensitic transformation in Au—Cd alloys, The Philosophical Magazine: A Journal of Theoretical Experimental and Applied Physics 34(3) (1976) 337-349.

[33] K.N. Melton, O. Mercier, The mechanical properties of NiTi-based shape memory alloys, Acta Metallurgica 29(2) (1981) 393-398.

[34] W. Tang, Thermodynamic study of the low-temperature phase B19′ and the martensitic transformation in near-equiatomic Ti-Ni shape memory alloys, Metallurgical and Materials Transactions A 28(3) (1997) 537-544.

[35] J. Zhang, W. Cai, X. Ren, K. Otsuka, M. Asai, The Nature of Reversible Change in Ms Temperatures of Ti-Ni Alloys with Alternating Aging, Materials Transactions, JIM 40(12) (1999) 1367-1375.

[36] S. Miyazaki, Y. Ohmi, K. Otsuka, Y. Suzuki, CHARACTERISTICS OF DEFORMATION AND TRANSFORMATION PSEUDOELASTICITY IN Ti-Ni ALLOYS, Journal de Physique Colloques 43(C4) (1982) C4-255-C4-260.

[37] R. Delville, B. Malard, J. Pilch, P. Sittner, D. Schryvers, Microstructure changes during non-conventional heat treatment of thin Ni-Ti wires by pulsed electric current studied by transmission electron microscopy, Acta Materialia 58(13) (2010) 4503-4515.

[38] A. Ahadi, Q.P. Sun, Stress-induced nanoscale phase transition in superelastic NiTi by in situ X-ray diffraction, Acta Materialia 90 (2015) 272-281.

[39] T. Waitz, T. Antretter, F.D. Fischer, N.K. Simha, H.P. Karnthaler, Size effects on the martensitic phase transformation of NiTi nanograins, Journal of the Mechanics and Physics of Solids 55(2) (2007) 419-444.

[40] W.-S. Ko, S.B. Maisel, B. Grabowski, J.B. Jeon, J. Neugebauer, Atomic scale processes of phase transformations in nanocrystalline NiTi shape-memory alloys, Acta Materialia 123 (2017) 90-101.

[41] K.N. Melton, O. Mercier, Fatigue of NITI thermoelastic martensites, Acta Metallurgica 27(1) (1979) 137-144.

[42] S. Miyazaki, T. Imai, Y. Igo, K. Otsuka, Effect of Cyclic Deformation on the Pseudoelasticity Characteristics of Ti-Ni Alloys, Metallurgical Transactions A 17(1) (1986) 115-120.

[43] K. Gall, H. Sehitoglu, Y.I. Chumlyakov, I.V. Kireeva, Pseudoelastic cyclic stress-strain response of over-aged single crystal Ti-50.8at%Ni, Scripta Materialia 40(1) (1998) 7-12.

[44] E. Polatidis, N. Zotov, E. Bischoff, E.J. Mittemeijer, The effect of cyclic tensile loading on the stress-induced transformation mechanism in superelastic NiTi alloys: an in-situ X-ray diffraction study, Scripta Materialia 100 (2015) 59-62.

[45] N. Zotov, M. Pfund, E. Polatidis, A.F. Mark, E.J. Mittemeijer, Change of transformation mechanism during pseudoelastic cycling of NiTi shape memory alloys, Materials Science and Engineering: A 682 (2017) 178-191.

[46] W.W. Schmahl, J. Khalil-Allafi, B. Hasse, M. Wagner, A. Heckmann, C. Somsen, Investigation of the phase evolution in a super-elastic NiTi shape memory alloy (50.7 at. %Ni) under extensional load with synchrotron radiation, Materials Science and Engineering: A 378(1-2) (2004) 81-85.

[47] E. Polatidis, N. Zotov, E.J. Mittemeijer, Stress-induced phase transformations in thermally cycled superelastic NiTi alloys: in situ X-ray diffraction studies, Powder Diffraction 30 (2015) S76-S82.

[48] P. Sedmak, P. Sittner, J. Pilch, C. Curfs, Instability of cyclic superelastic deformation of NiTi investigated by synchrotron X-ray diffraction, Acta Materialia 94 (2015) 257-270.

[49] K. Gall, H.J. Maier, Cyclic deformation mechanisms in precipitated NiTi shape memory alloys, Acta Materialia 50(18) (2002) 4643-4657.

[50] A.M. Condó, F.C. Lovey, J. Olbricht, C. Somsen, A. Yawny, Microstructural aspects related to pseudoelastic cycling in ultra fine grained Ni–Ti, Materials Science and Engineering: A 481-482 (2008) 138-141.

[51] J. Hurley, A.M. Ortega, J. Lechniak, K. Gall, H.J. Maier, Structural evolution during the cycling of NiTi shape memory alloys, Zeitschrift für Metallkunde 94(5) (2003) 547-552.

[52] A.R. Pelton, Nitinol Fatigue: A Review of Microstructures and Mechanisms, Journal of Materials Engineering and Performance 20(4) (2011) 613-617.

[53] A. Yawny, M. Sade, G. Eggeler, Pseudoelastic cycling of ultra-fine-grained NiTi shape-memory wires, Zeitschrift für Metallkunde 96(6) (2005) 608-618.

[54] D.M. Norfleet, P.M. Sarosi, S. Manchiraju, M.F.X. Wagner, M.D. Uchic, P.M. Anderson, M.J. Mills, Transformation-induced plasticity during pseudoelastic deformation in Ni–Ti microcrystals, Acta Materialia 57(12) (2009) 3549-3561.

[55] X. Ren, N. Miura, J. Zhang, K. Otsuka, K. Tanaka, M. Koiwa, T. Suzuki, Y.I. Chumlyakov, M. Asai, A comparative study of elastic constants of Ti–Ni-based alloys prior to martensitic transformation, Materials Science and Engineering: A 312(1) (2001) 196-206.

[56] T. Simon, A. Kröger, C. Somsen, A. Dlouhy, G. Eggeler, On the multiplication of dislocations during martensitic transformations in NiTi shape memory alloys, Acta Materialia 58(5) (2010) 1850-1860.

[57] M.L. Bowers, X. Chen, M. De Graef, P.M. Anderson, M.J. Mills, Characterization and modeling of defects generated in pseudoelastically deformed NiTi microcrystals, Scripta Materialia 78-79 (2014) 69-72.

[58] S. Miyazaki, K. Otsuka, Deformation and transition behavior associated with the R-phase in Ti-Ni alloys, Metallurgical Transactions A 17(1) (1986) 53-63.

[59] A. Condó, C. Somsen, J. Olbricht, G. Eggeler, A. Dlouhý, R-phase stabilization in ultra-fine grain NiTi wires after mechanical cycling, European Symposium on Martensitic Transformations (2009) 02006.

[60] X.B. Wang, B. Verlinden, J. Van Humbeeck, R-phase transformation in NiTi alloys, Materials Science and Technology 30(13) (2014) 1517-1529.

[61] J.A. Shaw, S. Kyriakides, Initiation and propagation of localized deformation in elasto-plastic strips under uniaxial tension, International Journal of Plasticity 13(10) (1997) 837-871.

[62] S. Daly, G. Ravichandran, K. Bhattacharya, Stress-induced martensitic phase transformation in thin sheets of Nitinol, Acta Materialia 55(10) (2007) 3593-3600.

[63] G. Murasawa, S. Yoneyama, T. Sakuma, Nucleation, bifurcation and propagation of local deformation arising in NiTi shape memory alloy, Smart Materials and Structures 16(1) (2007) 160-167.

[64] A. Schaefer, M.F.-X. Wagner, Strain mapping at propagating interfaces in pseudoelastic NiTi, European Symposium on Martensitic Transformations (2009) 06031.

[65] C. Großmann, A. Schäfer, M.F.X. Wagner, Finite Element Simulation of Localized Phase Transformations in Pseudoelastic NiTi Shape Memory Alloys Subjected to Multi-Axial Stress States, Proceeding of International Conference on Martensitic Transformations (ICOMAT) 2008, John Wiley & Sons, Inc., 2013, pp. 525-530.

[66] G.Z. Wang, F.Z. Xuan, S.T. Tu, Z.D. Wang, Effects of triaxial stress on martensite transformation, stress-strain and failure behavior in front of crack tips in shape memory alloy NiTi, Materials Science and Engineering: A 527(6) (2010) 1529-1536.

[67] C. Elibol, M.F.X. Wagner, Strain rate effects on the localization of the stress-induced martensitic transformation in pseudoelastic NiTi under uniaxial tension, compression and compression-shear, Materials Science and Engineering: A 643 (2015) 194-202.

[68] J.M. McNaney, V. Imbeni, Y. Jung, P. Papadopoulos, R.O. Ritchie, An experimental study of the superelastic effect in a shape-memory Nitinol alloy under biaxial loading, Mechanics of Materials 35(10) (2003) 969-986.

[69] T. Niendorf, J. Lackmann, B. Gorny, H.J. Maier, In situ characterization of martensite variant formation in nickel–titanium shape memory alloy under biaxial loading, Scripta Materialia 65(10) (2011) 915-918.

[70] R. Mehrabi, M.T. Andani, M. Kadkhodaei, M. Elahinia, Experimental Study of NiTi Thin-Walled Tubes Under Uniaxial Tension, Torsion, Proportional and Non-Proportional Loadings, Experimental Mechanics 55(6) (2015) 1151-1164.

[71] D. Song, G. Kang, Q. Kan, C. Yu, C. Zhang, Non-proportional multiaxial transformation ratchetting of super-elastic NiTi shape memory alloy: Experimental observations, Mechanics of Materials 70 (2014) 94-105.

[72] D. Song, G. Kang, Q. Kan, C. Yu, C. Zhang, Non-proportional multiaxial whole-life transformation ratchetting and fatigue failure of super-elastic NiTi shape memory alloy micro-tubes, International Journal of Fatigue 80 (2015) 372-380.

[73] H. Khodaei, P. Terriault, Experimental validation of shape memory material model implemented in commercial finite element software under multiaxial loading, Journal of Intelligent Material Systems and Structures 29(14) (2018) 2954-2965.

[74] I. Tamura, Deformation-Induced Martensitic-Transformation and Transformation-Induced Plasticity in Steels, Metal Science 16(5) (1982) 245-253.

[75] J. Mazur, Lattice Parameters of Martensite and of Austenite, Nature 166(4228) (1950) 828-828.

[76] O.D. Sherby, J. Wadsworth, D.R. Lesuer, C.K. Syn, Revisiting the Structure of Martensite in Iron-Carbon Steels, MATERIALS TRANSACTIONS 49(9) (2008) 2016-2027.

[77] G. Kurdjumow, G. Sachs, Über den Mechanismus der Stahlhärtung, Zeitschrift für Physik 64(5) (1930) 325-343.

[78] G. Wassermann, Einfluß der α-γ-Umwandlung eines irreversiblen Nickelstahls auf Kristallorientierung und Zugfestigkeit, Archiv für das Eisenhüttenwesen 6(8) (1933) 347-351.

[79] Z. Nishiyama, X-ray investigation of the mechanism of the transformation from face centered cubic lattice to body centered cubic, Sci. Rep. Tohoku Univ. 23 (1934) 637.

[80] J.A. Venables, The martensite transformation in stainless steel, The Philosophical Magazine: A Journal of Theoretical Experimental and Applied Physics 7(73) (1962) 35-44.

[81] J.W. Brooks, M.H. Loretto, R.E. Smallman, In situ observations of the formation of martensite in stainless steel, Acta Metallurgica 27(12) (1979) 1829-1838.

[82] S.M. Copley, B.H. Kear, The dependence of the width of a dissociated dislocation on dislocation velocity, Acta Metallurgica 16(2) (1968) 227-231.

[83] A.J. Bogers, W.G. Burgers, Partial dislocations on the {110} planes in the B.C.C. lattice and the transition of the F.C.C. into the B.C.C. lattice, Acta Metallurgica 12(2) (1964) 255-261.

[84] F. Lecroisey, A. Pineau, Martensitic transformations induced by plastic deformation in the Fe-Ni-Cr-C system, Metallurgical and Materials Transactions B 3(2) (1972) 391-400.

[85] A. Das, P.C. Chakraborti, S. Tarafder, H.K.D.H. Bhadeshia, Analysis of deformation induced martensitic transformation in stainless steels, Materials Science and Technology 27(1) (2011) 366-370.

[86] K. Nohara, Y. Ono, N. Ohashi, Composition and grain size dependencies of strain-induced martensitic transformation in metastable austenitic stainless steels, Tetsu-to-Hagane 63(5) (1977) 212-222.

[87] T. Angel, Formation of Martensite in Austenitic Stainless Steels, Journal of the Iron and Steel Institute 177 (1954) 165-174.

[88] G.L. Huang, D. Matlock, G. Krauss, Martensite formation, strain rate sensitivity, and deformation behavior of type 304 stainless steel sheet, Metallurgical Transactions A 20(7) (1989) 1239-1246.

[89] J. Talonen, H. Hänninen, P. Nenonen, G. Pape, Effect of strain rate on the strain-induced γ → α′-martensite transformation and mechanical properties of austenitic stainless steels, Metallurgical and Materials Transactions A 36(2) (2005) 421-432.

[90] J.A. Rodríguez-Martínez, R. Pesci, A. Rusinek, Experimental study on the martensitic transformation in AISI 304 steel sheets subjected to tension under wide ranges of strain rate at room temperature, Materials Science and Engineering: A 528(18) (2011) 5974-5982.

[91] S.S. Hecker, M.G. Stout, K.P. Staudhammer, J.L. Smith, Effects of Strain State and Strain Rate on Deformation-Induced Transformation in 304 Stainless-Steel .1. Magnetic Measurements and Mechanical-Behavior, Metallurgical Transactions A 13(4) (1982) 619-626.

[92] L.E. Murr, K.P. Staudhammer, S.S. Hecker, Effects of Strain State and Strain Rate on Deformation-Induced Transformation in 304 Stainless-Steel .2. Microstructural Study, Metallurgical Transactions A 13(4) (1982) 627-635.

[93] S. Nanga-Nyongha, Mechanical behaviour and martensitic transformations of two austenitic stainless steels: temperature, strain rate and loading effects, École Nationale Supérieure des Mines de Paris, 2008.

[94] A.M. Beese, Experimental investigation and constitutive modeling of the large deformation behavior of anisotropic steel sheets undergoing strain-induced phase transformation, Massachusetts Institute of Technology. Dept. of Mechanical Engineering., Massachusetts Institute of Technology, 2011.

[95] S. Chakrabarty, Deformation behavior of advanced high strength austenitic stainless steel, IIT Bombay, 2015.

[96] Y.H. Yan, G.Y. Kai, M.D. Jian, Transformation behavior of retained austenite under different deformation modes for low alloyed TRIP-assisted steels, Materials Science and Engineering: A 441(1-2) (2006) 331-335.

[97] V.V. Kosarchuk, L.V. Zaitseva, A.A. Lebedev, B.I. Koval'chuk, Effect of stressed state parameters on phase transformation kinetics in austenitic steels with plastic deformation, Strength of Materials 21(1) (1989) 60-64.

[98] D.L. Douglass, G. Thomas, W.R. Roser, Ordering, Stacking Faults and Stress Corrosion Cracking In Austenitic Alloys, CORROSION 20(1) (1964) 15t-28t.

[99] M. Moallemi, A. Kermanpur, A. Najafizadeh, A. Rezaee, H.S. Baghbadorani, P.D. Nezhadfar, Deformation-induced martensitic transformation in a 201 austenitic steel: The synergy of stacking fault energy and chemical driving force, Materials Science and Engineering: A 653 (2016) 147-152.

[100] E. Polatidis, W.N. Hsu, M. Šmíd, T. Panzner, S. Chakrabarty, P. Pant, H. Van Swygenhoven, Suppressed martensitic transformation under biaxial loading in low stacking fault energy metastable austenitic steels, Scripta Materialia 147 (2018) 27-32.

[101] A.E. Pontini, J.D. Hermida, X-Ray diffraction measurement of the stacking fault energy reduction induced by hydrogen in an AISI 304 steel, Scripta Materialia 37(11) (1997) 1831-1837.

[102] M.J. Whelan, Dislocation Interactions in Face-Centred Cubic Metals, with Particular Reference to Stainless Steel, The Proceedings of the Royal Society of London A 249(1256) (1959) 114-&.

[103] S. Van Petegem, A. Guitton, M. Dupraz, A. Bollhalder, K. Sofinowski, M.V. Upadhyay, H. Van Swygenhoven, A Miniaturized Biaxial Deformation Rig for in Situ Mechanical Testing, Experimental Mechanics 57(4) (2017) 569-580.

[104] A. Creuziger, M.A. Iadicola, T. Foecke, E. Rust, D. Banerjee, Insights into Cruciform Sample Design, JOM 69(5) (2017) 902-906.

[105] M.V. Upadhyay, T. Panzner, S. Van Petegem, H. Van Swygenhoven, Stresses and Strains in Cruciform Samples Deformed in Tension, Experimental Mechanics 57(6) (2017) 905-920.

[106] Superelasticity model in Abaqus. https://abaqus-docs.mit.edu/2017/English/SIMACAEMATRefMap/simamat-c-superelasticity.htm#simamat-c-superelasticity (accessed 25.04.2019).

[107] A. Matt, Designing sample geometry for biaxial loading using finite element modeling, École Polytechnique Fédérale de Lausanne, 2015.

[108] A. Guitton, A. Irastorza-Landa, R. Broennimann, D. Grolimund, S. Van Petegem, H. Van Swygenhoven, Picosecond pulsed laser for microscale sample preparation, Materials Letters 160 (2015) 589-591.

[109] K.P. Rajurkar, M.M. Sundaram, A.P. Malshe, Review of Electrochemical and Electrodischarge Machining, Procedia CIRP 6 (2013) 13-26.

[110] P.F. Chauvy, P. Hoffmann, D. Landolt, Electrochemical micromachining of titanium through a laser patterned oxide film, Electrochemical and Solid-State Letters 4(5) (2001) C31-C34.

[111] D. Landolt, P.F. Chauvy, O. Zinger, Electrochemical micromachining, polishing and surface structuring of metals: fundamental aspects and new developments, Electrochimica Acta 48(20-22) (2003) 3185-3201.

[112] A.C. West, C. Madore, M. Matlosz, D. Landolt, Shape Changes during through-Mask Electrochemical Micromachining of Thin Metal-Films, Journal of the Electrochemical Society 139(2) (1992) 499-506.

[113] S. Van Petegem, J. Wagner, T. Panzner, M.V. Upadhyay, T.T.T. Trang, H. Van Swygenhoven, In-situ neutron diffraction during biaxial deformation, Acta Materialia 105 (2016) 404-416.

[114] C. Gauss, I.R. Souza, M.J.R. Sandim, P.A. Suzuki, A.J. Ramirez, H.R.Z. Sandim, In situ synchrotron X-ray evaluation of strain-induced martensite in AISI 201 austenitic stainless steel during tensile testing, Materials Science and Engineering: A 651 (2016) 507-516.

[115] T. Roisnel, J. Rodríguez-Carvaja, WinPLOTR, A Graphic Tool for Powder Diffraction, Laboratoire Léon Brillouin-LCSI, France, 2005.

[116] H. Sitepu, Texture and structural refinement using neutron diffraction data from molybdite (MoO3) and calcite (CaCO3) powders and a Ni-rich Ni50.7Ti49.30 alloy, Powder Diffraction 24(4) (2009) 315-326.

[117] O. Arnold, J.C. Bilheux, J.M. Borreguero, A. Buts, S.I. Campbell, L. Chapon, M. Doucet, N. Draper, R. Ferraz Leal, M.A. Gigg, V.E. Lynch, A. Markvardsen, D.J. Mikkelson, R.L. Mikkelson, R. Miller, K. Palmen, P. Parker, G. Passos, T.G. Perring, P.F. Peterson, S. Ren, M.A. Reuter, A.T. Savici, J.W. Taylor, R.J. Taylor, R. Tolchenov, W. Zhou, J. Zikovsky, Mantid—Data analysis and visualization package for neutron scattering and µ SR experiments, Nuclear Instruments and Methods in Physics Research Section A: Accelerators, Spectrometers, Detectors and Associated Equipment 764 (2014) 156-166.

[118] J. Blaber, B. Adair, A. Antoniou, Ncorr: Open-Source 2D Digital Image Correlation Matlab Software, Experimental Mechanics 55(6) (2015) 1105-1122.

[119] F. Di Gioacchino, J. Quinta da Fonseca, Plastic Strain Mapping with Sub-micron Resolution Using Digital Image Correlation, Experimental Mechanics 53(5) (2013) 743-754.

[120] D.S. Yan, C.C. Tasan, D. Raabe, High resolution in situ mapping of microstrain and microstructure evolution reveals damage resistance criteria in dual phase steels, Acta Materialia 96 (2015) 399-409.

[121] A. Githens, S. Daly, Patterning corrosion-susceptible metallic alloys for digital image correlation in a scanning electron microscope, Strain 53(1) (2017) e12215.

[122] A. Orozco-Caballero, D. Lunt, J.D. Robson, J. Quinta da Fonseca, How magnesium accommodates local deformation incompatibility: A high-resolution digital image correlation study, Acta Materialia 133 (2017) 367-379.

[123] Q. Chen, G.A. Thouas, Metallic implant biomaterials, Materials Science and Engineering: R: Reports 87 (2015) 1-57.

[124] J. Mohd Jani, M. Leary, A. Subic, M.A. Gibson, A review of shape memory alloy research, applications and opportunities, Materials & Design (1980-2015) 56 (2014) 1078-1113.

[125] R. Delville, B. Malard, J. Pilch, P. Sittner, D. Schryvers, Transmission electron microscopy investigation of dislocation slip during superelastic cycling of Ni–Ti wires, International Journal of Plasticity 27(2) (2011) 282-297.

[126] E. Dordoni, L. Petrini, W. Wu, F. Migliavacca, G. Dubini, G. Pennati, Computational Modeling to Predict Fatigue Behavior of NiTi Stents: What Do We Need?, Journal of Functional Biomaterials 6(2) (2015) 299-317.

[127] X.Y. Gong, A.R. Pelton, T.W. Duerig, N. Rebelo, K. Perry, Finite element analysis and experimental evaluation of superelastic Nitinol stent, SMST-2003: Proceedings of the International Conference on Shape Memory and Superelastic Technologies (2004) 453-462.

[128] Y. Liu, The superelastic anisotropy in a NiTi shape memory alloy thin sheet, Acta Materialia 95 (2015) 411-427.

[129] N.J. Bechle, S. Kyriakides, Evolution of localization in pseudoelastic NiTi tubes under biaxial stress states, International Journal of Plasticity 82 (2016) 1-31.

[130] C. Grabe, O.T. Bruhns, Path dependence and multiaxial behavior of a polycrystalline NiTi alloy within the pseudoelastic and pseudoplastic temperature regimes, International Journal of Plasticity 25(3) (2009) 513-545.

[131] Q.-P. Sun, Z.-Q. Li, Phase transformation in superelastic NiTi polycrystalline micro-tubes under tension and torsion––from localization to homogeneous deformation, International Journal of Solids and Structures 39(13) (2002) 3797-3809.

[132] D. Helm, P. Haupt, Shape memory behaviour: modelling within continuum thermomechanics, International Journal of Solids and Structures 40(4) (2003) 827-849.

[133] L.C. Brinson, I. Schmidt, R. Lammering, Stress-induced transformation behavior of a polycrystalline NiTi shape memory alloy: micro and macromechanical investigations via in situ optical microscopy, Journal of the Mechanics and Physics of Solids 52(7) (2004) 1549-1571.

[134] J.A. Shaw, S. Kyriakides, Thermomechanical aspects of NiTi, Journal of the Mechanics and Physics of Solids 43(8) (1995) 1243-1281.

[135] P.R. Willmott, D. Meister, S.J. Leake, M. Lange, A. Bergamaschi, M. Böge, M. Calvi, C. Cancellieri, N. Casati, A. Cervellino, Q. Chen, C. David, U. Flechsig, F. Gozzo, B. Henrich, S. Jäggi-Spielmann, B. Jakob, I. Kalichava, P. Karvinen, J. Krempasky, A. Lüdeke, R. Lüscher, S. Maag, C. Quitmann, M.L. Reinle-Schmitt, T. Schmidt, B. Schmitt, A. Streun, I. Vartiainen, M. Vitins, X. Wang, R. Wullschleger, The Materials Science beamline upgrade at the Swiss Light Source, Journal of Synchrotron Radiation 20(Pt 5) (2013) 667-682.

[136] A.P. Hammersley, S.O. Svensson, M. Hanfland, A.N. Fitch, D. Hausermann, Two-dimensional detector software: From real detector to idealised image or two-theta scan, High Pressure Research 14(4-6) (1996) 235-248.

[137] T. Roisnel, J. Rodríquez-Carvajal, WinPLOTR: A Windows Tool for Powder Diffraction Pattern Analysis, Materials Science Forum 378-381 (2001) 118-123.

[138] H.P. Klug, L.E. Alexander, X-Ray Diffraction Procedures: For Polycrystalline and Amorphous Materials, Wiley, New York, 1974.

[139] S.I. Wright, M.M. Nowell, EBSD image quality mapping, Microscopy and microanalysis : the official journal of Microscopy Society of America, Microbeam Analysis Society, Microscopical Society of Canada 12(1) (2006) 72-84.

[140] E. Goo, T. Duerig, K. Melton, R. Sinclair, Mechanical Twinning in Ti50ni47fe3 and Ti49ni51 Alloys, Acta Metallurgica 33(9) (1985) 1725-1733.

[141] I. Karaman, A.V. Kulkarni, Z.P. Luo, Transformation behaviour and unusual twinning in a NiTi shape memory alloy ausformed using equal channel angular extrusion, Philosophical Magazine 85(16) (2005) 1729-1745.

[142] C.E. Krill, A short polemic on crystallite size/strain determination using x-ray diffraction, in: U.d. Saarlandes (Ed.) 1994.

[143] A.D. Kammers, S. Daly, Digital Image Correlation under Scanning Electron Microscopy: Methodology and Validation, Experimental Mechanics 53(9) (2013) 1743-1761.

[144] R. Heinen, K. Hackl, W. Windl, M.F.X. Wagner, Microstructural evolution during multiaxial deformation of pseudoelastic NiTi studied by first-principles-based micromechanical modeling, Acta Materialia 57(13) (2009) 3856-3867.

[145] S.C. Mao, J.F. Luo, Z. Zhang, M.H. Wu, Y. Liu, X.D. Han, EBSD studies of the stress-induced B2–B19′ martensitic transformation in NiTi tubes under uniaxial tension and compression, Acta Materialia 58(9) (2010) 3357-3366.

[146] M. Kimiecik, J.W. Jones, S. Daly, Grain orientation dependence of phase transformation in the shape memory alloy Nickel-Titanium, Acta Materialia 94 (2015) 214-223.

[147] H.M. Paranjape, P.P. Paul, H. Sharma, P. Kenesei, J.S. Park, T.W. Duerig, L.C. Brinson, A.P. Stebner, Influences of granular constraints and surface effects on the heterogeneity of elastic, superelastic, and

plastic responses of polycrystalline shape memory alloys, Journal of the Mechanics and Physics of Solids 102 (2017) 46-66.

[148] A. Mehta, X.Y. Gong, V. Imbeni, A.R. Pelton, R.O. Ritchie, Understanding the Deformation and Fracture of Nitinol Endovascular Stents Using In Situ Synchrotron X-Ray Microdiffraction, Advanced Materials 19(9) (2007) 1183-1186.

[149] G. Kang, D. Song, Review on structural fatigue of NiTi shape memory alloys: Pure mechanical and thermo-mechanical ones, Theoretical and Applied Mechanics Letters 5(6) (2015) 245-254.

[150] L. Orgeas, D. Favier, Non-symmetric tension-compression behaviour of NiTi alloy, Journal de Physique IV 5(C8) (1995) 605-610.

[151] K. Jacobus, H. Sehitoglu, M. Balzer, Effect of stress state on the stress-induced martensitic transformation in polycrystalline Ni-Ti alloy, Metallurgical and Materials Transactions A 27(10) (1996) 3066-3073.

[152] R. Plietsch, K. Ehrlich, Strength differential effect in pseudoelastic NiTi shape memory alloys, Acta Materialia 45(6) (1997) 2417-2424.

[153] W.-N. Hsu, E. Polatidis, M. Šmíd, N. Casati, S. Van Petegem, H. Van Swygenhoven, Load path change on superelastic NiTi alloys: In situ synchrotron XRD and SEM DIC, Acta Materialia 144 (2018) 874-883.

[154] G. Eggeler, E. Hornbogen, A. Yawny, A. Heckmann, M. Wagner, Structural and functional fatigue of NiTi shape memory alloys, Materials Science and Engineering: A 378(1) (2004) 24-33.

[155] M.J. Mahtabi, N. Shamsaei, M.R. Mitchell, Fatigue of Nitinol: The state-of-the-art and ongoing challenges, Journal of the Mechanical Behavior of Biomedical Materials 50 (2015) 228-254.

[156] B. Strnadel, S. Ohashi, H. Ohtsuka, S. Miyazaki, T. Ishihara, Effect of mechanical cycling on the pseudoelasticity characteristics of Ti⬚Ni and Ti⬚Ni⬚Cu alloys, Materials Science and Engineering: A 203(1) (1995) 187-196.

[157] H. Sehitoglu, R. Anderson, I. Karaman, K. Gall, Y. Chumlyakov, Cyclic deformation behavior of single crystal NiTi, Materials Science and Engineering: A 314(1) (2001) 67-74.

[158] S. Mao, X. Han, M.H. Wu, Z. Zhang, F. Hao, D. Liu, Y. Zhang, B. Hou, Effect of Cyclic Loading on Apparent Youngs Modulus and Critical Stress in Nano-Subgrained Superelastic NiTi Shape Memory Alloys, MATERIALS TRANSACTIONS 47(3) (2006) 735-741.

[159] X.M. Wang, Y.F. Wang, Z.Z. Lu, C.H. Deng, Z.F. Yue, An experimental study of the superelastic behavior in NiTi shape memory alloys under biaxial proportional and non-proportional cyclic loadings, Mechanics of Materials 42(3) (2010) 365-373.

[160] C. Maletta, E. Sgambitterra, F. Furgiuele, R. Casati, A. Tuissi, Fatigue properties of a pseudoelastic NiTi alloy: Strain ratcheting and hysteresis under cyclic tensile loading, International Journal of Fatigue 66 (2014) 78-85.

[161] S. Jaeger, B. Maaß, J. Frenzel, M. Schmidt, J. Ullrich, S. Seelecke, A. Schütze, O. Kastner, G. Eggeler, On the widths of the hysteresis of mechanically and thermally induced martensitic transformations in Ni–Ti-based shape memory alloys, International Journal of Materials Research 106(10) (2015) 1029-1039.

[162] B. Malard, J. Pilch, P. Sittner, R. Delville, C. Curfs, In situ investigation of the fast microstructure evolution during electropulse treatment of cold drawn NiTi wires, Acta Materialia 59(4) (2011) 1542-1556.

[163] H. Tobushi, Y. Shimeno, T. Hachisuka, K. Tanaka, Influence of strain rate on superelastic properties of TiNi shape memory alloy, Mechanics of Materials 30(2) (1998) 141-150.

[164] H. Soul, A. Isalgue, A. Yawny, V. Torra, F.C. Lovey, Pseudoelastic fatigue of NiTi wires: frequency and size effects on damping capacity, Smart Materials and Structures 19(8) (2010).

[165] E. Polatidis, W.-N. Hsu, M. Šmíd, H. Van Swygenhoven, A High Resolution Digital Image Correlation Study under Multiaxial Loading, Experimental Mechanics 59(3) (2019) 309-317.

[166] T.J. Lim, D.L. McDowell, Path dependence of shape memory alloys during cyclic loading, Journal of Intelligent Material Systems and Structures 6(6) (1995) 817-830.

[167] H. Sehitoglu, I. Karaman, R. Anderson, X. Zhang, K. Gall, H.J. Maier, Y. Chumlyakov, Compressive response of NiTi single crystals, Acta Materialia 48(13) (2000) 3311-3326.

[168] P. Šittner, V. Novák, Anisotropy of martensitic transformations in modeling of shape memory alloy polycrystals, International Journal of Plasticity 16(10) (2000) 1243-1268.

[169] J. Pfetzing-Micklich, R. Ghisleni, T. Simon, C. Somsen, J. Michler, G. Eggeler, Orientation dependence of stress-induced phase transformation and dislocation plasticity in NiTi shape memory alloys on the micro scale, Materials Science and Engineering: A 538 (2012) 265-271.

[170] K. Gall, T.J. Lim, D.L. McDowell, H. Sehitoglu, Y.I. Chumlyakov, The role of intergranular constraint on the stress-induced martensitic transformation in textured polycrystalline NiTi, International Journal of Plasticity 16(10) (2000) 1189-1214.

[171] Y. Liu, Z.L. Xie, J. Van Humbeeck, L. Delaey, Effect of texture orientation on the martensite deformation of NiTi shape memory alloy sheet, Acta Materialia 47(2) (1999) 645-660.

[172] Y. Liu, Z. Xie, J.V. Humbeeck, L. Delaey, Y. Liu, On the deformation of the twinned domain in Niti shape memory alloys, Philosophical Magazine A 80(8) (2000) 1935-1953.

[173] K. Gall, H. Sehitoglu, The role of texture in tension–compression asymmetry in polycrystalline NiTi, International Journal of Plasticity 15(1) (1999) 69-92.

[174] T. Ezaz, H. Sehitoglu, W. Abuzaid, H.J. Maier, Higher order twin modes in martensitic NiTi—The (201$^-$) case, Materials Science and Engineering: A 558 (2012) 422-430.

[175] S.C. Mao, X.D. Han, Y.B. Tian, J.F. Luo, Z. Zhang, Y. Ji, M.H. Wu, In situ EBSD investigations of the asymmetric stress-induced martensitic transformation in TiNi shape memory alloys under bending, Materials Science and Engineering: A 498(1) (2008) 278-282.

[176] G. Laplanche, J. Pfetzing-Micklich, G. Eggeler, Sudden stress-induced transformation events during nanoindentation of NiTi shape memory alloys, Acta Materialia 78 (2014) 144-160.

[177] K. Bhattacharya, Microstructure of Martensite: Why it Forms and how it Gives Rise to the Shape-memory Effect, OUP Oxford2003.

[178] K. Madangopal, The self accommodating martensitic microstructure of NiTi shape memory alloys, Acta Materialia 45(12) (1997) 5347-5365.

[179] A.R. Pelton, G.H. Huang, P. Moine, R. Sinclair, Effects of thermal cycling on microstructure and properties in Nitinol, Materials Science and Engineering: A 532 (2012) 130-138.

[180] M. Nishida, T. Nishiura, H. Kawano, T. Inamura, Self-accommodation of B19′ martensite in Ti–Ni shape memory alloys – Part I. Morphological and crystallographic studies of the variant selection rule, Philosophical Magazine 92(17) (2012) 2215-2233.

[181] F. Di Gioacchino, J. Quinta da Fonseca, An experimental study of the polycrystalline plasticity of austenitic stainless steel, International Journal of Plasticity 74 (2015) 92-109.

[182] E. Polatidis, W.N. Hsu, M. Šmíd, H. Van Swygenhoven, A high resolution digital image correlation study under multiaxial loading, Experimental Mechanics (2018).

[183] C.C. Tasan, J.P.M. Hoefnagels, M. Diehl, D. Yan, F. Roters, D. Raabe, Strain localization and damage in dual phase steels investigated by coupled in-situ deformation experiments and crystal plasticity simulations, International Journal of Plasticity 63 (2014) 198-210.

[184] Y.B. Das, A.N. Forsey, T.H. Simm, K.M. Perkins, M.E. Fitzpatrick, S. Gungor, R.J. Moat, In situ observation of strain and phase transformation in plastically deformed 301 austenitic stainless steel, Materials & Design 112 (2016) 107-116.

[185] D. Lunt, T. Busolo, X. Xu, J. Quinta da Fonseca, M. Preuss, Effect of nanoscale α2 precipitation on strain localisation in a two-phase Ti-alloy, Acta Materialia 129 (2017) 72-82.

[186] P. Platt, D. Lunt, E. Polatidis, M.R. Wenman, M. Preuss, In-situ digital image correlation for fracture analysis of oxides formed on zirconium alloys, Corrosion Science 111 (2016) 344-351.

[187] Z. Chen, S.H. Daly, Active Slip System Identification in Polycrystalline Metals by Digital Image Correlation (DIC), Experimental Mechanics 57(1) (2017) 115-127.

[188] J. Lackmann, T. Niendorf, M. Maxisch, G. Grundmeier, H.J. Maier, High-resolution in-situ characterization of the surface evolution of a polycrystalline NiTi SMA-alloy under pseudoelastic deformation, Materials Characterization 62(3) (2011) 298-303.

[189] G. Laplanche, J. Pfetzing-Micklich, G. Eggeler, Orientation dependence of stress-induced martensite formation during nanoindentation in NiTi shape memory alloys, Acta Materialia 68 (2014) 19-31.

[190] G. Laplanche, A. Kazuch, G. Eggeler, Processing of NiTi shape memory sheets – Microstructural heterogeneity and evolution of texture, Journal of Alloys and Compounds 651 (2015) 333-339.

[191] J.A. Shaw, S. Kyriakides, On the nucleation and propagation of phase transformation fronts in a NiTi alloy, Acta Materialia 45(2) (1997) 683-700.

[192] M.F.X. Wagner, A. Schaefer, Macroscopic versus local strain rates during tensile testing of pseudoelastic NiTi, Scripta Materialia 63(8) (2010) 863-866.

[193] Y.J. He, Q.P. Sun, Rate-dependent domain spacing in a stretched NiTi strip, International Journal of Solids and Structures 47(20) (2010) 2775-2783.

[194] B. Reedlunn, C.B. Churchill, E.E. Nelson, J.A. Shaw, S.H. Daly, Tension, compression, and bending of superelastic shape memory alloy tubes, Journal of the Mechanics and Physics of Solids 63 (2014) 506-537.

[195] S. Dilibal, Investigation of Nucleation and Growth of Detwinning Mechanism in Martensitic Single Crystal NiTi Using Digital Image Correlation, Metallography, Microstructure, and Analysis 2(4) (2013) 242-248.

[196] G. Laplanche, T. Birk, S. Schneider, J. Frenzel, G. Eggeler, Effect of temperature and texture on the reorientation of martensite variants in NiTi shape memory alloys, Acta Materialia 127 (2017) 143-152.

[197] S.C. Mao, X.D. Han, Z. Zhang, The nano- and mesoscopic cooperative collective mechanisms of inhomogenous elastic-plastic transitions in polycrystalline TiNi shape memory alloys, Journal of Applied Physics 101 (2007) 103522.

[198] X. Zhang, H. Sehitoglu, Crystallography of the B2 → R → B19′ phase transformations in NiTi, Materials Science and Engineering: A 374(1) (2004) 292-302.

[199] K. Otsuka, C.M. Wayman, K. Nakai, H. Sakamoto, K. Shimizu, Superelasticity effects and stress-induced martensitic transformations in Cu-Al-Ni alloys, Acta Metallurgica 24(3) (1976) 207-226.

[200] S. Miyazaki, K. Otsuka, C.M. Wayman, The shape memory mechanism associated with the martensitic transformation in Ti-Ni alloys-I. Self-accommodation, Acta Metallurgica 37(7) (1989) 1873-1884.

[201] T. Ezaz, J. Wang, H. Sehitoglu, H.J. Maier, Plastic deformation of NiTi shape memory alloys, Acta Materialia 61(1) (2013) 67-78.

[202] K. Gall, H. Sehitoglu, Y.I. Chumlyakov, I.V. Kireeva, Tension–compression asymmetry of the stress–strain response in aged single crystal and polycrystalline NiTi, Acta Materialia 47(4) (1999) 1203-1217.

[203] Y. Sutou, T. Omori, R. Kainuma, K. Ishida, Grain size dependence of pseudoelasticity in polycrystalline Cu–Al–Mn-based shape memory sheets, Acta Materialia 61(10) (2013) 3842-3850.

[204] W.Q. Yuan, S. Yi, Pseudo-elastic strain estimation of textured TiNi shape memory alloys, Materials Science and Engineering: A 271(1) (1999) 439-448.

[205] J. Luster, M.A. Morris, Compatibility of deformation in two-phase Ti-Al alloys: Dependence on microstructure and orientation relationships, Metallurgical and Materials Transactions A 26(7) (1995) 1745-1756.

[206] C. Guo, R. Xin, C. Ding, B. Song, Q. Liu, Understanding of variant selection and twin patterns in compressed Mg alloy sheets via combined analysis of Schmid factor and strain compatibility factor, Materials Science and Engineering: A 609 (2014) 92-101.

[207] H. Yu, Y. Xin, A. Chapuis, X. Huang, R. Xin, Q. Liu, The different effects of twin boundary and grain boundary on reducing tension-compression yield asymmetry of Mg alloys, Scientific Reports 6 (2016) 29283.

[208] R.P. Reed, The spontaneous martensitic transformations in 18% Cr, 8% Ni steels, Acta Metallurgica 10(9) (1962) 865-877.

[209] G.B. Olson, M. Cohen, Kinetics of strain-induced martensitic nucleation, Metallurgical Transactions A 6(4) (1975) 791.

[210] P. Behjati, A. Najafizadeh, Role of Chemical Driving Force in Martensitic Transformations of High-Purity Fe-Cr-Ni Alloys, Metallurgical and Materials Transactions A 42(12) (2011) 3752.

[211] M.C. McGrath, D.C. Van Aken, N.I. Medvedeva, J.E. Medvedeva, Work Hardening Behavior in Steel with Multiple TRIP Mechanisms, Metallurgical and Materials Transactions A 44(10) (2013) 4634-4643.

[212] K. Sato, M. Ichinose, Y. Hirotsu, Y. Inoue, Effects of Deformation Induced Phase Transformation and Twinning on the Mechanical Properties of Austenitic Fe-Mn-Al Alloys, ISIJ International 29(10) (1989) 868-877.

[213] T.-H. Lee, E. Shin, C.-S. Oh, H.-Y. Ha, S.-J. Kim, Correlation between stacking fault energy and deformation microstructure in high-interstitial-alloyed austenitic steels, Acta Materialia 58(8) (2010) 3173-3186.

[214] J.E. Wittig, M. Pozuelo, J.A. Jiménez, G. Frommeyer, Temperature Dependent Deformation Mechanisms of a High Nitrogen-Manganese Austenitic Stainless Steel, Steel Research International 80(1) (2009) 66-70.

[215] S. Papula, J. Talonen, H. Hänninen, Effect of Residual Stress and Strain-Induced α'-Martensite on Delayed Cracking of Metastable Austenitic Stainless Steels, Metallurgical and Materials Transactions A 45(3) (2014) 1238-1246.

[216] V. Talyan, R.H. Wagoner, J.K. Lee, Formability of stainless steel, Metallurgical and Materials Transactions A 29(8) (1998) 2161-2172.

[217] A.A. Lebedev, V.V. Kosarchuk, Influence of phase transformations on the mechanical properties of austenitic stainless steels, International Journal of Plasticity 16(7) (2000) 749-767.

[218] S.B. Nizhnik, B.I. Koval'chuk, É.S. Istomina, E.A. Dmitrieva, Structure and mechanical properties of austenitic steel with low-temperature deformation under linear and plane-stress conditions, Strength of Materials 10(1) (1978) 77-83.

[219] A.M. Beese, D. Mohr, Effect of stress triaxiality and Lode angle on the kinetics of strain-induced austenite-to-martensite transformation, Acta Materialia 59(7) (2011) 2589-2600.

[220] G.N. Haidemenopoulos, N. Aravas, I. Bellas, Kinetics of strain-induced transformation of dispersed austenite in low-alloy TRIP steels, Materials Science and Engineering: A 615(Supplement C) (2014) 416-423.

[221] R.G. Stringfellow, D.M. Parks, G.B. Olson, A constitutive model for transformation plasticity accompanying strain-induced martensitic transformations in metastable austenitic steels, Acta Metallurgica et Materialia 40(7) (1992) 1703-1716.

[222] P.J. Brofman, G.S. Ansell, On the Effect of Carbon on the Stacking Fault Energy of Austenitic Stainless Steels, Metallurgical Transactions A 9(6) (1978) 879-880.

[223] U. Stuhr, M. Grosse, W. Wagner, The TOF-strain scanner POLDI with multiple frame overlap—concept and performance, Materials Science and Engineering: A 437(1) (2006) 134-138.

[224] G.B. Olson, M. Cohen, A general mechanism of martensitic nucleation: Part I. General concepts and the FCC → HCP transformation, Metallurgical Transactions A 7(12) (1976) 1897-1904.

[225] T.S. Byun, On the stress dependence of partial dislocation separation and deformation microstructure in austenitic stainless steels, Acta Materialia 51(11) (2003) 3063-3071.

[226] S. Martin, C. Ullrich, D. Rafaja, Deformation of Austenitic CrMnNi TRIP/TWIP Steels: Nature and Role of the ε−martensite, Materials Today: Proceedings 2(Supplement 3) (2015) S643-S646.

[227] O. Grässel, L. Krüger, G. Frommeyer, L.W. Meyer, High strength Fe–Mn–(Al, Si) TRIP/TWIP steels development — properties — application, International Journal of Plasticity 16(10) (2000) 1391-1409.

[228] C.C. Tasan, J.P.M. Hoefnagels, E.C.A. Dekkers, M.G.D. Geers, Multi-Axial Deformation Setup for Microscopic Testing of Sheet Metal to Fracture, Experimental Mechanics 52(7) (2012) 669-678.

[229] J. Talonen, H. Hänninen, Formation of shear bands and strain-induced martensite during plastic deformation of metastable austenitic stainless steels, Acta Materialia 55(18) (2007) 6108-6118.

[230] S. Allain, J.P. Chateau, O. Bouaziz, S. Migot, N. Guelton, Correlations between the calculated stacking fault energy and the plasticity mechanisms in Fe–Mn–C alloys, Materials Science and Engineering: A 387-389 (2004) 158-162.

[231] S. Martin, S. Wolf, U. Martin, L. Krüger, D. Rafaja, Deformation Mechanisms in Austenitic TRIP/TWIP Steel as a Function of Temperature, Metallurgical and Materials Transactions A 47(1) (2016) 49-58.

[232] T.S. Byun, N. Hashimoto, K. Farrell, Temperature dependence of strain hardening and plastic instability behaviors in austenitic stainless steels, Acta Materialia 52(13) (2004) 3889-3899.

[233] D.-F. Li, N.P. O'Dowd, On the evolution of lattice deformation in austenitic stainless steels—The role of work hardening at finite strains, Journal of the Mechanics and Physics of Solids 59(12) (2011) 2421-2441.

[234] C. Caër, R. Pesci, Local behavior of an AISI 304 stainless steel submitted to in situ biaxial loading in SEM, Materials Science and Engineering: A 690 (2017) 44-51.

[235] D.M. Collins, T. Erinosho, F.P.E. Dunne, R.I. Todd, T. Connolley, M. Mostafavi, H. Kupfer, A.J. Wilkinson, A synchrotron X-ray diffraction study of non-proportional strain-path effects, Acta Materialia 124 (2017) 290-304.

[236] D. Kulawinski, K. Nagel, S. Henkel, P. Hübner, H. Fischer, M. Kuna, H. Biermann, Characterization of stress–strain behavior of a cast TRIP steel under different biaxial planar load ratios, Engineering Fracture Mechanics 78(8) (2011) 1684-1695.

[237] A. Hannon, P. Tiernan, A review of planar biaxial tensile test systems for sheet metal, Journal of Materials Processing Technology 198(1) (2008) 1-13.

[238] C.C. Tasan, J.P.M. Hoefnagels, M.G.D. Geers, Microstructural banding effects clarified through micrographic digital image correlation, Scripta Materialia 62(11) (2010) 835-838.

[239] A.D. ABAQUS (2011), DassaultSystèmes, Providence, RI, USA.

[240] P. Reu, Virtual strain gage size study, Experimental Techniques 39(5) (2015) 1-3.

[241] M.A. Sutton, N. Li, D.C. Joy, A.P. Reynolds, X. Li, Scanning Electron Microscopy for Quantitative Small and Large Deformation Measurements Part I: SEM Imaging at Magnifications from 200 to 10,000, Experimental Mechanics 47(6) (2007) 775-787.

[242] M.A. Sutton, N. Li, D. Garcia, N. Cornille, J.J. Orteu, S.R. McNeill, H.W. Schreier, X. Li, A.P. Reynolds, Scanning Electron Microscopy for Quantitative Small and Large Deformation Measurements Part II: Experimental Validation for Magnifications from 200 to 10,000, Experimental Mechanics 47(6) (2007) 789-804.

[243] Z.-H. Xu, X.-D. Li, M.A. Sutton, N. Li, Drift and spatial distortion elimination in atomic force microscopy images by the digital image correlation technique, The Journal of Strain Analysis for Engineering Design 43(8) (2008) 729-743.

[244] N. Li, M.A. Sutton, X. Li, H.W. Schreier, Full-field Thermal Deformation Measurements in a Scanning Electron Microscope by 2D Digital Image Correlation, Experimental Mechanics 48(5) (2008) 635-646.

[245] Z.-H. Xu, H. Jin, W.-Y. Lu, M.A. Sutton, X. Li, Influence of Scanning Rotation on Nanoscale Artificial Strain in Open-Loop Atomic Force Microscopy, Experimental Mechanics 51(4) (2011) 619-624.

[246] T. Zhu, M.A. Sutton, N. Li, J.-J. Orteu, N. Cornille, X. Li, A.P. Reynolds, Quantitative Stereovision in a Scanning Electron Microscope, Experimental Mechanics 51(1) (2011) 97-109.

[247] M. Zecevic, M.V. Upadhyay, E. Polatidis, T. Panzner, H. Van Swygenhoven, M. Knezevic, A crystallographic extension to the Olson-Cohen model for predicting strain path dependence of martensitic transformation, Acta Materialia 166 (2019) 386-401.

[248] J.W. Christian, S. Mahajan, Deformation twinning, Progress in Materials Science 39(1) (1995) 1-157.

[249] J.A. Venables, Deformation twinning in face-centred cubic metals, Philosophical Magazine 6(63) (1961) 379-396.

[250] S. Mahajan, G.Y. Chin, Formation of deformation twins in f.c.c. crystals, Acta Metallurgica 21(10) (1973) 1353-1363.

[251] H. Fujita, T. Mori, A formation mechanism of mechanical twins in F.C.C. Metals, Scripta Metallurgica 9(6) (1975) 631-636.

[252] I. Karaman, H. Sehitoglu, K. Gall, Y.I. Chumlyakov, H.J. Maier, Deformation of single crystal Hadfield steel by twinning and slip, Acta Materialia 48(6) (2000) 1345-1359.

[253] C. Ullrich, R. Eckner, L. Krüger, S. Martin, V. Klemm, D. Rafaja, Interplay of microstructure defects in austenitic steel with medium stacking fault energy, Materials Science and Engineering: A 649(Supplement C) (2016) 390-399.

[254] H. Ding, Z.-Y. Tang, W. Li, M. Wang, D. Song, Microstructures and Mechanical Properties of Fe-Mn-(Al, Si) TRIP/TWIP Steels, Journal of Iron and Steel Research, International 13(6) (2006) 66-70.

[255] D. Borisova, V. Klemm, S. Martin, S. Wolf, D. Rafaja, Microstructure Defects Contributing to the Energy Absorption in CrMnNi TRIP Steels, Advanced Engineering Materials 15(7) (2013) 571-582.

[256] Y.F. Shen, X.X. Li, X. Sun, Y.D. Wang, L. Zuo, Twinning and martensite in a 304 austenitic stainless steel, Materials Science and Engineering: A 552 (2012) 514-522.

[257] H.E. Sabzi, A. Zarei-Hanzaki, H.R. Abedi, A. Mateo, J.J. Roa, The sequential twinning-transformation induced plasticity effects in a thermomechanically processed high Mn austenitic steel, Materials Science and Engineering: A 725 (2018) 242-249.

[258] M.M. Wang, C.C. Tasan, D. Ponge, A. Kostka, D. Raabe, Smaller is less stable: Size effects on twinning vs. transformation of reverted austenite in TRIP-maraging steels, Acta Materialia 79 (2014) 268-281.

[259] O. Engler, V. Randle, Introduction to Texture Analysis: Macrotexture, Microtexture, and Orientation Mapping, CRC Press 2009.

[260] C. Rehrl, S. Kleber, T. Antretter, R. Pippan, A methodology to study crystal plasticity inside a compression test sample based on image correlation and EBSD, Materials Characterization 62(8) (2011) 793-800.

[261] T.R. Bieler, P. Eisenlohr, F. Roters, D. Kumar, D.E. Mason, M.A. Crimp, D. Raabe, The role of heterogeneous deformation on damage nucleation at grain boundaries in single phase metals, International Journal of Plasticity 25(9) (2009) 1655-1683.

Curriculum vitae

Wei-Neng Hsu

Date of birth: August 12, 1990 | Place of birth: Hsinchu, Taiwan | wnhsu@bluewin.ch

Education

École Polytechnique Fédérale de Lausanne (EPFL), Switzerland   09/2015 - Present
PhD, Materials Science and Engineering
Thesis: Deformation-induced martensitic transformation under multiaxial loading

National Tsing Hua University (NTHU), Taiwan   09/2012 – 07/2014
MSc, Engineering and System Science
Thesis: Effects of anisotropic β-Sn alloys on Cu diffusion under a temperature gradient

National Tsing Hua University (NTHU), Taiwan   09/2008 – 06/2012
BSc, Engineering and System Science

Honors

2018   Best poster award in European Symposium on Martensitic Transformations (ESOMAT)
2015   Honorary Member of The Phi Tau Phi Scholastic Honor Society, Taiwan
2014   Bronze-award poster in The Minerals, Metals and Materials Society (TMS)
2012   NTHU Graduate Teaching Assistant Scholarship
2012   NTHU Graduate School Entrance Scholarship

Publications

- E. Polatidis, M. Šmíd, **W.-N. Hsu**, M. Kubenova, J. Capek, T. Panzner, H. Van Swygenhoven, " The interplay between deformation mechanisms in austenitic 304 steel during uniaxial and equibiaxial loading," *Materials Science and Engineering A*, in press

- E. Polatidis, M. Šmíd, I. Kubena, **W.-N. Hsu**, G. Laplanche, H. Van Swygenhoven, "Strain Accommodation in a Superelastic NiTi Alloy: A High Resolution Digital Image Correlation and Transmission Electron Microscopy Study," *Acta Materialia*, under review

- E. Polatidis, **W.-N. Hsu**, M. Šmíd, H. Van Swygenhoven, "A High Resolution Digital Image Correlation Study under Multiaxial Loading," *Experimental Mechanics*, Vol. 59, 2019, pp. 309-317

- **W.-N. Hsu**, E. Polatidis, M. Šmíd, S. Van Petegem, N. Casati, H. Van Swygenhoven, "Deformation and degradation of superelastic NiTi under multiaxial loading," *Acta Materialia*, Vol. 167, 2019, pp. 149-158

- E. Polatidis, **W.-N. Hsu**, M. Šmíd, T. Panzner, S. Chakrabarty, P. Pant, H. Van Swygenhoven, "Suppressed martensitic transformation under biaxial loading in low stacking fault energy metastable austenitic steels," *Scripta Materialia*, Vol. 147, 2018, pp. 27-32

- **W.-N. Hsu**, E. Polatidis, M. Šmíd, N. Casati, S. Van Petegem, H. Van Swygenhoven, "Load path change on superelastic NiTi alloys: In situ synchrotron XRD and SEM DIC," *Acta Materialia*, Vol. 144, 2018, pp. 874-883

- **W.-N. Hsu**, F.-Y. Ouyang, "Effect of Ag3Sn: Effective suppression of thermomigration-induced Cu dissolution in micro-scale Pb-free interconnects," *Materials Chemistry and Physics*, Vol. 165, 2015, pp. 66-71

- **W.-N. Hsu**, F.-Y. Ouyang, "Effects of anisotropic β-Sn alloys on Cu diffusion under a temperature gradient," *Acta Materialia*, Vol. 81, 2014, pp. 141-150

Talks in conferences & workshops

- "Deformation and Degradation of Superelastic NiTi under Multiaxial Cyclic Loadings," TMS 2019, San Antonio, USA

- "How Austenitic TRIP Steels Accommodate Strain under Multiaxial Loading: The Effect of Stacking Fault Energy and Deformation State," TMS 2019, San Antonio, USA

- "Martensitic transition under multiaxial deformation", EPFL-EDMX Research Day 2018, Lausanne, Switzerland

- "Phase Transformation and Degradation of Superelastic NiTi during Uniaxial and Multiaxial Loading," ICSMA 2018, Columbus, USA

- "In-situ Biaxial Loading and Strain Path Change Tests on Superelastic NiTi Employing HRDIC and Synchrotron X-ray Diffraction," CAMTEC IV Symposium on Fine-Scale Mechanical Characterisation and Behaviours, 2018, Cambridge, UK

- "Phase Transformation in NiTi Alloys under Multiaxial Stress," PSI-SLS symposia 2017: Neutrons and X-rays for Mechanics of Materials, Villigen-PSI, Switzerland

- "Load path change on superelastic NiTi alloys: in-situ synchrotron XRD and SEM DIC," Materials Research Society (MRS) Fall Meeting & Exhibit 2017, Boston, USA

- "Martensitic transformation in austenitic steels under multiaxial loading," International Conference on Martensitic Transformations (ICOMAT) 2017, Chicago, USA

- "In-situ HRDIC on superelastic NiTi under strain path change," MRS 2016, Boston, USA

- "Effect of Sn grain orientation on thermomigration behavior in Sn3.5Ag solders," TMS 2014, San Diego, USA

- "Thermomigration in Micro-bumps of Three-dimensional Integrated Circuit Packaging," International Microsystems, Packaging, Assembly and Circuits Technology conference (IMPACT) 2013, Taipei, Taiwan

- "Grain rotation induced by thermomigration in Pb-free solder", TMS 2013, San Antonio, USA

- "Comparison of thermomigration behaviors between Pb-free flip chip solder joints and microbumps in three dimensional integrated circuits: Bump height effect," TMS 2013, San Antonio, USA

Posters in conferences & workshops

- "Phase transformation and degradation of superelastic NiTi during uniaxial and multiaxial loading," CCMX Powder Diffraction School 2018, Villigen-PSI, Switzerland

- "Phase transformation and degradation of superelastic NiTi during uniaxial and multiaxial loading," ESOMAT 2018, Metz, France

- "Martensitic phase transformation under multiaxial deformation", EPFL-EDMX Research Day 2017, Lausanne, Switzerland

  "Effect of grain orientation on the behavior of thermomigration in Sn3.5Ag solder," TMS 2014, San Diego, USA

Extracurricular activities

5th NTHU Volunteer team for IT education in Tanzania   2011-2012
- On-site service (07/2012 – 08-2012) in Libermann Primary School and Usa River Secondary School

NTHU Alumni Wind Orchestra & NTHU Wind Orchestra   2009-2014
- Clarinet player